Model Structure Analysis for Model-based Operation of Petroleum Reservoirs

MODEL STRUCTURE ANALYSIS FOR MODEL-BASED OPERATION OF PETROLEUM RESERVOIRS

PROEFSCHRIFT

ter verkrijging van de graad van doctor
aan de Technische Universiteit Delft,
op gezag van de Rector Magnificus prof. ir. K.C.A.M. Luyben,
voorzitter van het College voor Promoties,
in het openbaar te verdedigen op

maandag 14 juni 2010 om 15:00 uur

door

Jorn François Marie VAN DOREN

ingenieur in de aardwetenschappen
geboren te Sittard

Dit proefschrift is goedgekeurd door de promotoren:

Prof. dr. ir. P.M.J. Van den Hof
Prof. dr. ir. J.D. Jansen

Samenstelling promotiecommisie:

Rector Magnificus,	voorzitter
Prof. dr. ir. P.M.J. Van den Hof,	Technische Universiteit Delft, promotor
Prof. dr. ir. J.D. Jansen,	Technische Universiteit Delft, promotor
Prof. ir. O.H. Bosgra,	Technische Universiteit Delft
Prof. dr. B.E. Ydstie,	Carnegie Mellon
Prof. dr. ing. B.A. Foss,	Norwegian Institute of Technology
Prof. dr. W.R. Rossen,	Technische Universiteit Delft
Prof. dr. ir. A.W. Heemink,	Technische Universiteit Delft

This dissertation has been completed in partial fulfillment of the requirements of the Dutch Institute of Systems and Control DISC for graduate studies.

This research has been conducted in the framework of the "Integrated System Approach Petroleum Production" (ISAPP) programme. The knowledge center is a long-term co-operation of TNO, Shell and Delft University of Technology to increase hydrocarbon recovery through the application of innovative reservoir development and management technologies. Financial support has also been provided through the "Virtual Asset Learning and Understanding Environment" (VALUE) programme, which is sponsored by Shell and SenterNovem.

ISBN: 978-90-8570-570-3

Keywords: petroleum reservoir engineering, controllability, observability, identifiability.

Printed by Wöhrmann Print Service, Zutphen, The Netherlands.

Acknowledgments

Looking back to the time that I have worked on my thesis at DCSC, Applied Earth Sciences and Shell I can say that it has been a great experience. During this time I have had many opportunities to spent time on learning more on systems and control theory, reservoir engineering, doing research and reporting results. Most of all it is the interaction with others that I have enjoyed most.

Paul, Jan Dirk, Okko, thanks for your trust and guidance. You have added great value to this thesis and I truly enjoyed our discussions. I have learnt a lot and admire your ability to ask the right questions and to see it from a broader perspective.
Maarten, Sippe, Gijs and Gerben, thanks a lot for your invaluable input. It has been (and still is) a privilege to work with you. Rik and Dirk, it has been a pleasure to work with you during your theses and I was pleasantly surprised by your ability to learn and persevere during times that it was not completely clear if the results were going to be satisfying. All the best in your petroleum engineering careers!
Colleagues at DCSC and Applied Earth Sciences, thanks for your company in the breaks and all your help. Without you it would definitely not be as good to do a PhD!

Friends of Laga, Erres41 and fraternity, thanks for the great times we had together. It was nice to have so many of you unexpectedly together in Amsterdam in the summer of 2009.
Meike, thanks for traveling considerable distances to take care of the kids and for the holidays we have spent together. I certainly hope that we can continue this for many years to come.
Dear parents, thanks for making the arrangements for the cover and for your unconditional support. I hope I can do the same for my kids!
Dear Emma and Hanna, everyday you manage to amaze me again and allow me to put everything into perspective. I truly enjoy to spend time with you. Eeke, thank you very much for your love and patience. I truly love your 'just do it' mentality!

Jorn Van Doren
Delft, May 2010

Contents

1 CHAPTER

Introduction

The demand for fossil fuels is expected to increase. To meet this demand petroleum reservoirs should be operated more efficiently. This chapter gives an overview of the operation of hydrocarbons reservoirs in which models play an increasingly important role, and provides the research objective and motivations of this thesis.

1.1 Increasing demand for fossil fuels

Since the industrial revolution the world has been depending on fossil fuels; mainly as energy source but also as providers of e.g. lubricants and plastics. Fossil fuels consist of coal, oil and natural gas. The latter two are also called petroleum, meaning literally 'rock oil'. Also today the world's main energy sources are fossil fuels. A smaller fraction of the total energy (14%) is delivered by nuclear fission, hydro-electric, wind, solar and biomass energy.

In some parts of the world there is a trend to minimize energy consumption, mainly motivated by environmental reasons. For example, in the European Union the energy consumption in 2007 has decreased by 2.2 % (BP Statistical Review of World Energy, 2008). However, in rapidly developing countries such as China and India the demand for energy is increasing drastically. As a result, worldwide there is a growing demand for energy. It is expected that oil and gas will remain the largest energy source for the next decades (International Energy Outlook, 2009). See Figure 1.1 for a historic overview of the marketed energy per energy type, and a projection until 2030.

Considering the estimated reserves of oil and gas (USGS World Petroleum Assessment, 2000) as well as the projected demand for oil and gas (International Energy Outlook, 2009), it can be concluded that the reserves are sufficient for the coming decades. However, as will be explained in the next section, the recovery of these reserves becomes increasingly demanding, and a more efficient operation of petroleum reservoirs would be beneficial to increase petroleum production.

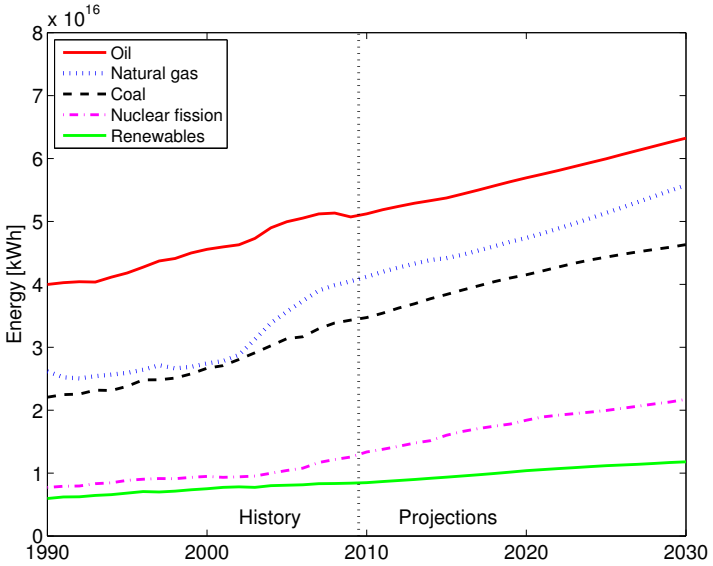

Figure 1.1: World marketed energy use by energy type, 1980-2030 (International Energy Outlook, 2009).

1.2 Petroleum production

1.2.1 Overview of petroleum production

Petroleum is produced from subsurface reservoirs, where it is contained in the pores of the reservoir rock under high pressure and temperature. Once a promising reservoir structure is found by conducting and interpreting geological and seismic surveys, an exploration well is drilled to investigate if it contains petroleum. Subsequently, it is investigated if the petroleum can be recovered in an economically and environmentally sound way. To this purpose several decisions need to be made during the depletion design of the petroleum reservoir. An example of such a decision is where to drill a well such that the total amount of produced hydrocarbons can be maximized.

These decisions directly influence the dynamic processes that play a role during the recovery of the fluids from the reservoir. These processes mainly concern reservoir pressure and saturations, i.e. the fractions of oil, gas and water occupying the pore space. Initially, during the primary recovery phase, the large pressure in the reservoir is driving the oil and gas towards the wells and the surface. However, due to production the reservoir pressure declines and at a certain point in time the pressure is insufficient to drive the oil and gas to the wells and the surface. During the secondary recovery phase the reservoir pressure is increased by injecting water via injection wells - see Figure 1.2. Besides giving pressure support, the injected water can also drive the oil towards the production wells.

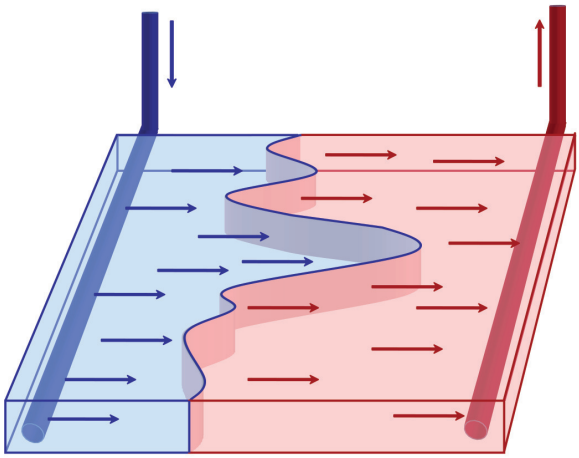

Figure 1.2: Process of water flooding using a horizontal injection and production well. The irregular-shaped oil-water front is a result of the reservoir heterogeneities (after Brouwer 2004; van Essen et al. 2009).

This process is called water flooding. Water flooding can increase the recovery of oil and gas with a few percent to several tens of percent - see Jansen et al. (2008) and references therein for examples. In certain cases, during the tertiary recovery phase, additional oil and gas is recovered by injecting CO_2 or chemicals.

One of the reservoir properties that can have a large influence on the dynamic processes in the reservoir is the permeability of the rock. The permeability describes how easily fluids can move through the rock, and since the rock is heterogeneous the permeability can greatly vary throughout the reservoir: through some parts of the reservoir the fluids cannot flow at all, and through other parts the fluids can flow easily. As a result, there can exist preferential flow paths in the reservoir through which fluids can move faster. For example, water is injected into the reservoir with the aim to drive the remaining oil towards a production well, see Figure 1.2. However, in some cases the water encounters a high-permeable area in the reservoir and directly flows to the production well, bypassing the oil in some parts of the reservoir. The production well is then producing water, which at the surface needs to be disposed of in an environmentally friendly way.

After production the petroleum is transported to refineries where it is refined to e.g. gasoline or bitumen. So in addition also decisions about the surface facilities and infrastructure need to be made. However, in this thesis only the reservoir and the wells are considered, which will be considered as the system of interest.

1.2.2 Recent trends in hydrocarbon production

It becomes more and more challenging to meet the increasing demand for hydrocarbons. The production rates of currently producing oil reservoirs decline more

rapidly than expected. In addition, recently discovered reservoirs are often found in environments that are challenging to operate in. This is referred to as that the easy oil has been found (e.g. Voss and Patel 2007). Examples of such environments are arctic or deep sea environments. The increasing complexity in hydrocarbon production is combined with an expected loss of experience and knowledge, for a large part due to the expected retirement of 40% of the E&P workforce within the coming decade (e.g. Parry et al. 2006). This demands for a more efficient and rationalized operation of petroleum reservoirs.

Fortunately, in the last decades the control possibilities, i.e. the influence that decisions can have on the processes in the reservoir, have increased due to increased capabilities of hardware. There are currently wells with internal control valves that can be remotely operated such that some parts of the well are open and other parts are closed to flow from the reservoir. Also, because of increased control over the drilling process it is possible to drill complex well configurations such as horizontal wells or multi-lateral wells with multiple branches, offering extra possibilities to increase hydrocarbon production.

For the decision making it is beneficial to know the relevant properties of the reservoir, such as the heterogeneities in the reservoir rock that are relevant for the flow. These properties are to a large extent unknown, certainly in the beginning of the reservoir life. Therefore, wellbore measurements in the form of core samples or wireline logs are taken to increase the knowledge of the reservoir. Moreover, production measurements such as pressure and rate measurements also contain indirect information about the permeability distribution in the reservoir. Furthermore, recently measurement devices have been developed and implemented that nearly continuously give information about the downhole pressures and oil, water and gas rates. In addition, time-lapse seismic measurements offer the possibility to monitor the displacement of oil-water or oil-gas fronts in the reservoir at quarterly intervals.

These trends in petroleum production have offered new decision possibilities for the operation of petroleum reservoir. Examples of new decision possibilities are:

- how to operate the control valves in the wells such that the total amount of produced oil is maximized over the life of the reservoir;
- around which well should the reservoir rock be fractured such that the production is increased;
- where to install measurement devices such that the maximum amount of information on the relevant reservoir properties is gained.

Note that there are still processes in the reservoir that can not be controlled. For example, in the situation that gravity effects or capillary pressure effects play a large role in the recovery, the reservoir pressure and saturations are difficult to manipulate and thus the control possibilities are limited. In addition, the number of control possibilities and measurements locations are limited due to economic constraints.

It is desirable to take decisions related to the optimal depletion design and oper-

ation of petroleum reservoirs based on knowledge and measurement data. This can be done by using models of subsurface hydrocarbon reservoirs, in which the relevant dynamic processes are represented, and which support the decisions that need to be taken to increase the reservoir performance. For initial depletion design the use of models can be considered to be standard practice in the oil industry. However, model-based operation of hydrocarbon reservoirs is not standard practice yet. In the next subsection this is discussed in more detail.

1.2.3 Model-based depletion design and operation of hydrocarbon reservoirs

Reservoir modeling

To aid the optimal depletion design of a reservoir often a detailed, physics-based model of the subsurface reservoir is made that integrates all relevant information, e.g. seismic information, geological information, well information. From the detailed model a less detailed reservoir model is derived (i.e. the model is upscaled). To make long-term predictions of the reservoir fluids flowing through the porous rocks and into the wells the partial differential equations (pde's) for mass balance, Darcy's law, equations of state and the relevant initial and boundary conditions are temporally and spatially discretized (i.e. divided into time steps and grid blocks), resulting in a set of ordinary differential equations (ode's). See Chapter 2 for more details. For the remainder of the thesis this will be referred to as the reservoir model. Based on the model the effect of decisions on the future behavior of the reservoir can be predicted, and those decisions can be selected that maximize reservoir performance, e.g. total production or net present value over the life of the reservoir. Examples of decisions during depletion design are the number and type of wells and the size of the platform.

Each grid block in the temporally and spatially discretized reservoir model is associated with its own values for pressure, saturation and rock properties (e.g. permeability). The dynamically varying pressures and saturations in each grid block of the reservoir model are referred to as states, and are denoted by $\mathbf{x}$. The decisions regarding the wells (e.g how to operate the wells, where to position the next well) are referred to as inputs to the reservoir model, and are denoted by $\mathbf{u}$. The resulting petroleum production rates and pressures that are measured in the wells or at the surface are referred to as outputs of the reservoir model, and are denoted by $\mathbf{y}$. The remaining variables in the model are referred to as parameters, and are denoted by $\boldsymbol{\theta}$. They can concern fluid properties (e.g. viscosity, density, compressibility), rock properties (e.g. permeability in each grid block, porosity in each grid block, compressibility) and rock-fluid interaction properties (e.g. capillary pressure, relative permeability), and can be a function of the states.

Since the number of grid blocks in a realistic reservoir model is often chosen in the order of $10^4 - 10^6$, the number of states and parameters is enormous. An advantage of the finely gridded reservoir model is that the fine scale measurements in the wells can be accommodated in the model, and also that the processes in

the reservoir model can be modeled in great detail. E.g. a thin, high permeable streak, which can possibly have a large effect on the flow behavior, can be accurately modeled. A disadvantage of the finely gridded reservoir model is that simulation times are large. This is not a major problem, since the relevant reservoir processes are slow and computing capabilities increase steadily. A more important disadvantage is that the values of the model parameters and states cannot all be verified with measurements, not only due to the large number of states and parameters, but also due to the relatively low information content present in the measurements.

The predicted flow behavior contains uncertainty arising from uncertainty in the model parameters, initial model states and inputs. Also, discretization errors (in time and place) and disturbances on the measurements and inputs are unknown. It can even be uncertain if the relevant physical processes are adequately captured by the model. In case it is assumed that the relevant physical processes are captured, the inputs are known and the discretization errors are minor, then the uncertainty in the model parameters and states can be reduced by estimating the values of parameters and states from measured data. Furthermore, it is difficult to integrate a priori information such as geological information into the model such that after parameter estimation the geological information is still preserved.

To summarize, reservoir models are typically

- physics-based;
- nonlinear in the dynamics;
- after spatial discretization large-scale;
- limited in number of observation and control possibilities;
- uncertain in e.g. parameters, initial states, inputs, boundary conditions, a priori information such as geological information.

Reservoir performance optimization

As mentioned in the previous subsection model-based depletion design can be considered as standard practice in the oil industry and is performed before the reservoir has started production. Model-based operation of hydrocarbon reservoirs is however not standard practice in the oil industry, mainly because the models are considered to be too uncertain and too complex, and at the moment the models are kept up-to-date only on a periodic basis of several years.

One aspect in which a model could aid during the operation of the reservoir is to maximize reservoir performance by manipulating the well rates or pressures, see e.g. Jansen et al. (2009); Van den Hof et al. (2009). The optimal well rates or pressures that maximize reservoir performance can be calculated for a given reservoir model and configuration of wells by model-based control. A model-based control technique that has received a considerable amount of attention is model-based optimal control using a gradient method, in which gradients point into the direction

of an improved performance of the reservoir model. The gradients are usually obtained through the use of adjoint equations. Early applications of adjoint equations to calculate gradients are Ramirez (1987), Asheim (1987), Virnovsky (1991) and Sudaryanto and Yortsos (2000). More recent applications are Brouwer and Jansen (2004) and Zandvliet et al. (2007). Recently, adjoint-based techniques have also been applied to optimize well locations - see Zandvliet et al. (2008) for a promising example. Furthermore, in Van Essen et al. (2009) an approach is presented to deal with the uncertainty in the optimal well rates or pressures that arise from uncertainty in the model. Here, a so-called robust optimal strategy is calculated based on optimal strategies of an ensemble of reservoir models.

The calculated optimal well rates or pressures that maximize the flooding performance over the life of the reservoir can be regarded as the optimum targets that are to be tracked. In process control this type of control is called real-time optimization (RTO), and the optimum targets are subsequently tracked by advanced process control techniques (e.g. model predictive control (MPC)). In daily production operations for hydrocarbon reservoirs this is often not the case: decisions involving e.g. daily well production settings are generally taken without the use of the previously discussed reservoir models, also since the targets that maximize long-term reservoir performance possibly lead to a decrease in short-term production performance. In Van Essen et al. (2009) an hierarchal approach is presented, that offers a promising route to unite long-term production optimization, (i.e. the primary objective) and short-term production optimization (i.e. the secondary objective). Here it is shown that there are remaining degrees of freedom after optimizing the primary objective, and these can be used to solve the secondary optimization problem, while still adhering to the primary optimization solution.

Parameter and state estimation

State and parameter estimation in reservoir engineering are often called history matching (see e.g. Shah et al. 1978). This term seems to indicate that the goal of state and parameter estimation is solely to match the historical production behavior, while the goal should be to obtain models that can predict the future behavior of the reservoir. Furthermore, generating multiple models and selecting only those models that best match the measured data is also called history matching. To avoid this ambiguity in the term history matching the terms parameter estimation and state estimation are used throughout this thesis.

Typically, the physical parameters in reservoir models cannot be uniquely estimated from measurements, meaning that the model parameterization is not identifiable. As a result, the parameter estimation problem is ill-posed. This is problematic, because an incorrect parameter estimate can lead to incorrect long-term predictions (see e.g. Tavassoli et al. 2004, for an example). There are basically two approaches to overcome this. The first approach is to regularize the problem by adding an extra term to the cost function that penalizes deviations from a prior model. This is referred to as the Bayesian approach, and an estimate of the co-

variance of the prior model is needed. The second way is to reparameterize the parameter space, such that the number of parameters is reduced, while at the same time it may be possible to better maintain geological realism.

Reparameterization techniques previously applied in reservoir engineering include zonation (Jacquard and Jain 1965; Jahns 1966), where the parameters in each zone are grouped into one parameter. Grad zones (Bissell et al. 1994; Brun et al. 2004) and adaptive multiscale methods (Grimstad et al. 2003; Berre et al. 2007) are more advanced methods that divide the reservoir model into zones. The number of parameters that need to be estimated is reduced, but these methods possibly lead to discontinuities between the zones that are considered as non-geological. In Shah et al. (1978) the eigenvectors of the sensitivity matrix (i.e. derivative of model outputs with respect to parameters) corresponding to the largest eigenvalues are used to reparameterize the parameter space. Both in Oliver (1996) and Reynolds et al. (1996) this approach is applied to determine permeability and/or porosity parameters. In Reynolds et al. (1996) and Abacioglu et al. (2001) the subspace algorithm as introduced by Oldenburg and Li (1994) is used to solve the identification problem in a computationally efficient way. In Rodrigues (2006) the parameter space is reparameterized based on the right singular vectors of the dimensionless sensitivity matrix as presented in Zhang et al. (2002).

Other parameterizations that have been used in reservoir engineering are wavelets (Sahni and Horne 2005), principle component analysis of the permeability vector (Sarma et al. 2007), and discrete cosine transform (Jafarpour and McLaughlin 2007). Furthermore, the pilot-point method (RamaRao et al. 1995) and gradual deformation (Hu 2000) are reparameterization techniques which are both based on spatial variograms. According to Oliver et al. (2008) the pilot point method possibly introduces non-physical artifacts in the permeability and porosity fields, and the gradual deformation method might experience difficulties converging to a model that is able to match the measurements. Finally, geological parameterizations are available where geologically realistic shapes are used to populate the permeability distribution of the reservoir model. Examples of channel parameterizations are given in Rahon et al. (1998), Bi et al. (1999) and Phan and Horne (2002).

In practice, the problem of estimating the physical parameters and states in reservoir models based on measured data is often approached as an optimization problem. A cost function is defined, typically the weighted squared difference between predicted and measured data, and subsequently minimized over the parameter and state values using a gradient-based optimization procedure. The gradients are usually computed using the adjoint method. Alternatively, in Vasco et al. (1999) streamline simulation models are used to derive gradients of saturation changes with respect to parameters. Parameter and state estimation methods that have recently received considerable attention in reservoir engineering include the representer method (Bennett 2002) and the Ensemble Kalman filter (EnKF, Evensen 2007). The representer method is a gradient-based method which uses the cost function that includes the weighted squared difference between predicted and measured data and also penalizes deviations from a prior model. The representer method has been applied to estimate parameters and states in reservoir mod-

els by e.g. Rommelse et al. (2006) and Przybysz-Jarnut et al. (2007). The EnKF takes a Monte Carlo approach and uses an ensemble of model realizations, represented by the augmented states $\mathbf{x}_\theta := \begin{bmatrix} \mathbf{x}^T & \boldsymbol{\theta}^T \end{bmatrix}^T$, to approximate the gradient of the model predictions with respect to the parameters. Each model is simulated up to the time that measurements become available. Next, the augmented states of each model are estimated using the information in the measurements. The EnKF has been applied to estimate parameters and states in reservoir models by e.g. Naevdal et al. (2005); Reynolds et al. (2006); Rommelse et al. (2006); Evensen (2007).

Model reduction

Reservoir simulation models contain a large number of states and parameters. Research in the area of model reduction of reservoir engineering models has been pursued by e.g. Markovinović et al. (2002), Heijn et al. (2004) and Gildin et al. (2006). They have applied model reduction techniques such as modal decomposition and balanced truncation. Also, proper orthogonal decomposition (POD) is successfully applied to nonlinear reservoir models, e.g. in finding optimal production settings (Van Doren et al. 2004; Cardoso et al. 2008), for reduction of computation time in reservoir simulation (Markovinović and Jansen 2006), and in finding parameter estimates (Kaleta et al. 2009). The fact that these early attempts at model reduction have been successful indicates that the relevant reservoir dynamics can be represented by much simpler models than are used today.

Closed-loop control

In Figure 1.3 the petroleum production process is represented as a model-based, closed-loop controlled process, in which reservoir states and parameters are estimated once measurements become available, and subsequently the most recent model is used to calculate new inputs that are expected to optimize the reservoir performance. Because of the batch-type nature of the reservoir process, the optimization strategy becomes a receding horizon approach. In reservoir engineering this is called 'real-time' or 'closed-loop' reservoir management. Examples of closed-loop reservoir management can be found in Brouwer (2004); Naevdal et al. (2006); Sarma et al. (2006); Jansen et al. (2009). In these examples it is demonstrated that closed-loop reservoir management has the potential to considerably improve the reservoir performance, certainly if the states and parameters are estimated more often. Here it is found that although the estimated parameters do not necessarily resemble the parameters that have generated the measurements (i.e. the true reservoir parameters), the computed control strategy is still able to considerably improve the reservoir performance. Apparently, the estimated models are able to predict the future behavior of the reservoir sufficiently well for the purpose of control. Again, this indicates that the relevant reservoir dynamics can be represented by much simpler models than are used today.

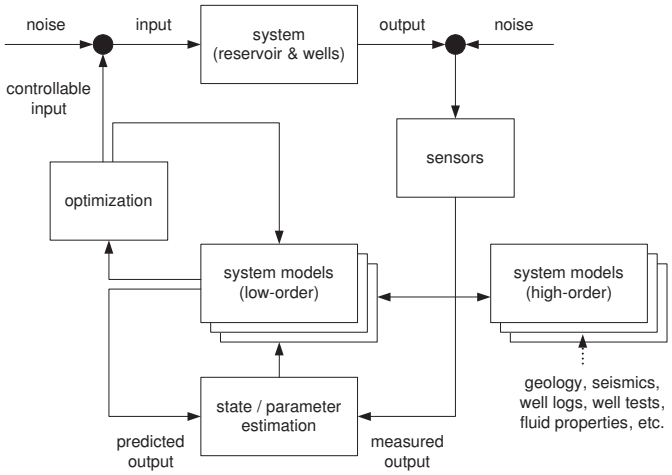

Figure 1.3: Petroleum production represented as a model-based closed-loop controlled process (after Jansen et al. 2005).

1.3 Research objective and thesis outline

1.3.1 Research objective

In the previous part it has been described how models can aid in increasing petroleum production in order to meet the increasing demand for energy. An overview has been given of the research activities related to model-based depletion design and model-based operation of petroleum reservoirs. This has lead to the following research objective of this thesis:

Research objective:
Investigate the possibilities to obtain petroleum reservoir models that are suitable for model-based operation, and that can be validated from production measurements

The balance that plays a role in the research objective is to determine on the one hand models with a complexity that is sufficient for being used for model-based operation of petroleum reservoirs, i.e. the relevant dynamic processes can be adequately described, and on the other hand physics-based models that only contain parameters that can be validated by measurement data, i.e. production measurements.

The most relevant dynamics of the model are to a large extent determined by the controllability and observability properties of the model[1]. Hence, these properties

[1]Controllability is related to the extent to which the states can be influenced by manipulating the inputs to the reservoir model, and observability is related to the extent to which the states can be

play a role as to why the model dynamics can be represented by much simpler models, i.e. models of lower order, which are still suitable for model-based operation. It is first of all unknown how to quantify and interpret the controllability and observability properties of reservoir models, and secondly which pressures and saturations are most relevant for operating the hydrocarbon reservoir. The analysis of controllability and observability can aid in understanding which processes should be accurately captured by reduced-order models, but also in finding optimal positions for a well to increase production, or finding optimal positions of measurement devices.

Then we turn to the second part of the research objective: the model should be validated or estimated from measurement data. Measurement data only contains a limited amount of information, and consequently the models that can be estimated or validated from measurements are also of limited model complexity. If the dynamics of the considered process are linear, then a model can be estimated by applying black-box system identification, which provides a well-studied set of tools for identifying linear models on the basis of experimental data (Ljung 1999). If there is a particular interest in the identification of physical parameters, this often does not raise any additional problems: one has to choose the correct physics-based model structure[2] and identify the parameters through one of the available (possibly non-convex) optimization methods. The only issue that has to be taken care of is that the model structure is identifiable, which implies that the physical parameters can be distinguished from each other on the basis of the model's input-output behavior.

If the dynamics of the considered process are nonlinear, then it can often be linearized around an operating point and the above mentioned linear approach can be followed leading to a linear (approximate) model. However, when essential nonlinear dynamical phenomena are involved and one needs to capture this dynamics in the model, it is much harder to come up with generic black-box techniques for identification. Although there are interesting attempts to capture the nonlinear phenomena in (black-box) model structures as Wiener and/or Hammerstein models (Bai 1998; Zhu 2002), and linear parameter-varying (LPV) models (Verdult and Verhaegen 2002; Toth et al. 2007; Van Wingerden and Verhaegen 2009), information on the underlying physical structure of the nonlinearities is very often required for selection of an appropriate model structure. For models such as reservoir models it is desirable to capture the underlying nonlinear dynamic structure of the process in order to make reliable long-term predictions. First principles model then provide the structure of the model, while incorporated physical parameters have to be estimated from measurement data.

As mentioned before, identifying extremely large number of parameters from measurement data leads to serious problems, and at least it leads to the question which model properties can be reliably estimated from the available measurement data. From a model-based operations point of view (monitoring, control,

estimated from measurement data. The concepts of controllability and observability are defined in Chapter 2.

[2]One formally speaks of a model structure in case the parameters of the model are not yet fixed to a certain value, whereas as soon as all model parameters have been fixed, then one speaks of a model.

optimization) it makes sense to limit the complexity of an identified model to a level where the model can be reliably validated from measurement data. If not, the parameter estimates might be highly determined by the -random- experiment that is done (overfit), leading to unreliable model predictions. In identification this problem is addressed by the notion of identifiability of a model structure, and is directly coupled to the variance of estimated parameters.

Hence it is relevant to analyze the model structure since it can give answers to questions like which parameters can be reliably estimated from specific output variables, and equally important, which parameters cannot be reliably estimated from the output variables? Furthermore, how can the model structure be approximated in terms of its parameter space, such that the parameters in the approximated model structure are identifiable, and the physical interpretation of the parameters are kept?

1.3.2 Outline of thesis

The outline of this thesis is as follows:

- Chapter 2 is an introductory chapter and gives a brief overview of the reservoir modeling process, paying special attention to geological processes. In addition, notions that are used in the remainder of the thesis are presented, such as controllability and observability, identifiability and structural identifiability. Also an overview of parameter estimation techniques in a prediction error setting is presented.
- In Chapter 3 the controllability and observability of single-phase and two-phase reservoir models are analyzed in order to find the most relevant processes during the life of the reservoir. This chapter is partly based on Zandvliet et al. (2008).
- Chapter 4 deals with identifiability and model structure approximation of linear and nonlinear models, including structural identifiability. It is shown how the model structure can be approximated, leading to identifiable parameterizations with parameters that can be physically interpreted. Also, identifiability properties are related to iterative and recursive parameter estimation algorithms. This chapter is for a large part based on Van Doren et al. (2008a, 2009); Van den Hof et al. (2009).
- In Chapter 5 an identifiable parameterization is derived and applied to estimate the grid block permeability of single-phase and two-phase reservoir models. In addition, an alternative, geological parameterization is introduced and applied to estimate reservoir properties. This chapter is partly based on Van Doren et al. (2008a,b).
- In Chapter 6 conclusions are drawn and recommendations for further research are given.

2 CHAPTER

Reservoir Modeling and Estimation

This chapter presents the notation and concepts from literature that will be used in the remainder of this thesis. The first section gives an overview of the geological formation of hydrocarbon reservoirs. Next, the single-phase and two-phase flow models in porous media are described. The subsequent section presents the concepts of controllability and observability, and finally a short overview is given of parameter estimation methods in the prediction error framework.

2.1 Geological background and data sources

2.1.1 Introduction

The main purpose of this section is to give an overview of the geological processes that play a role during the formation of the hydrocarbon reservoir. These processes determine the properties of the reservoir rock through which the fluids move. This material presented in this section is described in e.g. Bell et al. (1989) and Press and Siever (1994). In addition, an overview is given of the data sources that give information about the hydrocarbon reservoir.

2.1.2 Hydrocarbon play

A hydrocarbon play is a set of geological conditions necessary to form a hydrocarbon reservoir. The conditions are:

- Presence of source rock, reservoir rock and seal rock.
- Sufficient burial of source rock to 'cook' the source rock.
- Presence of a suitable trap structure.

- Presence of a migration route for the hydrocarbons from the source rock to the reservoir rock and the trap.

Source rocks are lithified sediments containing large amounts of organic matter, which can liberate hydrocarbons when heated and pressurized during burial (so-called cooking of source rock). Examples of source rocks are coal and organic rich shales. Before burial these sediments could be deposited in a swamp or ocean. Knowledge of the depositional environment helps in predicting the amount of source rock and the properties of the hydrocarbons. Via migration paths (e.g. fractures and joints) the hydrocarbons migrate to the reservoir rock.
Reservoir rocks are lithified sediments containing carbonates or clastic particles as sand grains. The hydrocarbons are in the pores between the sand grains. The volume between the particles divided by the bulk rock volume is called the porosity. When the pores are connected, the hydrocarbons can move and the rock is said to be permeable. Analysis of the reservoir rocks enables to determine the depositional environment (e.g. deposited by a river), the diagenesis (e.g. compaction or cementation) and the structural changes that have occurred over time (e.g. folding and faulting). These processes can help in predicting reservoir characteristics and will be further discussed in the following subsections.
Seals are impermeable rocks that prevent hydrocarbons from migrating further upwards. An example of a seal is a continuous layer of salt or an impermeable shale. Knowledge of the depositional environment helps in determining the quality of the seal (e.g. lateral extent and continuity).

Trap structures prevent the hydrocarbons from migrating in the lateral direction. There are structural traps, stratigraphic traps and a combination of these two. The most common structural trap is the anticline, a dome structure formed in a compressional setting, where the hydrocarbons are below the anticline. Another structural trap is a fault trap where a sealing fault prevents the hydrocarbons from migrating further. The reservoir models discussed in Section 2.2 mainly focus on the reservoir rock with no-flow boundaries.

2.1.3 Deposition and diagenesis

The architecture of the reservoir and seal rock, including the heterogeneities in porosity and permeability distribution, is influenced by many geological processes. In the first part of this subsection the scales of sedimentary heterogeneities in reservoirs are discussed with a special focus on river deposits. In the second part the processes associated with deposition and transport of fluvial sediment are described, including the diagenetic effects and lithification that occur after deposition.

Scales of sedimentary heterogeneities

The porous medium in hydrocarbon reservoirs exhibits heterogeneities at different scales. The different scales are:

- From microns to centimeter scale the *texture* of the reservoir particles plays a role. The texture is the range of grain sizes and the shape of the grains. Data sources that give information for this scale are cuttings and cores obtained during drilling.
- From centimeter to meter scale *sedimentary structures* play a role. A sedimentary structure is any structure of sedimentary rock that was formed at the time of deposition. Examples of sedimentary structures are ripples and sand dunes formed during the sedimentation. The thin layers that can be formed are called laminae, and layers consisting of stacked laminae are called beds. The stacked beds are again grouped in sequences. The transitions between laminae, beds and sequences can result in transitions in porosity and permeability. Data sources that can give information at this scale are cores obtained during drilling and well bore logs.
- From meter to 100 meter scale the *geometry of individual bodies* play a role. The geometry is influenced by the depositional environment. An example of a body is a sinuous sand body formed by river channels. Data sources that can give information about the reservoir at this scale are continuous cores, well bore logs and high resolution seismic surveys.
- At the largest scale the *interrelationship between the bodies* plays a role. Also the connectedness of the bodies and the architecture at this scale is strongly influenced by depositional processes. Data sources that can give information about the reservoir at this scale are continuous cores, well bore logs and seismic surveys.

The texture, sedimentary structures, geometry of individual bodies, and interrelationship between bodies can be studied in detail from outcrops, especially the latter two. Outcrops are rocks that are exposed at the surface and are studied to increase the understanding of depositional environments and other geological processes.

Example: river deposits

As example of a promising hydrocarbon play river deposits are described in more detail. River deposits, or fluvial deposits , are deposited by braided of meandering rivers. Braided rivers have frequently braided channels with a low sinuosity. They form on steep slopes near mountainous areas and carry coarse sediments. In between the channels are sand and gravel bars or small islands. In the case of high discharge new channels are formed. In the case of low discharge the flow in some channels gradually decreases and sometimes is completely stopped. The deposits of braided river systems fine upwards due to the abating flow in the channel(s), starting with coarse gravel. The gravel is overlain with cross-bedded sands and finally a thin sheet of muds. The proportion of muds is low and therefore the channel sands are well connected.

Meandering rivers have a single channel with a high sinuosity - see Figure 2.1. They form on gentle slopes and carry fine sediments. On the outside of the river

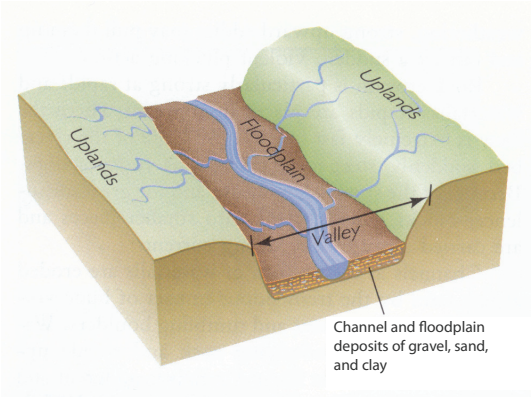

Figure 2.1: Block diagram of a meandering river. Figure from Press and Siever (1994), used with permission.

bend the water flows faster and the channel is eroded. The eroded material is deposited at the inside of the next river bend forming a point bar. As a result the sinuosity is increasing slowly and a characteristic vertical sequence of sediments is formed. Herein the grain size of the sediments decreases from bottom to top, forming a fining upwards sequence. During flooding of the river thin sheets of mud are deposited across the flood plain, forming overbank deposits. Sometimes levées are formed during flooding, which consist of coarse material deposited along the channel. As the meandering channel is increasing in sinuosity and is moving laterally, it incises the flood plains or previously deposited point bars.

All these processes lead to complex reservoirs with long, narrow sand bodies with fining upwards particles, coarse grained levees and sheets of mud. The connectedness of the sand bodies depends on the proportion of overbank to channel deposits, which is controlled by both subsidence rates and the sediment load carried by the original river.

Diagenesis

The processes that take place after deposition are called diagenetic processes. They usually result in a reduction of depositional porosity and permeability. During burial the sediment is compacted under the influence of increasing pressure. The freshly deposited sand particles are repacked and the porosity consequently reduces from 30-40% to 20-30%. Freshly deposited clays contain around 70-90 % of water, which is slowly expelled during compaction. The water contains minerals and slowly moves through overlying sediments to the surface.
Another process that takes place after deposition is cementation, which leads to lithification, where the soft sediment is hardened into rock. During cementation mineral crystals grow within the pore space of the sediment. The crystals precipitate from the pore waters expelled by underlying clay sediments. The cementation

leads to lower porosity, while also the pore throats are clogged by the minerals and as a result the permeability is decreased.

2.1.4 Deformation

The previous subsection described how reservoir rocks are deposited as layers which are close to horizontal. However, real reservoirs are deformed by faults, folds or fractures due to compressional and tensional forces. Faults are brittle failure planes within rocks, across which the rocks have been displaced. Faults can be closed or open to flow, dependent on the differential pressures across the fault, the availability of sufficient clay during the faulting, and the activity along the fault.
Folds are classified as anticlines if the layers are upfold (limbs are lower than its center), and as synclines if the layers are downfold. They can have dimensions ranging from kilometers to centimeters. Anticlines form the most important trapping structure for hydrocarbons. Another important trapping structure is a dome, formed under the influence of volcanic activity, or under the influence of a body of salt, which has a lower density than the surrounding rocks, that pierces through shallower layers and pushes overlying rocks towards the surface.
Fractures are planes of brittle failure which show no movement across the planes. They are common in reservoir rocks, and when they are open to flow they are important fluid paths through the reservoir. Fractures often occur at a scale invisible for seismic.

Figure 2.2 gives an example of the different stages in the development of a geological structure. In stage (a) stratified sediments are deposited on the seafloor, in stage (b) the sediments are compressed horizontally and folded and faulted. In stage (c) the top part of the structure is eroded away as the structure is lifted above sea level, creating a new horizontal surface. In the next stage volcanic eruptions deposit a sheet of lava onto the erosion surface. In stage (e) the tensional forces cause new faults, breaking up the earlier formed features in blocks.

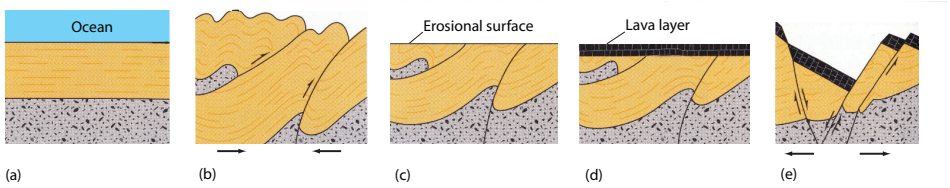

Figure 2.2: Stages in the development of a geological structure. Figure from Press and Siever (1994), used with permission.

2.1.5 Data sources for hydrocarbon reservoirs

Data sources that assist in finding a hydrocarbon reservoir of economic size and deriving its properties are:

- Regional geology
- Seismic measurements
- Well bore measurements and correlation
- Well tests
- Production measurements

Regional geology

Many areas have a description of the regional geology and geological maps. From the description of the regional geology it is possible to deduce the depositional environments and the tectonic settings of a larger area. The depositional environment gives information about the possible texture, sedimentary structures, geometry of the sand and mud bodies and their interconnectedness. The tectonic setting (compressional or tensional) gives information about possible faults, folds and fractures, and their direction.

Seismic measurements

Geophysical or seismic measurements are taken before drilling expensive exploration wells. Their aim is to indicate structures that can serve as an oil trap, the geometry of the potential reservoir and potentially the fluid content. Seismic measurements are based on differences in the rock density and the speed of the wave traveling through the rock. The waves are generated on land by exploding dynamite in shallow holes or vibrator trucks, and on sea by using airguns. The waves sent through the earth are refracted and/or reflected when a medium with other properties is encountered. The intensity and the arrival time(s) of the reflected waves are measured by geophones on land and hydrophones at sea. The arrival times of the reflected waves can be converted to depth using a velocity model of the rock and the seismic velocity log obtained in the well bore. As high frequency waves can travel less far than low frequency waves, the resolution of the seismic image decreases with depth.
Time-lapse seismic or four-dimensional seismic is three-dimensional seismic data acquired at different times over the same area to detect time-dependent changes in a reservoir. The changes can be explained by changes in fluid content (saturation), pressure or temperature.

Well bore measurements and correlation

To prove the presence of hydrocarbons it is necessary to drill exploration wells. During drilling the cuttings of the drilling are gathered and inspected for the presence of fossils, liquids and gasses. It is also possible to retrieve cores with a hollow drill bit. The cores, long cylinders of rock, are used to see the fluid content, the depositional environment, the diagenetic effects and the presence of fractures.

After drilling the well it is common to lower well bore measurement devices, which make logs of the rock. There is a multitude of logs available. Examples are:

- Electrical resistance logs. The electrical resistance indicates water or salt content.
- Density logs. The density, measured by the number of detected neutrons that are emitted from the logging tool, indicates the age of the rocks and its porosity.
- Gamma ray logs. The gamma radiation indicates sand and shale minerals. Shale minerals contain potassium which radiates gamma rays.
- Geomagnetic logs. Magnetism helps in indicating the age of rocks. It is known that the magnetic field of the Earth has switched several times, which can be measured as geomagnetic anomalies in rocks.
- Seismic velocity logs. The seismic velocity of the rock layers is important for the time-depth conversion of the geophysical measurements.
- Temperature logs. Temperature anomalies indicate differences in the geothermal gradient, the entry of fluids into the borehole or the exit of fluid into the formation.
- Formation Micro Image (FMI) logs. FMI logs can visualize sedimentary structures in three dimensions.

Subsequently, during well correlation, logs from several wells are correlated, i.e. the logs of different wells are compared, and structural and sedimentological features are identified and interpreted. The purpose is to map the possibilities of reservoir structures, including the thickness of units and their connectedness. Of course, these are only interpretations and the quality depends among others on the well spacing. In other words, if more wells are drilled and logged, the interpretations can change drastically.

Well tests

Once a well is drilled and it is found that the reservoir contains hydrocarbons, a production test can be done. There are basically three production tests: a drawdown test, a shut-in test and a tracer test. In a drawdown test the fluids are free to flow for a short period. If the pressure declines rapidly, the reservoir is expected to be insignificant. If the pressure declines negligibly, the reservoir is expected

to be significant. Pressure measurements during a drawdown are usually noisy, especially for new wells where well cleanup occurs after begin of production.
During a buildup or shut-in test the bottom hole pressure is measured and analyzed after a producing well is shut in. Buildup tests are used to determine well flow capacity, average permeability, layer thickness, skin and other information. The skin is the zone between the well bore and the reservoir, which is either less permeable than the rest of the reservoir rock (often due to formation damage or mud-filtrate invasion), or more permeable than the rest of the reservoir rock (often due to well stimulation).
Finally, during a tracer test a tracer fluid, usually a fluid with radioactive particles, is injected into the flow stream of one well and measured at other wells to determine fluid paths and velocities. For multi-phase flow special tracer fluids exist that only move with one phase, which result in a velocity log per phase.

Dynamic production measurements

When the wells of a reservoir are injecting and producing it is possible to take production measurements. Available production measurements are

- Bottomhole pressures, i.e. the pressures are measured at the bottom of the well, typically on a daily basis. This requires downhole pressure sensors.
- Tubing head pressures, i.e. the pressures are measured at the top of the well, typically on a daily basis.
- Flow rates, i.e. production rates for a well or a group of wells, typically on a monthly basis. After separation of the produced fluid in its phases the phase rates can be determined.
- 4D seismic measurements, can be regarded as production measurements since the movement of the fluid front can be determined; typically obtained with a frequency of a few years.

2.1.6 Modeling overview

In Figure 2.3 a flowchart is given of the current modeling process. The grey boxes represent analysis and modeling steps and the white boxes represent data sources. Starting with the sedimentology, the cores, cuttings and well bore measurements are examined for sedimentary structures, like texture, laminae and beds. Also the diagenetic history is determined. In the following step the facies are determined by analyzing characteristic sequences and depositional processes. The term facies has two meanings: in the first meaning facies describe a set of features that characterizes a body of rock. For a sedimentary rock the relevant characteristics include geometry, mineral content, color, texture, sedimentary structures and fossil content. In the second meaning facies imply the process that produced the rock body, such as a fluvial facies. Now a depositional model can be constructed using regional geological insight. Next the wells are correlated, the gross thickness,

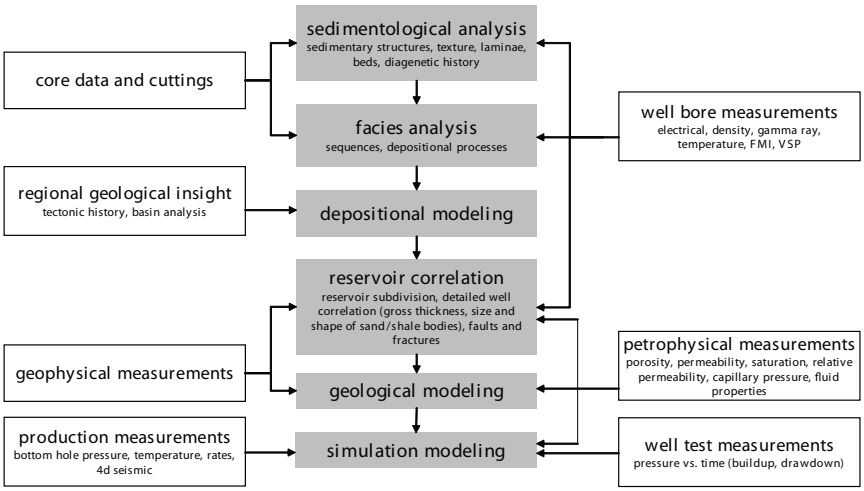

Figure 2.3: Overview of the modeling process, after Bell et al. (1989).

size and shape of sand bodies are determined, and faults which can subdivide the reservoir in zones are determined. Petrophysical measurements from laboratory experiments on reservoir samples, well bore measurements and geophysical measurements are used as data source for this step. In the geological model detailed maps are constructed of the properties such as net sand thickness, porosity, permeability and initial saturation. These property maps are largely based on the measured property values in the wells, and the area in between the wells is often populated using geostatistical methods, e.g. variograms (Deutsch 2001). Well test measurements, petrophysical and geophysical measurements are used as data sources and are integrated into detailed geological models with a large number of grid blocks ($10^7 - 10^8$).

These large-scale geological models are usually not suitable for multi-phase fluid simulations, and therefore the geological models are 'upscaled' to simulation models. Numerous techniques have been proposed to 'upscale' the problem so that computations can be performed on a coarser scale but still retain sufficient information about the fine-scale flow (Farmer 2002). The model parameters and states of the simulation model are estimated using well test measurements and production measurements including 4D (or time-lapse) geophysical measurements. In Section 2.4 this will be described in more detail.

2.2 Modeling of flow in porous media

2.2.1 Single-phase flow equations

Single-phase flow models are considered in Chapters 3 and 5 of this thesis. Its description here is largely based on Jansen (2007) and Zandvliet et al. (2008). Con-

sider the usual equations for isothermal, weakly compressible single-phase flow through porous media, based on conservation of mass and Darcy's law (Aziz and Settari 1986). It is assumed that there is no flow across the boundaries of the reservoir other than through the wells. Furthermore, permeability is isotropic, parameters are not dependent on pressure and gravity is absent. This results in the linear equation

$$\phi c_t \frac{\partial p_t}{\partial t} = \nabla \cdot \left(\frac{k}{\mu} \nabla p_t \right) + q_t, \tag{2.1}$$

where ϕ is porosity, c_t is total compressibility, p_t is fluid pressure, t is time, k is permeability, μ is viscosity, ∇ is the nabla operator, and q_t is flow rate per unit volume.

After spatial discretization we obtain continuous-time model equations, which can be written in partitioned form as:

$$\begin{bmatrix} \mathbf{V}_{11} & \mathbf{0} & \mathbf{0} \\ \mathbf{0} & \mathbf{V}_{22} & \mathbf{0} \\ \mathbf{0} & \mathbf{0} & \mathbf{V}_{33} \end{bmatrix} \begin{bmatrix} \dot{\mathbf{p}}_1 \\ \dot{\mathbf{p}}_2 \\ \dot{\mathbf{p}}_3 \end{bmatrix} + \begin{bmatrix} \mathbf{T}_{11} & \mathbf{T}_{12} & \mathbf{T}_{13} \\ \mathbf{T}_{21} & \mathbf{T}_{22} & \mathbf{T}_{23} \\ \mathbf{T}_{31} & \mathbf{T}_{32} & \mathbf{T}_{33} + \mathbf{J}_p \end{bmatrix} \begin{bmatrix} \mathbf{p}_1 \\ \mathbf{p}_2 \\ \mathbf{p}_3 \end{bmatrix} = \begin{bmatrix} \mathbf{0} \\ \breve{\mathbf{q}}_{well} \\ \mathbf{J}_p \breve{\mathbf{p}}_{well} \end{bmatrix} \tag{2.2}$$

where the diagonal block matrices $\mathbf{V}_{ii}$, $i = 1, 2, 3$, are accumulation matrices with entries that depend on the grid block size, grid block porosities and total compressibility, and the band-diagonal block matrices $\mathbf{T}_{ij}$, $i = 1, 2, 3$, $j = 1, 2, 3$, are transmissibility matrices with entries that depend on the grid block size, fluid viscosity, and permeabilities at the grid block interfaces. The permeability at the grid block interface is given by the harmonic average of the permeability in the grid blocks, i.e. for a one-dimensional reservoir model the permeability at the grid block interface between grid blocks j and $j+1$, denoted by $k^{j+\frac{1}{2}}$, is given by the harmonic average of k^j and k^{j+1}:

$$k^{j+\frac{1}{2}} = \frac{2}{\frac{1}{k^j} + \frac{1}{k^{j+1}}}. \tag{2.3}$$

The elements of vector $\mathbf{p}_1$ are the pressures in those grid blocks (elements) that are not penetrated by a well. The elements of $\mathbf{p}_2$ are the pressures in the blocks where the source terms are prescribed well flow rates $\breve{\mathbf{q}}_{well}$, and those of $\mathbf{p}_3$ are the pressures in the blocks where the source terms are obtained through prescription of the bottom hole pressures with the aid of a well inflow model

$$\bar{\mathbf{q}}_{well} = \mathbf{J}_p \left(\breve{\mathbf{p}}_{well} - \mathbf{p}_3 \right), \tag{2.4}$$

where $\mathbf{J}_p$ is a diagonal matrix of well indices, the elements of $\breve{\mathbf{p}}_{well}$ are the prescribed pressures and those of $\bar{\mathbf{q}}_{well}$ are the resulting well flow rates. Well indices reflect the effect of near-well flow which is normally not properly represented because the grid block dimensions are usually much larger than the well diameter. Throughout this thesis the well indices are computed using the Peaceman model (Peaceman 1978):

$$J = \frac{2\pi k^j \Delta z}{\mu \ln \left(0.14 \sqrt{\Delta x^2 + \Delta y^2} / r_w \right) + S}, \tag{2.5}$$

where Δx, Δy and Δz are the grid block dimensions in x, y and z direction, r_w is the wellbore radius, and S is the skin factor.

To compute the bottom hole pressures $\bar{\mathbf{p}}_{well}$ in the wells where the flow rates have been prescribed we need an additional diagonal matrix $\mathbf{J}_q$ of well indices such that

$$\breve{\mathbf{q}}_{well} = \mathbf{J}_q \left(\bar{\mathbf{p}}_{well} - \mathbf{p}_2 \right). \tag{2.6}$$

Equations (2.4) and (2.6) can be combined to give

$$\begin{bmatrix} \mathbf{0} \\ \bar{\mathbf{p}}_{well} \\ \bar{\mathbf{q}}_{well} \end{bmatrix} = \begin{bmatrix} \mathbf{0} & \mathbf{0} & \mathbf{0} \\ \mathbf{0} & \mathbf{I} & \mathbf{0} \\ \mathbf{0} & \mathbf{0} & -\mathbf{J}_p \end{bmatrix} \begin{bmatrix} \mathbf{p}_1 \\ \mathbf{p}_2 \\ \mathbf{p}_3 \end{bmatrix} + \begin{bmatrix} \mathbf{0} & \mathbf{0} & \mathbf{0} \\ \mathbf{0} & \mathbf{J}_q^{-1} & \mathbf{0} \\ \mathbf{0} & \mathbf{0} & \mathbf{J}_p \end{bmatrix} \begin{bmatrix} \mathbf{0} \\ \breve{\mathbf{q}}_{well} \\ \breve{\mathbf{p}}_{well} \end{bmatrix}. \tag{2.7}$$

If we define the vectors

$$\mathbf{x} := \begin{bmatrix} \mathbf{p}_1 \\ \mathbf{p}_2 \\ \mathbf{p}_3 \end{bmatrix} \in \mathbb{R}^{N_{gb}}, \quad \mathbf{u} := \begin{bmatrix} \breve{\mathbf{q}}_{well} \\ \breve{\mathbf{p}}_{well} \end{bmatrix} \in \mathbb{R}^{m}, \quad \mathbf{y} := \begin{bmatrix} \bar{\mathbf{p}}_{well} \\ \bar{\mathbf{q}}_{well} \end{bmatrix} \in \mathbb{R}^{p},$$

equations (2.2) and (2.7) can be rewritten as

$$\dot{\mathbf{x}} = \mathbf{A}_c \mathbf{x} + \mathbf{B}_c \mathbf{u} \tag{2.8}$$

$$\mathbf{y} = \mathbf{C}\mathbf{x} + \mathbf{D}\mathbf{u}, \tag{2.9}$$

where

$$\mathbf{A}_c = -\begin{bmatrix} \mathbf{V}_{11}^{-1}\mathbf{T}_{11} & \mathbf{V}_{11}^{-1}\mathbf{T}_{12} & \mathbf{V}_{11}^{-1}\mathbf{T}_{13} \\ \mathbf{V}_{22}^{-1}\mathbf{T}_{21} & \mathbf{V}_{22}^{-1}\mathbf{T}_{22} & \mathbf{V}_{22}^{-1}\mathbf{T}_{23} \\ \mathbf{V}_{33}^{-1}\mathbf{T}_{31} & \mathbf{V}_{33}^{-1}\mathbf{T}_{32} & \mathbf{V}_{33}^{-1}\left(\mathbf{T}_{33} + \mathbf{J}_p\right) \end{bmatrix}$$

$$\mathbf{B}_c = \begin{bmatrix} \mathbf{0} & \mathbf{0} \\ \mathbf{V}_{22}^{-1} & \mathbf{0} \\ \mathbf{0} & \mathbf{V}_{33}^{-1}\mathbf{J}_p \end{bmatrix}, \ \mathbf{C} = \begin{bmatrix} \mathbf{0} & \mathbf{I} & \mathbf{0} \\ \mathbf{0} & \mathbf{0} & -\mathbf{J}_p \end{bmatrix}, \ \mathbf{D} = \begin{bmatrix} \mathbf{J}_q^{-1} & \mathbf{0} \\ \mathbf{0} & \mathbf{J}_p \end{bmatrix}.$$

Equations (2.8) and (2.9) are the standard continuous-time, linear time-invariant state space equations as used in the systems and control literature. The parameters in these equations represent the grid block size, grid block porosities, total compressibilities, grid block permeabilities, and fluid viscosity. The states $\mathbf{x}$ represent the pressures in each grid block. The inputs $\mathbf{u}$ represent the prescribed well flow rates $\breve{\mathbf{q}}_{well}$ and the prescribed bottom hole pressure $\breve{\mathbf{p}}_{well}$. The outputs $\mathbf{y}$ represent the resulting bottom hole pressures $\bar{\mathbf{p}}_{well}$ and the resulting well flow rates $\bar{\mathbf{q}}_{well}$.

For simulation of reservoir models time discretization is necessary. A common method for time discretization is the first-order Euler scheme

$$\dot{\mathbf{x}} \approx \frac{\mathbf{x}_{k+1} - \mathbf{x}_k}{\Delta t},$$

where Δt is the discretization time step and where we have applied the notation $\mathbf{x}_k$ to indicate $\mathbf{x}(k\Delta t)$, where the subscript k is the time step counter or discrete time,

and where $\mathbf{x}_k = \begin{bmatrix} x^1 & x^2 & \dots & x^{N_{gb}} \end{bmatrix}^T$ represents the pressure in each grid block $i \in \begin{bmatrix} 1 & \dots & N_{gb} \end{bmatrix}$. In case the remaining terms in (2.8) and (2.9) are evaluated at time t the discretization is called explicit, while if these are evaluated at time $t + \Delta t$ the discretization is called implicit. In practice, implicit time discretization schemes are applied in reservoir model simulation, since this leads to shorter simulation times. However, in the analysis of controllability and observability of single-phase reservoir models in Chapter 3 an explicit time discretization scheme is used, since the dynamics can be more accurately captured in combination with small time steps. As a result, equations (2.8) and (2.9) can be rewritten in general discrete-time state-space form as

$$\mathbf{x}_{k+1} = \mathbf{A}\mathbf{x}_k + \mathbf{B}\mathbf{u}_k \tag{2.10}$$

$$\mathbf{y}_k = \mathbf{C}\mathbf{x}_k + \mathbf{D}\mathbf{u}_k, \tag{2.11}$$

where $\mathbf{A} = (\mathbf{I} + \Delta t \mathbf{A}_c)$ and $\mathbf{B} = \Delta t \mathbf{B}_c$. The discretization time step Δt is set in Chapter 3 to

$$\Delta t = \frac{1}{2} \left| \lambda_{\min} (\mathbf{A}_c) \right|^{-1}, \tag{2.12}$$

where $\lambda_{\min}$ represents the most negative eigenvalue. This leads to quite small time steps, and is referred to as the Nyquist-Shannon sampling time that is needed to accurately capture the dynamics in (2.8) - see e.g. Astrom and Wittenmark (1990). The time steps derived from the Nyquist-Shannon sampling time are smaller than the time steps that are required to meet the Courant-Friedrich-Lewy (CFL) condition to ensure numerical stability of an explicitly discretized model. This is given by

$$\Delta t = 2 \left| \lambda_{\min} (\mathbf{A}_c) \right|^{-1}. \tag{2.13}$$

Note that although here an explicit discretization scheme is presented, the results in this thesis remain valid for implicit discretization schemes.

2.2.2 Two-phase flow equations

Two-phase flow models are considered in Chapter 3 and 5, and its description is largely based on Jansen (2007). Again we consider the usual equations for isothermal weakly compressible flow through porous media, but now for oil and water (Aziz and Settari 1986). It is assumed that there is no flow across the boundaries of the reservoir other than through the wells. Furthermore, permeability is isotropic, parameters are not dependent on pressure and gravity is absent. This results in the nonlinear equations

$$\phi s (c_r + c_w) \frac{\partial p_f}{\partial t} = \nabla \cdot \left(\frac{k k_{rw}}{\mu_w} \nabla p \right) + q_w, \tag{2.14}$$

$$\phi (1 - s) (c_r + c_o) \frac{\partial p_f}{\partial t} = \nabla \cdot \left(\frac{k k_{ro}}{\mu_o} \nabla p \right) + q_o, \tag{2.15}$$

where s is water saturation, c_r is rock compressibility, c_i is compressibility for phase i, μ_i is viscosity for phase i, k_{ri} relative permeability for phase i, and q_i the

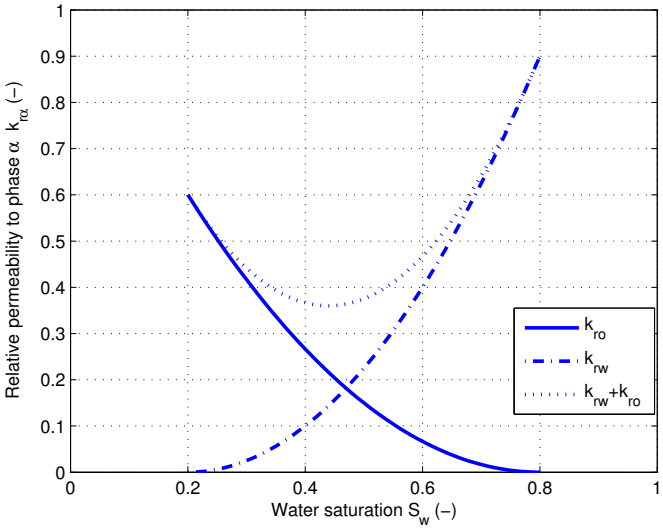

Figure 2.4: Example of the relative permeability of oil and water as function of water saturation.

rate of phase i, where $i \in \{o, w\}$ and where w and o denote the water and oil phase, respectively.

The relative permeabilities k_{ro} and k_{rw} are parameters that represents the physical mechanism that the presence of more than one fluid generally adds resistance to flow. Relative permeability is defined as the ratio of the effective permeability of a fluid at a particular saturation to the absolute permeability of that fluid at total saturation. In this thesis we use the Corey model for saturation-dependent relative permeability, given by

$$k_{rw} = k_{r0,w}\bar{S}^{n_w}, \tag{2.16}$$
$$k_{ro} = k_{r0,o}(1-\bar{S})^{n_o}, \tag{2.17}$$

with

$$\bar{S} := \frac{s - s_{wc}}{1 - s_{or} - s_{wc}}, \quad 0 \le \bar{S} \le 1, \tag{2.18}$$

where $k_{r0,w}$ and $k_{r0,o}$ are the end-point relative permeabilities, n_w and n_o are the Corey exponents, s_{wc} is the connate water saturation (i.e. the water saturation present during formation of the rock, usually the lowest water saturation found in the reservoir), and s_{or} the residual oil saturation. See Figure 2.4 for an example of relative permeability of oil and water as function of water saturation. Note that in case the sum of both relative permeabilities is equal to one, then the phases do not interfere with each other.

After spatial discretization with upstream weighting we obtain continuous-time model equations. In case a well inflow model similar as in (2.7) is included these

can be written in partitioned form as:

$$\begin{bmatrix} \mathbf{V}_{wp} & \mathbf{V}_{ws} \\ \mathbf{V}_{op} & \mathbf{V}_{os} \end{bmatrix} \begin{bmatrix} \dot{\mathbf{p}} \\ \dot{\mathbf{s}} \end{bmatrix} + \begin{bmatrix} \mathbf{T}_w + \mathbf{F}_w \mathbf{J}_p & \mathbf{0} \\ \mathbf{T}_o + \mathbf{F}_o \mathbf{J}_p & \mathbf{0} \end{bmatrix} \begin{bmatrix} \mathbf{p} \\ \mathbf{s} \end{bmatrix} = \begin{bmatrix} \mathbf{F}_w \\ \mathbf{F}_o \end{bmatrix} \left(\mathbf{I}_q + \mathbf{J}_p^* \right) \mathbf{q}_t, \quad (2.19)$$

where submatrices $\mathbf{V}_{wp}$, $\mathbf{V}_{ws}$, $\mathbf{V}_{op}$, $\mathbf{V}_{os}$ are accumulation matrices with entries that depend on grid block dimensions, grid block porosity, compressibility and saturation terms, submatrices $\mathbf{T}_w$ and $\mathbf{T}_o$ are transmissibility matrices with entries that are a function of saturation and depend on grid block dimensions, viscosity, grid block permeability and relative permeability, submatrices $\mathbf{F}_w$ and $\mathbf{F}_o$ are fractional flow matrices with entries that are a function of saturation and depend on viscosity and relative permeability, $\mathbf{p}$ represents the oil pressures in each grid block, $\mathbf{s}$ the water saturations in each grid block, $\mathbf{I}_q$ is a selection matrix containing zeros and ones at appropriate places, $\mathbf{J}_p^*$ contains zeros and $\mathbf{J}_p$ as submatrix, and $\mathbf{q}_t$ is the flow rate per unit volume.

If we define the vectors

$$\mathbf{x} := \begin{bmatrix} \mathbf{p} \\ \mathbf{s} \end{bmatrix} \in \mathbb{R}^{2N_{gb}}, \quad \mathbf{u} := \begin{bmatrix} \check{\mathbf{q}}_{well} \\ \check{\mathbf{p}}_{well} \end{bmatrix} \in \mathbb{R}^{m}, \quad \mathbf{y} := \begin{bmatrix} \bar{\mathbf{p}}_{well} \\ \bar{\mathbf{q}}_{well,w} \\ \bar{\mathbf{q}}_{well,o} \end{bmatrix} \in \mathbb{R}^{p},$$

equation (2.19) can be rewritten in state-space form as

$$\dot{\mathbf{x}} = \mathbf{A}_c^* \mathbf{x} + \mathbf{B}_c^* \mathbf{u} \quad (2.20)$$

$$\mathbf{y} = \mathbf{C}_c^* \mathbf{x} + \mathbf{D}_c^* \mathbf{u}, \quad (2.21)$$

where

$$\mathbf{A}_c^* = -\begin{bmatrix} \mathbf{V}_{wp} & \mathbf{V}_{ws} \\ \mathbf{V}_{op} & \mathbf{V}_{os} \end{bmatrix}^{-1} \begin{bmatrix} \mathbf{T}_w + \mathbf{F}_w \mathbf{J}_p^* & \mathbf{0} \\ \mathbf{T}_o + \mathbf{F}_o \mathbf{J}_p^* & \mathbf{0} \end{bmatrix},$$

$$\mathbf{B}_c^* = \begin{bmatrix} \mathbf{V}_{wp} & \mathbf{V}_{ws} \\ \mathbf{V}_{op} & \mathbf{V}_{os} \end{bmatrix}^{-1} \begin{bmatrix} \mathbf{F}_w \\ \mathbf{F}_o \end{bmatrix} \left(\mathbf{I}_q + \mathbf{J}_p^* \right),$$

$$\mathbf{C}_c^* = \begin{bmatrix} \mathbf{0} & \mathbf{I} & \mathbf{0} \\ \mathbf{0} & \mathbf{0} & -\mathbf{F}_w \mathbf{J}_p \\ \mathbf{0} & \mathbf{0} & -\mathbf{F}_o \mathbf{J}_p \end{bmatrix}, \; \mathbf{D}_c^* = \begin{bmatrix} \mathbf{J}_q^{-1} & \mathbf{0} \\ \mathbf{0} & -\mathbf{F}_w \mathbf{J}_p \\ \mathbf{0} & -\mathbf{F}_o \mathbf{J}_p \end{bmatrix}.$$

After explicit temporal discretization we obtain the nonlinear state-space equations

$$\mathbf{x}_{k+1} = \mathbf{A}(\mathbf{x}_k)\mathbf{x}_k + \mathbf{B}(\mathbf{x}_k)\mathbf{u}_k \quad (2.22)$$

$$\mathbf{y}_k = \mathbf{C}(\mathbf{x}_k)\mathbf{x}_k + \mathbf{D}(\mathbf{x}_k)\mathbf{u}_k \quad (2.23)$$

where $\mathbf{x}_k = \begin{bmatrix} \mathbf{p}_k^T & \mathbf{s}_k^T \end{bmatrix}^T$ represent the states, $\mathbf{p}_k$ the oil pressures in each grid block at time step k and $\mathbf{s}_k$ the water saturations in each grid block at time step k, $\mathbf{y}_k$ the outputs at time step k, and $\mathbf{u}_k$ the inputs at time step k. Matrix $\mathbf{A}$ contains elements that are a function of grid block porosities, fluid densities, fluid compressibilities, grid block interface permeabilities, grid block size, fluid viscosities,

and relative permeabilities. Matrix $\mathbf{B}$ is a matrix with nonzero elements at positions that correspond to well grid blocks and zeros otherwise, where the elements are a function of grid block porosities, fluid densities, fluid compressibilities, grid block interface permeabilities, grid block volume, and fractional flow rates of water and oil.

In the situation that capillary pressure is ignored, (2.22) can be rewritten as

$$\begin{bmatrix} \mathbf{p}_{k+1} \\ \mathbf{s}_{k+1} \end{bmatrix} = \begin{bmatrix} \mathbf{A}_{11}(\mathbf{s}_k) & \mathbf{0} \\ \mathbf{A}_{21}(\mathbf{s}_k) & \mathbf{0} \end{bmatrix} \begin{bmatrix} \mathbf{p}_k \\ \mathbf{s}_k \end{bmatrix} + \begin{bmatrix} \mathbf{B}_1(\mathbf{s}_k) \\ \mathbf{B}_2(\mathbf{s}_k) \end{bmatrix} \mathbf{u}_k, \tag{2.24}$$

showing that both pressures and saturations are driven by the pressures of the previous time step. However, due to the saturation dependency of the relative permeabilities k_r in matrix $\mathbf{A}_{21}$, the saturations are also influenced by the saturations of the previous time step. Furthermore, note that including gravity effects and aquifers leads to extra terms on the right-hand side of (2.22) over which we have no control.

As discussed in Brouwer (2004), the eigenvalue decomposition of $\mathbf{A}_c$ in (2.20) shows a clear distinction between the eigenvalues. The pressure states, part of a diffusive process, are associated with eigenvalues with a high absolute value and exhibit a fast behavior, while the saturation states, part of a convective process, are associated with eigenvalues with a low absolute value and exhibit a slow behavior. This knowledge can be exploited to separate the pressure and saturation states and obtain a singularly perturbed slow approximation of the reservoir model in which the time scales are separated (see e.g. Kokotovic et al. 1986). Consider the reservoir model given in (2.24). Since we are interested in the saturation behavior we assume that the pressure behavior is stationary, leading to setting $\mathbf{p}_{k+1} = \mathbf{p}_k$ in (2.24). We can rewrite this equation to

$$\mathbf{p}_k = \left(\mathbf{I} - \mathbf{A}_{11}(\mathbf{p}_k, \mathbf{s}_k)\right)^{-1} \left(\mathbf{A}_{12}(\mathbf{p}_k, \mathbf{s}_k)\mathbf{s}_k + \mathbf{B}_1(\mathbf{s}_k)\mathbf{u}_k\right). \tag{2.25}$$

If we substitute this in (2.24), we obtain

$$\mathbf{s}_{k+1} = \mathbf{A}_{21}(\mathbf{p}_k, \mathbf{s}_k) \left(\mathbf{I} - \mathbf{A}_{11}(\mathbf{p}_k, \mathbf{s}_k)\right)^{-1} \left(\mathbf{A}_{12}(\mathbf{p}_k, \mathbf{s}_k)\mathbf{s}_k + \mathbf{B}_1(\mathbf{s}_k)\mathbf{u}_k\right) + \mathbf{B}_2(\mathbf{s}_k)\mathbf{u}_k. \tag{2.26}$$

This is a nonlinear equation in terms of water saturation, and this will be used in Chapter 3 to calculate the controllability and observability of the saturation states.

2.3 Controllability and observability

2.3.1 Controllability

The concept of controllability allows us to determine to what extent the state of the model can be influenced by manipulating the input. In this subsection this concept is presented, and in the remainder of this section the concepts of observability,

duality, and balancing and truncation are presented. In Chapter 3 these concepts are applied to analyze (nonlinear) reservoir models.

Following Nijmeijer and van der Schaft (1996) we consider the discrete-time, control affine[1], nonlinear model

$$\mathbf{x}_{k+1} = \mathbf{f}(\mathbf{x}_k) + \sum_{j=1}^{m} \mathbf{g}^j(\mathbf{x}_k)u^j, \quad \mathbf{u} = [u^1, \ldots, u^m]^T \in \mathcal{U} \subset \mathbb{R}^m, \tag{2.27}$$

where $\mathbf{x} = [x^1, \ldots, x^n]^T$ are local coordinates for a state space manifold $\mathcal{M}$, and $\mathbf{f}, \mathbf{g}^1, \ldots, \mathbf{g}^m$ are smooth vectorfields on $\mathcal{M}$. Furthermore it is assumed that the input $\mathbf{u}$ consists of piecewise constant functions. In most applications, and also in reservoir engineering, this is a reasonable assumption. The unique solution of (2.27) at time k for a particular input function $\mathbf{u}$ and initial condition $\mathbf{x}_0$ at time 0 is denoted as $\mathbf{x}(k, 0, \mathbf{x}_0, \mathbf{u})$, or simply as $\mathbf{x}_k$. Following Nijmeijer and van der Schaft (1996) controllability is defined as follows:

Definition 2.1 *The nonlinear model (2.27) is called controllable if for any $\mathbf{x}_1$, $\mathbf{x}_2$ in $\mathcal{M}$ there exists a finite time T and input $\mathbf{u} : [0,\ T] \to \mathcal{U}$ such that $\mathbf{x}(T, 0, \mathbf{x}_1, \mathbf{u}) = \mathbf{x}_2$.*

For a linear time-invariant model (2.10, 2.11) the controllability is determined by the matrix pair $(\mathbf{A}, \mathbf{B})$. After writing (2.10) as

$$\begin{bmatrix} \mathbf{x}_1 \\ \mathbf{x}_2 \\ \mathbf{x}_3 \\ \vdots \end{bmatrix} = \begin{bmatrix} \mathbf{A} \\ \mathbf{A}^2 \\ \mathbf{A}^3 \\ \vdots \end{bmatrix} \mathbf{x}_0 + \begin{bmatrix} \mathbf{B} & & \\ \mathbf{AB} & \mathbf{B} & \\ \mathbf{A}^2\mathbf{B} & \mathbf{AB} & \mathbf{B} \\ & & \end{bmatrix} \begin{bmatrix} \mathbf{u}_0 \\ \mathbf{u}_1 \\ \mathbf{u}_2 \\ \vdots \end{bmatrix} \tag{2.28}$$

one can see that controllability can be analyzed by evaluating the rank of the controllability matrix, which is defined as

$$\mathcal{C}_n \ := \ \begin{bmatrix} \mathbf{B} & \mathbf{AB} & \mathbf{A}^2\mathbf{B} & \ldots & \mathbf{A}^{n-1}\mathbf{B} \end{bmatrix} \in \mathbb{R}^{n \times nm}. \tag{2.29}$$

If $\mathcal{C}_n$ has full rank, then the controllable subspace $\mathbb{X}^{\text{con}} = \text{im}(\mathcal{C}_n) = \mathbb{R}^n$ and any $\mathbf{x}$ can be reached by an admissible choice of $\mathbf{u}$ and the linear model is called controllable[2]. If $\text{rank}(\mathcal{C}_n) < n$, then $\mathbb{X}^{\text{con}} = \text{im}(\mathcal{C}_n) \subset \mathbb{R}^n$.

Alternatively, the controllability Gramian can be used to analyze the controllability properties. The controllability Gramian for finite time is defined as

$$\mathcal{P}_n := \sum_{k=0}^{n} (\mathbf{A}^k\mathbf{B})(\mathbf{A}^k\mathbf{B})^T = \mathcal{C}_n\mathcal{C}_n^T. \tag{2.30}$$

The controllability Gramian for infinite time can be computed by solving the so-called discrete-time Lyapunov or Stein equation

$$\mathbf{A}\mathcal{P}\mathbf{A}^T + \mathbf{B}\mathbf{B}^T = \mathcal{P}. \tag{2.31}$$

[1]For our purpose it suffices to consider the control affine case as is also considered in Nijmeijer and van der Schaft (1996). See the references cited in Nijmeijer and van der Schaft (1996) for the general nonlinear case.

[2]Under these conditions the system is actually called reachable in the systems and control literature, which is equivalent to controllable if $\mathbf{A}$ is nonsingular (Antoulas 2005). Since $\mathbf{A}$ is nonsingular throughout this thesis, we stick to the term controllable.

If the controllability Gramian (2.30) for a state-space model given in (2.10, 2.11) is positive definite (as opposed to semi-definite), then the state-space model is controllable.

There are states of $\mathbb{X}^{\text{con}}$ that require significantly more energy[3] in terms of

$$J_{\text{con}} := \sum_{k=0}^{n} \mathbf{u}_k^T \mathbf{u}_k \tag{2.32}$$

to be reached than others. In Glover (1984) it is shown that the minimal energy required to steer the state from $\mathbf{x}_1$ to $\mathbf{x}_2$ is

$$J_{\text{con}}(\mathbf{x}_1, \mathbf{x}_2) = (\mathbf{x}_2 - \mathbf{x}_1)^T \mathcal{P}_n^{-1} (\mathbf{x}_2 - \mathbf{x}_1) \tag{2.33}$$

assuming $\mathcal{P}_n^{-1}$ exists and where $\mathbf{x}_1$ and $\mathbf{x}_2$ are n time steps apart. This means that the states in $\mathbb{X}^{\text{con}}$ that require the least energy to reach (i.e. are most controllable) have a significant component in the span of the eigenvectors of $\mathcal{P}_n$ corresponding to large (absolute) eigenvalues, where the eigenvalue decomposition (EVD) is given by

$$\mathcal{P}_n = \mathbf{U}\mathbf{\Lambda}\mathbf{U}^T, \tag{2.34}$$

where $\mathbf{\Lambda}$ contains positive, real eigenvalues λ_k, $k = 1, \ldots, n$, on the diagonal and $\mathbf{U}$ contains the eigenvectors. In a similar manner a singular value decomposition (SVD) can be applied to quantify controllability. An advantage of an SVD over an EVD is that the SVD can be applied to any $m \times n$ matrix. In case an SVD is applied to the controllability matrix we can write

$$\mathcal{C}_n = \mathbf{U}\mathbf{\Sigma}\mathbf{V}^T = \begin{bmatrix} \mathbf{U}_1 & \mathbf{U}_2 \end{bmatrix} \begin{bmatrix} \mathbf{\Sigma}_1 & \mathbf{0} \\ \mathbf{0} & \mathbf{\Sigma}_2 \end{bmatrix} \begin{bmatrix} \mathbf{V}_1^T \\ \mathbf{V}_2^T \end{bmatrix}, \tag{2.35}$$

where matrices $\mathbf{U}$ and $\mathbf{V}$ are unitary matrices, $\mathbf{\Sigma} = \text{diag}(\sigma_1, \ldots, \sigma_n)$ with $\sigma_1 \geq \cdots \geq \sigma_l$, and where $\sigma_{l+1}, \ldots, \sigma_n$ are equal to zero or significantly smaller than σ_l. If $l = n$ then $\mathcal{C}_n$ has full rank and controllability is confirmed. Alternatively, an SVD can be applied to the controllability Gramian

$$\mathcal{P}_n = \mathcal{C}_n \mathcal{C}_n^T = \mathbf{U}\mathbf{\Sigma}^2\mathbf{U}^T, \tag{2.36}$$

resulting in the same matrices $\mathbf{U}$ and $\mathbf{\Sigma}$ as in (2.35). Note that matrix $\mathbf{\Lambda}$ in (2.34) is identical to the square of $\mathbf{\Sigma}$ in (2.35).

The column space of $\mathbf{U}_1$ represents the subspace of the state space that is most controllable. The singular values on the diagonal of $\mathbf{\Sigma}$ can be seen as the weights of each column in $\mathbf{U}$. A large singular value indicates that the corresponding direction is a dominant direction in the controllable subspace, while a small singular value indicates that the corresponding direction is a direction that only plays a minor role in the controllable subspace.

[3]The term 'energy' is used loosely here, motivated by the fact that energy can often be written as a quadratic form (e.g., kinetic energy as a function of squared velocity). A more precise term is the squared l_2 norm of the input.

2.3.2 Observability

The problem of observing or reconstructing the state from the output involves the observability of the model. Consider the nonlinear system (2.27) but now together with an output map

$$\mathbf{y} = \mathbf{h}(\mathbf{u}; \mathbf{x}_0), \tag{2.37}$$

where $\mathbf{h} : \mathcal{M} \to \mathcal{Y} = \mathbb{R}^p$ is the smooth output map of the system. Again following Nijmeijer and van der Schaft (1996) the notion of observability is defined as follows:

Definition 2.2 *States $\mathbf{x}_1$, $\mathbf{x}_2$ are said to be indistinguishable (denoted $\mathbf{x}_1 I \mathbf{x}_2$) for (2.37) if for every input $\mathbf{u}$ the output $\mathbf{h}(\mathbf{u}; \mathbf{x}_1)$ of the system for initial state $\mathbf{x}_1$ is identical to the output of $\mathbf{h}(\mathbf{u}; \mathbf{x}_2)$ for initial condition $\mathbf{x}_2$ on their common domain of definition. The system is called observable if $\mathbf{x}_1 I \mathbf{x}_2$ implies $\mathbf{x}_1 = \mathbf{x}_2$.*

For a linear time-invariant model (2.10, 2.11) the observability is determined by the matrix pair $(\mathbf{A}, \mathbf{C})$. After rewriting

$$\begin{bmatrix} \mathbf{y}_0 \\ \mathbf{y}_1 \\ \mathbf{y}_2 \\ \vdots \end{bmatrix} = \begin{bmatrix} \mathbf{C} \\ \mathbf{CA} \\ \mathbf{CA}^2 \\ \vdots \end{bmatrix} \mathbf{x}_0 + ... \tag{2.38}$$

one can see that observability can be analyzed by evaluating the rank of the observability matrix, which is defined as

$$\mathcal{O}_n \quad := \quad \begin{bmatrix} \mathbf{C} \\ \mathbf{CA} \\ \mathbf{CA}^2 \\ \vdots \\ \mathbf{CA}^{n-1} \end{bmatrix}. \tag{2.39}$$

If $\mathcal{O}_n$ has full rank, then the unobservable subspace $\mathbb{X}^{\text{unobs}} := \ker(\mathcal{O}_n) = \emptyset$. The model is then called observable. If $\text{rank}(\mathcal{O}_n) < n$, then $\mathbb{X}^{\text{unobs}} = \ker(\mathcal{O}_n) \subset \mathbb{R}^n$.

Alternatively, the observability Gramian can be used to analyze the observability properties. The observability Gramian for finite time is defined as

$$\mathcal{Q}_n := \sum_{k=0}^{n} (\mathbf{CA}^k)^T (\mathbf{CA}^k) = \mathcal{O}_n^T \mathcal{O}_n. \tag{2.40}$$

The observability Gramian for infinite time can be computed by solving the so-called discrete-time Lyapunov or Stein equation

$$\mathbf{A}^T \mathcal{Q} \mathbf{A} + \mathbf{C}^T \mathbf{C} = \mathcal{Q}. \tag{2.41}$$

If the observability Gramian in (2.40) for a state-space model given in (2.10, 2.11) is positive definite (as opposed to semi-definite) then the state-space model is observable.

There are states not in $\mathbb{X}^{\text{unobs}}$ that induce outputs with significantly more energy in terms of

$$J_{\text{obs}} := \sum_{k=0}^{n} \mathbf{y}_k^T \mathbf{y}_k \tag{2.42}$$

when observed than others. In Glover (1984) it is shown that the maximal energy of the output of the model with initial state $\mathbf{x}_1$ and current state $\mathbf{x}_2$, is given by

$$J_{\text{obs}}(\mathbf{x}_1, \mathbf{x}_2) = (\mathbf{x}_2 - \mathbf{x}_1)^T \mathcal{Q}_n (\mathbf{x}_2 - \mathbf{x}_1), \tag{2.43}$$

where $\mathbf{x}_1$ and $\mathbf{x}_2$ are n time steps apart. This means that the states not in $\mathbb{X}^{\text{unobs}}$ that produce the least energy when observed, have a significant component in the span of the eigenvectors of $\mathcal{Q}_n$ corresponding to small (absolute) eigenvalues. In a similar manner as for controllability, a singular value decomposition (SVD) can be applied to the observability matrix or observability Gramian:

$$\mathcal{O}_n^T = \mathbf{U}\mathbf{\Sigma}\mathbf{V}^T = \begin{bmatrix} \mathbf{U}_1 & \mathbf{U}_2 \end{bmatrix} \begin{bmatrix} \mathbf{\Sigma}_1 & \mathbf{0} \\ \mathbf{0} & \mathbf{\Sigma}_2 \end{bmatrix} \begin{bmatrix} \mathbf{V}_1^T \\ \mathbf{V}_2^T \end{bmatrix}, \tag{2.44}$$

$$\mathcal{Q}_n = \mathcal{O}_n^T \mathcal{O}_n = \mathbf{U}\mathbf{\Sigma}^T\mathbf{U}. \tag{2.45}$$

The left singular vectors $\mathbf{U}_1$ contain the directions in state space that are most observable.

2.3.3 Duality

Alternatively, the observability Gramian of model (2.10, 2.11) can be calculated using the dual model, since the observability Gramian is equivalent to the controllability Gramian of the dual model (e.g. Antoulas 2005). The dual model running backward in time is given by

$$\mathbf{x}'_k = -\mathbf{A}^*\mathbf{x}'_{k+1} - \mathbf{C}^*\mathbf{y}_{k+1}, \tag{2.46}$$

$$\mathbf{u}_{k+1} = \mathbf{B}^*\mathbf{x}'_{k+1} + \mathbf{D}^*\mathbf{y}_{k+1}, \tag{2.47}$$

where * denotes the conjugate transpose, $\mathbf{x}'$ is the dual state, $\mathbf{u}$ is the output and $\mathbf{y}$ the input. As can be seen, in the dual model the inputs have become outputs and vice versa. For nonlinear models the dual model is defined as the dual model of the linearized tangent linear model of the nonlinear model. This property will be exploited in the observability analysis of reservoir models in Chapter 3.

2.3.4 Balancing and truncation

The controllability and observability Gramians are coordinate dependent. For example, for another set of coordinates a transformed state can become more controllable (i.e. requires less energy to reach) and less observable (i.e. produces less energy). This can be seen by considering a linear combination of the states

$$\check{\mathbf{x}}_k = \mathbf{T}\mathbf{x}_k, \tag{2.48}$$

with $\mathbf{T} \in \mathbb{R}^{n \times n}$ a nonsingular transformation matrix. The associated Gramians $\tilde{\mathcal{P}}_n$ and $\tilde{\mathcal{Q}}_n$ satisfy

$$\tilde{\mathcal{P}}_n = \mathbf{T}\mathcal{P}_n\mathbf{T}^T, \quad \tilde{\mathcal{Q}}_n = \mathbf{T}^{-T}\mathcal{Q}_n\mathbf{T}^{-1}. \tag{2.49}$$

In Moore (1981) it is proven for linear models that there exists a balancing transformation matrix $\mathbf{T} = \mathbf{U}_{PQ}$ that makes the controllability and observability Gramians diagonal and equal, resulting in a balanced system:

Definition 2.3 *The system* $(\mathbf{A}, \mathbf{B}, \mathbf{C}, \mathbf{D})$ *is said to be balanced if*

$$\mathcal{P}_n = \mathcal{Q}_n = \mathbf{\Sigma} \tag{2.50}$$

and have the Hankel singular values σ_k, $k = 1, \ldots, n$, *on their diagonal.*

The Hankel singular values are coordinate-*independent*, and σ_k can be interpreted as the energy contribution of the k-th component of the balanced state $\breve{\mathbf{x}}$ to the input-output behavior of the system. If the Hankel singular values decrease rapidly, it can be concluded that most of the input-output behavior is determined by only the first few balanced states. The Hankel singular values can be computed by decomposing the product of both Gramians

$$\mathcal{P}_n\mathcal{Q}_n = \mathbf{U}_{PQ}\mathbf{\Lambda}\mathbf{U}_{PQ}^{-1}, \tag{2.51}$$

where $\mathbf{\Lambda}$ contains positive, real eigenvalues λ_k, $k = 1, \ldots, n$, on the diagonal and $\mathbf{U}_{PQ}$ contains the eigenvectors. Next, the Hankel singular values are computed as

$$\sigma_k \quad := \quad \sqrt{\lambda_k}, \quad k = 1, \ldots, n. \tag{2.52}$$

The eigenvectors of $\mathcal{P}_n\mathcal{Q}_n$ correspond to (combinations of) states that are relevant for the input-output behavior of the model, and the value of the corresponding Hankel singular value gives the relative importance of these (combinations of) states. Alternatively, the product of controllability and observability matrices $\bar{\mathcal{C}}_n\bar{\mathcal{C}}_n^T\bar{\mathcal{O}}_n^T\bar{\mathcal{O}}_n$ can be decomposed to calculate the Hankel singular values.

Finally, it can be shown that truncating the last $n - k$ components of the balanced state leads to a reduced k-th order approximation of the full-order system, for which the error in input-output behavior, measured in terms of the worst-case energy norm (i.e. $\mathcal{H}_\infty$ norm) is given by

$$2\left(\sigma_{k+1} + \ldots + \sigma_n\right), \tag{2.53}$$

or twice the sum of the truncated $n - k$ Hankel singular values (Moore 1981).

2.3.5 Controllability and observability of nonlinear models

Introduction

The definitions of controllability and observability for nonlinear models have been given, and for linear models it has been described how to determine if a model is

controllable or observable. In this subsection two approaches are presented that can be used to analyze the controllability and observability of nonlinear reservoir simulation models. As presented in Chapter 1 reservoir models are large-scale and consequently not all approaches to analyze the controllability and observability of nonlinear models are currently computationally feasible for reservoir models with a large number of state variables. Examples hereof are the nonlinear local controllability and observability analysis with a differential geometric approach (Hermann and Krener 1977) and the application of the nonlinear controllability and observability function (Scherpen 1993; Isidori 1995). Approaches that are currently feasible to analyze the (local) controllability and observability of reservoir models are:

1. Linearize the model equations around a steady-state operating point and analyze the linearized model with controllability and observability tools for LTI models, or linearize along a nominal trajectory and analyze the model with controllability and observability tools for linear time varying (LTV) models;
2. Use empirical Gramians (Lall et al. 2002; Hahn et al. 2003) to approximate the controllability and observability Gramians.

Both approaches will be described in the following subsections.

Linearization

In the first approach the controllability and observability of the nonlinear model are analyzed after linearization. After linearization the controllability and observability of the linearized model can be analyzed with the controllability and observability matrices or Gramians for linear models, as described in Section 2.3. Note that in Nijmeijer and van der Schaft (1996) can be found that the controllability and observability rank conditions of an LTI model are only a sufficient condition for the controllability and observability of the nonlinear model given by (2.27, 2.37). This means that a nonlinear model can be controllable or observable, while its linearization is not since the higher-order derivatives are not taken into account. See e.g. Nijmeijer and van der Schaft (1996) for an example.

Alternatively, the nonlinear model (2.27, 2.37) can be linearized along a state trajectory, resulting in an LTV model. More specifically, the nonlinear model is at time steps $k \in [1, \ldots, N]$ linearized around its current state $\mathbf{x}_k$. The linearized system reads:

$$\mathbf{x}_{k+1} = \mathbf{A}_k(\mathbf{x}_k)\mathbf{x}_k + \mathbf{B}_k(\mathbf{x}_k)\mathbf{u}_k \tag{2.54}$$

$$\mathbf{y}_k = \mathbf{C}_k(\mathbf{x}_k)\mathbf{x}_k \tag{2.55}$$

where

$$\mathbf{A}_k(\mathbf{x}_k) = \left.\frac{\partial \mathbf{f}(\mathbf{x}_k)}{\partial \mathbf{x}}\right|_{\mathbf{x}=\mathbf{x}_k}, \quad \mathbf{B}_k(\mathbf{x}_k) = \left.\frac{\partial \mathbf{g}(\mathbf{x}_k)}{\partial \mathbf{x}}\right|_{\mathbf{x}=\mathbf{x}_k}, \quad \mathbf{C}_k(\mathbf{x}_k) = \left.\frac{\partial \mathbf{h}(\mathbf{x}_k)}{\partial \mathbf{x}}\right|_{\mathbf{x}=\mathbf{x}_k}.$$

In the following the state-dependency of the system matrices is omitted in the notation.

The LTV controllability matrix $\mathcal{C}_{k_i:k_f}$ and observability matrix $\mathcal{O}_{k_i:k_f}$ for this model are given by

$$\mathcal{C}_{k_i:k_f} = \begin{bmatrix} \mathbf{B}_{k_f-1} & \mathbf{A}_{k_f-1}\mathbf{B}_{k_f-2} & \dots & (\mathbf{A}_{k_f-1}\dots\mathbf{A}_{k_i+1}\mathbf{B}_{k_i}) \end{bmatrix}, \tag{2.56}$$

$$\mathcal{O}_{k_i:k_f} := \begin{bmatrix} \mathbf{C}_{k_i} \\ \mathbf{C}_{k_i+1}\mathbf{A}_{k_i} \\ \vdots \\ \mathbf{C}_{k_f}\mathbf{A}_{k_f-1}\dots\mathbf{A}_{k_i} \end{bmatrix}, \tag{2.57}$$

where k_i is the initial time step and k_f is the final time step. If $\mathcal{C}_{k_i:k_f}$ has full rank, then the LTV model is called controllable. If $\mathcal{O}_{k_i:k_f}$ has full rank, then the LTV model is called observable. Note that an SVD can be applied to $\mathcal{C}_{k_i:k_f}$ to quantify controllability, or to $\mathcal{O}^T_{k_i:k_f}$ to quantify observability.

Empirical Gramians

Another option to investigate the controllability and observability of nonlinear models is with empirical Gramians (Lall et al. 2002; Hahn et al. 2003). Empirical Gramians can be computed for nonlinear large-scale models such as reservoir models. Note that they cannot represent the global behavior of nonlinear models, but they can be used for the analysis of nonlinear models for specific inputs $\mathbf{u}_1, \dots, \mathbf{u}_N$ and specific initial conditions $\mathbf{x}_0$.

The controllability Gramian (2.30) can be interpreted as the covariance of the states under specific input conditions. The *empirical* controllability Gramian is computed from the covariance of the states trajectories that result from the chosen input signals. First the input signals with specific excitation sizes and patterns are chosen in a systematic way. For the empirical controllability Gramian consider

$$\mathcal{T}^m = \{(\mathbf{T}_1, \dots, \mathbf{T}_r), \mathbf{T}_l^T\mathbf{T}_l = \mathbf{I} \; \forall \; l, \mathbf{T}_l \in \mathbb{R}^{m\times m}\}, \tag{2.58}$$

$$\mathcal{N} = \{(c_1, \dots, c_s), c_u > 0 \; \forall \; u, c_u \in \mathbb{R}\}, \tag{2.59}$$

$$\mathcal{E}^m = \{(\mathbf{e}_1, \dots, \mathbf{e}_m), \mathbf{e}_i \text{ denote standard unit vectors in } \mathbb{R}^m\}, \tag{2.60}$$

where r represents the number of matrices for excitation patterns $\mathbf{T}_l$, s the number of different excitation sizes c_u for each direction, and m the number of inputs to the system. The matrix $\mathbf{T}_i$ is usually chosen as $\mathbf{I}, -\mathbf{I}$, where $\mathbf{I}$ is the identity matrix and refers to positive perturbations in the state variables, and $-\mathbf{I}$ refers to negative perturbations. The input signal is given by

$$\mathbf{u}_k = c_u\mathbf{T}_l\mathbf{e}_i\mathbf{v}_k + \bar{\mathbf{u}}, \tag{2.61}$$

where c_u is the input size, $\mathbf{T}_l\mathbf{e}_i$ describes the input pattern, $\mathbf{v}_k$ is the nature of the input (e.g. impulse or step input) and $\bar{\mathbf{u}}$ is the mean input. The inputs should be chosen such that they resemble typical inputs of the system.

Next, the input signal in (2.61) is used to generate state trajectories, and the empirical controllability Gramian is defined as

$$\mathcal{P}_e := \sum_{i=1}^{m}\sum_{l=1}^{r}\sum_{u=1}^{s}\frac{1}{rsc_u^2}\sum_{k=k_i}^{k_f}\mathbf{\Phi}_k^{ilu}, \tag{2.62}$$

where $\mathbf{\Phi}_k^{ilu} \in \mathbb{R}^{n\times n}$ is given by

$$\mathbf{\Phi}_k^{ilu} = (\mathbf{x}_k^{ilu} - \bar{\mathbf{x}}^{ilu})^T(\mathbf{x}_k^{ilu} - \bar{\mathbf{x}}^{ilu}), \tag{2.63}$$

where $\bar{\mathbf{x}}_k^{ilu}$ is the mean state and $\mathbf{x}_k^{ilu}$ is the state of the nonlinear system. Here one clearly sees that the covariance of the states are calculated, where the states result from input signal $\mathbf{u}_k$ in (2.61).

If the system is stable, linear and excited with an impulse input, the empirical controllability Gramian is *identical* to the controllability Gramian (Lall et al. 2002). Note that the empirical controllability Gramian calculated based on the snapshots of *one* state trajectory is identical to POD using the method of snapshots (Lall et al. 2002).

Next the empirical observability Gramian is presented. The observability Gramian (2.40) can be interpreted as the covariance of the output under specific initial state conditions. The *empirical* observability Gramian is computed from the outputs for various initial conditions of the system state, while the inputs are kept at their nominal values. Alternatively, as presented in Section 2.3.3 for the linear system, the empirical observability Gramian can also be computed from the dual linearized system trajectories resulting from different dual input signals.

First the initial conditions are chosen in a systematic way. Consider

$$\mathcal{T}^n = \{(\mathbf{T}_1,\ldots,\mathbf{T}_r), \mathbf{T}_l^T\mathbf{T}_l = \mathbf{I}\ \forall\, l, \mathbf{T}_l \in \mathbb{R}^{n\times n}\}, \tag{2.64}$$

$$\mathcal{N} = \{(c_1,\ldots,c_s), c_u > 0\ \forall\, u, c_i \in \mathbb{R}\}, \tag{2.65}$$

$$\mathcal{E}^n = \{(\mathbf{e}_1,\ldots,\mathbf{e}_n), \mathbf{e}_i \text{ denote standard unit vectors in } \mathbb{R}^n\}, \tag{2.66}$$

where r represents the number of matrices for the perturbation directions, s the number of different excitation sizes for each direction, and n the number of states of the system. The initial condition is given by

$$\mathbf{x}_0 = c_u\mathbf{T}_l\mathbf{e}_i + \bar{\mathbf{x}}_0. \tag{2.67}$$

Next, the initial condition in (2.67) is used to generate state trajectories with $\mathbf{u}_k = \bar{\mathbf{u}}$, and the empirical observability Gramian is defined as

$$\mathcal{Q}_e := \sum_{l=1}^{r}\sum_{u=1}^{s}\frac{1}{rsc_u^2}\sum_{k=k_i}^{k_f}\mathbf{T}_l\mathbf{\Psi}_k^{lu}\mathbf{T}_l^T, \tag{2.68}$$

where $\mathbf{\Psi}_k^{lu} \in \mathbb{R}^{n\times n}$ is given by

$$\mathbf{\Psi}_{ij,k}^{lu} = (\mathbf{y}_k^{ilu} - \bar{\mathbf{y}}^{ilu})^T(\mathbf{y}_k^{jlu} - \bar{\mathbf{y}}^{jlu}), \tag{2.69}$$

where $\bar{\mathbf{y}}^{ilu}$ is the mean output and $\mathbf{y}_k^{ilu}$ is the output of the system. Here one clearly sees that the covariance of the states are calculated, where the states result from initial condition $\mathbf{x}_0$ in (2.67). If the system is stable and linear, then the empirical observability Gramian is identical to the observability Gramian (Lall et al. 2002).

The empirical observability Gramian (2.68) is calculated based on the outputs of the model for various initial conditions. However, for applications with a large number of states this approach would be computationally demanding, and in Willcox and Peraire (2002) and Rowley (2005) an alternative approach is presented to approximate the observability Gramian. In their work the observability Gramian is approximated by taking snapshots of the dual linearized system, as is described in Section 2.3. This is computationally more efficient in the case the number of outputs is smaller than the number of states. Note that in this work only one state trajectory is analyzed. In other words, we have chosen $r = s = 1$. However, choosing different inputs to generate other state trajectories can be easily implemented.

2.4 Parameter estimation

2.4.1 Introduction

Parameter estimation basically consists of defining a model structure parameterized in $\boldsymbol{\theta}$, collecting measurements of the dynamic system and estimating parameters from the measurements using a specific parameter estimation method. In this section a short overview hereof is presented, and the notation and definitions are given that will be used in the remainder of the work.

Consider a discrete-time, nonlinear dynamical model parameterized in $\boldsymbol{\theta}$ that generates output predictions according to:

$$\hat{\mathbf{y}} = \mathbf{h}(\boldsymbol{\theta}, \mathbf{u}; \mathbf{x}_0), \tag{2.70}$$

where $\hat{\mathbf{y}}$ is a prediction of $\mathbf{y} := \begin{bmatrix} \mathbf{y}_1^T & \dots & \mathbf{y}_N^T \end{bmatrix}^T$ denoting output signal measurements $\mathbf{y}_k \in \mathbb{R}^p$ stacked over time, $\boldsymbol{\theta} \in \Theta \subset \mathbb{R}^q$ the parameter vector, $\boldsymbol{\Theta}$ the parameter set and $\mathbf{u} := \begin{bmatrix} \mathbf{u}_1^T & \dots & \mathbf{u}_N^T \end{bmatrix}^T$ the input vector $\mathbf{u}_k \in \mathbb{R}^m$ stacked over time, and $\mathbf{x}_0 \in \mathbb{R}^n$ the initial state vector. For the purpose of analysis it is assumed that $\mathbf{u}$ is a quasi-stationary signal of finite power that can be either a stochastic signal, a deterministic signal or a combination of a stochastic and deterministic signal (Ljung 1999). A stochastic process or deterministic sequence $\mathbf{u}_k$ is called quasi-stationary if there exist $c_1, c_2 \in \mathbb{R}$ such that $|\mathbb{E}\mathbf{u}_k| < c_1$ for all k, and

$$\mathbf{R}_u(i) := \bar{\mathbb{E}}\left(\mathbf{u}_k \mathbf{u}_{k-i}\right) \tag{2.71}$$

satisfies $|\mathbf{R}_u(i)| < c_2$ for all i. Here, $\bar{\mathbb{E}}$ denotes the generalized expectation

$$\bar{\mathbb{E}} := \lim_{N\to\infty} \sum_{k=0}^{N-1} \mathbb{E}. \tag{2.72}$$

(Ljung 1999). This indicates that the average properties of the signal hardly vary with time, and therefore the signal can be treated as if it is a stationary signal. The power of such a signal can be expressed as

$$\bar{\mathcal{P}}_u := \bar{\mathbb{E}}\left(\mathbf{u}_k^2\right). \tag{2.73}$$

In the remainder of the chapter the shorthand notation $\mathbf{h}(\boldsymbol{\theta})$ is used to indicate $\mathbf{h}(\boldsymbol{\theta}, \mathbf{u}; \mathbf{x}_0)$. Note that since the model (2.70) is parameterized it represents an input/output model structure.

After linearization of the nonlinear process dynamics around a chosen operating point or trajectory, a linear dynamical system results. This system can be modeled by an LTI input-output model, represented by the transfer function $\mathbf{G}(q, \boldsymbol{\theta})$ under the condition $\mathbf{x}_0 = 0$, leading to an output predictor

$$\hat{\mathbf{y}}_k = \mathbf{G}(q, \boldsymbol{\theta})\mathbf{u}_k, \tag{2.74}$$

with q the forward shift operator $q\mathbf{u}_k = \mathbf{u}_{k+1}$.

The parameterization of $\mathbf{G}(q, \boldsymbol{\theta})$ is defined as a mapping:

$$\mu : \boldsymbol{\Theta} \rightarrow \mathbf{G}(q, \boldsymbol{\theta}). \tag{2.75}$$

There are many different ways of parameterizing sets of models. In this thesis a parameterization in state-space representation is chosen

$$\mathbf{x}_{k+1} = \mathbf{A}(\boldsymbol{\theta})\mathbf{x}_k + \mathbf{B}(\boldsymbol{\theta})\mathbf{u}_k \tag{2.76}$$
$$\mathbf{y}_k(\boldsymbol{\theta}) = \mathbf{C}(\boldsymbol{\theta})\mathbf{x}_k + \mathbf{D}(\boldsymbol{\theta})\mathbf{u}_k, \tag{2.77}$$

similar as described in Section 2.2. The number of parameters in the model should be large in order to be flexible (i.e. the set of models is large), which reduces the bias error of the estimated model. However, the number of parameters should be small in order to keep the variance of the estimated parameters small, where the variance of an estimate is a measure for the variation in an estimate resulting from taking different realizations of the noise process. This is the so-called bias-variance trade-off. In case appropriate basis functions are introduced, the number of parameters can be reduced, resulting in a more favorable variance error of the estimated parameters, while the bias error is also more favorable. The difficulty is indeed to choose appropriate basis functions.

The corresponding transfer function of (2.76, 2.77) is given by

$$\mathbf{G}(q, \boldsymbol{\theta}) = \mathbf{D}(\boldsymbol{\theta}) + \mathbf{C}(\boldsymbol{\theta})\left(qI - \mathbf{A}(\boldsymbol{\theta})\right)^{-1}\mathbf{B}(\boldsymbol{\theta}). \tag{2.78}$$

A state-space model (2.76, 2.77) is called a realization of $\mathbf{G}(q, \boldsymbol{\theta})$ if it satisfies (2.78), and it is called minimal if it additionally has a minimal state dimension n. The latter is also referred to as the McMillan degree of the dynamical system.

2.4.2 Structural identifiability and identifiability

Consider the model (2.70) parameterized in $\boldsymbol{\theta}$. It is possible to estimate the parameters $\boldsymbol{\theta}$ from measured data if the input/output model structure is identifiable. Local identifiability is defined after Grewal and Glover (1976) as:

Definition 2.4 *An input/output model structure $\mathbf{h}(\boldsymbol{\theta}, \mathbf{u}; \mathbf{x}_0)$ is called locally identifiable in $\boldsymbol{\theta}_m \in \Theta$ for a given $\mathbf{u}$ and $\mathbf{x}_0$, if for all $\boldsymbol{\theta}_1, \boldsymbol{\theta}_2$ in the neighborhood of $\boldsymbol{\theta}_m$ it holds that*

$$\{\mathbf{h}(\mathbf{u}, \boldsymbol{\theta}_1; \mathbf{x}_0) = \mathbf{h}(\mathbf{u}, \boldsymbol{\theta}_2; \mathbf{x}_0)\} \Rightarrow \boldsymbol{\theta}_1 = \boldsymbol{\theta}_2.$$

The parameter estimation problem discussed until now basically consists of two parts. The first part is a property of the model structure itself: is it possible at all to distinguish two given parameters sets, provided the input is chosen the best possible way? This property is called the structural identifiability of a model parameterization. The second part is related to the actual input and will be considered later in this subsection.

In this thesis the local structural identifiability formulation of Glover and Willems (1974) is adopted, where the notion is defined by considering the properties of the parameterized transfer function (2.74):

Definition 2.5 *An input/output model structure $\mu : \Theta \rightarrow \mathbf{G}(z, \boldsymbol{\theta})$ with $\Theta \subset \mathbb{R}^q$ and $\mathbf{G}(z, \boldsymbol{\theta}) \subset \mathbb{R}(z)^{p \times m}$ is called locally structurally identifiable in $\boldsymbol{\theta}_m \in \Theta$ if for all $\boldsymbol{\theta}_1, \boldsymbol{\theta}_2$ in the neighborhood of $\boldsymbol{\theta}_m$ holds that*

$$\{\mathbf{G}(z, \boldsymbol{\theta}_1) = \mathbf{G}(z, \boldsymbol{\theta}_2)\} \Rightarrow \boldsymbol{\theta}_1 = \boldsymbol{\theta}_2. \tag{2.79}$$

with z the z-transform variable and $\mathbf{G}(z, \boldsymbol{\theta}) \subset \mathbb{R}(z)^{p \times m}$, where $\mathbb{R}(z)^{p \times m}$ denotes the set of matrices with dimension $p \times m$ and entries contained in $\mathbb{R}(z)$. Note that in contrast with (2.70) this notion does neither include the input vector nor the initial state, and is valid for linear models. Structural identifiability will be considered in Section 4.6, where a link is made between structural identifiability and identifiability.

The second part of the parameter estimation problem is to find out if the actual input is informative enough to allow this distinction. This leads to the requirement that the input signal is persistently exciting. Here we characterize persistently exciting inputs of order n in terms of the covariance matrix $\mathbf{R}_u$ (2.71) after Ljung (1999):

Definition 2.6 *Let $\mathbf{u}$ be a quasi-stationary signal, and let matrix $\bar{\mathbf{R}}_n$ be defined as*

$$\bar{\mathbf{R}}_n = \begin{bmatrix} \mathbf{R}_u(0) & \mathbf{R}_u(1) & \dots & \mathbf{R}_u(n-1) \\ \mathbf{R}_u(1) & \mathbf{R}_u(0) & \dots & \mathbf{R}_u(n-2) \\ \vdots & \ddots & \ddots & \vdots \\ \mathbf{R}_u(n-1) & \dots & \mathbf{R}_u(1) & \mathbf{R}_u(0) \end{bmatrix}, \tag{2.80}$$

then $\mathbf{u}_k$ is persistently exciting of order n if $\bar{\mathbf{R}}_n$ is nonsingular.

An example of a persistently exciting input of any finite order is a sequence of zero mean independent random variables, which is also called white noise.

2.4.3 Prediction error estimation

Least-squares estimation

Until now we have a model parameterized in $\boldsymbol{\theta}$. Furthermore, suppose we have collected measurements of the dynamic system. As a next step the parameters are estimated from the measurements using a specific parameter estimation method. In the prediction error framework (Ljung 1999) parameter estimation methods are considered that are obtained by minimizing a cost function $V(\boldsymbol{\theta})$. Commonly, the cost function $V(\boldsymbol{\theta})$ is chosen as:

$$V(\boldsymbol{\theta}) := \frac{1}{2}\boldsymbol{\epsilon}(\boldsymbol{\theta})^T \mathbf{P}_v^{-1} \boldsymbol{\epsilon}(\boldsymbol{\theta}), \tag{2.81}$$

where the prediction error $\boldsymbol{\epsilon}(\boldsymbol{\theta})$ is defined as

$$\boldsymbol{\epsilon}(\boldsymbol{\theta}) = \mathbf{y} - \hat{\mathbf{y}}, \tag{2.82}$$

where $\mathbf{y}$ denotes the measured outputs and $\hat{\mathbf{y}}$ the predictor as in (2.70), and $\mathbf{P}_v$ is (an estimate of) the covariance matrix of the noise $\mathbf{v}$ that is supposed to act on the measured output. Note that the parameter vector $\boldsymbol{\theta}$ can be extended to include components of $\mathbf{P}_v$.

Parameter estimation then consists of finding a parameter estimate as a minimizing argument of the cost function $V(\boldsymbol{\theta})$

$$\hat{\boldsymbol{\theta}} := \arg\min_{\boldsymbol{\theta}} V(\boldsymbol{\theta}). \tag{2.83}$$

Minimization of cost function (2.81) generally involves a non-convex, gradient based optimization problem (described later in this subsection). However, in case a model structure is chosen that is linear in $\boldsymbol{\theta}$, the cost function $V(\boldsymbol{\theta})$ is a quadratic function in $\boldsymbol{\theta}$, and the resulting convex optimization problem has an analytical solution.

An example of a model that is linear in $\boldsymbol{\theta}$ is a linear regression model with predictor

$$\hat{\mathbf{y}} = \boldsymbol{\Phi}\boldsymbol{\theta}, \tag{2.84}$$

where $\boldsymbol{\Phi}$, given by

$$\boldsymbol{\Phi} := \begin{bmatrix} \boldsymbol{\phi}_1^T & \dots & \boldsymbol{\phi}_N^T \end{bmatrix}^T, \tag{2.85}$$

contains the regression vectors. In a Finite Impulse Response (FIR) model structure (Ljung 1999) the regression vectors are a function of the input $\mathbf{u}$ only. For cost function (2.81) the minimizing argument is given by

$$\hat{\boldsymbol{\theta}} = (\boldsymbol{\Phi}^T \mathbf{P}_v^{-1} \boldsymbol{\Phi})^{-1} \boldsymbol{\Phi}^T \mathbf{P}_v^{-1} \hat{\mathbf{y}}, \tag{2.86}$$

where $(\boldsymbol{\Phi}^T \mathbf{P}_v^{-1} \boldsymbol{\Phi})^{-1} \boldsymbol{\Phi}^T \mathbf{P}_v^{-\frac{1}{2}}$ is also the pseudo-inverse of $\mathbf{P}_v^{-\frac{1}{2}} \boldsymbol{\Phi}$. This is the least-squares estimate.

In the situation that cost function (2.81) is applied to linear models and the input signal is quasi-stationary, the asymptotic properties of the resulting parameter estimate can be derived, i.e. results for convergence and consistency. It is assumed that the underlying system that generates the measurements, the data-generating process, is an LTI discrete-time process

$$\hat{\mathbf{y}}_k = \mathbf{G}_0(q)\mathbf{u}_k + \mathbf{v}_k, \tag{2.87}$$

where $\mathbf{v}_k = \mathbf{P}_v\mathbf{e}_k$, and $\mathbf{e}$ is associated with a probability density function f_e.
The convergence result in this context is that for an infinite amount of measurements the parameter estimate converges with probability 1 to $\boldsymbol{\theta}^*$, where

$$\boldsymbol{\theta}^* := \arg\min_{\boldsymbol{\theta}} \bar{\mathbb{E}}\boldsymbol{\epsilon}(\boldsymbol{\theta})^T\mathbf{P}_v^{-1}\boldsymbol{\epsilon}(\boldsymbol{\theta}). \tag{2.88}$$

This implies that the parameter estimate is in the asymptotic case independent of the particular noise realization in the measurements.
The consistency result is that if $\mathbf{u}$ is persistently exciting of sufficient order (see Definition 2.6), if $\mathbf{G}_0(z)$ is in the model set and if $\mathbf{G}(z,\boldsymbol{\theta}^*)$ is parameterized independently from the noise model, then $\mathbf{G}(z,\boldsymbol{\theta}^*) = \mathbf{G}_0(z)$. This implies that the measurements contain enough information on the dynamics in $\mathbf{G}_0(z)$ to estimate n parameters.

Finally, estimation errors are present in $\mathbf{G}(z,\hat{\boldsymbol{\theta}})$ due to e.g. noise and lack of information. The estimation error can be decomposed in a term related to the bias error and a term related to the variance error:

$$\mathbf{G}_0(z) - \mathbf{G}(z,\hat{\boldsymbol{\theta}}) = \mathbf{G}_0(z) - \mathbf{G}(z,\boldsymbol{\theta}^*) + \mathbf{G}(z,\boldsymbol{\theta}^*) - \mathbf{G}(z,\hat{\boldsymbol{\theta}}), \tag{2.89}$$

where $\mathbf{G}_0(z) - \mathbf{G}(z,\boldsymbol{\theta}^*)$ is the bias error and $\mathbf{G}(z,\boldsymbol{\theta}^*) - \mathbf{G}(z,\hat{\boldsymbol{\theta}})$ is the variance error. In Ljung (1999) results are presented that characterize the bias and variance error in the asymptotic case. For linear regression models (2.84) the variance of the least squares estimate is given by

$$\operatorname{cov}(\hat{\boldsymbol{\theta}}) \simeq \frac{\sigma_e^2}{N}\left(\bar{\mathbb{E}}\boldsymbol{\Phi}^T\boldsymbol{\Phi}\right)^{-1}, \tag{2.90}$$

where σ_e^2 denotes the variance of the noise. This equation clearly indicates that the variance of the estimate can be reduced by reducing the variance of the noise σ_e^2, increasing the number of measurements, and/or increasing the power of the input signal, since that increases the term $\boldsymbol{\Phi}^T\boldsymbol{\Phi}$.

Maximum likelihood estimation

The maximum likelihood method for parameter estimation can also be seen as a special case in the prediction-error framework (Ljung 1999). Suppose that we have chosen a model structure that includes besides a predictor also an assumed pdf $f_e(\mathbf{y};\boldsymbol{\theta})$ of $\mathbf{e}$. Substitution of the mismatch between the measured output values and predictions results in the likelihood function $L(\boldsymbol{\theta};\mathbf{y})$. This is a deterministic

function of the unknown parameter $\boldsymbol{\theta}$. The maximum likelihood (ML) estimate is found by minimizing the negative value of log likelihood. If f_e is a Gaussian pdf with variance σ_e^2, then

$$-\log L(\boldsymbol{\theta};\mathbf{y}) = \text{constant} + N\log\sigma_e + \frac{1}{N\sigma_e^2}\boldsymbol{\epsilon}(\boldsymbol{\theta})^T\boldsymbol{\epsilon}(\boldsymbol{\theta}). \tag{2.91}$$

The resulting ML estimate is

$$\hat{\boldsymbol{\theta}}_{ML} = \arg\min_{\boldsymbol{\theta}}\left(N\log\sigma_e + \frac{1}{N\sigma_e^2}\boldsymbol{\epsilon}(\boldsymbol{\theta})^T\boldsymbol{\epsilon}(\boldsymbol{\theta})\right) = \arg\min_{\boldsymbol{\theta}}\left(\frac{1}{N}\boldsymbol{\epsilon}^T\boldsymbol{\epsilon}\right). \tag{2.92}$$

As can be seen from (2.92) in the Gaussian situation the ML estimate is equal to the least squares estimate. ML estimates are known for their attractive properties, which also hold for non-Gaussian distributions: ML estimates are consistent in case the observations are independent (i.e. white noise). Furthermore, for $N \to \infty$ the ML estimate has an asymptotic Gaussian distribution with variance given by J^{-1}, with J the Fisher Information Matrix:

$$J = \mathbb{E}\left(\frac{\partial\log L(\boldsymbol{\theta};\mathbf{y})}{\partial\boldsymbol{\theta}}\left(\frac{\partial\log L(\boldsymbol{\theta};\mathbf{y})}{\partial\boldsymbol{\theta}}\right)^T\right)\Bigg|_{\boldsymbol{\theta}=\boldsymbol{\theta}^*}. \tag{2.93}$$

For a Gaussian pdf it can be shown that the Fisher Information Matrix satisfies

$$J = \frac{1}{N\sigma_e}\mathbb{E}\left(\frac{\partial\hat{\mathbf{y}}}{\partial\boldsymbol{\theta}}\left(\frac{\partial\hat{\mathbf{y}}}{\partial\boldsymbol{\theta}}\right)^T\right)\Bigg|_{\boldsymbol{\theta}=\boldsymbol{\theta}^*}. \tag{2.94}$$

Bayesian approach

In the Bayesian approach to parameter estimation the parameter is considered as a random variable with a certain prior probability $p(\boldsymbol{\theta})$. The measured output $\mathbf{y}$ is associated with a probability $p(\mathbf{y})$. The conditional probability $\mathbf{y}$ given $\boldsymbol{\theta}$ is denoted by $p(\mathbf{y}|\boldsymbol{\theta})$. With Bayes rule $p(\boldsymbol{\theta}|\mathbf{y})$, the posterior probability of $\boldsymbol{\theta}$ given $\mathbf{y}$, can be calculated according to

$$p(\boldsymbol{\theta}|\mathbf{y}) = \frac{p(\mathbf{y}|\boldsymbol{\theta})p(\boldsymbol{\theta})}{p(\mathbf{y})}. \tag{2.95}$$

The maximum a posteriori (MAP) estimate of $p(\boldsymbol{\theta}|\mathbf{y})$ is the value of $\boldsymbol{\theta}$ for which the pdf takes its maximum value.

Let the prior knowledge of $\boldsymbol{\theta}$ be represented by assuming that $\boldsymbol{\theta}$ is Gaussian distributed with mean $\boldsymbol{\theta}_p$ and covariance $\mathbf{P}_{\boldsymbol{\theta}}$. For linear models it can then be shown that maximizing $p(\boldsymbol{\theta}|\mathbf{y})$ is equivalent to minimizing the cost function

$$V(\boldsymbol{\theta}) = (\bar{\mathbf{y}}_k - \mathbf{y}_k)^T\mathbf{P}_v^{-1}(\bar{\mathbf{y}}_k - \mathbf{y}_k) + (\boldsymbol{\theta} - \boldsymbol{\theta}_p)\mathbf{P}_{\boldsymbol{\theta}}^{-1}(\boldsymbol{\theta} - \boldsymbol{\theta}_p), \tag{2.96}$$

where the first term in $V(\boldsymbol{\theta})$ represents the weighted mismatch between observed measurements and model outputs, and the second term represents the weighted mismatch between the parameter vector and the a priori mean $\boldsymbol{\theta}_p$. The latter term penalizes deviations of $\hat{\boldsymbol{\theta}}$ from $\boldsymbol{\theta}_p$ and can be seen as an approach to regularize the parameter estimation problem (see e.g. Tarantola 2005).

Nonlinear optimization methods

Since the cost function is in general not convex, it needs to be minimized using an iterative method. If we iteratively solve for a parameter estimate $\hat{\boldsymbol{\theta}}$ by minimizing a cost function $V(\boldsymbol{\theta})$, the general update rule in step m of a Newton-type algorithm is given by

$$\hat{\boldsymbol{\theta}}_{m+1} = \hat{\boldsymbol{\theta}}_m + \gamma \left(\frac{\partial^2 V}{\partial \boldsymbol{\theta}^2} \right) \Bigg|^{-1}_{\boldsymbol{\theta}=\hat{\boldsymbol{\theta}}_m} \frac{\partial V}{\partial \boldsymbol{\theta}} \Bigg|_{\boldsymbol{\theta}=\hat{\boldsymbol{\theta}}_m}, \tag{2.97}$$

where γ denotes a scalar damping factor . Note that in this expression the partial derivatives are evaluated in the local parameter $\hat{\boldsymbol{\theta}}_m$, which are usually calculated with the aid of an adjoint-based method. See Chavent (1975); Li et al. (2003) for applications of an adjoint-based method for estimating reservoir parameters. The term $\frac{\partial^2 V}{\partial \boldsymbol{\theta}^2}$ is usually approximated, leading to e.g. Gauss-Newton or Steepest-Descent methods, see Chapter 4 for more details. Alternatively, parameter estimation methods as discussed here can be solved recursively, where the parameters are estimated on-line as the measurements are gathered. This will be further discussed in Chapter 4, where also a link is made between recursive estimation methods and filtering methods such as Kalman filters.

2.5 Summary

This chapter has presented the basic concepts and notation that will be used in the remainder of this thesis. The section on the geological formation of oil and gas reservoirs has mainly served to show that the structures in the subsurface can be diverse as a result of the greatly varying processes that have taken place during the formation of an oil and gas reservoir. The section has focused mainly on channelized structures since in Chapter 5 a channel and barrier parameterization will be introduced.

The result of the greatly varying geological processes is a heterogeneous porous medium that contains oil and/or water. For petroleum production single-phase and two-phase flow models in porous media are generated (described in Section 2.2) that aim to predict the flow behavior resulting from certain decisions. The currently used petroleum reservoir models are nonlinear models that contain a large number of states and physical parameters (typically $10^5 - 10^6$), resulting from the spatial and temporal discretization of the relevant partial differential equations. The states are the grid block pressures and grid block saturations. Physical parameters that play a large role in the long-term flow behavior are the grid block permeabilities.

For a better understanding of the key processes in reservoir models the controllability and observability properties of the models will be analyzed in the next chapter, concepts which have been presented in this chapter. To increase the predictive capacity of these models the model parameters are to be estimated from

measurements. In Section 2.4 the notions of identifiability and structural identifiability have been defined and a short overview has been given of parameter estimation methods in a prediction error framework.

3 CHAPTER

Controllability and Observability in Porous Media Flow

In this chapter it is shown how the controllability and observability of single-phase and two-phase flow reservoir simulation models can be analyzed. With this analysis one can find which processes are most relevant during the life of the reservoir. Examples are presented to illustrate the results. Also the influence of well locations and heterogeneity on the controllability and observability properties of reservoir models is investigated.

3.1 Introduction

As discussed in Chapter 1 determining optimal control settings based on models of limited complexity (e.g. obtained from reducing large-scale models) works surprisingly well. The question is why do these simple models work so well? In pursuit of an answer of this question the notions of controllability and observability of reservoir models are analyzed. Only recently, the controllability and observability of reservoir simulation models have been analyzed for single-phase reservoir models (Zandvliet et al. 2008), and in this chapter the controllability and observability properties of two-phase reservoir models will be analyzed.

The analysis gives insight into which processes in the reservoir are most relevant for the input-output behavior, and also which processes should be modeled carefully such that the model is suitable for model-based operations of petroleum reservoirs. To this end the controllability and observability of the reservoir model are quantified such that the most controllable and most observable (combinations of) states can be determined.

Single-phase reservoir simulation models for slightly compressible liquid flow are linear and therefore their controllability and observability can be readily analyzed using the tools available for linear systems (summarized in Subsections 2.3.1 and

2.3.2). Two-phase reservoir simulation models are nonlinear and the controllability and observability analysis of nonlinear models is more complicated. In Section 2.3.5 two approaches have been presented that are suitable for controllability and observability analysis of nonlinear large-scale models. In Section 3.2 it is described how these tools are used to determine which (combinations of) states are most relevant for the input-output behavior of reservoir models. Next, in Section 3.3 the controllability and observability of grid block pressures in two-dimensional (2D), single-phase models are analyzed. In Section 3.4 the controllability and observability of grid block saturations in a one-dimensional (1D) two-phase reservoir model are analyzed, where the reservoir model is represented by a linear and nonlinear convection-diffusion equation. Finally, in Section 3.5, the controllability and observability of grid block pressures and saturations in 2D, two-phase reservoir models are analyzed.

3.2 Quantifying controllability and observability in porous media flow

In Section 2.3 singular value decompositions (SVD) have been used to quantify controllability and observability, and thereby specifying the state space that is most controllable or observable. The controllable subspace can be approximated as

$$\mathcal{C}_n = \mathbf{U}\mathbf{\Sigma}\mathbf{V}^T = \begin{bmatrix} \mathbf{U}_1 & \mathbf{U}_2 \end{bmatrix} \begin{bmatrix} \mathbf{\Sigma}_1 & \mathbf{0} \\ \mathbf{0} & \mathbf{\Sigma}_2 \end{bmatrix} \begin{bmatrix} \mathbf{V}_1^T \\ \mathbf{V}_2^T \end{bmatrix} \approx \mathbf{U}_1\mathbf{\Sigma}_1\mathbf{V}_1^T, \tag{3.1}$$

where the separation between $\mathbf{\Sigma}_1$ and $\mathbf{\Sigma}_2$ is chosen in such a way that the singular values in $\mathbf{\Sigma}_2$ are considerably smaller than those in $\mathbf{\Sigma}_1$. Alternatively, an SVD can be applied to the controllability Gramian

$$\mathcal{P}_n = \mathcal{C}_n\mathcal{C}_n^T = \mathbf{U}\mathbf{\Sigma}^2\mathbf{U}^T, \tag{3.2}$$

or to the empirical controllability Gramian $\mathcal{P}_e$ (2.62), resulting in the same matrices $\mathbf{U}$ and $\mathbf{\Sigma}$ as in (3.1).

The observable subspace can be specified by applying an SVD to the transpose of the observability matrix or the observability Gramian

$$\mathcal{O}_n^T = \mathbf{U}\mathbf{\Sigma}\mathbf{V}^T = \begin{bmatrix} \mathbf{U}_1 & \mathbf{U}_2 \end{bmatrix} \begin{bmatrix} \mathbf{\Sigma}_1 & \mathbf{0} \\ \mathbf{0} & \mathbf{\Sigma}_2 \end{bmatrix} \begin{bmatrix} \mathbf{V}_1^T \\ \mathbf{V}_2^T \end{bmatrix}, \tag{3.3}$$

$$\mathcal{Q}_n = \mathcal{O}_n^T\mathcal{O}_n = \mathbf{U}\mathbf{\Sigma}^T\mathbf{U}. \tag{3.4}$$

Note that the SVD is applied to the transpose of $\mathcal{O}_n$ such that the left singular vectors of $\mathcal{O}_n$ and $\mathcal{Q}_n$ are equal. Alternatively, the empirical observability Gramian $\mathcal{Q}_e$ (2.68) can be used to specify the observable subspace.

Consider the case in which the controllable subspace is approximated by removing columns in $\mathbf{U}$ that correspond to (very) small singular values as in (3.1). In case the values of the input variables vary several orders of magnitude, the values

of **B** related to those input variables appear to influence the numerical values that occur in $\mathbf{\Sigma}_1$ and $\mathbf{\Sigma}_2$, and as such can influence the separation between $\mathbf{\Sigma}_1$ and $\mathbf{\Sigma}_2$. In order to make the selection mechanism scaling-independent matrix **B** can be scaled to

$$\bar{\mathbf{B}} = \mathbf{B}\mathbf{\Gamma}_u, \tag{3.5}$$

where in this chapter $\mathbf{\Gamma}_u = \text{diag}\begin{pmatrix} |u_1| & \dots & |u_p| \end{pmatrix}$ and where $u_i, i = 1, \dots, p$ represents typical input values. Subsequently, the controllability matrix and Gramians are calculated. This is illustrated in Sections 3.3 and 3.5 in which examples are presented where the inputs contain pressures that have values in the range of 10^7 and rates that have values in the range of unity.

The same reasoning also applies to the output variables. In order to make the selection mechanism scaling-independent, matrix **C** can be scaled to

$$\bar{\mathbf{C}} = \mathbf{\Gamma}_y\mathbf{C}, \tag{3.6}$$

where in this chapter $\mathbf{\Gamma}_y = \text{diag}\begin{pmatrix} |y_1|^{-1} & \dots & |y_p|^{-1} \end{pmatrix}$ and where $y_i, i = 1, \dots, p$ represents typical output values. Subsequently, the observability matrix and observability Gramians are calculated. This is illustrated in Sections 3.3 and 3.5 in which examples are presented that support this scaling.

The controllability properties of a nonlinear model can change with time, i.e. states can become more or less controllable with time. In this work we have chosen to analyze the controllability per time interval. To this end the total simulation time of N time steps is split into intervals $k_{i,f} = [\, k_i, \, \dots \, , \, k_f \,]$ where k_i and k_f denote the first and last time step of the interval. Next, the controllability of each interval is analyzed using the approaches presented in Subsection 2.3.5. This approach is comparable to the Sliding Interval Gramians mentioned in Verriest and Kailath (1983).

Each column of **U** in (3.1), (3.2), (3.3) or (3.4) contains a singular vector with dimension n, where n is the total number of states. In the case of spatially discretized reservoir models the states represent grid block pressures and/or grid block saturations. Since each state is connected to a grid block, each column of **U** can be interpreted as a spatial pattern or a basis function. The spatial patterns contained in $\mathbf{U}_1$ that correspond to large singular values can be interpreted as the combination of states that are most controllable or observable.

To present the spatial patterns more compactly, we have chosen to depict the weighted singular vector, which consists of the sum of the singular vectors corresponding to the first z singular vectors weighted by their singular value. In this way one can immediately see which parts of the reservoir model contain states that are most controllable or observable, and which parts of the reservoir model only contain states that are almost not controllable or observable. The weighted left singular vector $\mathbf{U}_{1:z}$ of a certain matrix is given by

$$\mathbf{U}_{1:z}(\cdot) := \sum_{i=1}^{z} \frac{\sigma_i}{\sigma_1}\tilde{\mathbf{U}}_i, \tag{3.7}$$

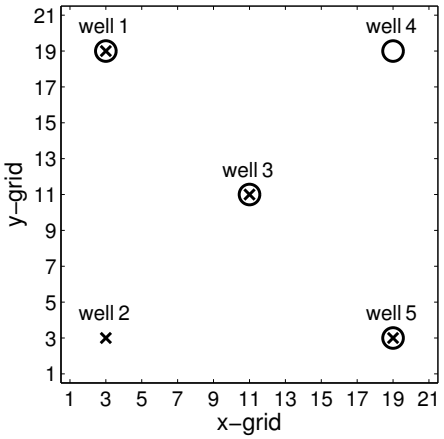

Figure 3.1: Well locations: wells 1, 3 and 5 are bottom-hole pressure controlled production or injection wells containing a flow meter (⊗), well 4 is a flow rate controlled production or injection well without a pressure gauge (◯), and well 2 is an observation well containing a pressure gauge (×)

.

where σ_i is the i-th singular value on the diagonal of $\mathbf{\Sigma}$, and $\tilde{\mathbf{U}}_i$ is the i-th column vector of $\mathbf{U}$ in (3.1), (3.2), (3.3) or (3.4) with length n. In a geometric interpretation the columns of the unitary matrix $\mathbf{U}$ represent a direction in the controllable or observable subspace, where the length of the vectors is given by the corresponding singular values. The vectors weighted by their singular value as in (3.7) can then be considered as a vector sum, characterizing the dominant directions in the controllable or observable subspace.

3.3 Controllability and observability of pressures in single-phase porous media flow

3.3.1 Introduction

The work in this section has been done in cooperation with Maarten Zandvliet and has previously been published in a joint publication Zandvliet et al. (2008) and in his thesis Zandvliet (2008). The controllability and observability of pressures in 2D single-phase porous media flow are analyzed to find out which states are most controllable and observable.

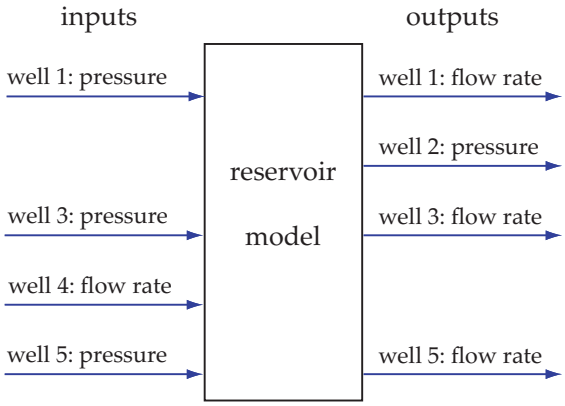

Figure 3.2: Input-output scheme: wells 1, 3, 4 and 5 are flow rate or bottom-hole pressure controlled production or injection wells. Wells 1, 2, 3 and 5 are wells in which either flow rate or bottom-hole pressure is measured

.

3.3.2 Example 1: homogeneous permeability

Consider a homogeneous reservoir containing one phase and modeled as in Section 2.2.1. The model has $21 \times 21 \times 1$ grid blocks of 10 m $\times$ 10 m $\times$ 10 m. The absolute permeability is 10 mDarcy. The porosity is chosen constant in every grid block and is given by $\phi = 0.20$. The fluid compressibility is $c = 10^{-10}$ Pa^{-1} and viscosity $\mu = 10^{-3}$ Pa s. There are five wells configured in a standard 5-spot pattern depicted in Figure 3.1. The input-output block scheme of the inputs and outputs is depicted in Figure 3.2.

Four of the wells can inject or produce (inputs), i.e. wells 1, 3, 5 and 4. These are in Figure 3.1 indicated by a circle, either with or without a cross. In the first three of these wells, i.e. wells 1, 3 and 5 the bottom-hole pressure can be controlled and in well 4 the flow rate. Of the total number of wells four have measurement capabilities (outputs), i.e. wells 1, 3, 5 and 2 can measure either flow rate or bottom hole pressure. These are in Figure 3.1 indicated by a cross, either with or without a circle. In the first three of these wells, i.e. wells 1, 3 and 5 the flow rate can be measured, and in well 2 (a non-producing or injecting well) the bottom-hole pressure can be measured. The well indices $\mathbf{J}_p$ and $\mathbf{J}_q$ are computed using a Peaceman model (2.5) with a wellbore radius $r_{\mathrm{w}} = 0.1$ m and skin factor $S = 0$.

The matrices $\mathbf{A}$, $\mathbf{B}$, $\mathbf{C}$ and $\mathbf{D}$ are computed as in Section 2.2.1 with a discretization time step given by (2.12), which in this example leads to $\Delta t = 1.2$ s. In this particular example, the nonzero entries in $\mathbf{C}$ corresponding to the flow rate measurements $\bar{\mathbf{q}}_{well}$ (i.e. the well indices of wells 1, 3 and 5) are in the order of 10^{-8}: much smaller than the nonzero entry in $\mathbf{C}$ corresponding to the pressure measurement $\bar{\mathbf{p}}_{well}$ in well 2, which is equal to 1. This is problematic, because the in Section 2.3 discussed energy produced by observing pressures in well 2 (in $[\mathrm{Pa}]^2$) will then generally be much larger than the energy produced by observing flow rates in

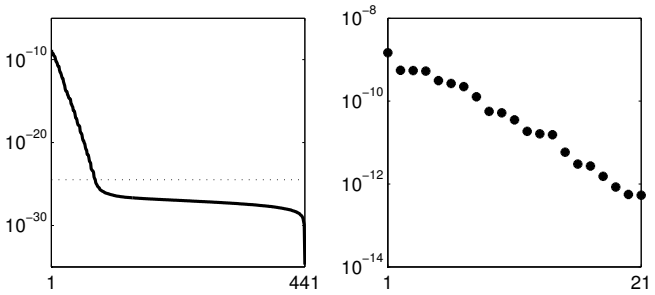

Figure 3.3: All 441 Hankel singular values $\sigma_1, \ldots, \sigma_{441}$ (left) and 21 largest ones $\sigma_1, \ldots, \sigma_{21}$ (right) for homogeneous example. The dashed line represents machine precision.

wells 1, 3 and 5 (in $[\mathrm{m}^3/\mathrm{s}]^2$). In the following examples, $\mathbf{C}$ is therefore scaled with $\mathbf{\Gamma}_y$ such that the entries in $\bar{\mathbf{C}} = \mathbf{\Gamma}_y \mathbf{C}$ are of the same order. Similarly, the nonzero entries in $\mathbf{B}$ corresponding to the bottom-hole pressure controlled wells $\breve{\mathbf{q}}_{well}$ (i.e. wells 1, 3 and 5) are much smaller than the nonzero entry in $\mathbf{B}$ corresponding to the flow rate controlled well $\breve{\mathbf{q}}_{well}$ (i.e. well 4). In the following examples, $\mathbf{B}$ is therefore scaled with $\mathbf{\Gamma}_u$ such that the entries in $\bar{\mathbf{B}} = \mathbf{B}\mathbf{\Gamma}_u$ are of the same order. The Gramians and Hankel singular values are subsequently computed using the scaled $\bar{\mathbf{B}}$ and $\bar{\mathbf{C}}$ matrices. Note that the sign of the input signal decides if fluid is injected or produced, and hence the Gramians are indifferent to injection or production of fluids, only to the type of control, i.e. rate-controlled or bottom-hole pressure.

The Hankel singular values, depicted on a logarithmic scale in Figure 3.3, decrease very rapidly, indicating that the 441^{th} order reservoir model behaves like a model of considerably lower order.

The singular vectors corresponding to the three largest singular values of the Gramians $\mathcal{P}_n$ and $\mathcal{Q}_n$, as well as the eigenvectors corresponding to the three largest eigenvalues of $\mathcal{P}\mathcal{Q}$ are depicted in Figure 3.4. In each of the plots, the vector under consideration is projected onto the model grid. Since each component of the state relates to the pressure in a specific grid block, and thereby a specific physical location, this projection allows us to interpret how the reservoir model's controllability and observability properties vary over space. Note that the scales of these plots differ and that the nonzero areas are of particular interest, as these represent areas where reference pressures are controllable and / or observable. Since the observation well (well 2 in Figure 3.1) is the only well that does not appear as a nonzero area in the plots of the controllability Gramian, we conclude that reference pressures in areas near production or injection wells require are most controllable. Similarly, since the production or injection well without any measurement (well 4 in Figure 3.1) is the only well that does not appear as a nonzero area in the plots of the observability Gramian, we conclude that reference pressures in areas near wells with flow meters or pressure gauges are most observable. In short, pressures near wells in which we can control the flow rate or bottom-hole pressure

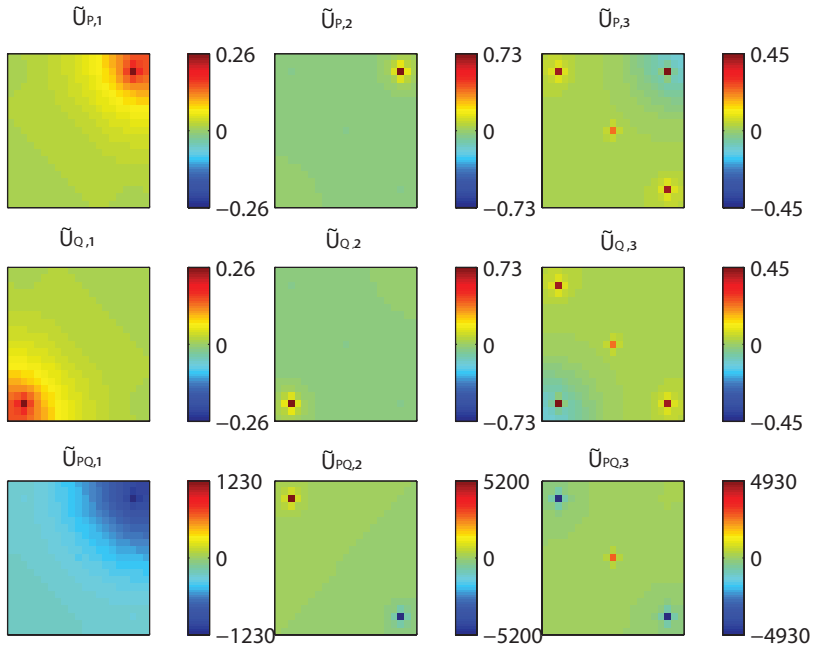

Figure 3.4: Singular vectors corresponding to the three largest singular values of controllability Gramian $\mathcal{P}_n$ (top row) and observability Gramian $\mathcal{Q}_n$ (middle row), and eigenvectors corresponding the three largest singular values of $\mathcal{PQ}$ (bottom row), projected onto model grid for homogeneous example.

are controllable, whereas pressures near wells in which we can measure the flow rate or bottom-hole pressure are observable. The wells in which we can control *and* observe (wells 1, 3 and 5 in Figure 3.1) appear as nonzero areas in the bottom row of Figure 3.4. Since a eigenvector of $\mathcal{PQ}$ represents a state (i.e. a vector of pressures) that is equally difficult to reach as observe, it makes sense that particularly the wells in which we can control *and* observe (wells 1, 3 and 5 in Figure 3.1) appear as nonzero areas in the plots of $\mathcal{PQ}$.

Remark: It is important to mention that the previously mentioned scalings of the entry in **C** corresponding to the pressure measurement in well 2 and entry in **B** corresponding to the flow-rate controlled well 4 have a large influence on Figure 3.4. For example, smaller scaling factors (i.e. smaller entries in **B** and **C**) make the non-zero areas surrounding wells 2 and 4 in Figure 3.4 less pronounced. Recall that the main reason for these scalings is that 'energy' in $[\mathrm{Pa}^2]$ will generally be much larger than in $[\mathrm{m}^3/\mathrm{s}]^2$. Therefore, if in *each* well the bottom-hole pressure is controlled and the flow rate is measured (and 'required energy' is thereby consistently in $[\mathrm{Pa}^2]$ while 'produced energy' is consistently in $[\mathrm{m}^3/\mathrm{s}]^2$), then these scaling are no longer necessary.

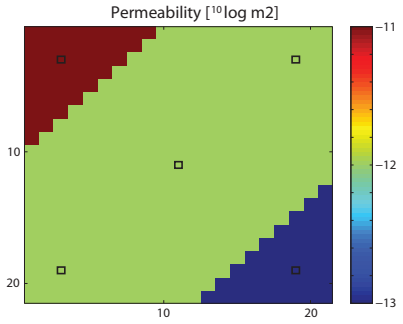

Figure 3.5: Heterogeneous permeability distribution as used in Section 3.3.3.

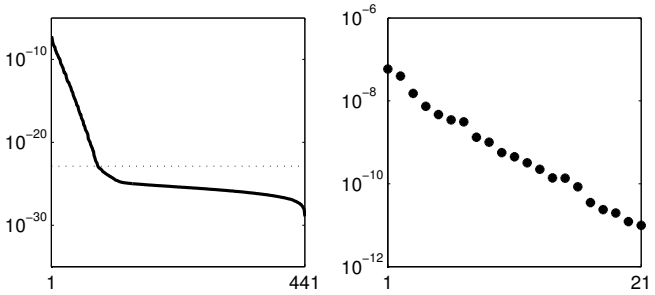

Figure 3.6: All 441 Hankel singular values $\sigma_1, \ldots, \sigma_{441}$ (left) and 21 largest ones $\sigma_1, \ldots, \sigma_{21}$ (right) for heterogeneous example. The dashed line represents machine precision.

3.3.3 Example 2: heterogeneous permeability

Consider the same reservoir model as in the previous example, but with a high permeability zone of 1000 mDarcy in the North-West corner, a low permeability zone of 10 mDarcy in the South-East corner, and a permeability of 100 mDarcy throughout the rest of the reservoir - see Figure 3.5. The discretization time step Δt is still given by (2.12) and its value is therefore different than before, namely $\Delta t = 0.013$ s.

The Hankel singular values, depicted in Figure 3.6, decrease very rapidly. As before, this indicates that the 441^{th} order reservoir model behaves like a model of considerably lower order.

The singular vectors corresponding to the three largest singular values of the Gramians $\mathcal{P}_n$ and $\mathcal{Q}_n$ as well as the eigenvectors corresponding to the three largest eigenvalues of $\mathcal{P}_n \mathcal{Q}_n$ are depicted in Figure 3.7. Contrary to Figure 3.4, only the production well in the high permeable zone (well 1 in Figure 3.1) appears as a nonzero area in the plots of the controllability Gramian. From this we conclude that reference pressures in areas near production wells in high permeable zones

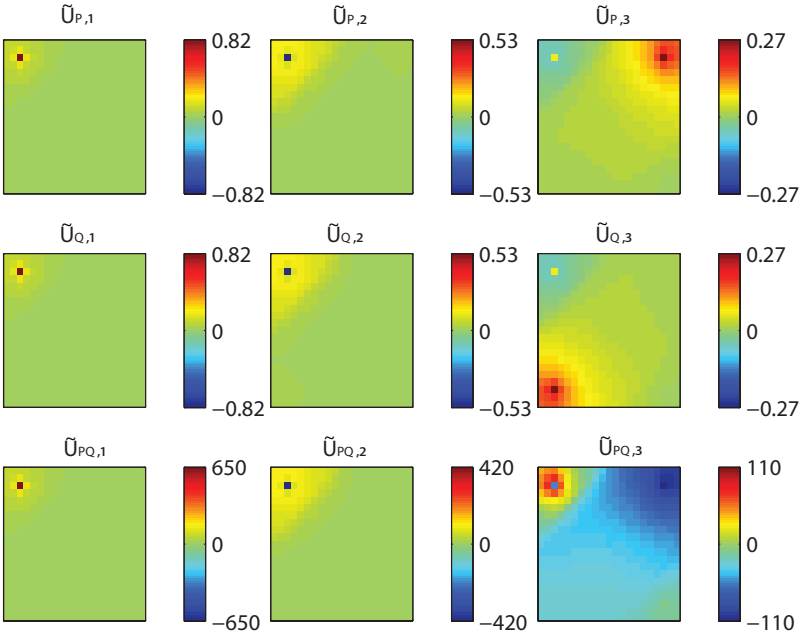

Figure 3.7: Singular vectors corresponding to the three largest singular values of controllability Gramian $\mathcal{P}_n$ (top row), and observability Gramian $\mathcal{Q}_n$ (middle row), and eigenvectors corresponding to the largest eigenvalues of $\mathcal{P}_n\mathcal{Q}_n$ (bottom row), projected onto model grid for heterogeneous example.

require the least energy to reach. Contrary to Figure 3.4, only the well with a measurement in the high permeable zone (well 1 in Figure 3.1) appears as a nonzero area in the plots of the observability Gramian. From this we conclude that reference pressures in areas near observation wells in high permeable zones produce the most energy when observed. Also the eigenvectors of $\mathcal{P}_n\mathcal{Q}_n$ show that the reference pressures in areas in high permeability are most relevant for the input-output behavior, and that the reference pressures in areas in low permeability are least relevant for the input-output behavior (values close to 0).

3.3.4 Effect of physical reservoir parameters

This subsection shows how the controllability and observability results depend on the physical reservoir parameters, the time discretization and the spatial discretization. Recall that the matrices $\mathbf{A}$ and $\mathbf{B}$ in (2.10) are given by:

$$\mathbf{A} = I + \mathbf{A}_c\Delta t, \quad \mathbf{B} = \mathbf{B}_c\Delta t,$$

where $\mathbf{A}_c$ and $\mathbf{B}_c$ contain entries that are inverse proportional to compressibility c, the entire porosity field $\boldsymbol{\phi} = \begin{bmatrix} \phi_1 & \dots & \phi_{N_{gb}} \end{bmatrix}$, viscosity μ, and proportional to the *entire* permeability distribution $\mathbf{k} = \begin{bmatrix} k_1 & \dots & k_{N_{gb}} \end{bmatrix}$. Therefore, scaling the value of

- compressibility c to $(1/\epsilon)c$, or
- the entire porosity field $\boldsymbol{\phi}$ to $(1/\epsilon)\boldsymbol{\phi}$, or
- viscosity μ to $(1/\epsilon)\mu$, or
- the *entire* permeability distribution $\mathbf{k}$ to $\epsilon\mathbf{k}$,

for some constant value $\epsilon > 0$ leads to

$$\mathbf{A} = I + \epsilon\mathbf{A}_c\Delta t, \quad \mathbf{B} = \epsilon\mathbf{B}_c\Delta t.$$

In other words, scaling the above mentioned physical parameters by ϵ has the same effect on $\mathbf{A}$ and $\mathbf{B}$ as scaling the discretization time step Δt by ϵ. Furthermore, it can be shown that for the viscosity or the entire permeability this also leads to a scaling of the values of $\mathbf{C}$ and $\mathbf{D}$ in (2.11) to $\epsilon\mathbf{C}$ and $\epsilon\mathbf{D}$, respectively. Note that in Section 3.3.3 only certain grid block permeability values are scaled and not the *entire* permeability distribution. Therefore there is an effect on the controllability and observability properties.

It is important to note that the dynamics of the discrete-time reservoir model (2.10, 2.11) are unaffected by scaling Δt, provided that $\epsilon\Delta t$ is still smaller than the value given by (2.12)[1]. In fact, the results obtained in this section (in terms of Hankel singular values and spatial variation of controllability and observability properties) using the original continuous-time matrices $(\mathbf{A}_c, \mathbf{B}_c)$ are virtually the same. This therefore also holds for the compressibility and porosity scalings mentioned above. The viscosity and permeability scalings on the other hand also influence $\mathbf{C}$, leading to a scaling of diagonal matrix with Hankel singular values $\text{diag}\begin{pmatrix} \sigma_1 & \dots & \sigma_{N_{gb}} \end{pmatrix}$ in (2.52) to $\epsilon\,\text{diag}\begin{pmatrix} \sigma_1 & \dots & \sigma_{N_{gb}} \end{pmatrix}$. The spatial discretization also does not have a significant influence on the results: the spatial patterns depicted in Figure 3.4 and Figure 3.7 resemble the ones obtained by modeling the reservoir with, say, $11 \times 11 \times 1$ or $31 \times 31 \times 1$ grid blocks. This is important, as it points out that controllability and observability are reservoir properties, and not just reservoir model properties. Furthermore, the overall decrease in Hankel singular values from 10^{-9} to approximately 10^{-25} is very similar - see Figure 3.8. This is important, as it points out that the number of grid blocks, often chosen as high as computationally possible, does not have a significant influence on the relevant order of the pressure dynamics throughout the reservoir.

[1] Recall that a discrete-time model (2.10) obtained with a time step larger than (2.12) does not capture all of the dynamics of the original continuous-time model (2.8)-(2.9).

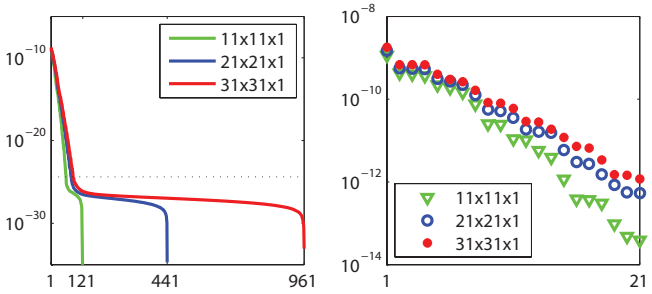

Figure 3.8: All Hankel singular values (left) and 21 largest ones (right) of three reservoir models based on the reservoir model treated in homogenous example, where each model is spatially discretized by a different number of grid blocks.

3.3.5 Summary

In this section the controllability and observability properties of single-phase flow reservoir models have been analyzed, showing that pressures near wells in which we can control the flow rate or bottom-hole pressure are controllable, whereas pressures near wells in which we can measure the flow rate or bottom-hole pressure are observable. Based on the examples we conclude that these properties are determined by the well configuration, and to a lesser extent by the heterogeneity of the reservoir at hand. The Hankel singular values of single-phase flow reservoir models decrease rapidly, indicating that they behave as models of much lower order than the order that follows from the number of discretization grid blocks.

3.4 Controllability and observability of saturations in two-phase porous media flow

3.4.1 Introduction

In this section the controllability and observability of grid block saturations in a horizontal, one-dimensional (1D) reservoir model will be analyzed to find which processes are most relevant during the life of the reservoir. The reservoir model, schematically depicted in Figure 3.9, initially contains oil which is flooded by water that is injected at the left boundary of the reservoir model. The oil and/or water are produced at the right boundary. Oil and water are both assumed to be incompressible, and consequently the total fluid velocity is constant. Furthermore, gravity forces are ignored. As described in e.g. Aziz and Settari (1986) and Vakili et al. (2005) this can be modeled by a linear or nonlinear 1D convection-diffusion equation (CDE). In Section 3.4.2 the linear CDE is described and next its controllability and observability properties are analyzed using the approaches

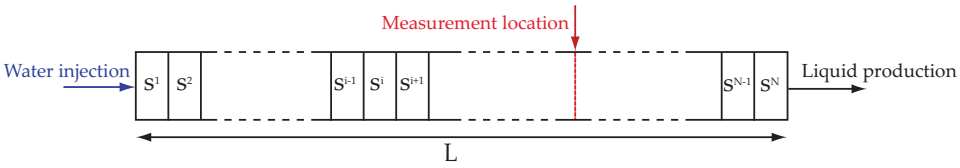

Figure 3.9: Sketch of 1D reservoir model after spatial discretization.

for linear and nonlinear models described in Section 2.3. The advantage of using the linear CDE is that the results of the different approaches can be compared. In Section 3.4.3 the controllability and observability is analyzed for the nonlinear CDE.

3.4.2 Linear convection-diffusion equation

The advantage of analyzing the controllability and observability of this CDE is that it is a *linear* two-phase reservoir model. This greatly simplifies the analysis. The linear CDE is given by

$$D\frac{\partial^2 s}{\partial x^2} - v\frac{\partial s}{\partial x} = \varphi\frac{\partial s}{\partial t}, \tag{3.8}$$

where coefficient D represents the effects of molecular diffusion and dispersion resulting from mechanical mixing through subgrid geological heterogeneities, $s = s(x,t)$ is water saturation, v is total liquid velocity, ϕ is porosity, x is position and t is time. The initial condition is $s(x,0) = s_{wc}$, where s_{wc} is connate water saturation. The boundary conditions are:

$$s(0,t) = s_{wc}, \qquad \left.\frac{\partial s(x,t)}{\partial x}\right|_{x=L} = 0,$$

where L represents the length of the reservoir (see Figure 3.9). An analytical solution for the linear CDE is (Aziz and Settari 1986)

$$s = s_{wc} + \frac{(1 - s_{or} - s_{wc})}{\operatorname{erfc}\left(-t_D\sqrt{\frac{P}{4t_D}}\right)}\operatorname{erfc}\left((x_D - t_D)\sqrt{\frac{P}{4t_D}}\right), \tag{3.9}$$

where s_{or} is residual oil saturation, erfc is the complementary error function and the dimensionless variables are given by

$$x_D = \frac{x}{L}, \quad t_D = \frac{vt}{L\varphi}, \quad P = \frac{vL}{D},$$

where P is the Peclet number reflecting the relative importance of convection relative to diffusion.

Symbol	Value	Unit
D	10^{-5}	m^2/s
ϕ	0.20	$-$
v	2×10^{-4}	m/s
s_{inj}	1	$-$
s_{wc}	0	$-$
L	200	m
Δx	1	m
Δt	1000	s
t_{end}	15000	s

Table 3.1: Model coefficients and discretization variables of the linear 1D reservoir model.

The linear equation is spatially discretized using a finite-difference scheme with block-centered grids with an upstream weighting or backward difference approximation for the convection term. The temporal discretization is performed with forward Euler. This results for grid block s^i at time step $k+1$ in

$$s_{k+1}^i = \left(\frac{D\Delta t}{\phi \Delta x^2} + \frac{v\Delta t}{\phi \Delta x}\right) s_k^{i-1} + \left(1 - 2\frac{D\Delta t}{\phi \Delta x^2} + \frac{v\Delta t}{\phi \Delta x}\right) s_k^i + \left(\frac{D\Delta t}{\phi \Delta x^2}\right) s_k^{i+1}, \quad (3.10)$$

where we have used superscripts to indicate grid block numbers, and subscripts to indicate time steps.

The linear equation is casted in an LTI discrete-time state-space form to enable the analysis of controllability and observability. The state $\mathbf{x}$ is the water saturation in each grid block, the input $\mathbf{u}$ is the water injection saturation s_{inj} in the first grid block, and the output $\mathbf{y}$ is the water saturation that is observed at $\frac{2}{3}L$. In the example, the length L is chosen as 200 m, and as a result the water saturation is observed 133 m from the left boundary - see the red dashed line in Figure 3.9.

The initial water saturation is chosen as $s_0 = s_{wc} = 0$ equal in every grid block. This means that the reservoir model only contains oil. Water is injected at the left boundary and produced from the right boundary, meaning $s^0 = s_{inj} = 1$. The remaining coefficients and discretization variables are listed in Table 3.1. In Figure 3.10 the saturation profiles at $t = 10^5$s for the analytical solution (3.9) and numerical solution (3.10) are shown. The difference between the analytical and numerical solution is caused by numerical dispersion. The red dashed line in Figure 3.10 indicates the measurement location. For this example the model order of the numerical model is $n = 200$, which is equal to the number of grid blocks $L/\Delta x = 200$. The Courant-Friedrichs-Lewy (CFL) condition C for the linear CDE, given by

$$C = \frac{v\Delta t}{\phi \Delta x}, \quad (3.11)$$

satisfies for this example $C = 0.9$. Since $C < 1$ this indicates that the solution is stable.

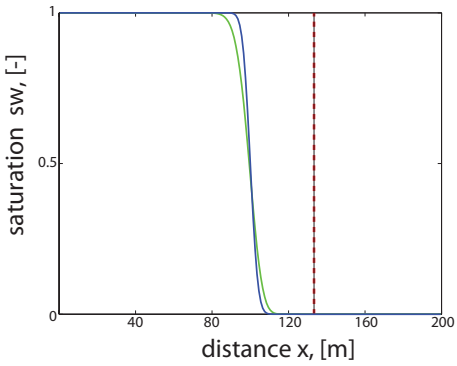

Figure 3.10: Water saturation profile calculated with linear numerical CDE (green) and analytical CDE (blue) after 10^5 s with $v = 0.0002$ m/s. The red dashed line indicates the measurement location.

Controllability and observability of the linear 1D reservoir model

The controllability and observability properties of the linear 1D reservoir model in state-space form will be first analyzed with the controllability and observability Gramians as calculated with the discrete Lyapunov or Stein equations (2.31, 2.41), since this is known to be a numerically reliable method. Secondly, for comparison purposes, the controllability and observability properties will also be analyzed with the controllability and observability matrices (2.29, 2.39) and with empirical Gramians (2.62, 2.68). These approaches should lead to the same results, although, for large numbers of grid blocks numerical issues can be expected to cause differences.

Firstly, the controllability and observability Gramians of the linear 1D reservoir model are calculated using the Stein equations (2.31, 2.41) as implemented in MATLAB in the function `balreal`. The Hankel singular values $\sigma_i, i = 1, \ldots, 200$, are calculated as in (2.51) and are plotted in Figure 3.11. It can be seen that the Hankel singular values decrease rapidly, indicating that the dynamical behavior of the model is of an order that is significantly less than $n = 200$ (which is equal to the number of grid blocks). This is in line with results from Markovinović et al. (2002), Heijn et al. (2004) and Gildin et al. (2006).

The eigenvectors of the product of the controllability and observability Gramian $\mathcal{P}_n\mathcal{Q}_n$ that correspond to dominant Hankel singular values, contain those combinations of states that are most relevant for the input-output behavior. The absolute value of the first nine eigenvectors of the product $\mathcal{P}_n\mathcal{Q}_n$ are plotted in Figure 3.12 as function of the distance x from the left boundary of the reservoir model. We have chosen to depict the absolute value of the eigenvectors since it is easier to see that the highest values are at the left boundary of the reservoir. The red dashed line indicates the position of the measurement location. The weighted sum (3.7) of the singular vectors and singular values of $\mathcal{P}_n\mathcal{Q}_n$ is plotted in Figure 3.13, bottom row, middle plot. Here is chosen for singular vectors since singu-

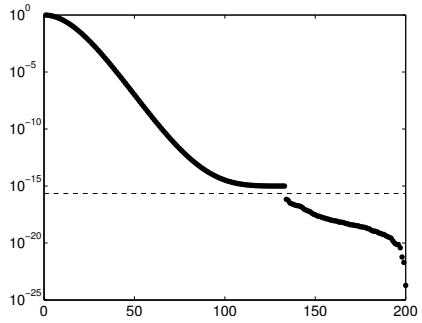

Figure 3.11: Hankel singular values of the linear 1D reservoir model. The dashed line represents machine precision.

lar vectors are contrary to eigenvectors orthogonal to each other, and the singular vectors only show minor differences when compared to the eigenvectors plotted in Figure 3.12.

From Figure 3.12 several observations can be made. While moving downstream from left to right we observe that close to the left boundary, where water is injected, the values of the eigenvectors of the product $\mathcal{P}_n\mathcal{Q}_n$ are higher than further away from the left boundary, indicating that these states are more relevant for the input-output behavior. Furthermore, the states directly upstream of the measurement location are more relevant for the input-output behavior than further upstream. The states downstream of the observing well are apparently not relevant for the input-output behavior. This is caused by the upstream weighting scheme that is used for the spatial discretization, which implies that the water saturation of grid block i is only dependent on the water saturation upstream of grid block i. This is in line with the physical behavior of the flow in the reservoir. In case e.g. a central difference scheme is used to spatially discretize the model, the observability results would be different and would not reflect the physical behavior, as is also mentioned by Singh and Hahn (2007).

Secondly, the controllability and observability properties of the model are analyzed using controllability and observability matrices, controllability and observability Gramians and empirical Gramians. Note that the empirical observability Gramian of the CDE is calculated using snapshots of the dual model with an initial condition $\mathbf{x}'(0) = 0$ and excited with an impulse input. For each approach the weighted singular vector is calculated according to (3.7) for $z = 20$ and plotted in Figure 3.13. These plots give insight into which (combinations) of states are most controllable, most observable and most relevant for the input-output behavior of the flow. In the top row the weighted singular vectors of the controllability matrix $\mathbf{U}_{1:20}(\mathcal{C}_{200})$, the controllability Gramian $\mathbf{U}_{1:20}(\mathcal{P}_n)$ and empirical controllability Gramian $\mathbf{U}_{1:20}(\mathcal{P}_e)$ are plotted. From these plots it can be seen that for all three approaches it holds that states close to the left boundary, where water is injected, are most controllable, and the states further away from the left boundary are less controllable. States close to the right boundary are not controllable

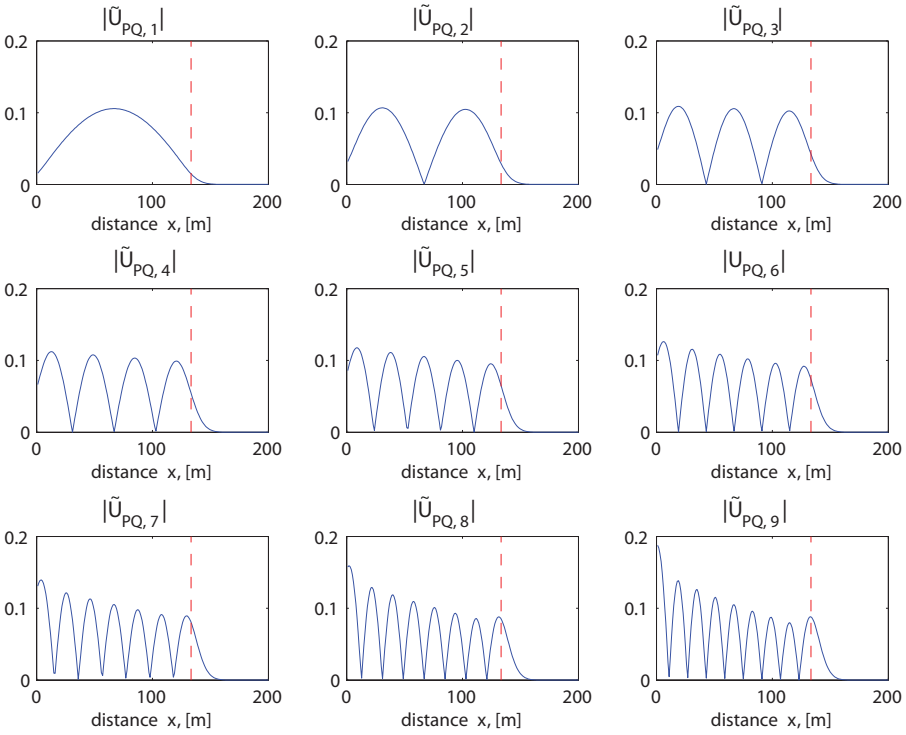

Figure 3.12: First nine eigenvectors of $\mathcal{P}_n \mathcal{Q}_n$ (absolute value).

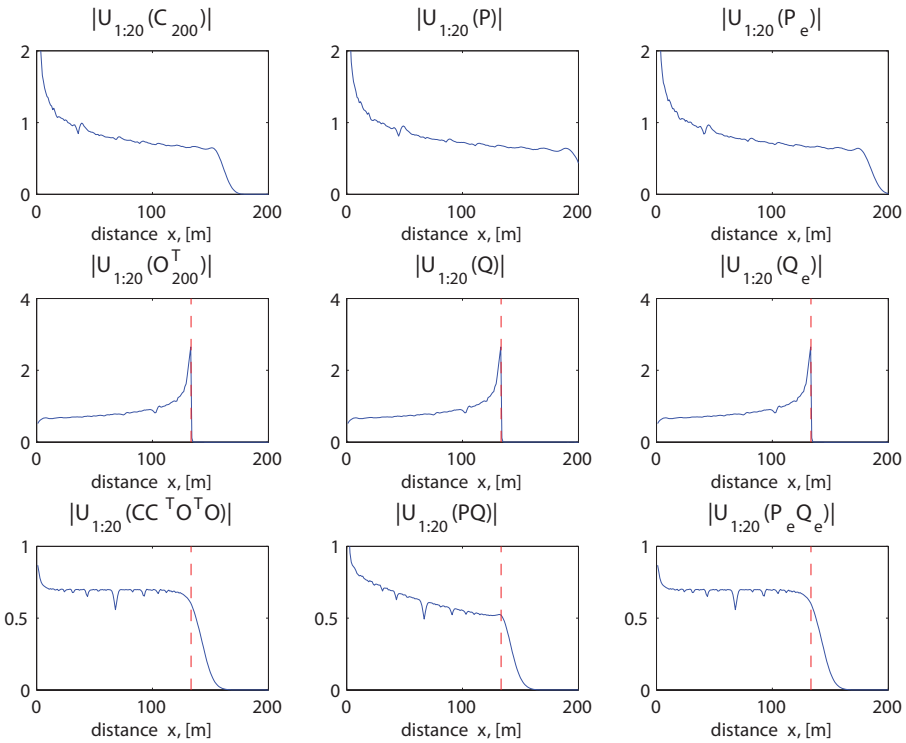

Figure 3.13: First row: weighted singular vectors of controllability matrix $\mathcal{C}_{200}$, controllability Gramian $\mathcal{P}_n$ and empirical controllability Gramian $\mathcal{P}_e$ of the linear 1D reservoir model. Middle row: weighted singular vectors of the observability matrix $\mathcal{O}_{200}^T$, observability Gramian $\mathcal{Q}_n$ and empirical observability Gramian $\mathcal{Q}_e$. Bottom row: weighted singular vectors of $\mathcal{C}_{200}\mathcal{C}_{200}^T\mathcal{O}_{200}^T\mathcal{O}_{200}$, $\mathcal{P}_n\mathcal{Q}_n$ and $\mathcal{P}_e\mathcal{Q}_e$.

anymore. At the right boundary, where the controllability is smallest, there are differences between the plots, probably caused by numerical issues during the computation of the controllability matrix which involves multiplication of a large number of system matrices with each other, see (2.29).

In the middle row of Figure 3.13 the weighted singular vectors of the observability matrix $\mathbf{U}_{1:20}(\mathcal{O}_{200}^T)$, the observability Gramian $\mathbf{U}_{1:20}(\mathcal{Q}_n)$ and the empirical observability Gramian $\mathbf{U}_{1:20}(\mathcal{Q}_e)$ are plotted, where the red dashed line indicates the measurement location. From these plots it can be seen that states upstream of the observation point are most observable and that the observable is slowly decreasing for states in the upstream direction. States downstream of the observation point are not observable. As explained earlier, the reason for this is that an upstream weighting scheme for the spatial discretization is applied.

Finally, the model is balanced and the Hankel singular values and eigenvectors of $\mathcal{P}_n\mathcal{Q}_n$ are calculated. The results are plotted in the bottom row of Figure 3.13, and it can be observed that the weighted singular vector is at its maximum at the location where water is injected and then slowly decreases. Downstream of the measurement location, indicated by the red dashed line, the weighted singular vector drops fast to zero. Apparently, the most relevant states are between the left boundary and the measurement location.

3.4.3 Nonlinear convection-diffusion equation

In this subsection the nonlinear CDE (Aziz and Settari 1986) is used to model the flow in a 1D two-phase horizontal reservoir model that contains both water and oil (Figure 3.9). The model is given by

$$\frac{\partial}{\partial x}\left(h_w\frac{\partial s}{\partial x}\right) - v\frac{\partial f_w}{\partial x} = \phi\frac{\partial s}{\partial t}, \tag{3.12}$$

where h_w is a nonlinear function of water saturation representing a term with capillary pressure, and f_w is the water fractional flow function that plays a role in the description of the flow of the water fraction. These terms are defined by

$$h_w = h_w(s) = -\frac{\lambda_o\lambda_w}{\lambda_o+\lambda_w}\frac{dP_c}{ds} \tag{3.13}$$

$$f_w = f_w(s) = \frac{\lambda_w}{\lambda_o+\lambda_w}, \tag{3.14}$$

where $P_c = p_o - p_w$ is the capillary pressure, $\lambda_o = \frac{kk_{ro}(s)}{\mu_o}$ is the oil mobility, $\lambda_w = \frac{kk_{rw}(s)}{\mu_w}$ is the water mobility, k is the absolute permeability, k_{rw} is the water relative permeability, k_{ro} is the oil relative permeability, μ_o is the oil viscosity and μ_w is the water viscosity. The relative permeability is modeled with a Corey model (2.16, 2.17). In this work capillary pressure is ignored since during displacement processes on reservoir scale the dispersive effect of sub grid block size geological heterogeneities is usually considerably larger than the diffusive effect

of capillary pressure. The dispersive effect of geological heterogeneities can be taken into account by using velocity-dependent dispersion tensors (Russell and Wheeler 1983). This is not included here and in many cases numerical diffusion is of the same order of magnitude as or even larger than the physical diffusion and dispersion. As a result the first term in (3.12) is excluded.

The initial condition is given by $s(x,0) = s_{wc}$. The boundary conditions are given by:

$$s(0,t) = s_{wc}, \qquad \frac{\delta s(L,t)}{\delta x} = 0.$$

An analytical solution to the nonlinear CDE in the absence of capillary pressure was derived by Buckley and Leverett (1942). A numerical solution is obtained by spatial and temporal discretization. The equation is spatially discretized using a finite-difference scheme with block-centered grids and with an upstream weighting approximation. For the discretization in space this leads to

$$v\frac{\partial f_w}{\partial x} = v\frac{f_{w,i} - f_{w,i-1}}{\Delta x}. \tag{3.15}$$

The temporal discretization is performed with forward Euler. This results in

$$s_{k+1}^i = \frac{v\Delta t}{(\phi \Delta x)}\left(f_{w,k}^{i-1} - f_{w,k}^k\right). \tag{3.16}$$

The nonlinear equation (3.16) can also be written in discrete-time state-space form where the matrices are state-dependent.

The output $\mathbf{y}$ is the water saturation that is observed at $\frac{2}{3}L$. In the example, the length L is chosen as 200 m, and as a result the water saturation is observed at the left boundary and 133 m from the left boundary - see the red dashed line in Figure 3.9. The input $\mathbf{u}$ is the water injection saturation s_{inj} in the first grid block. See Figure 3.14 for the saturation profiles using the model coefficients and discretization variables listed in Table 3.2. The analytical solution is obtained with the Buckley-Leverett solution. The difference between the analytical and numerical solution is due to numerical diffusion resulting from the discretization.

Controllability and observability of a nonlinear 1D reservoir model

The controllability and observability properties of the nonlinear CDE in state-space form are analyzed with the LTV controllability and observability *matrices* of the linearized model where the system matrices in intervals $k_{i,j} = [\, k_i, \ldots, k_j \,]$ are used to calculate the controllability and observability properties in the interval. These results are depicted in Figure 3.15. Additionally, the controllability and observability properties are analyzed with empirical Gramians, where we have chosen $r = s = 1$, and a snapshot is generated at each time step. These results are depicted in Figure 3.16. For both approaches the interval length is chosen as 50 time steps and the model coefficients and discretization variables are listed in Table 3.2.

Symbol	Value	Unit
ϕ	0.20	$-$
μ_o, μ_w	10^{-3}	[Pas]
v	2×10^{-4}	m/s
k	10^{-12}	m^2
n_o, n_w	2	$-$
k_{ro}, k_{rw}	1	$-$
L	200	m
Δx	5	m
Δt	600	s
t_{end}	1.5×10^5	s
s_{init}	1	$-$

Table 3.2: Model coefficients and discretization variables of the nonlinear 1D reservoir model.

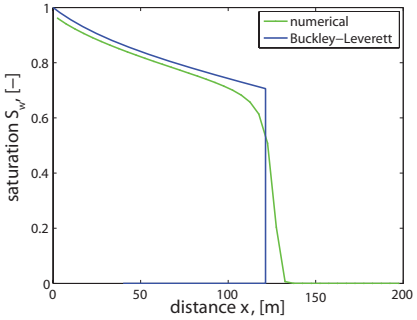

Figure 3.14: Water saturation profile calculated with nonlinear numerical CDE and analytical Buckley-Leverett model after $10^5\,s$ with $v = 0.0002\,m/s$

The plots in Figures 3.15 and 3.16 will be discussed row by row. The top row in each figure depicts the snapshots of the water saturation at the start of each interval. The oil-water front is in these plots indicated by the (close to) vertical line, where downstream of the oil-water front oil is found and upstream water. The weighted singular vector related to controllability (second row) clearly indicates for both approaches that the states around the oil-water front are most controllable. Note that the controllability for the *complete* interval is analyzed, e.g. for the first column the weighted singular vector related to controllability is the result of the controllability analysis for the time interval in which the oil-water front moves from the position in the first saturation plot to the position in the second saturation plot. Next, the observability analysis (third row) indicates for both approaches that states close to the observation well are most observable, where the measurement location is indicated by the red dashed line. Finally, the weighted singular vector of $\mathcal{C}_{k:k_i}\mathcal{C}_{k:k_i}^T\mathcal{O}_{k:k_f}^T\mathcal{O}_{k:k_f}$ and $\mathcal{P}_e\mathcal{Q}_e$ (bottom row) shows that the most relevant states for the input-output behavior are located around the oil-water front.

For reasons of comparison also the controllability and observability properties

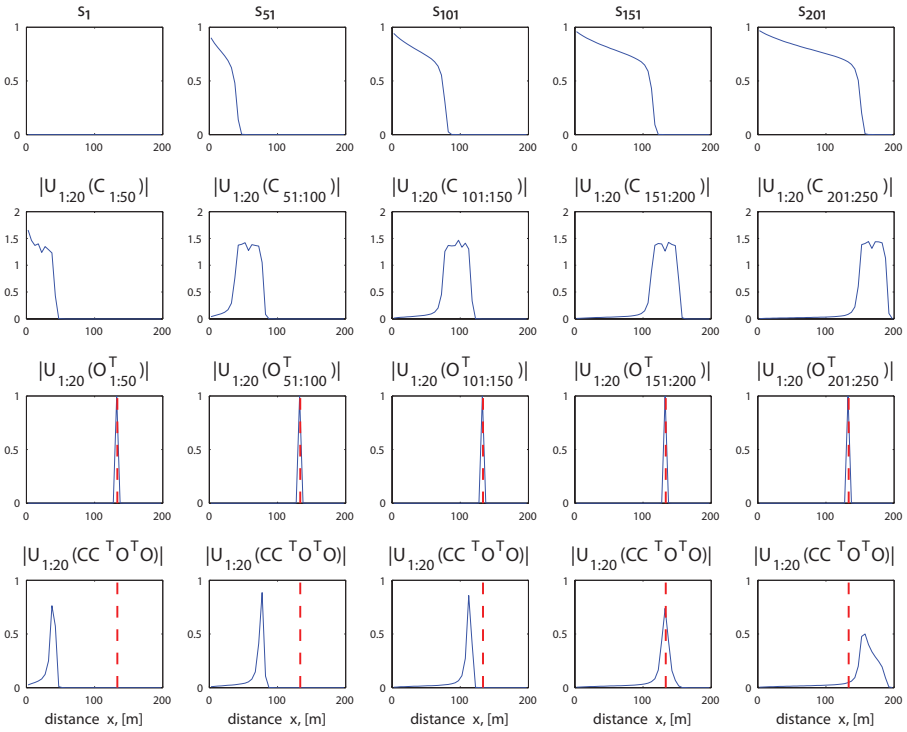

Figure 3.15 - Saturations with LTV controllability and observability matrices: Water saturation **s** calculated with nonlinear CDE at different time steps (first row); weighted singular vector of LTV controllability matrix $\mathcal{C}_{k:k_i}$ (second row) and LTV observability matrix $\mathcal{O}_{k:k_f}$ (third row) for the interval. Weighted singular vector of $\mathcal{C}_{k:k_i}\mathcal{C}_{k:k_i}^T\mathcal{O}_{k:k_f}^T\mathcal{O}_{k:k_f}$ (bottom row).

of the linear CDE model have been analyzed per time interval using empirical Gramians. In Figure 3.17 the results are plotted. Since the total number of time steps is 230 an interval length of 46 has been chosen instead of an interval length of 50. The conclusions that can be drawn from this figure are identical to the conclusions for the nonlinear case shown in Figure 3.16.

3.4.4 Summary

In this section the controllability and observability of a linear and nonlinear model for two-phase flow in a 1D horizontal reservoir model have been analyzed. Based on the examples we conclude that

- The water saturation states of the nonlinear CDE are most controllable near the front and the states of the linear CDE are most controllable close to the boundary where water is injected. The reason why the linear model is ap-

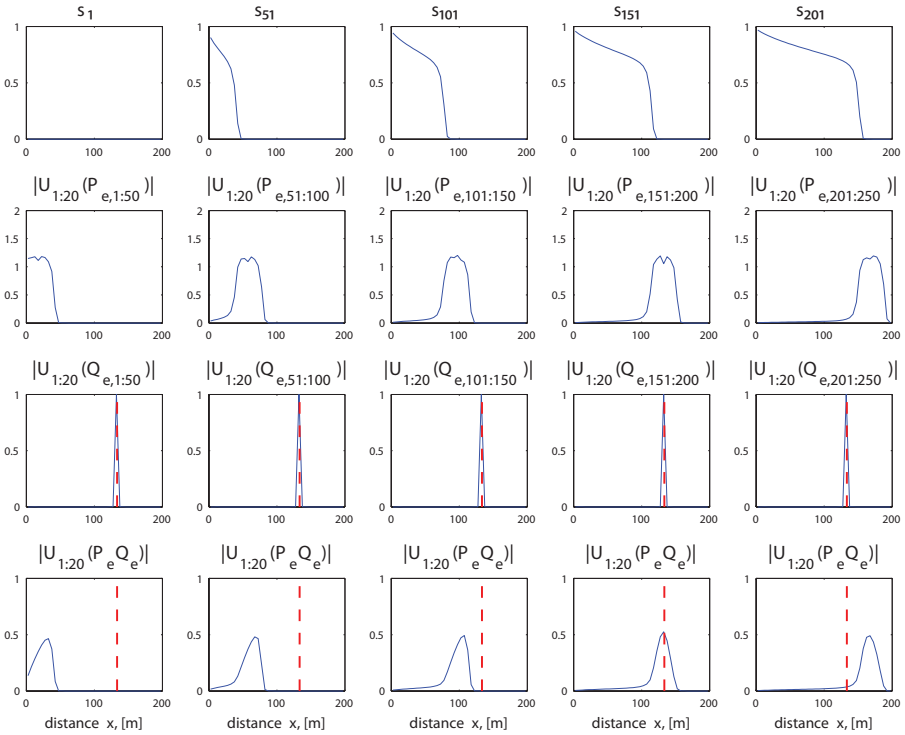

Figure 3.16 - Saturations with empirical controllability and observability Gramians: Water saturation **s** at different time steps calculated with nonlinear CDE (first row); weighted singular vector of empirical controllability Gramian $\mathcal{P}_{e,k:k_i}$ (second row) and empirical observability Gramian $\mathcal{Q}_{e,k:k_f}$ (third row) for the interval. Weighted singular vector of $\mathcal{P}_{e,k:k_i}\mathcal{Q}_{e,k:k_i}$ (bottom row).

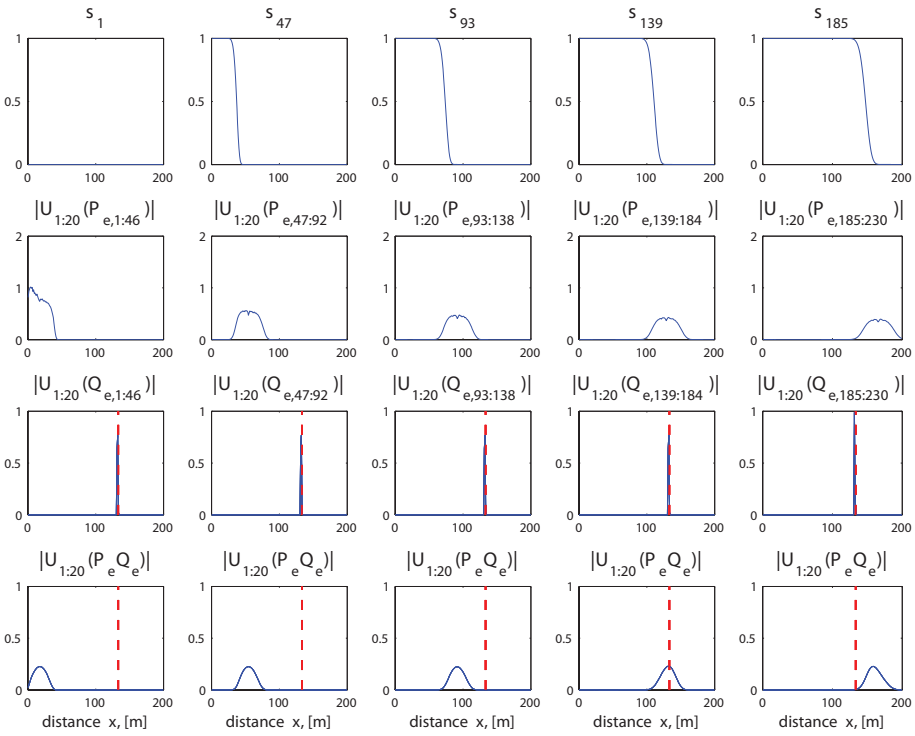

Figure 3.17 - Saturations with empirical controllability and observability Gramians: Water saturation **s** at different time steps calculated with linear CDE (first row); weighted singular vector of empirical controllability Gramian $\mathcal{P}_{e,k:k_i}$ (second row) and empirical observability Gramian $\mathcal{Q}_{e,k:k_f}$ (third row) for the interval. Weighted singular vector of $\mathcal{P}_{e,k:k_i}\mathcal{Q}_{e,k:k_i}$ (bottom row).

parently not only controllable around the front is that the controllability and observability is analyzed for the total period, instead of intervals. If for the linear model the empirical Gramians are calculated for intervals, then the water saturation states also appear to be most controllable around the front, since the empirical Gramians are based on snapshots of the saturation states which show for both the linear and nonlinear model similar behavior. This is supported by Figure 3.17.

- Water saturation states located at the observation point are most observable.
- After balancing the linear model the states that are most relevant for the input-output behavior are located near the left boundary where water is injected and also upstream of the observation point. For models for which the controllability and observability of an interval is analyzed we conclude that the states that are most relevant for the input-output behavior are situated around the oil-water front.
- The Hankel singular values decrease rapidly, indicating that reservoir models behave as models of much lower order than the order that follows from the number of discretization grid blocks. These results are in line with the results of the controllability and observability analysis in Section 3.3.

3.5 Controllability and observability of pressures and saturations in two-phase porous media flow

3.5.1 Introduction

In Section 3.3 the controllability and observability of pressures have been analyzed. In Section 3.4 the controllability and observability of saturations have been analyzed. In this section we turn our attention to 2D two-phase reservoir models, where the states are the pressure and saturation in each grid block. The aim is to find which grid block pressures and saturations are most controllable and observable during the life of the reservoir. The first example is a reservoir model with a homogeneous permeability field, and the second example is a reservoir model with a heterogeneous permeability field.

3.5.2 Example 1: homogeneous permeability

For the first example consider a 2D homogeneous reservoir model in which the oil will be replaced by water in a water flooding process. The model description has been given in Section 2.2.2. The model has $21 \times 21 \times 1$ grid blocks of $10\text{ m} \times 10\text{ m} \times 10\text{ m}$. For the first example the absolute permeability is 10 Darcy in every grid block. The porosity $\phi = 0.30$ and is constant in every grid block. The oil compressibility is $c_o = 10^{-10}\text{ Pa}^{-1}$ and water compressibility is $c_w = 10^{-10}\text{ Pa}^{-1}$. The oil viscosity is $\mu_o = 10^{-3}$ Pa and the water viscosity is $\mu_w = 10^{-3}$ Pa. For the

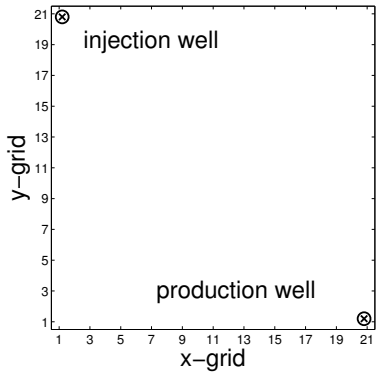

Figure 3.18: Locations of injection and production well. Both wells can measure the bottom hole pressure and the oil and water rates.

relative permeability the Corey model (2.16, 2.17) is used, which has Corey exponents $n_o = n_w = 2$, $k_{ro,0} = 0.9$ and $k_{rw,0} = 0.6$. The resulting curves for relative permeability as function of water saturation are plotted in Figure 2.4. Capillary pressure is not included in the model. The initial pressure is $p_0 = 100 \times 10^5$ Pa and the initial water saturation is $S_{init} = S_{wc} = 0.2$, and both are uniform throughout the reservoir model.

The reservoir model contains an injection well and a production well at opposite corners of the reservoir model - see Figure 3.18. The inputs $\mathbf{u}$ represent the prescribed rate in the injection well (no pressure constraint) and the prescribed pressure in the production well (no rate constraint). The well indices are computed with a Peaceman model (2.5) with well bore radius $r_w = 0.1$ m and skin factor $S = 0$. Similarly as in Section 3.3.2, the nonzero entry in $\mathbf{B}$ corresponding to the flow rate controlled injection well is scaled with $\mathbf{\Gamma}_u$ to the well index of the pressure controlled production well. Both wells have the capability to measure the bottom hole pressure and the oil and water rates. The reservoir model is simulated for 10 years.

Since we consider the controllability and observability around a certain state trajectory, we need to choose input signals which can be considered as realistic during the operation of a petroleum reservoir. For this example we have chosen pseudo-random binary signals (PRBS, Ljung 1999) with rate related input levels between 0.4 m^3/s and 0.5 m^3/s and pressure related input signals between 90×10^5 Pa and 99×10^5 Pa. The signal is constant over intervals with a length of at least 25 time steps before it switches to another input level.

Recall from Section 2.2.2 that the equations of two-phase flow in porous media are given by

$$\mathbf{x}_{k+1} = \begin{bmatrix} \mathbf{A}_{11}(\mathbf{x}_k) & \mathbf{A}_{12}(\mathbf{x}_k) \\ \mathbf{A}_{21}(\mathbf{x}_k) & \mathbf{A}_{22}(\mathbf{x}_k) \end{bmatrix} \mathbf{x}_k + \begin{bmatrix} \mathbf{B}_1(\mathbf{x}_k) \\ \mathbf{B}_2(\mathbf{x}_k) \end{bmatrix} \mathbf{u}_k \tag{3.17}$$

$$\mathbf{y}_k = \begin{bmatrix} \mathbf{C}_1(\mathbf{x}_k) & \mathbf{C}_2(\mathbf{x}_k) \end{bmatrix} \mathbf{x}_k + \mathbf{D}(\mathbf{x}_k)\mathbf{u}_k, \tag{3.18}$$

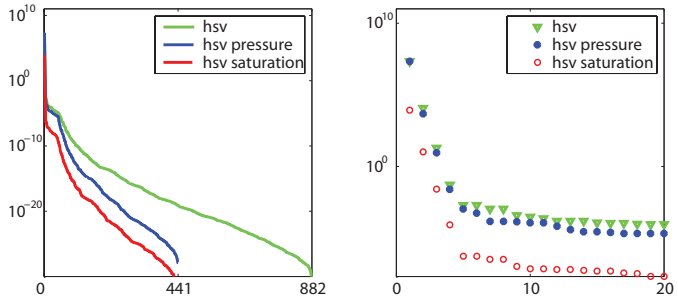

Figure 3.19: All Hankel singular values (left) and 20 largest ones (right) for the complete simulation time, calculated with empirical Gramians.

where the state vector $\mathbf{x}$ consists of a stacked pressure state vector and saturation state vector, both with dimension n. The time scales of the dynamic behavior of the pressure and saturation states are very different from each other, as indicated by the clear separation in eigenvalues of system matrix $\mathbf{A}_c$ (see Section 2.2.2). The pressure states are associated with eigenvalues with a high absolute value and exhibit a fast behavior, while the saturation states are associated with eigenvalues with a low absolute value and exhibit a slow behavior. Therefore it is reasonable to analyze the controllability and observability of the pressure and saturation states separately. First the controllability and observability of the pressures will be analyzed with LTV observability and controllability matrices and empirical Gramians. Next, the controllability and observability of the saturations will be analyzed with LTV observability and controllability matrices, empirical Gramians and also, after time scale separation (see Section 2.2.2) and linearization, with LTI controllability and observability Gramians. This analysis will be done for two examples: one with a homogeneous and one with a heterogeneous permeability distribution.

For the first example with a homogeneous permeability distribution the Hankel singular values of all states and of the pressure and saturation states separately are calculated using empirical Gramians. These are shown in Figure 3.19. The values decrease rapidly, indicating that the reservoir model behaves as a model of much lower order. For a reservoir model with a homogeneous permeability distribution and only two wells this seems reasonable. The reason that empirical Gramians are chosen to calculate the Hankel singular values is that this method is applicable to both pressure and saturation states (as opposed to the approach that involves time scale separation), and gives good results for both pressures and saturations.

Analysis of pressure behavior

First the pressure behavior of the model is analyzed with LTV controllability and observability matrices. To this end model (3.17, 3.18) is linearized around the state trajectory resulting from a realization of the PRBS signal. Subsequently the

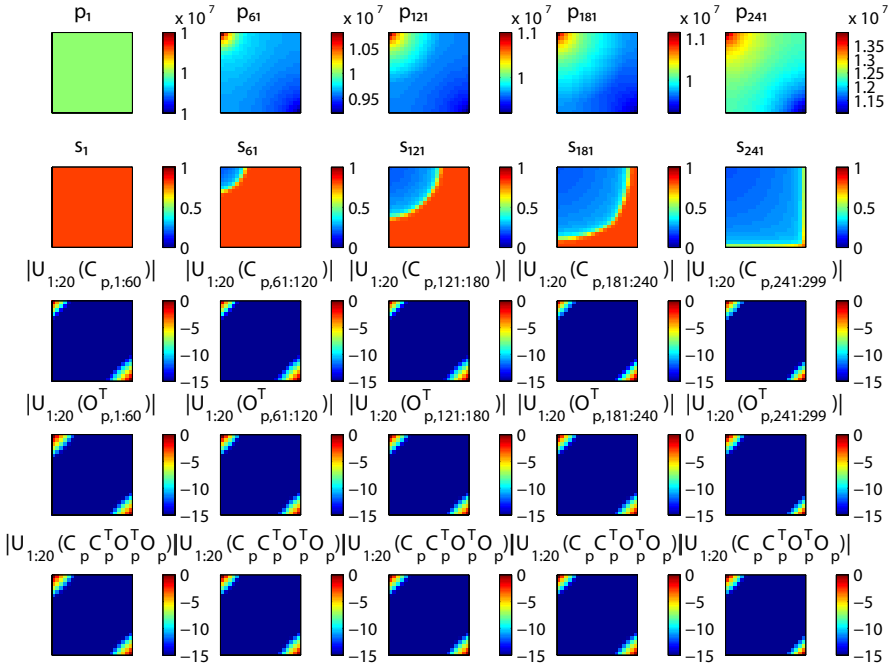

Figure 3.20 - Pressures with LTV controllability and observability matrices: The first two rows depict the grid block pressures and saturations at the start of each interval. The third row depicts for each interval the (^{10}log) weighted singular vector of the LTV controllability matrix related to pressures. The fourth row depicts for each interval the (^{10}log) weighted singular vector of the LTV observability matrix related to pressures. The last row depicts for each interval the (^{10}log) weighted singular vector of the product of LTV controllability and observability matrices related to pressures.

total simulation time is divided into five intervals of 60 time steps each. For each interval the LTV controllability matrix $\mathcal{C}_{k:k_i}$ (2.56) and the LTV observability matrix $\mathcal{O}_{k:k_f}$ (2.57) are calculated.

Next, the LTV controllability and observability matrices are divided into two parts: a pressure related part and a saturation related part. Rows 1 to n of the LTV controllability matrix $\mathcal{C}_{k:k_i}$ and columns 1 to n of the LTV observability matrix $\mathcal{O}_{k:k_f}$ are related to the pressure states, and these are indicated by subscript p, resulting in $\mathcal{C}_{p,k:k_i}$ and $\mathcal{O}_{p,k:k_f}$. The weighted singular vectors (3.7) of these matrices give an indication which pressure states are most controllable and most observable, respectively.

In Figure 3.20 the results are shown. The first two rows show snapshots of the grid block pressures and saturation at the start of each interval, i.e. time steps 1, 61, 121, 181 and 241. The third row shows for each interval the weighted sin-

gular vectors (3.7) related to the 20 most dominant singular vectors of the LTV controllability matrix ${}^{10}\log|\mathbf{U}_{1:20}(\mathcal{C}_{p,k:k_i})|$. For the first interval this is indicated by ${}^{10}\log|\mathbf{U}_{1:20}(\mathcal{C}_{p,1:60})|$. According to the Hankel singular values this is more than sufficient. The fourth row shows for each interval the ${}^{10}\log$ of the absolute weighted sum of the 20 most dominant singular vectors of the LTV observability matrix ${}^{10}\log|\mathbf{U}_{1:20}(\mathcal{O}_{p,k:k_f})|$. The red colors indicate high controllability and observability, and the blue colors low controllability and observability. The bottom row shows the weighted singular vector of the balancing transformation matrix

$$ {}^{10}\log|\mathbf{U}_{1:20}(\mathcal{C}_{p,k:k_i}\mathcal{C}_{p,k:k_i}^T\mathcal{O}_{p,k:k_f}^T\mathcal{O}_{p,k:k_f})|. $$

As can be seen from this example the most dominant controllable and observable pressures are around the wells. The larger the distance from the well, the more difficult it is to control or observe the pressure. This is similar to the single-phase example described in Section 3.3. Not surprisingly, after balancing it appears that the pressure states that are most relevant for the input-output behavior are located around the wells.

Next, for the same example empirical controllability and observability Gramians are calculated for intervals around the state $\mathbf{x}_{ss}$, where $\bar{\mathbf{x}}$ is chosen as the state vector in the middle of the interval. The interval length is again chosen as 60, and $r = s = 1$. The results are shown in Figure 3.21. The plots related to observability depicted in the fourth row are identical to the plots in Figure 3.20. The plots related to controllability have values with a different range (note the scale). The reason for this is that the pressure states have high values (in the order 10^7) and therefore the values of the empirical Gramians and specifically $\mathbf{\Phi}_k^{ilu}$ in (2.63) are also higher. However, the key observation still holds, namely that the pressures are most controllable around the wells. Also, after balancing the pressures most relevant for the input-output behavior are located directly around the wells. This is completely in line with the observations for the 2D single-phase reservoir models discussed in the previous section.

Analysis of saturation behavior

Next, we analyze the controllability and observability of the saturation behavior in two-phase flow in porous media. Three approaches are used: LTV controllability and observability matrices, empirical controllability and observability Gramians, and controllability and observability Gramians after time scale separation and linearization.

First the controllability and observability of the model given in (3.17, 3.18) are analyzed with LTV controllability and observability matrices after linearization at each time step. Rows $n+1$ to $2n$ of the controllability matrix $\mathcal{C}_{k:k_i}$ in (2.56) and columns $n+1$ to $2n$ of the observability matrix $\mathcal{O}_{k:k_f}$ in (2.57) are related to the saturation behavior. This is indicated by subscript s, resulting in $\mathcal{C}_{s,k:k_i}$ and $\mathcal{O}_{s,k:k_f}$.

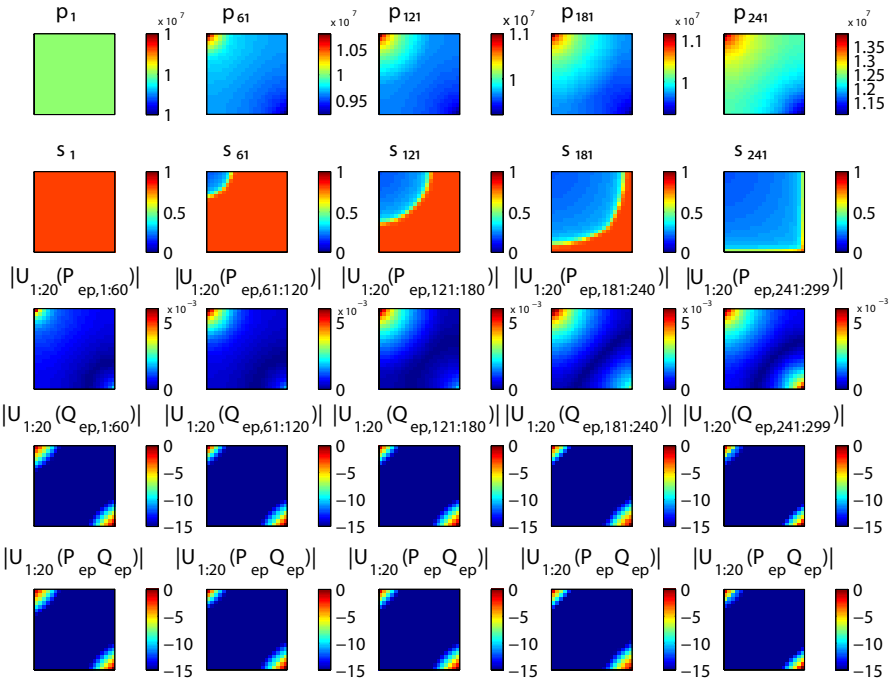

Figure 3.21 - Pressures with empirical controllability and observability Gramians: The first two rows depict the grid block pressures and saturations at the start of each interval. The third row depicts for each interval the (^{10}log) weighted singular vector of the empirical controllability Gramian related to pressures. The fourth row depicts for each interval the (^{10}log) weighted singular vector of the empirical observability Gramian related to pressures. The last row depicts for each interval the (^{10}log) weighted singular vector of the product of empirical controllability and observability Gramian related to pressures.

The first two rows in Figure 3.22 show the snapshots of pressure and saturation at the start of each interval. The third row shows for each interval the weighted singular vectors (3.7) related to the 20 most dominant singular vectors of the LTV controllability matrix $^{10}\log|\mathbf{U}_{1:20}(\mathcal{C}_{s,k:k_i})|$. The fourth row shows for each interval $^{10}\log|\mathbf{U}_{1:20}(\mathcal{O}_{s,k:k_f})|$. The bottom row shows for each interval the weighted singular vector of the balancing transformation matrix

$$^{10}\log|\mathbf{U}_{1:20}(\mathcal{C}_{s,k:k_i}\mathcal{C}_{s,k:k_i}^T\mathcal{O}_{s,k:k_f}^T\mathcal{O}_{s,k:k_f})|.$$

The controllability and observability results for saturations obtained with the LTV controllability and controllability matrices are suspicious, and are not in line with the results presented hereafter obtained with empirical Gramians or after time-scale separation and linearization. The plots in Figure 3.22 show a strong resemblance to the plots in Figure 3.20 related to pressures. A probable reason for this is that the pressure behavior is fast relative to the saturation behavior and therefore is more dominant. Furthermore, the submatrices of $\mathbf{A}$ after linearization that are related to saturation, i.e. $\mathbf{A}_{21}$ and $\mathbf{A}_{22}$, contain values that are approximately a factor 10^{10} lower than the values in submatrices related to pressures, i.e. $\mathbf{A}_{11}$ and $\mathbf{A}_{12}$. This possibly results in numerical issues, since to calculate the LTV controllability and observability matrices (2.56, 2.57) the system matrices are multiplied several times with each other.

Next, we analyze the controllability and observability of the saturation states with empirical controllability and observability Gramians. These are calculated for sliding intervals around the state $\bar{\mathbf{x}}$, where $\bar{\mathbf{x}}$ is chosen as the state vector in the middle of the interval. The interval length in Figure 3.23 is chosen as 60, and $r = s = 1$. The first two rows in Figure 3.23 shows again the snapshots of pressure and saturation. The third row shows the weighted singular vector of the empirical controllability Gramian $^{10}\log|\mathbf{U}_{1:20}(\mathcal{P}_{es,1:60})|$, indicating that the saturation states are most controllable in the grid blocks where the fluid front is located. This is understandable since the saturation values around the front are the only values that change using the specific input signal. All other saturation values are either at their maximum value (upstream of the front) or at their minimum value (downstream of the front). The fourth row in Figure 3.23 shows the weighted singular value of the empirical observability Gramian $^{10}\log|\mathbf{U}_{1:20}(\mathcal{Q}_{es,1:60})|$, indicating that the saturation in the grid blocks close to the wells are most observable. There seems to be no influence of the arrival of the saturation front on the observability. The fifth row shows the weighted value of the balanced states $^{10}\log|\mathbf{U}_{1:20}(\mathcal{P}_{es,1:60}\mathcal{Q}_{es,1:60})|$, indicating that the saturation states around the front are most relevant for the input-output behavior. Furthermore, upstream of the front the states are more relevant than downstream of the front, since the values of the weighted singular vector are higher upstream of the front.

Finally, time scale separation (see Section 2.2.2) is used to separate the pressure and saturation states and obtain a singularly perturbed slow approximation of the reservoir model. Consider (2.26), a nonlinear equation in terms of water saturation. This equation is linearized around the state and input in the middle of the interval, and subsequently the LTI controllability and observability Gramians

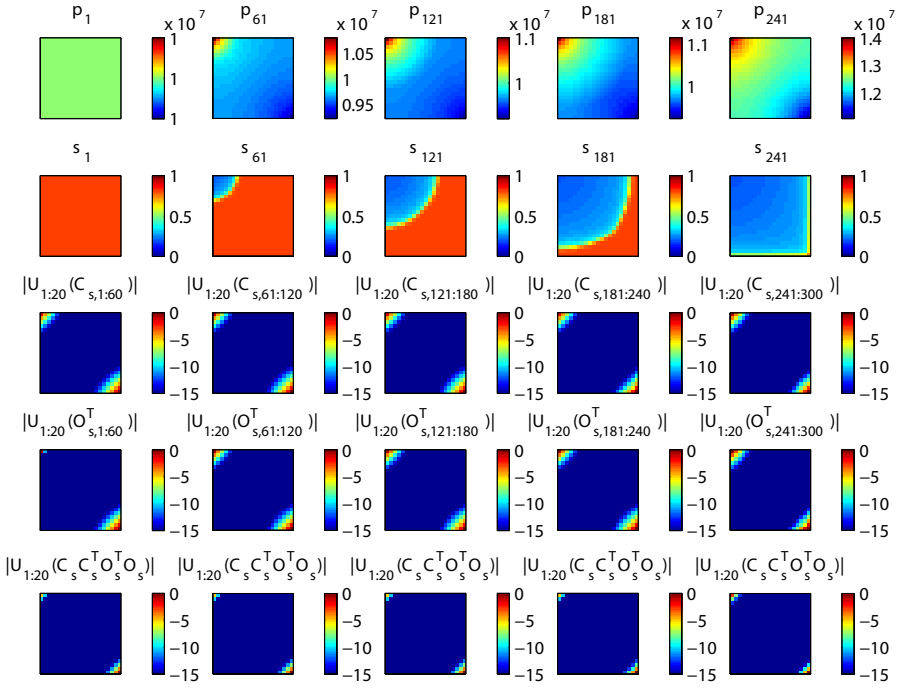

Figure 3.22 - Saturations with LTV controllability and observability matrices: The first two rows depict the grid block pressures and saturations at the start of each interval. The third row depicts for each interval the (^{10}log) weighted singular vector of the LTV controllability matrix related to saturations. The fourth row depicts for each interval the (^{10}log) weighted singular vector of the LTV observability matrix related to saturations. The last row depicts for each interval the (^{10}log) weighted singular vector of the product of LTV controllability and observability matrices related to saturations.

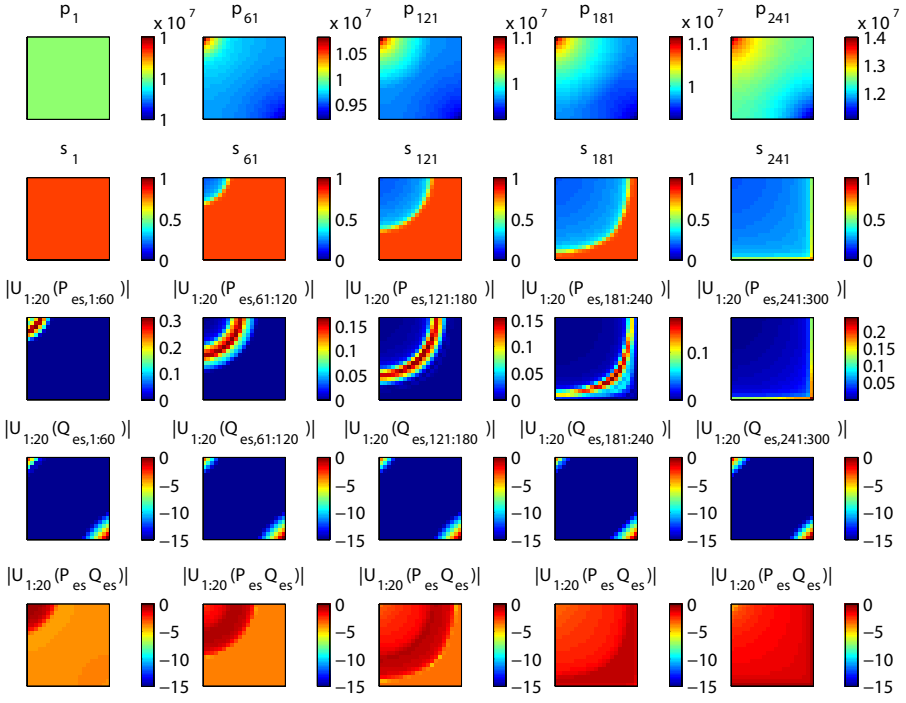

Figure 3.23 - Saturations with empirical controllability and observability Gramians: The first two rows depict the grid block pressures and saturations at the start of each interval. The third row depicts for each interval the (^{10}log) weighted singular vector of the empirical controllability Gramian related to saturations. The fourth row depicts for each interval the (^{10}log) weighted singular vector of the empirical observability Gramian related to saturations. The last row depicts for each interval the (^{10}log) weighted singular vector of the product of empirical controllability and observability Gramian related to saturations.

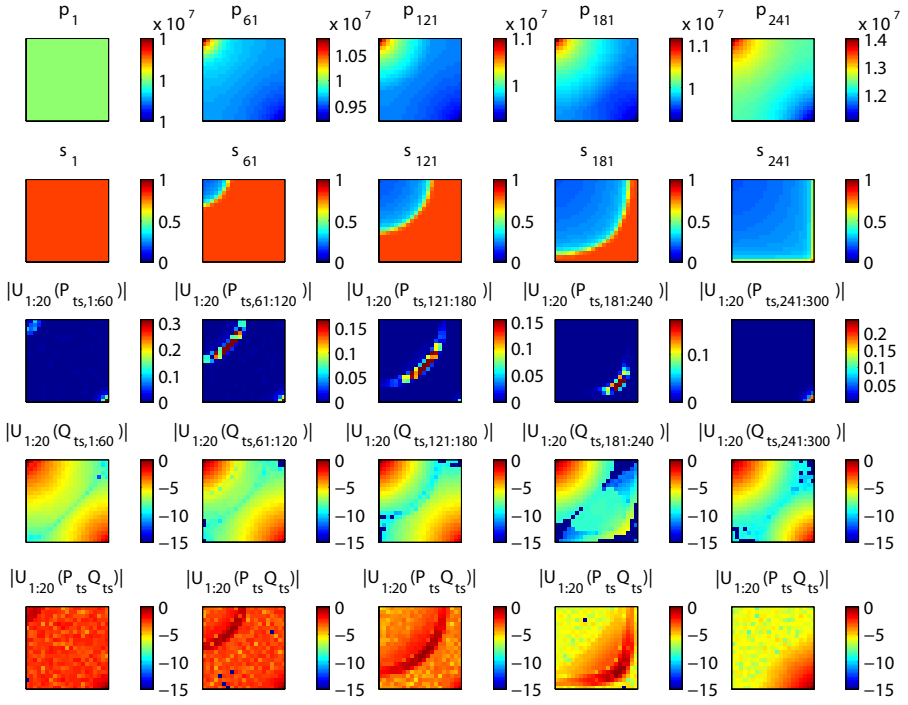

Figure 3.24 - Saturations with time scale separation and linearization: The first two rows depict the grid block pressures and saturations at the start of each interval. The third row depicts for each interval the (^{10} log) weighted singular vector of the controllability Gramian related to saturations after time scale separation and linearization. The fourth row depicts for each interval the (^{10} log) weighted singular vector of the observability Gramian related to saturations. The last row depicts for each interval the (^{10} log) weighted singular vector of the product of controllability and observability Gramian related to saturations.

are calculated. In Figure 3.24 the results of this analysis are shown. The third row shows the weighted singular vector of the controllability Gramian, denoted by ${}^{10}\log|\mathbf{U}_{1:20}(\mathcal{P}_{ts,1:60})|$, indicating that the saturation states are most controllable in the grid blocks where the fluid front is located. This is similar to results from the analysis with empirical controllability Gramians. The fourth row in Figure 3.24 shows ${}^{10}\log|\mathbf{U}_{1:20}(\mathcal{Q}_{ts,1:60})|$, indicating that the saturation in the grid blocks close to the wells are most observable. Probably due to numerical issues in linearizing the saturation equation (2.26) the plots look different from the plots in Figure 3.23. However, the key observation still holds, namely that the saturation states are most controllable around the front and most observable around the wells where the saturation is measured. The fifth row shows the weighted value of the balanced states ${}^{10}\log|\mathbf{U}_{1:20}(\mathcal{P}_{ts,1:60}\mathcal{Q}_{ts,1:60})|$, indicating that the saturation states around the front are most relevant for the input-output behavior. Furthermore, upstream of the front the states are more relevant than downstream of the front, since the values of the weighted singular value are higher upstream of the front. Although the plots look 'noisy', they still show that the relevant saturation states are located around the front.

3.5.3 Example 2: heterogenous permeability

As a next step, the controllability and observability of a reservoir model with a heterogenous permeability distribution is analyzed. The permeability distribution contains a high permeable streak from the injector to the producer with an absolute permeability of 9.1×10^{-9} m^2. The absolute permeability in the other grid blocks is 10^{-10} m^2 - see Figure 3.25.

First, the controllability and observability of the pressure states are analyzed. The plots in Figure 3.26 show the weighted singular vector of the LTV controllability and observability matrices. The weighted singular vectors of the empirical Gramians are identical to the ones of the LTV controllability and observability matrices, and are therefore not shown. From Figure 3.26 we can conclude that the pressure states are controllable around the wells and in the high permeable streak down-

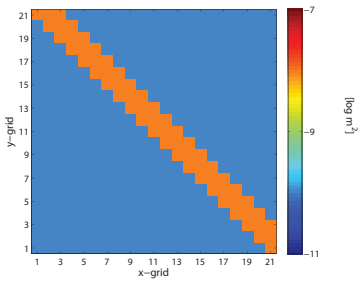

Figure 3.25: Heterogeneous permeability distribution as used in Section 3.5.3.

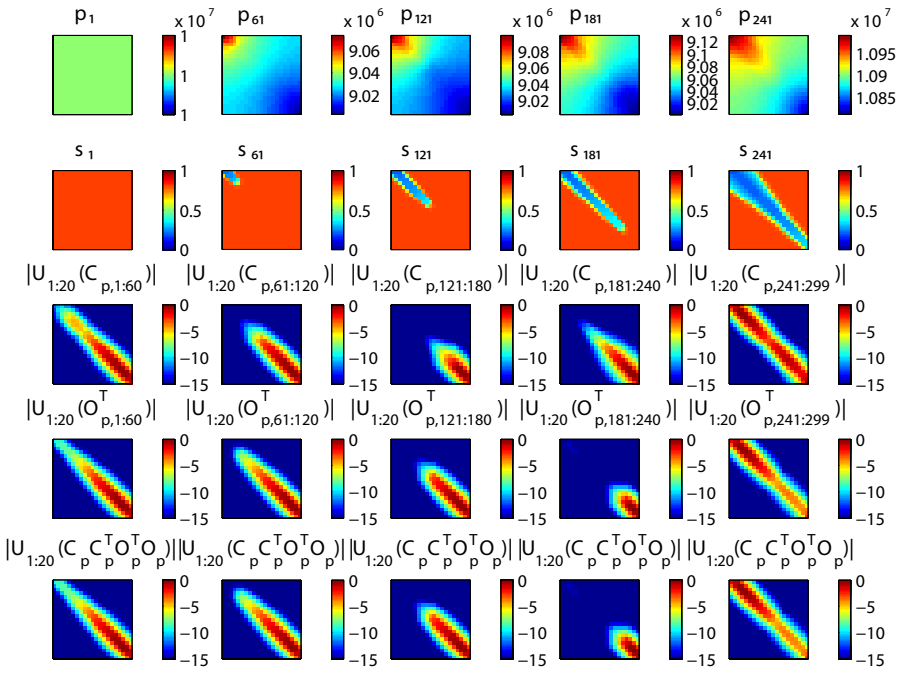

Figure 3.26 - Pressures with LTV controllability and observability matrices: The first two rows depict the grid block pressures and saturations at the start of each interval for the *heterogeneous* permeability distribution depicted in Figure 3.25. The third row depicts for each interval the (^{10}log) weighted singular vector of the LTV controllability matrix related to pressures. The fourth row depicts for each interval the (^{10}log) weighted singular vector of the LTV observability matrix related to pressures. The last row depicts for each interval the (^{10}log) weighted singular vector of the product of LTV controllability and observability matrices related to pressures.

stream of the oil-water front. When the front has reached the producer, the most controllable states are again located around the wells and in the high permeable streak. The most observable pressure states coincide with the most controllable pressure states. For this example the pressure states that are most relevant for the input-output behavior are according to the bottom row in Figure 3.26 also around the wells and in the high permeable streak.

Next, the controllability and observability of the saturation states are analyzed. Since the results of the analysis with LTV controllability and observability matrices for saturation states were unsatisfactory for the previous example, this approach is not used. In Figure 3.27 the results are shown using empirical Gramians, and in Figure 3.28 the results are shown for controllability and observability Gramians after time scale separation and linearization. As in the previous case, the saturation states are most controllable around the oil-water front. The satura-

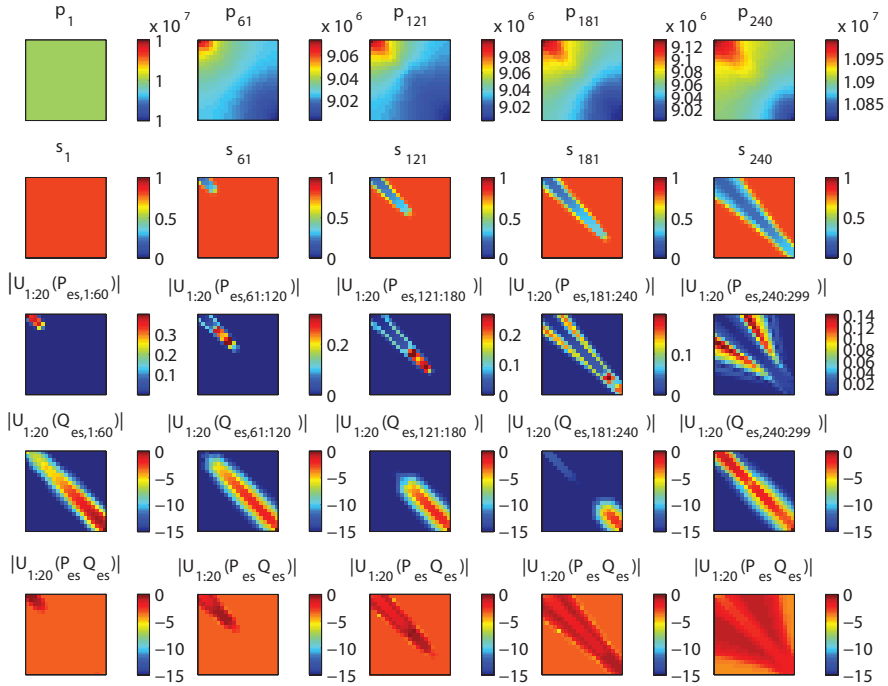

Figure 3.27 - Saturations with empirical controllability and observability Gramians: The first two rows depict the grid block pressures and saturations at the start of each interval for the *heterogeneous* permeability distribution depicted in Figure 3.25. The third row depicts for each interval the (^{10}log) weighted singular vector of the empirical controllability Gramian related to saturations. The fourth row depicts for each interval the (^{10}log) weighted singular vector of the empirical observability Gramian related to saturations. The last row depicts for each interval the (^{10}log) weighted singular vector of the product of empirical controllability and observability Gramian related to saturations.

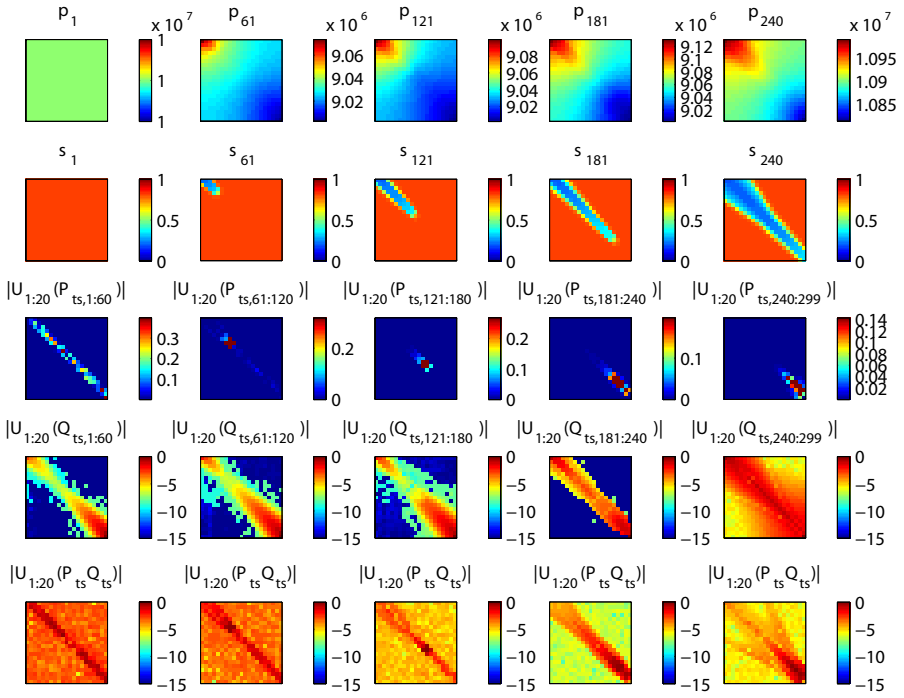

Figure 3.28 - Saturations with time scale separation and linearization: The first two rows depict the grid block pressures and saturations at the start of each interval for the *heterogeneous* permeability distribution depicted in Figure 3.25. The third row depicts for each interval the (^{10}log) weighted singular vector of the controllability Gramian related to saturations after time scale separation and linearization. The fourth row depicts for each interval the (^{10}log) weighted singular vector of the observability Gramian related to saturations. The last row depicts for each interval the (^{10}log) weighted singular vector of the product of controllability and observability Gramian related to saturations.

tion states that are most observable are located close to the wells and furthermore in the high-permeable streak. The last row in both figures indicate that the saturation states around the front are most relevant for the input-output behavior, where the states upstream of the front are more relevant than downstream of the front.

3.6 Chapter conclusions

In this chapter the controllability and observability of single-phase and two-phase reservoir models have been analyzed to determine the processes that are most relevant during the life of the reservoir. For the linear models we have used con-

trollability and observability matrices, Gramians and empirical Gramians. For the nonlinear models, the controllability and observability around a state trajectory have been analyzed using LTV controllability and observability matrices after linearization, empirical Gramians and with time-scale separation and linearization.

Based on the analyzed examples we conclude that the Hankel singular values of reservoir models decrease rapidly, indicating that they behave as models of much lower order than the state-space models that results after discretization. Furthermore, pressures are most controllable and observable around the wells that can control and observe the pressure states. The saturations are most controllable around the fluid front and most observable around the wells. After balancing the model we can conclude that the most relevant pressure states are located around the wells and the most relevant saturation states are located around the fluid front. Following from the examples dealing with a heterogenous permeability distribution we can conclude that model parameters, such as permeability, that alter the shape and position of the fluid front, do influence the observability and controllability properties of the reservoir, and hence generalize the results.

Based on the examples we conclude that the position of the wells and the dynamics of the front between reservoir fluids determine the controllability and observability properties of the reservoir. Therefore, for fixed well positions, reduced-order models should focus on modeling the fluid front(s).

Possible applications of the controllability and observability analysis are e.g. control of the fluid front as described in e.g. Fyrozjaee and Yortsos (2006); Jansen et al. (2009), and sensor or measurement location optimization. The latter deals with the problem to choose an optimal sensor location that maximizes observability - see e.g. Brewer et al. (2007).

4 CHAPTER

Identifiability: From Qualitative Analysis to Model Structure Approximation

To increase the predictive capacity of a reservoir model its parameters are estimated from measurements. It is well known that not all parameters can be estimated from measurements, in other words, the model is not identifiable. To analyze which parameters can be best estimated the notions of (local) identifiability and structural identifiability are used in a quantitative way. Considering large-scale (nonlinear) physical models the question is addressed how to approximate the model structure. This implies addressing the question how the model structure can be approximated so as to achieve identifiability, while retaining the interpretation of the physical parameters. In this chapter this problem is addressed in a prediction error setting, and it is shown how the construction of best identifiable model structure approximations relates to notions of controllability and observability. Additionally the analysis in terms of an off-line prediction error approach relates to iterative optimization algorithms (like Gauss-Newton and Steepest-Descent) as well as to sequential (recursive) parameter estimation methods, either in a Bayesian or a non-Bayesian framework.

4.1 Introduction

When building dynamic models from physical first-principles relations often model structures occur that are large-scale in their dimensions (due to spatial discretization of pde's) and include a high number of physically interpretable parameters. If subsequently the model parameters have to be identified from measurement data with prediction error methods (PEM) or (extended) Kalman filtering methods the question occurs whether the parameters are identifiable. The

notion of identifiability refers -roughly speaking- to the question whether parameter changes can be observed in the model output signal (output identifiability) or in the model's transfer function (structural identifiability). This is specifically important in the case of reservoir models, since these models are used to make long-term predictions of the reservoir flow behavior and therefore a good match with historical measurement data alone is not enough.

The notion of output identifiability has been studied in e.g. Grewal and Glover (1976) and Ljung (1999). The notion of structural identifiability was first stated by Bellman and Åström (1970) and has been extensively studied in the field of compartmental modeling (Godfrey 1983), Norton (1980). State-space model parameterizations have been analyzed by Glover and Willems (1974) and Walter (1987). Lately there has been a renewed interest in structural identifiability analysis, with contributions from Stigter and Peeters (2007) and Van Doren et al. (2008a).

In general identifiability questions are considered qualitatively, i.e. through deciding whether a model structure is identifiable or not. The tests required for this decision are typically rank evaluations of matrices, as e.g. Fisher's information matrix, around a particular local operating point in the parameter space, see e.g. Dötsch and Van den Hof (1996). Restricting attention to a local analysis is often the only situation that is feasible in terms of computational complexity. For issues around global properties see e.g. Ljung and Glad (1994).

However, when considering parameters in large scale (nonlinear) physical models it is relevant to raise the question how the notion of identifiability can be quantified. This implies addressing the question which part of the parameter space is best identifiable, and which part of the model structure can be approximated so as to achieve local identifiability, while retaining the interpretation of the physical parameters. For structural identifiability this question was preliminary addressed in Van Doren et al. (2008a). In Berntsen and Balchen (1973) the degree of identifiability was introduced. In Vajda et al. (1989) principal component analysis was applied to determine which parameters can be identified. McKelvey et al. (2004) introduced data driven local coordinates to overcome numerical difficulties in identification of overparameterized state-space systems.

In this chapter we will further investigate how the notions of identifiability and structural identifiability can be quantified to allow for a reduction in the parameter space with physically interpretable parameters. The analysis will be restricted to the local case, considering (linearized) nonlinear dynamical models that are non-linear in the parameters.

First the problem will be considered in the context of an off-line prediction error identification approach, while appropriate attention is given to the effect of parameter-scaling. Next, the analysis in terms of an off-line prediction error approach will be related to iterative optimization algorithms (like Gauss-Newton and Steepest-Descent) as well as to sequential (recursive) parameter estimation methods. In Section 4.6 the problem will be considered in the context of structural identifiability, where in addition an analytical expression is derived to evaluate structural identifiability. In Section 4.7 the identifiable parameter spaces are related to controllability and observability. Finally, in Section 4.8 a few small exam-

ples are presented.

4.2 Identifiability

4.2.1 Introduction

Consider the nonlinear dynamical model (2.70) that generates output predictions according to:

$$\hat{\mathbf{y}} = \mathbf{h}(\boldsymbol{\theta}, \mathbf{u}; \mathbf{x}_0). \tag{4.1}$$

where $\hat{\mathbf{y}}$ is a prediction of $\mathbf{y} := \begin{bmatrix} \mathbf{y}_1^T & \dots & \mathbf{y}_N^T \end{bmatrix}^T$ denoting output signal measurements $\mathbf{y}_k \in \mathbb{R}^p$ stacked over time, $\boldsymbol{\theta} \in \Theta \subset \mathbb{R}^q$ the parameter vector, $\mathbf{u} := \begin{bmatrix} \mathbf{u}_1^T & \dots & \mathbf{u}_N^T \end{bmatrix}^T$ the input vector $\mathbf{u}_k \in \mathbb{R}^m$ stacked over time, and $\mathbf{x}_0$ the initial state vector. Since the model (4.1) is parameterized it represents an input/output model structure.

In a prediction error framework we consider parameter estimation methods that are obtained by minimizing a cost function $V(\boldsymbol{\theta})$:

$$V(\boldsymbol{\theta}) := \frac{1}{2}\boldsymbol{\epsilon}(\boldsymbol{\theta})^T \mathbf{P}_v^{-1} \boldsymbol{\epsilon}(\boldsymbol{\theta}), \tag{4.2}$$

where the prediction error $\boldsymbol{\epsilon}$ is defined as

$$\boldsymbol{\epsilon}(\boldsymbol{\theta}) = \mathbf{y} - \hat{\mathbf{y}} = \mathbf{y} - \mathbf{h}(\boldsymbol{\theta}, \mathbf{u}; \mathbf{x}_0), \tag{4.3}$$

where $\mathbf{y}$ denotes the measured outputs and $\hat{\mathbf{y}}$ the predictor, and $\mathbf{P}_v$ is (an estimate of) the covariance matrix of the noise $\mathbf{v}$ that is supposed to act on the measured output. In the rest of the chapter the shorthand notation $\mathbf{h}(\boldsymbol{\theta})$ is used to indicate $\mathbf{h}(\boldsymbol{\theta}, \mathbf{u}; \mathbf{x}_0)$.
The Jacobian of $V(\boldsymbol{\theta})$ with respect to the parameters is

$$\frac{\partial V(\boldsymbol{\theta})}{\partial \boldsymbol{\theta}} = \frac{\partial \boldsymbol{\epsilon}(\boldsymbol{\theta})^T}{\partial \boldsymbol{\theta}} \mathbf{P}_v^{-1} \boldsymbol{\epsilon}(\boldsymbol{\theta}) = -\frac{\partial \mathbf{h}(\boldsymbol{\theta})^T}{\partial \boldsymbol{\theta}} \mathbf{P}_v^{-1} \left(\mathbf{y} - \mathbf{h}(\boldsymbol{\theta})\right). \tag{4.4}$$

The Hessian of $V(\boldsymbol{\theta})$ with respect to the parameters is

$$\frac{\partial^2 V(\boldsymbol{\theta})}{\partial \boldsymbol{\theta}^2} = \frac{\partial \boldsymbol{\epsilon}(\boldsymbol{\theta})^T}{\partial \boldsymbol{\theta}} \mathbf{P}_v^{-1} \left(\frac{\partial \boldsymbol{\epsilon}(\boldsymbol{\theta})^T}{\partial \boldsymbol{\theta}}\right)^T + \mathbf{S} = \frac{\partial \mathbf{h}(\boldsymbol{\theta})^T}{\partial \boldsymbol{\theta}} \mathbf{P}_v^{-1} \left(\frac{\partial \mathbf{h}(\boldsymbol{\theta})^T}{\partial \boldsymbol{\theta}}\right)^T + \mathbf{S}, \tag{4.5}$$

where $\mathbf{S}$ denotes the second-order information in $\frac{\partial^2 V(\boldsymbol{\theta})}{\partial \boldsymbol{\theta}^2}$. The Jacobian and Hessian are for a given $\boldsymbol{\theta}$ and a given operating point (given by $\mathbf{u}$ and $\mathbf{x}_0$). Parameter estimation then consists in finding a parameter estimate as a minimizing argument of the cost function $V(\boldsymbol{\theta})$

$$\hat{\boldsymbol{\theta}} := \arg\min_{\boldsymbol{\theta}} V(\boldsymbol{\theta}). \tag{4.6}$$

At $\hat{\boldsymbol{\theta}}$ the cost function $V(\boldsymbol{\theta})$ is minimized and the Jacobian (4.4) is zero, i.e. $\frac{\partial V(\boldsymbol{\theta})}{\partial \boldsymbol{\theta}} = \mathbf{0}$ at $\hat{\boldsymbol{\theta}}$.

4.2.2 Analyzing identifiability

Local identifiability in $\hat{\boldsymbol{\theta}}$, defined in Definition 2.4, is generally evaluated by the test whether the optimization problem (4.6) has an unique solution in the parameter space. By locally approximating the cost function $V(\boldsymbol{\theta})$ by a quadratic function[1], and thus neglecting the second order term $\mathbf{S}$ in (4.5), uniqueness of $\hat{\boldsymbol{\theta}}$ is guaranteed if the Hessian at $\hat{\boldsymbol{\theta}}$ is positive definite, i.e. $\frac{\partial^2 V(\boldsymbol{\theta})}{\partial \boldsymbol{\theta}^2} > 0$ at $\hat{\boldsymbol{\theta}}$, which in this case is equivalent to rank $\frac{\partial^2 V(\boldsymbol{\theta})}{\partial \boldsymbol{\theta}^2} = q$. This is a sufficient condition for local identifiability in $\hat{\boldsymbol{\theta}}$, see e.g. Bellman and Åström (1970), Glover and Willems (1974) and Ljung (1999).

The considered rank test is naturally performed by applying a singular value decomposition (SVD):

$$\frac{\partial^2 V(\boldsymbol{\theta})}{\partial \boldsymbol{\theta}^2} = \mathbf{U}\boldsymbol{\Sigma}\mathbf{V}^T = \begin{bmatrix} \mathbf{U}_1 & \mathbf{U}_2 \end{bmatrix} \begin{bmatrix} \boldsymbol{\Sigma}_1 & \mathbf{0} \\ \mathbf{0} & \mathbf{0} \end{bmatrix} \begin{bmatrix} \mathbf{V}_1^T \\ \mathbf{V}_2^T \end{bmatrix}, \tag{4.7}$$

where matrices $\mathbf{U}$ and $\mathbf{V}$ are unitary matrices, $\boldsymbol{\Sigma}_1 = \operatorname{diag}(\sigma_1, \ldots, \sigma_p)$ with $\sigma_1 \geq \cdots \geq \sigma_p$. If $p = q$ then identifiability is confirmed. If $p < q$ then the column space of $\mathbf{U}_1$ represents the subspace of the parameter space that is identifiable, and the column space of $\mathbf{U}_2$ is its orthogonal complement, characterizing the subspace that is not identifiable.

As a result, the SVD of the Hessian can be used to extend the qualitative treatment of the question whether or not a particular model structure is identifiable, to a quantitative property of specifying the identifiable parameter space. The columns of $\mathbf{U}_1$ represent basis functions in the parameter space, determining the linear combinations of the original parameters that will be identifiable from the measurements. This implies that it is possible to reparameterize the model structure by defining a reduced-order parameter $\boldsymbol{\rho}$ defined by

$$\boldsymbol{\theta} = \mathbf{U}_1 \boldsymbol{\rho} \tag{4.8}$$

leading to an identifiable model structure in the parameter $\boldsymbol{\rho}$ through the mapping (4.8). The limitation of the approach is of course that only linear transformations are considered.

4.2.3 Model structure approximation

When in the SVD of the Hessian singular values are found that are (very) small, this points to directions in the parameter space that have a very limited (but nonzero) influence on the cost function V. In identification terms this corresponds to directions in the parameter space in which the variance is large. The Hessian evaluated at $\hat{\boldsymbol{\theta}}$ is connected with the variance of $\hat{\boldsymbol{\theta}}$, since for the Gaussian case (and provided that $\hat{\boldsymbol{\theta}}$ is a consistent estimate) it follows that

$$\operatorname{cov}(\hat{\boldsymbol{\theta}}) = \mathbf{J}^{-1} \tag{4.9}$$

[1] This is achieved by approximating $\mathbf{h}(\boldsymbol{\theta})$ with a first-order Taylor expansion around $\hat{\boldsymbol{\theta}}$

with $\mathbf{J}$ the Fisher information matrix

$$\mathbf{J} = \mathbb{E}\left[\left. \frac{\partial^2 V(\boldsymbol{\theta})}{\partial \boldsymbol{\theta}^2} \right|_{\hat{\theta}} \right], \tag{4.10}$$

where $\mathbb{E}$ denotes expectation (Ljung 1999). For (4.7), where $\boldsymbol{\Sigma}_2 = \mathbf{0}$, this leads to

$$\mathrm{cov}(\hat{\boldsymbol{\theta}}) = \infty. \tag{4.11}$$

We are interested in specifying that part of the parameter space that is best identifiable by removing the subspace that has only a very small influence on the cost function V. This reasoning would point to removing those parameter (combinations) from the model structure for which the variances are very large (and the corresponding singular values are very small), as also addressed in Vajda et al. (1989) and Hjalmarsson (2005) for nonlinear parameter mappings, and in Lund and Foss (2008) for single parameters.

The appropriate selection of the identifiable parameter space is then obtained from

$$\frac{\partial \mathbf{h}(\boldsymbol{\theta})^T}{\partial \boldsymbol{\theta}} \mathbf{P}_v^{-\frac{1}{2}} = \begin{bmatrix} \mathbf{U}_1 & \mathbf{U}_2 \end{bmatrix} \begin{bmatrix} \boldsymbol{\Sigma}_1 & \mathbf{0} \\ \mathbf{0} & \boldsymbol{\Sigma}_2 \end{bmatrix} \begin{bmatrix} \mathbf{V}_1^T \\ \mathbf{V}_2^T \end{bmatrix}, \tag{4.12}$$

where the separation between $\boldsymbol{\Sigma}_1$ and $\boldsymbol{\Sigma}_2$ is chosen in such a way that the singular values in $\boldsymbol{\Sigma}_2$ are considerably smaller than those in $\boldsymbol{\Sigma}_1$. After reparameterizing the model structure using (4.8) the parameters $\boldsymbol{\rho}$ are well identifiable with a limited variance and the physical interpretation of the parameters is untouched. Specifically in the case of parameters in spatially distributed systems with all parameters having the same physical unit, the singular vectors can be seen as basis functions in the parameter space. Examples hereof will be provided in the next chapter.

For (4.12), where $\mathrm{trace}(\boldsymbol{\Sigma}_2) > \mathbf{0}$, this leads to

$$\mathrm{cov}(\hat{\boldsymbol{\theta}}) = \begin{bmatrix} \mathbf{U}_1 & \mathbf{U}_2 \end{bmatrix} \begin{bmatrix} \boldsymbol{\Sigma}_1^{-2} & \mathbf{0} \\ \mathbf{0} & \boldsymbol{\Sigma}_2^{-2} \end{bmatrix} \begin{bmatrix} \mathbf{U}_1^T \\ \mathbf{U}_2^T \end{bmatrix}, \tag{4.13}$$

while the sample estimate of the reparameterized parameter estimate is given by

$$\mathrm{cov}(\mathbf{U}_1 \hat{\boldsymbol{\rho}}) = \mathbf{U}_1 \boldsymbol{\Sigma}_1^{-2} \mathbf{U}_1^T < \mathrm{cov}(\hat{\boldsymbol{\theta}}), \tag{4.14}$$

showing a variance that is reduced by the reparameterization.

4.3 Parameter scaling in identifiability

The notions of identifiability are defined in such a way that the result is independent of any particular scaling of parameters, where scaling is related to the choice of physical units in which the parameters are represented. For the case where $\boldsymbol{\Sigma}_2 = \mathbf{0}$ as in (4.7), scaling clearly has no influence on identifiability issues, since

scaling of the parameters leads to scaling of the singular values in $\mathbf{\Sigma}_1$ and the zeros in $\mathbf{\Sigma}_2$ are not affected.

However, for the case where $\mathbf{\Sigma}_2$ contains nonzero singular values, the numerical values in $\mathbf{\Sigma}_1$ and $\mathbf{\Sigma}_2$ are affected by the scaling and can possibly influence the separation between $\mathbf{\Sigma}_1$ and $\mathbf{\Sigma}_2$ in (4.12) and hence the identifiable parameter space. This particularly plays a role in case the physical parameters contain different physical quantities. For example, in reservoir models the parameters to be estimated can be grid block permeabilities and porosities. The question is then how to balance the variability in the different physical parameters.

It appears that in the approach presented in Section 4.2.3 the absolute variance is used as a measure of selection, and as a result the selected parameter space is dependent on the scaling of the parameters. In case one prefers a selection mechanism that is scaling independent, the relative variance of parameters can be chosen, i.e.

$$\mathrm{cov}(\mathbf{\Gamma}_{\hat{\theta}}^{-1}\hat{\boldsymbol{\theta}}) \tag{4.15}$$

where

$$\mathbf{\Gamma}_{\hat{\theta}} = \mathrm{diag}\left(\begin{array}{ccc} |\hat{\theta}_1| & \ldots & |\hat{\theta}_q| \end{array} \right). \tag{4.16}$$

This motivates the analysis of a scaled Hessian

$$\mathbf{\Gamma}_{\hat{\theta}} \left. \frac{\partial^2 V(\boldsymbol{\theta})}{\partial \boldsymbol{\theta}^2} \right|_{\hat{\boldsymbol{\theta}}} \mathbf{\Gamma}_{\hat{\theta}}, \tag{4.17}$$

related to the scaled Fisher information matrix $\tilde{\mathbf{J}}$:

$$\tilde{\mathbf{J}} = \mathbb{E}\left[\mathbf{\Gamma}_{\hat{\theta}} \left. \frac{\partial^2 V(\boldsymbol{\theta})}{\partial \boldsymbol{\theta}^2} \right|_{\hat{\boldsymbol{\theta}}} \mathbf{\Gamma}_{\hat{\theta}} \right]. \tag{4.18}$$

The appropriate selection of the identifiable parameter space is then obtained from:

$$\mathbf{\Gamma}_{\hat{\theta}} \frac{\partial \mathbf{h}(\boldsymbol{\theta})^T}{\partial \boldsymbol{\theta}} \mathbf{P}_v^{-\frac{1}{2}} = \left[\begin{array}{cc} \mathbf{U}_1 & \mathbf{U}_2 \end{array} \right] \left[\begin{array}{cc} \mathbf{\Sigma}_1 & \mathbf{0} \\ \mathbf{0} & \mathbf{\Sigma_2} \end{array} \right] \left[\begin{array}{c} \mathbf{V}_1^T \\ \mathbf{V}_2^T \end{array} \right]. \tag{4.19}$$

Consequences of the parameter scaling are illustrated later on for some simple examples in Section 4.8.

Note that the evaluation of the relative variance of parameter estimates for model structure selection is also done in classical methods when considering the standard deviation of an estimated parameter related to the parameter value itself (see e.g. Ljung 1999; Hjalmarsson 2005). However usually the analysis is performed for single parameters and not for linear combinations of parameters. For example, in Figure 4.1 zero is included in the parameter confidence interval, and hence according to Hjalmarsson (2005) parameter θ_2 can be removed. In the analysis presented here linear combinations of parameters are evaluated, thus focussing on the ratio between the lengths of the principle axes of the uncertainty ellipsoids representing the parameter confidence bounds for $\hat{\boldsymbol{\theta}}$ - see Figure 4.1 in which the principle axis marked in blue is preserved. The parameter uncertainty ellipsoid is expressed by

$$\mathcal{D}(\alpha, \hat{\boldsymbol{\theta}}) = \left(\boldsymbol{\theta} \mid N(\boldsymbol{\theta} - \hat{\boldsymbol{\theta}})^T \mathbf{P}^{-1} (\boldsymbol{\theta} - \hat{\boldsymbol{\theta}}) \leq \chi^2_{q,\alpha} \right), \tag{4.20}$$

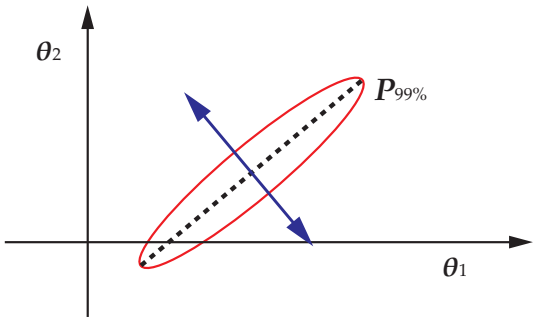

Figure 4.1: Uncertainty ellipsoid in a two-dimensional parameter space showing the principle axes of the ellipsoid.

where $\mathbf{P} = \mathbf{J}^{-1}$ is the covariance matrix of the estimator, and $\chi^2_{q,\alpha}$ corresponds to a probability level α in the χ^2_q-distribution with q degrees of freedom. This parameter uncertainty ellipsoid is used to specify that $\boldsymbol{\theta}_0 \in \mathcal{D}(\alpha, \hat{\boldsymbol{\theta}})$ with probability α.

4.4 A Bayesian approach

In the previous sections we have dealt with the lack of identifiability and the non-uniqueness in the estimated parameters by reducing the parameter space. Alternatively, additional prior information can be added to the identification problem, usually in the form of a Bayesian cost function that takes account of prior knowledge on the parameters to be estimated. In this setting the use of an alternative cost function is considered:

$$V_p(\boldsymbol{\theta}) := V(\boldsymbol{\theta}) + \frac{1}{2}(\boldsymbol{\theta} - \boldsymbol{\theta}_p)\mathbf{P}_{\boldsymbol{\theta}}^{-1}(\boldsymbol{\theta} - \boldsymbol{\theta}_p), \tag{4.21}$$

where the second term represents the weighted mismatch between the parameter vector and the prior parameter vector $\boldsymbol{\theta}_p$ with covariance $\mathbf{P}_{\boldsymbol{\theta}}$. When again the model output $\mathbf{h}(\boldsymbol{\theta})$ is approximated using a first-order Taylor expansion around $\boldsymbol{\theta}_p$, the Jacobian and Hessian are given by

$$\frac{\partial V_p(\boldsymbol{\theta})}{\partial \boldsymbol{\theta}} = -\frac{\partial \mathbf{h}(\boldsymbol{\theta})^T}{\partial \boldsymbol{\theta}}\mathbf{P}_v^{-1}\left(\mathbf{y} - \mathbf{h}(\boldsymbol{\theta})\right) + \mathbf{P}_{\boldsymbol{\theta}}^{-1}\left(\boldsymbol{\theta}_p - \boldsymbol{\theta}_m\right), \tag{4.22}$$

$$\frac{\partial^2 V_p(\boldsymbol{\theta})}{\partial \boldsymbol{\theta}^2} = \frac{\partial \mathbf{h}(\boldsymbol{\theta})^T}{\partial \boldsymbol{\theta}}\mathbf{P}_v^{-1}\left(\frac{\partial \mathbf{h}(\boldsymbol{\theta})^T}{\partial \boldsymbol{\theta}}\right)^T + \mathbf{P}_{\boldsymbol{\theta}}^{-1}, \tag{4.23}$$

respectively. The Hessian (4.23) consists of two terms: the first term is positive and the second term $\mathbf{P}_{\boldsymbol{\theta}}^{-1}$ is positive definite by construction. Therefore, since prior

information is added to the problem, the Hessian has full rank and the parameter estimate

$$\hat{\boldsymbol{\theta}}_{Bayes} := \arg\min_{\boldsymbol{\theta}} V_p(\boldsymbol{\theta}) \tag{4.24}$$

is unique. However, the parameter estimate can be severely influenced by the prior knowledge. If prior knowledge is not included, then there will be adaptations in the parameter space $\mathbf{U}_1$ only, while leaving the remainder of the space completely untouched. Furthermore, when parameter space $\mathbf{U}_2$ is made explicit, other sources of information can freely be applied when projected onto $\mathbf{U}_2$, without pinning oneself down from the start to one specific prior model, since this has no influence on $V_p(\boldsymbol{\theta})$.

The covariance matrix of the Bayesian parameter estimate can also be analyzed using the classical prediction error theory (Ljung 1999). Assuming consistent estimation and $\boldsymbol{\theta}_p = \boldsymbol{\theta}_0$ it can be shown that

$$\operatorname{cov}\left(\hat{\boldsymbol{\theta}}_{Bayes}\right) = \left(\mathbb{E}\left[\left.\frac{\partial^2 V_p(\boldsymbol{\theta})}{\partial \boldsymbol{\theta}^2}\right|_{\boldsymbol{\theta}_0}\right]\right)^{-1}, \tag{4.25}$$

In other words, the inverse of the Hessian of the identification criterion remains to play the role of (sample estimate of) the parameter covariance matrix, and the same considerations as discussed in the earlier sections can be applied to the SVD analysis of this Hessian.
The Hessian (4.23) can be rewritten as

$$\mathbf{P}_{\boldsymbol{\theta}}^{\frac{1}{2}}\left(\mathbf{P}_{\boldsymbol{\theta}}^{\frac{T}{2}}\frac{\partial \mathbf{h}(\boldsymbol{\theta})^T}{\partial \boldsymbol{\theta}}\mathbf{P}_v^{-1}\left(\frac{\partial \mathbf{h}(\boldsymbol{\theta})^T}{\partial \boldsymbol{\theta}}\right)^T\mathbf{P}_{\boldsymbol{\theta}}^{\frac{1}{2}}+\mathbf{I}\right)^{-1}\mathbf{P}_{\boldsymbol{\theta}}^{\frac{T}{2}}, \tag{4.26}$$

where we have used that $\mathbf{P}_{\boldsymbol{\theta}} = \mathbf{P}_{\boldsymbol{\theta}}^{\frac{1}{2}}\mathbf{P}_{\boldsymbol{\theta}}^{\frac{T}{2}}$, which exists since $\mathbf{P}_{\boldsymbol{\theta}}$ is a symmetric positive definite matrix by construction. In (4.26) the term

$$\mathbf{P}_{\boldsymbol{\theta}}^{\frac{T}{2}}\frac{\partial \mathbf{h}(\boldsymbol{\theta})^T}{\partial \boldsymbol{\theta}}\mathbf{P}_v^{-\frac{1}{2}} \tag{4.27}$$

can be discerned, where we have implicitly assumed that $\mathbf{P}_v$ is also a symmetric positive definite matrix. This is equivalent to the so-called dimensionless sensitivity matrix described in Zhang et al. (2002); Tavakoli and Reynolds (2009). The SVD of (4.27) is given by

$$\mathbf{P}_{\boldsymbol{\theta}}^{\frac{T}{2}}\frac{\partial \mathbf{h}(\boldsymbol{\theta})^T}{\partial \boldsymbol{\theta}}\mathbf{P}_v^{-\frac{1}{2}} = \breve{\mathbf{U}}\breve{\boldsymbol{\Sigma}}\breve{\mathbf{V}}^T. \tag{4.28}$$

The SVD of the inverse Hessian in (4.26) is given by

$$\mathbf{P}_{\boldsymbol{\theta}}^{\frac{T}{2}}\frac{\partial \mathbf{h}(\boldsymbol{\theta})^T}{\partial \boldsymbol{\theta}}\mathbf{P}_v^{-1}\left(\frac{\partial \mathbf{h}(\boldsymbol{\theta})^T}{\partial \boldsymbol{\theta}}\right)^T\mathbf{P}_{\boldsymbol{\theta}}^{\frac{1}{2}}+\mathbf{I} = \tilde{\mathbf{U}}\tilde{\boldsymbol{\Sigma}}\tilde{\mathbf{V}}^T. \tag{4.29}$$

where $\tilde{\mathbf{V}} = \tilde{\mathbf{U}}$ since the matrix is positive definite. It can be easily seen that $\tilde{\mathbf{U}} = \breve{\mathbf{U}}$, and that $\tilde{\boldsymbol{\Sigma}} = \breve{\boldsymbol{\Sigma}} + \mathbf{I}$. This means that expression (4.27) can be analyzed to

determine orthonormal basis functions that can be used to approximate the model structure in a Bayesian approach. The expression in (4.27) is of a similar form as the expression in (4.19) for the non-Bayesian framework; the weighting matrix $\mathbf{\Gamma}_{\hat{\theta}}$ in (4.19) is now replaced by the prior covariance matrix $\mathbf{P}_{\theta}^{\frac{T}{2}}$ in (4.19). From this analysis it can be concluded that in the Bayesian framework it seems natural to scale the Hessian with $\mathbf{P}_{\theta}^{\frac{T}{2}}$, possibly complemented with the weighting matrix $\mathbf{\Gamma}_{\hat{\theta}}$ as in (4.19).

4.5 Cost function minimization in identification

4.5.1 Iterative parameter estimation methods

In this section we will show how identifiability properties of the model structure relate to gradient-based iterative parameter estimation algorithms (e.g. Gauss-Newton and Steepest-Descent). These algorithms are referred to as off-line identification or batch identification, since first a batch of data is collected from the system and subsequently this batch is used to update the model. If we iteratively solve for a parameter estimate $\hat{\boldsymbol{\theta}}$ by minimizing a cost function $V(\boldsymbol{\theta})$, the general update rule in step m of a Newton-type algorithm is given by

$$\hat{\boldsymbol{\theta}}_{m+1} = \hat{\boldsymbol{\theta}}_m - \gamma \left(\frac{\partial^2 V}{\partial \boldsymbol{\theta}^2}\bigg|_{\hat{\boldsymbol{\theta}}_m} \right)^{-1} \frac{\partial V}{\partial \boldsymbol{\theta}}\bigg|_{\hat{\boldsymbol{\theta}}_m}, \tag{4.30}$$

where γ denotes a scalar damping factor. Note that in this expression the partial derivatives are evaluated in the local parameter $\hat{\boldsymbol{\theta}}_m$ whereas in the previous section we evaluated the Hessian in a (local) minimum $\hat{\boldsymbol{\theta}}$ of the cost function V. For notational simplicity

If we consider the prediction error cost function as used before, then for the model structure considered and after linearization of $\mathbf{h}(\boldsymbol{\theta})$ around parameter $\hat{\boldsymbol{\theta}}$ the update rule becomes

$$\hat{\boldsymbol{\theta}}_{m+1} = \hat{\boldsymbol{\theta}}_m - \gamma \left(\frac{\partial \mathbf{h}(\boldsymbol{\theta})^T}{\partial \boldsymbol{\theta}} \mathbf{P}_v^{-1} \left(\frac{\partial \mathbf{h}(\boldsymbol{\theta})^T}{\partial \boldsymbol{\theta}} \right)^T \right)^{-1} \frac{\partial \mathbf{h}(\boldsymbol{\theta})^T}{\partial \boldsymbol{\theta}} \mathbf{P}_v^{-1} \left(\mathbf{y} - \mathbf{h}(\boldsymbol{\theta}) \right) \tag{4.31}$$

where we have omitted, for brevity, the dependence of the Jacobian and Hessian on $\mathbf{h}(\boldsymbol{\theta})$. The parameter update (4.31) is actually a Gauss-Newton step (Dennis Jr. and Schnabel 1996), employing a first order Taylor expansion of $\mathbf{h}(\boldsymbol{\theta})$ around $\boldsymbol{\theta}_m$, similar to the approximation in Section 4.2.3. As an alternative, a Steepest-Descent algorithm (Dennis Jr. and Schnabel 1996) approximates the Hessian with any positive definite matrix, where standard the identity matrix is chosen. As a result, the update rule in the considered situation becomes:

$$\hat{\boldsymbol{\theta}}_{m+1} = \hat{\boldsymbol{\theta}}_m - \gamma \frac{\partial \mathbf{h}(\boldsymbol{\theta})^T}{\partial \boldsymbol{\theta}} \mathbf{P}_v^{-1} (\mathbf{y} - \mathbf{h}(\boldsymbol{\theta})).$$

Note that in case the Hessian (4.5) has full rank in $\hat{\boldsymbol{\theta}}_m$ scaling of the parameters influences the estimate of Steepest-Descent, but does not influence the estimate provided by Gauss-Newton - see e.g. Dennis Jr. and Schnabel (1996).

If the model structure is not identifiable in $\hat{\boldsymbol{\theta}}$ the matrix inverse in (4.31) will not exist. Although this is often indicated as a serious problem for iterative optimization algorithms it can simply be overcome by restricting the update rule to make steps only in that part of the parameter space that does influence the output predictor, see e.g. McKelvey and Helmersson (1997); McKelvey et al. (2004); Verdult (2002). This actually comes down to utilizing the pseudo-inverse of the Jacobian in (4.31) using again the SVD

$$\frac{\partial \mathbf{h}(\boldsymbol{\theta})^T}{\partial \boldsymbol{\theta}} \mathbf{P}_v^{-\frac{1}{2}} = \begin{bmatrix} \mathbf{U}_1 & \mathbf{U}_2 \end{bmatrix} \begin{bmatrix} \boldsymbol{\Sigma}_1 & \mathbf{0} \\ \mathbf{0} & \boldsymbol{\Sigma}_2 \end{bmatrix} \begin{bmatrix} \mathbf{V}_1^T \\ \mathbf{V}_2^T \end{bmatrix}. \tag{4.32}$$

In case $\boldsymbol{\Sigma}_2 = \mathbf{0}$ it follows that the update rule for the Gauss-Newton iteration can be expressed by

$$\hat{\boldsymbol{\theta}}_{m+1} = \hat{\boldsymbol{\theta}}_m - \gamma \mathbf{U}_1 \boldsymbol{\Sigma}_1^{-1} \mathbf{V}_1^T \mathbf{P}_v^{-\frac{1}{2}} (\mathbf{y} - \mathbf{h}(\boldsymbol{\theta})),$$

while the update rule of Steepest-Descent is given by

$$\hat{\boldsymbol{\theta}}_{m+1} = \hat{\boldsymbol{\theta}}_m - \gamma \mathbf{U}_1 \boldsymbol{\Sigma}_1 \mathbf{V}_1^T \mathbf{P}_v^{-\frac{1}{2}} (\mathbf{y} - \mathbf{h}(\boldsymbol{\theta})).$$

Both algorithms update the parameter only in the subspace that is determined by the column space of $\mathbf{U}_1$, being the identifiable subspace of the parameter space, provided that we would have evaluated identifiability in the local point $\hat{\boldsymbol{\theta}}_m$.

Note that the difference between the two update mechanisms is that Steepest-Descent emphasizes the vectors of $\mathbf{U}_1$ that correspond to large singular values of the Jacobian, while Gauss-Newton emphasizes the vectors of $\mathbf{U}_1$ that correspond to small singular values of the Jacobian (Douma 2008). Large singular values of the Jacobian are associated with directions in which the predictions are most sensitive to a change in the parameters. Steepest-Descent looks for the direction in which the cost function decreases as fast as possible. In other words, the algorithm looks for decreasing the cost function with the least amount of effort in changing the parameters. Gauss-Newton and PEM follow the opposite strategy: these algorithms look for a change in predicted outputs (i.e. cost function) that is induced by the largest change in the parameters. In other words, the most uncertain parameters are changed, i.e. those parameters are adapted to which the predicted outputs (i.e. cost function) are least sensitive.

Similar to the analysis in the previous sections the rank reduction of the Jacobian, as represented in (4.32) can of course be enforced if the SVD shows a large number of small singular values in $\boldsymbol{\Sigma}_2$, and the Jacobian is approximated by setting $\boldsymbol{\Sigma}_2 = \mathbf{0}$. A similar approach of Jacobian reduction is employed in the fully parameterized state-space model identification, using so-called data-driven local coordinates of McKelvey and Helmersson (1997); McKelvey et al. (2004) as well as in subspace identification Verdult (2002). In these approaches a parameter space is constructed that is orthogonal to the tangent space of the manifold representing equivalent

models. This parameterization has numerically attractive properties compared to the fully parameterized model structure, although it leads to the same search directions as Gauss-Newton (Wills and Ninness 2008). However, in this work we focus more on preserving the physical interpretation of the parameters since we are interested to obtain reliable long-term (non-linear) model predictions.

Finally for the sake of completeness, in Section 4.4 the Jacobian (4.22) and Hessian (4.23) are given for a Bayesian approach. The resulting Gauss-Newton iterative update rule (4.31) is given by

$$\hat{\boldsymbol{\theta}}_{m+1} = \hat{\boldsymbol{\theta}}_m - \gamma \left(\frac{\partial \mathbf{h}(\boldsymbol{\theta})}{\partial \boldsymbol{\theta}}^T \mathbf{P}_v^{-1} \left(\frac{\partial \mathbf{h}(\boldsymbol{\theta})}{\partial \boldsymbol{\theta}}^T \right)^T + \mathbf{P}_{\boldsymbol{\theta}}^{-1} \right)^{-1} \times \left(\frac{\partial \mathbf{h}(\boldsymbol{\theta})}{\partial \boldsymbol{\theta}}^T \mathbf{P}_v^{-1} (\mathbf{y} - \mathbf{h}(\boldsymbol{\theta})) + \mathbf{P}_{\boldsymbol{\theta}}^{-1} \left(\boldsymbol{\theta}_p - \boldsymbol{\theta}_m \right) \right). \quad (4.33)$$

The resulting Steepest-Descent iterative update rule (4.32) is given by

$$\hat{\boldsymbol{\theta}}_{m+1} = \hat{\boldsymbol{\theta}}_m - \gamma \left(\frac{\partial \mathbf{h}(\boldsymbol{\theta})}{\partial \boldsymbol{\theta}}^T \mathbf{P}_v^{-1} (\mathbf{y} - \mathbf{h}(\boldsymbol{\theta})) + \mathbf{P}_{\boldsymbol{\theta}}^{-1} \left(\boldsymbol{\theta}_p - \boldsymbol{\theta}_m \right) \right). \quad (4.34)$$

4.5.2 Recursive estimation and filtering

Identifiability properties of the model structure are also to be considered in recursive parameters estimation algorithms. Recursive estimation algorithms update the model at each time instant that new data becomes available. Synonyms for recursive estimation are online and sequential estimation. Advantages of recursive estimation algorithms are that the estimate of the parameter variance is usually included in the algorithm, that they can be computationally more efficient than off-line algorithms, and that the properties of the model are allowed to vary with time (Ljung 1999). Recursive algorithms in a prediction error framework (RPE) are extensively described in Ljung and Söderström (1983) and Ljung (1999).

Recursive algorithms can be derived from off-line algorithms by including a new observation at the same time as performing an iteration. The recursive least-squares and off-line least-squares algorithms are exactly the same (Ljung 1999). In Ho (1962) the least-squares algorithm is also related to the Kalman filter, where the matrix inversion equations of Sherman-Morrison-Woodbury are used. The matrix inversion equations of Sherman-Morrison-Woodbury (see e.g. Golub and Van Loan 1996) are useful to rewrite a matrix expression in such a way that the matrix expression that is to be inverted has the smallest possible dimensions.

Gradient-based, iterative algorithms such as the Gauss-Newton algorithm (4.33) can also be solved recursively. The parameter estimate at the next time step is given by

$$\hat{\boldsymbol{\theta}}_{k+1} = \hat{\boldsymbol{\theta}}_k - \gamma \mathbf{R}_k^{-1} \frac{\partial \mathbf{h}_k(\boldsymbol{\theta})}{\partial \boldsymbol{\theta}}^T \left(\mathbf{y}_k - \mathbf{h}_k(\boldsymbol{\theta}) \right), \quad (4.35)$$

where $\mathbf{R}_k$ is given by

$$\mathbf{R}_k = \mathbf{R}_{k-1} + \gamma \left(\frac{\partial \mathbf{h}_k(\boldsymbol{\theta})^T}{\partial \boldsymbol{\theta}} \left(\frac{\partial \mathbf{h}_k(\boldsymbol{\theta})^T}{\partial \boldsymbol{\theta}} \right)^T - \mathbf{R}_{k-1} \right), \tag{4.36}$$

subscript k denotes the time step, and the derivatives are evaluated at the currently available parameter estimate $\hat{\boldsymbol{\theta}}_k$. In this case every recursive step can be interpreted as solving Bayes' rule since the posterior covariance of the previous recursive step is the prior covariance in the next recursive step. The asymptotic properties for the estimates obtained by this algorithm are for time-invariant systems with identifiable parameters equal to those of the corresponding iterative algorithms (Ljung and Söderström 1983). For smaller numbers of measurements the recursive algorithm can result in parameter estimates that are worse than those of the corresponding iterative algorithms due to transient effects in the algorithm. For example, an unsuitable choice of initial covariance matrix $\mathbf{R}_0$ can give worse estimates in the beginning, but in the limit of an infinite number of measurements the estimates of both algorithms become identical. In case the system contains non-identifiable parameters then the parameter values of the non-identifiable parameters cannot be estimated from the measurements and remain equal to the prior estimate, equal as in the Bayesian approach.

The recursive implementation of Gauss-Newton (4.35, 4.36) can be directly related to the extended Kalman filter (EKF) for estimating parameters in linear models (see Ljung 1979; Ljung and Söderström 1983, p.430)[2]. The EKF is a commonly used observer technique for nonlinear models such as reservoir models. It processes the measurement data based on the linear Kalman filter equations, using a locally linearized model of the process and assuming a Gaussian distribution of the state and output. In reservoir engineering the Ensemble Kalman Filter (EnKF, Evensen 1994, 2007) has become popular, which can be seen as a generalization of the EKF. In the EnKF the analytical propagation of the error covariance matrix is replaced by a Monte Carlo approach, in which the covariance matrix is computed from an ensemble of models. The EnKF does not require a linearization of the model and uses the availability of the reservoir simulation model. Not only states but also parameters can be included in the estimation problem. Following a Bayesian approach the unknown parameters are added to the states, leading to an extended state vector $\mathbf{x}_\theta = [\mathbf{x}^T \boldsymbol{\theta}^T]^T$. This extended state is then estimated with an EnKF on the basis of an ensemble of $\mathbf{x}_\theta$. The EnKF algorithm encompasses the following steps:

- As prior information an ensemble of initial states $\{\hat{\mathbf{x}}_{\theta,k|k}\}$ is synthetically generated from a given distribution;
- By simulating every ensemble member through the model corresponding ensembles $\{\hat{\mathbf{x}}_{\theta,k+1|k}\}$ and $\{\hat{\mathbf{y}}_{k+1|k}\}$ are generated, that are stored as columns of matrices $\hat{\mathbf{X}}$ and $\hat{\mathbf{Y}}$ respectively;

[2]The most important difference between both algorithms is that the gradient of the Kalman gain with respect to the parameters is in the EKF approximated by the identity matrix, while it is present in the recursive algorithm. This enables faster computation of the parameters, but can deteriorate the convergence of the EKF

- The measurement update of a common Extended Kalman Filter is applied to every element of the ensemble, where the covariance matrices are replaced by sampled estimates from the ensembles generated in the previous step;
- The measurement update then becomes

$$\{\hat{\mathbf{x}}_{\theta,k+1|k+1}\} = \{\hat{\mathbf{x}}_{\theta,k+1|k}\} + \mathbf{K}_{k+1}\left(\mathbf{y}_{k+1} - \hat{\mathbf{y}}_{k+1|k}\right) \tag{4.37}$$

  where $\mathbf{K}_{k+1}$ is generated by applying the best linear unbiased estimate, given by

$$\mathbf{K}_{k+1} = \hat{\mathbf{X}}\hat{\mathbf{Y}}^T\left(\hat{\mathbf{Y}}\hat{\mathbf{Y}}^T + \mathbf{R}\right)^{-1} \tag{4.38}$$

- The result is a new ensemble $\{\hat{\mathbf{x}}_{\theta,k+1|k+1}\}$.

Similar to the ordinary Kalman Filter the EnKF can be interpreted as an optimization algorithm where the Jacobian and Hessian are approximated with a perturbation-based gradient (Douma 2008). In reservoir engineering problems the EnKF has been applied to models with number of state variables in the order of 10^6 (Naevdal et al. 2005; Gu and Oliver 2007). Since also grid block parameters such as grid block permeability and porosity are estimated with the EnKF an extremely large number of variables has to be estimated from the available measurement data.

To summarize, off-line prediction error algorithms such as the Gauss-Newton algorithm (4.33) can be related to recursive algorithms (e.g. RPE with Gauss-Newton update direction (4.35, 4.36)), and also to filtering algorithms (e.g. EKF and EnKF). Therefore, identifiability issues of the model structure also play a role in recursive and filtering algorithms for parameter estimation.

4.6 Structural identifiability

4.6.1 Analyzing structural identifiability

The question as to whether parameters can be uniquely identified from data basically consists of two parts. The first part concerns the model structure: is it possible at all to distinguish two given parameters, provided that the input is chosen in the best possible way? This property is reflected by the structural identifiability of a model structure. The second part concerns the issue whether the actual input is informative enough to allow this distinction. In the previous sections both parts were considered simultaneously. In this section only the first part is investigated.

Consider Definition 2.5 on structural identifiability. Structural identifiability of nonlinear dynamical systems can be analyzed by using different approaches (Walter 1987): linearization around an operating point (Grewal and Glover 1976), power series (Pohjanpalo 1978), similarity transformation (Vajda et al. 1989, only valid

for minimal systems), and differential algebra (e.g. Ljung and Glad 1994). Since reservoir models are known to be non-minimal (i.e. not observable and not controllable) and large-scale the latter two approaches are not applicable and we choose to linearize the model around an operating point. Subsequently, the structural identifiability of the linearized state-space model is analyzed.

Note that $\mathbf{G}(z, \boldsymbol{\theta})$ in (2.74) can be written as:

$$\mathbf{G}(z, \boldsymbol{\theta}) = \sum_{k=1}^{\infty} \mathbf{M}(k, \boldsymbol{\theta}) z^{-k}, \tag{4.39}$$

where $\mathbf{M}(k, \boldsymbol{\theta}) = \mathbf{C}(\boldsymbol{\theta})\mathbf{A}^{k-1}(\boldsymbol{\theta})\mathbf{B}(\boldsymbol{\theta})$ are the Markov parameters. Based on (4.39) we argue that equality of $\mathbf{G}(z, \boldsymbol{\theta}_1)$ and $\mathbf{G}(z, \boldsymbol{\theta}_2)$ is related to equality of the Markov parameters of $\mathbf{G}(z, \boldsymbol{\theta}_1)$ and $\mathbf{G}(z, \boldsymbol{\theta}_2)$. For reasons that become clear later the MIMO Markov parameters are decomposed into p multi-input, single-output (MISO) Markov parameters

$$\overrightarrow{\mathbf{M}}(k, \boldsymbol{\theta}) := \left[\begin{array}{cccc} \mathbf{M}_{1*}(k, \boldsymbol{\theta})^T & \mathbf{M}_{2*}(k, \boldsymbol{\theta})^T & \dots & \mathbf{M}_{p*}(k, \boldsymbol{\theta})^T \end{array} \right]^T \in \mathbb{R}^{1 \times pm}, \tag{4.40}$$

where $\mathbf{M}_{j*}(k, \boldsymbol{\theta})$ denotes the j-th row of Markov parameter $\mathbf{M}(k, \boldsymbol{\theta})$.
We now present Lemma 4.1 on injective maps, which will lead together with Definition 2.5 to Proposition 4.1 (see also Glover and Willems (1974), Grewal and Glover (1976), Norton (1980) and Van Doren et al. (2008a)):

Lemma 4.1 *Let Ω be an open set in $\mathbb{R}^n$ and $f : \Omega \to \mathbb{R}^m$ be a k-times continuously differentiable map with $k \geq 1$. If $\frac{\partial f(\boldsymbol{\theta})}{\partial \boldsymbol{\theta}}$ has constant rank l in a neighborhood of $\boldsymbol{\theta}_m$, then f is locally injective at $\boldsymbol{\theta}_m$ if and only if $l = n$.*

Proposition 4.1 *Consider the map $\overrightarrow{\mathbf{S}}_r(\boldsymbol{\theta}) : \Theta \subset \mathbb{R}^q \to \mathbb{R}^{pmr}$ defined by:*

$$\overrightarrow{\mathbf{S}}_r(\boldsymbol{\theta}) := \left[\begin{array}{cccc} \overrightarrow{\mathbf{M}}(1, \boldsymbol{\theta}) & \overrightarrow{\mathbf{M}}(2, \boldsymbol{\theta}) & \dots & \overrightarrow{\mathbf{M}}(r, \boldsymbol{\theta}) \end{array} \right]^T \in \mathbb{R}^{pmr \times 1}. \tag{4.41}$$

Then the model structure is locally structural identifiable in $\boldsymbol{\theta}_m$ if, for sufficiently large r,

$$\operatorname{rank} \left(\frac{\partial \overrightarrow{\mathbf{S}}_r(\theta)^T}{\partial \boldsymbol{\theta}} \right) = q \tag{4.42}$$

in $\boldsymbol{\theta} = \boldsymbol{\theta}_m$.

This is equivalent to a rank test on the matrix

$$\frac{\partial \overrightarrow{\mathbf{S}}_r(\boldsymbol{\theta})^T}{\partial \boldsymbol{\theta}} \left(\frac{\partial \overrightarrow{\mathbf{S}}_r(\boldsymbol{\theta})^T}{\partial \boldsymbol{\theta}} \right)^T$$

evaluated at $\boldsymbol{\theta} = \boldsymbol{\theta}_m$, which has dimension $q \times q$. It expresses the sensitivity of the parameters and linear combinations of parameters on the input-output behavior.

Both the qualitative question of structural identifiability, and the determination of the structurally most identifiable subspace of parameters can now be examined by applying an SVD to the matrix

$$\frac{\partial \overrightarrow{\mathbf{S}}_r(\boldsymbol{\theta})^T}{\partial \boldsymbol{\theta}} \left(\frac{\partial \overrightarrow{\mathbf{S}}_r(\boldsymbol{\theta})^T}{\partial \boldsymbol{\theta}} \right)^T = \begin{bmatrix} \mathbf{U}_1 & \mathbf{U}_2 \end{bmatrix} \begin{bmatrix} \boldsymbol{\Sigma}_1 & \mathbf{0} \\ \mathbf{0} & \mathbf{0} \end{bmatrix} \begin{bmatrix} \mathbf{V}_1^T \\ \mathbf{V}_2^T \end{bmatrix}, \tag{4.43}$$

and examining the column space of this matrix, see Van Doren et al. (2008a). This means that the SVD of (4.43) can be utilized to determine a locally structurally identifiable parameterization. The columns of $\mathbf{U}_1$ are regarded as directions in the parameter space that are structurally identifiable and serve as a mapping from high-dimensional parameter space $\boldsymbol{\theta}$ to a low-dimensional parameter space $\boldsymbol{\rho} = \mathbf{U}_1^T \boldsymbol{\theta}$. It can be shown that

$$\frac{\partial \overrightarrow{\mathbf{S}}_r(\boldsymbol{\theta})^T}{\partial \boldsymbol{\rho}} \left(\frac{\partial \overrightarrow{\mathbf{S}}_r(\boldsymbol{\theta})^T}{\partial \boldsymbol{\rho}} \right)^T = \boldsymbol{\Sigma}_1,$$

evaluated at $\boldsymbol{\rho} = \boldsymbol{\rho}_m = \mathbf{U}_1^T \boldsymbol{\theta}_m$ The columns of $\mathbf{U}_2$ provide an orthogonal basis of the null space of (4.42). The columns of $\mathbf{U}_2$ are regarded as directions in the parameter space that are locally structurally *not* identifiable.

Also in this problem we need to take care that the result of our (approximate) identifiability test is not dependent on a user-chosen parameter scaling, and so we need a premultiplication of (4.43) with a scaling matrix $\boldsymbol{\Gamma}_{\theta_m}$. This scaling matrix $\boldsymbol{\Gamma}_{\theta_m}$ can be chosen in such a way that it is suitable for the application in mind. Here we have chosen to scale with the value of the Markov parameter, where we reasoned that if a parameter has a high impact on a particular Markov parameter, but the Markov parameter itself has a very small value, the considered parameter is still a good candidate to be removed in our model structure approximation problem. Therefore an additional weighting of (4.43) is desired that takes the values of the Markov parameters into account. As a result we consider the column space of the matrix

$$\boldsymbol{\Gamma}_{\theta_m} \frac{\partial \overrightarrow{\mathbf{S}}_r(\boldsymbol{\theta})^T}{\partial \boldsymbol{\theta}} \boldsymbol{\Gamma}_S^2 \left(\frac{\partial \overrightarrow{\mathbf{S}}_r(\boldsymbol{\theta})^T}{\partial \boldsymbol{\theta}} \right)^T \boldsymbol{\Gamma}_{\theta_m}. \tag{4.44}$$

where $\boldsymbol{\Gamma}_S$ denotes the diagonal matrix with on each diagonal element the values of $\overrightarrow{\mathbf{S}}_r(\boldsymbol{\theta})$. In the SISO case this is equivalent to the absolute value $\overrightarrow{\mathbf{M}}(i, \boldsymbol{\theta})$. The consequence is that Markov parameters that have a high value are considered to be more important to include than Markov parameters with a small value. The column space of (4.44) that relates to the dominant singular values of the matrix, now is a representation of the parameter space of the approximated model structure.

The structural identifiability problem and the identifiability problem are of course closely related. This can be observed by realizing that for the SISO case

$$\frac{\partial \mathbf{h}(\boldsymbol{\theta})^T}{\partial \boldsymbol{\theta}} = \frac{\partial \overrightarrow{\mathbf{S}}_r(\boldsymbol{\theta})^T}{\partial \boldsymbol{\theta}} \boldsymbol{\Phi}_r, \tag{4.45}$$

where $\mathbf{\Phi}_r$ is given by

$$\mathbf{\Phi}_r = \begin{bmatrix} \mathbf{u}_1 & \mathbf{u}_2 & \dots & \mathbf{u}_r \\ & \mathbf{u}_1 & & \vdots \\ & & \ddots & \\ & & & \mathbf{u}_1 \end{bmatrix} \tag{4.46}$$

and the derivatives are evaluated at $\boldsymbol{\theta} = \boldsymbol{\theta}_0$.
Note that the matrix $\mathbf{\Phi}_r$ with input signals acts as a weighting matrix in (4.45) in a similar way as the weighting matrix $\mathbf{\Gamma}_S$ does in (4.44).

4.6.2 Derivation of analytical expression

In this part an analytical expression is derived for (4.43) for a parameterized linear state-space model. First recall that the chain rule for differentiating a matrix $\mathbf{A}^k(\boldsymbol{\theta})$ with respect to $\theta_i \in \mathbb{R}$ gives us

$$\frac{\partial \mathbf{A}^k(\boldsymbol{\theta})}{\partial \theta_i} = \frac{\partial \mathbf{A}(\boldsymbol{\theta})\mathbf{A}^{k-1}(\boldsymbol{\theta})}{\partial \theta_i} = \mathbf{A}(\boldsymbol{\theta})\frac{\partial \mathbf{A}^{k-1}(\boldsymbol{\theta})}{\partial \theta_i} + \frac{\partial \mathbf{A}(\boldsymbol{\theta})}{\partial \theta_i}\mathbf{A}^{k-1}(\boldsymbol{\theta}) = \mathbf{A}^2(\boldsymbol{\theta})\frac{\partial \mathbf{A}^{k-2}(\boldsymbol{\theta})}{\partial \theta_i} + \mathbf{A}(\boldsymbol{\theta})\frac{\partial \mathbf{A}(\boldsymbol{\theta})}{\partial \theta_i}\mathbf{A}^{k-2}(\boldsymbol{\theta}) + \frac{\partial \mathbf{A}(\boldsymbol{\theta})}{\partial \theta_i}\mathbf{A}^{k-1}(\boldsymbol{\theta}), \tag{4.47}$$

where $\frac{\partial \mathbf{A}^k(\boldsymbol{\theta})}{\partial \theta_i}$ has dimensions equal to that of $\mathbf{A}(\boldsymbol{\theta})$. After repeatedly applying (4.47) we can write

$$\frac{\partial \mathbf{A}^k(\boldsymbol{\theta})}{\partial \theta_i} = \sum_{l=1}^{k} \mathbf{A}^{l-1}(\boldsymbol{\theta})\frac{\partial \mathbf{A}(\boldsymbol{\theta})}{\partial \theta_i}\mathbf{A}^{k-l}(\boldsymbol{\theta}). \tag{4.48}$$

The Jacobian matrix of $\mathbf{A}^k(\boldsymbol{\theta}) \in \mathbb{R}^{n\times n}$ with respect to the parameter vector $\boldsymbol{\theta} \in \mathbb{R}^q$ is consequently given by:

$$\frac{\partial \mathbf{A}^k(\boldsymbol{\theta})}{\partial \boldsymbol{\theta}} = \sum_{l=1}^{k} \left(\left(\mathbf{I}_q \otimes \mathbf{A}^{l-1}(\boldsymbol{\theta}) \right) \frac{\partial \mathbf{A}(\boldsymbol{\theta})}{\partial \boldsymbol{\theta}} \mathbf{A}^{k-l}(\boldsymbol{\theta}) \right), \tag{4.49}$$

where $\mathbf{I}_q$ is the identity matrix with dimensions $q \times q$, $\otimes$ denotes the Kronecker product (Golub and Van Loan 1996), and where $\frac{\partial \mathbf{A}(\boldsymbol{\theta})}{\partial \boldsymbol{\theta}} \in \mathbb{R}^{qn\times n}$ consists of the partial derivatives $\frac{\partial \mathbf{A}(\boldsymbol{\theta})}{\partial \theta_i}$ organized column-wise.

Similarly, the Jacobian matrix of $\mathbf{M}_{\mathbf{j}*}(k, \boldsymbol{\theta}) \in \mathbb{R}^{1\times m}$ with respect to $\boldsymbol{\theta}$ is:

$$\frac{\partial \mathbf{M}_{j*}(k,\boldsymbol{\theta})}{\partial \boldsymbol{\theta}} = \frac{\partial \mathbf{C}_{j*}(\boldsymbol{\theta})\mathbf{A}^{k-1}(\boldsymbol{\theta})\mathbf{B}(\boldsymbol{\theta})}{\partial \boldsymbol{\theta}} = \frac{\partial \mathbf{C}_{j*}(\boldsymbol{\theta})}{\partial \boldsymbol{\theta}}\mathbf{A}^{k-1}(\boldsymbol{\theta})\mathbf{B}(\boldsymbol{\theta}) + \left(\mathbf{I}_q \otimes \mathbf{C}_{j*}(\boldsymbol{\theta})\mathbf{A}^{k-1}(\boldsymbol{\theta}) \right) \frac{\partial \mathbf{B}(\boldsymbol{\theta})}{\partial \boldsymbol{\theta}} + \sum_{l=1}^{k-1} \left(\mathbf{I}_q \otimes \mathbf{C}_{j*}(\boldsymbol{\theta})\mathbf{A}^{l-1}(\boldsymbol{\theta}) \right) \frac{\partial \mathbf{A}(\boldsymbol{\theta})}{\partial \boldsymbol{\theta}} \mathbf{A}^{k-1-l}(\boldsymbol{\theta})\mathbf{B}(\boldsymbol{\theta}). \tag{4.50}$$

Equation (4.50) shows that the Jacobian of each Markov parameter can be expressed using the system matrices $\mathbf{A}(\boldsymbol{\theta})$, $\mathbf{B}(\boldsymbol{\theta})$, $\mathbf{C}(\boldsymbol{\theta})$, and the analytical partial derivatives of the state-space system matrices with respect to the parameter vector. As stated in (4.41) the Markov parameters are organized in the vector

$$\overrightarrow{\mathbf{S}}_r := \left[\begin{array}{cccc} \overrightarrow{\mathbf{M}}(1) & \overrightarrow{\mathbf{M}}(2) & \dots & \overrightarrow{\mathbf{M}}(r) \end{array} \right]^T \in \mathbb{R}^{1\times pmr}, \tag{4.51}$$

where we have omitted, for brevity, the dependence of $\mathbf{S}_r$ and $\mathbf{M}(k)$ on $\boldsymbol{\theta}$. The Jacobian of $\overrightarrow{\mathbf{S}}_r$ with respect to the parameter vector $\boldsymbol{\theta} \in \mathbb{R}^q$ is denoted as:

$$\frac{\partial \overrightarrow{\mathbf{S}}_r^T}{\partial \boldsymbol{\theta}} := \left[\begin{array}{cccc} \frac{\partial \overrightarrow{\mathbf{M}}(1)}{\partial \boldsymbol{\theta}} & \frac{\partial \overrightarrow{\mathbf{M}}(2)}{\partial \boldsymbol{\theta}} & \dots & \frac{\partial \overrightarrow{\mathbf{M}}(r)}{\partial \boldsymbol{\theta}} \end{array} \right]^T \in \mathbb{R}^{q\times pmr}, \tag{4.52}$$

where $\frac{\partial \overrightarrow{\mathbf{M}}(k)}{\partial \boldsymbol{\theta}} \in \mathbb{R}^{q\times pm}$, for $k = (1, \dots, r)$.

To summarize, using the notational conventions stated before, for a multi-input multi-output system the expression $\frac{\partial \overrightarrow{\mathbf{S}}_r^T}{\partial \boldsymbol{\theta}} \frac{\partial \overrightarrow{\mathbf{S}}_r^T}{\partial \boldsymbol{\theta}}^T$ is given by

$$\left. \frac{\partial \overrightarrow{\mathbf{S}}_r^T}{\partial \boldsymbol{\theta}} \frac{\partial \overrightarrow{\mathbf{S}}_r^T}{\partial \boldsymbol{\theta}}^T \right|_{\boldsymbol{\theta}_0} = \sum_{i=1}^{r} \sum_{j=1}^{p} \frac{\partial \mathbf{M}_{j*}(i)}{\partial \boldsymbol{\theta}} \left(\frac{\partial \mathbf{M}_{j*}(i)}{\partial \boldsymbol{\theta}} \right)^T \Bigg|_{\boldsymbol{\theta}_0} \tag{4.53}$$

with dimensions $q \times q$ and where $\frac{\partial \mathbf{M}_{j*}(i)}{\partial \boldsymbol{\theta}}$ is given by (4.50). As in Dötsch and Van den Hof (1996), the expression in (4.53) is computed using the matrices $\mathbf{A}(\boldsymbol{\theta})$, $\mathbf{B}(\boldsymbol{\theta})$, $\mathbf{C}(\boldsymbol{\theta})$, $\frac{\partial \mathbf{A}(\boldsymbol{\theta})}{\partial \boldsymbol{\theta}}$, $\frac{\partial \mathbf{B}(\boldsymbol{\theta})}{\partial \boldsymbol{\theta}}$ and $\frac{\partial (\mathbf{C}\boldsymbol{\theta})}{\partial \boldsymbol{\theta}}$. Computation of the partial derivatives of $\mathbf{A}(\boldsymbol{\theta})$, $\mathbf{B}(\boldsymbol{\theta})$, $\mathbf{C}(\boldsymbol{\theta})$ with respect to θ_i $(i = 1, \dots, q)$, for $\boldsymbol{\theta} = \boldsymbol{\theta}_0$ is done analytically. However, the procedure given here is strongly simplified and much more direct compared to the one proposed by Dötsch and Van den Hof (1996) since the "thought" identification problem is not needed anymore. Furthermore, it has been extended to MIMO models. Also, computing (4.53) is computationally more efficient because the matrix is calculated as a whole, instead of element by element.

4.6.3 Number of Markov parameters

One of the questions is how many Markov parameters r should be taken into account in order to arrive at correct expressions for the local identifiability analysis. In the SISO case it is well known that $2n + 1$ Markov parameters uniquely determine a linear system with McMillan degree n (see Section 2.4). In the MIMO case the minimum number of Markov parameters that uniquely determines the underlying linear system is given by $\mu + \nu$, with μ the observability index and ν the controllability index (see e.g. Kailath 1980). The controllability index is the smallest number for which is satisfied that $\text{rank}(\mathcal{C}_\mu) = \text{rank}(\mathcal{C}_{\mu+1})$, and the observability index ν is the smallest number for which is satisfied that $\text{rank}(\mathcal{O}_\nu) = \text{rank}(\mathcal{O}_{\nu+1})$. It implies that r is sufficient if $\text{rank}(\mathbf{H}_{r-1}) = \text{rank}(\mathbf{H}_r)$, where $\mathbf{H}_r$ denotes a block

Hankel matrix containing r Markov parameters (Damen et al. 1985)

$$\begin{bmatrix} \mathbf{M}(1) & \mathbf{M}(2) & \mathbf{M}(3) & \dots \\ \mathbf{M}(2) & \mathbf{M}(3) & & \\ \mathbf{M}(3) & & & \\ \vdots & & & \\ \vdots & & \ddots & \mathbf{M}(r-1) \\ \vdots & & \mathbf{M}(r-1) & \mathbf{M}(r) \end{bmatrix}. \tag{4.54}$$

4.7 Relation with controllability and observability

4.7.1 Identifiability, controllability and observability

In this section we will show how the identifiable parameter space that results from (4.19) is related to properties of controllability and observability. We consider the strictly proper deterministic linear time-varying (LTV) model in discrete-time state-space form, that could result from linearizing a nonlinear model in the vicinity of the nominal trajectory. The model is

$$\begin{aligned} \mathbf{x}_{k+1} &= \mathbf{A}_k(\boldsymbol{\theta})\mathbf{x}_k + \mathbf{B}_k(\boldsymbol{\theta})\mathbf{u}_k \\ \mathbf{h}(\boldsymbol{\theta})_{k+1} &= \mathbf{C}_{k+1}(\boldsymbol{\theta})\mathbf{x}_{k+1}, \end{aligned}$$

where subscript k denotes the time index. The sensitivity of the outputs with respect to the parameter vector $\boldsymbol{\theta}$ is element-wise given by

$$\frac{\partial \mathbf{h}(\boldsymbol{\theta})_{k+1}}{\partial \theta_i} = \mathbf{C}_{k+1}(\boldsymbol{\theta})\frac{\partial \mathbf{x}_{k+1}}{\partial \theta_i} + \frac{\partial \mathbf{C}_{k+1}(\boldsymbol{\theta})}{\partial \theta_i}\mathbf{x}_{k+1}, \tag{4.55}$$

where $\frac{\partial \mathbf{x}_{k+1}}{\partial \theta_i}$ is given by

$$\frac{\partial \mathbf{x}_{k+1}}{\partial \theta_i} = \mathbf{A}_k(\boldsymbol{\theta})\frac{\partial \mathbf{x}_k}{\partial \theta_i} + \underbrace{\frac{\partial \mathbf{A}_k(\boldsymbol{\theta})}{\partial \theta_i}\mathbf{x}_k + \frac{\partial \mathbf{B}_k(\boldsymbol{\theta})}{\partial \theta_i}\mathbf{u}_k}_{:=\tilde{\mathbf{u}}_k^{\theta_i}}. \tag{4.56}$$

Without loss of generality we can assume that $\frac{\partial \mathbf{C}_{k+1}}{\partial \theta_i} = \mathbf{0}$, since $\mathbf{C}_{k+1}$ can be made independent of $\boldsymbol{\theta}$ by redefining the state using a similarity transformation.

Note that the effect of a parameter change is weighted by the value of current state and input, i.e. in (4.56) $\frac{\partial \mathbf{A}_k(\boldsymbol{\theta})}{\partial \theta_i}$ is weighted by $\mathbf{x}_k$ and $\frac{\partial \mathbf{B}_k}{\partial \theta_i}$ is weighted by $\mathbf{u}_k$ in (4.56). This means that, given a specific model structure, outputs $\mathbf{h}(\boldsymbol{\theta})$ are more sensitive to parameters associated with states and inputs that have a large value since $\frac{\partial \mathbf{h}(\boldsymbol{\theta})_{k+1}}{\partial \theta_i}$ in (4.55) is higher.

In stacked form we can write

$$\left(\frac{\partial \mathbf{h}(\boldsymbol{\theta})^T}{\partial \boldsymbol{\theta}}\right)^T = \underbrace{\begin{bmatrix} \mathbf{C}_1 & & & \mathbf{0} \\ & \mathbf{C}_2 & & \\ & & \ddots & \\ \mathbf{0} & & & \mathbf{C}_N \end{bmatrix} \begin{bmatrix} \mathbf{I} & \mathbf{0} & \dots & & \\ \mathbf{A}_1 & \mathbf{I} & & & \\ \mathbf{A}_2\mathbf{A}_1 & \mathbf{A}_2 & \mathbf{I} & & \\ \vdots & & & \ddots & \\ \mathbf{A}_{N-2}\dots\mathbf{A}_1 & \mathbf{A}_{N-2}\dots\mathbf{A}_2 & \dots & \mathbf{A}_{N-2} & \mathbf{I} \\ \mathbf{A}_{N-1}\dots\mathbf{A}_1 & \mathbf{A}_{N-1}\dots\mathbf{A}_2 & \dots & \dots & \mathbf{A}_{N-1} \quad \mathbf{I} \end{bmatrix}}_{\tilde{\mathcal{O}} \in \mathbb{R}^{N(p\times n)}} \times \underbrace{\begin{bmatrix} \tilde{\mathbf{u}}_0^{\theta_1} & \dots & \tilde{\mathbf{u}}_0^{\theta_i} & \dots & \tilde{\mathbf{u}}_1^{\theta_q} \\ \tilde{\mathbf{u}}_1^{\theta_1} & \dots & \tilde{\mathbf{u}}_1^{\theta_i} & \dots & \tilde{\mathbf{u}}_2^{\theta_q} \\ \vdots & & \vdots & & \vdots \\ \tilde{\mathbf{u}}_{N-1}^{\theta_1} & \dots & \tilde{\mathbf{u}}_{N-1}^{\theta_i} & \dots & \tilde{\mathbf{u}}_{N-1}^{\theta_q} \end{bmatrix}}_{\tilde{\mathcal{U}} \in \mathbb{R}^{Nn\times q}}, \quad (4.57)$$

where we have defined $\tilde{\mathcal{O}}$ and $\tilde{\mathcal{U}}$. For a change in the model parameters the term $\tilde{\mathbf{u}}_k^{\theta_i}$ in (4.56) is given by

$$\frac{\partial \mathbf{A}(\boldsymbol{\theta})}{\partial \theta_i}\mathbf{x}_k + \frac{\partial \mathbf{B}(\boldsymbol{\theta})}{\partial \theta_i}\mathbf{u}_k.$$

In stacked form this is can be written with abuse of notation as

$$\left(\frac{\partial \mathbf{h}(\boldsymbol{\theta})^T}{\partial \boldsymbol{\theta}}\right)^T = \tilde{\mathcal{O}} \begin{bmatrix} \frac{\partial \mathbf{A}}{\partial \boldsymbol{\theta}} & \frac{\partial \mathbf{B}}{\partial \boldsymbol{\theta}} \end{bmatrix} \begin{bmatrix} \mathbf{x} \\ \mathbf{u} \end{bmatrix}. \quad (4.58)$$

The identifiability of the model parameters is seen to be determined by three factors:

- the current state and input, where the current state is related to the mapping from input to state, which is related to controllability;
- the mapping from a model parameter perturbation to a change in the system matrices (sensitivity)
- the mapping from a state perturbation to a change in the output (observability), given by $\tilde{\mathcal{O}}$ in (4.57)

Indeed only parameter changes that result in state perturbations contained in the row space of $(\tilde{\mathcal{O}})$ can be identified.

4.7.2 Structural identifiability, controllability and observability

Also expression (4.53) can be expressed in terms of observability, sensitivity of the state matrices with respect to the parameter vector $\boldsymbol{\theta}$, and controllability. Expression (4.53) is valid for parameterized linear state-space models and therefore

we have linearized the model around an operating point instead of in the vicinity of a nominal trajectory, leading to the desired LTI model. Furthermore, to arrive at compact expressions that are more insightful we assume that system matrices $\mathbf{B}$ and $\mathbf{C}$ are independent of $\boldsymbol{\theta}$, leading to an expression (4.53) without $\frac{\partial \mathbf{B}}{\partial \boldsymbol{\theta}}$ and $\frac{\partial \mathbf{C}}{\partial \boldsymbol{\theta}}$.

First consider the most simple situation that $q = 1$, $p = 1$ and $r = 4$. We can write $\frac{\partial \overrightarrow{\mathbf{S}}_4}{\partial \boldsymbol{\theta}} = \begin{bmatrix} 0 & \mathbf{X} \end{bmatrix}$, where

$$\mathbf{X} = \begin{bmatrix} \mathbf{C} & \mathbf{CA} & \mathbf{CA}^2 \end{bmatrix} \begin{bmatrix} \frac{\partial \mathbf{A}}{\partial \boldsymbol{\theta}} & & \\ & \frac{\partial \mathbf{A}}{\partial \boldsymbol{\theta}} & \\ & & \frac{\partial \mathbf{A}}{\partial \boldsymbol{\theta}} \end{bmatrix} \begin{bmatrix} \mathbf{B} & \mathbf{AB} & \mathbf{A}^2\mathbf{B} \\ & \mathbf{B} & \mathbf{AB} \\ & & \mathbf{B} \end{bmatrix}. \tag{4.59}$$

In this expression a block diagonal matrix of the sensitivity of the state space matrices with respect to the parameter vector is left multiplied with the observability matrix, and right multiplied with a block Toeplitz matrix containing the controllability matrix and shifted controllability matrices.

Next, consider the situation that $q > 1$, $p = 1$ and $r = 4$, the expression becomes

$$\mathbf{X} = \begin{bmatrix} (\mathbf{I}_q \otimes \mathbf{C}) & (\mathbf{I}_q \otimes \mathbf{CA}) & (\mathbf{I}_q \otimes \mathbf{CA^2}) \end{bmatrix} \times \begin{bmatrix} \frac{\partial \mathbf{A}}{\partial \boldsymbol{\theta}} & & \\ & \frac{\partial \mathbf{A}}{\partial \boldsymbol{\theta}} & \\ & & \frac{\partial \mathbf{A}}{\partial \boldsymbol{\theta}} \end{bmatrix} \begin{bmatrix} \mathbf{B} & \mathbf{AB} & \mathbf{A}^2\mathbf{B} \\ & \mathbf{B} & \mathbf{AB} \\ & & \mathbf{B} \end{bmatrix},$$

which possesses a similar structure as (4.59).

Finally, consider system matrices with the parameters on the diagonal only. The diagonal structure in this example is relevant since reservoir models also display a diagonally banded structure in the system matrix, resulting from the spatial discretization.

$$\mathbf{A} = \begin{bmatrix} \theta_1 & & & \\ & \theta_2 & & \\ & & \ddots & \\ & & & \theta_q \end{bmatrix},$$

where $\boldsymbol{\theta} : \theta_i \neq \theta_j$ and where the input and output matrices do not degenerate the observability and controllability matrix. In that case

$$\operatorname{rank}\left(\frac{\partial \overrightarrow{\mathbf{S}}_r^T}{\partial \boldsymbol{\theta}} \left(\frac{\partial \overrightarrow{\mathbf{S}}_r^T}{\partial \boldsymbol{\theta}} \right)^T \right) = q = n, \tag{4.60}$$

where n is the McMillan degree. In Appendix 4A equation (4.60) is tested for different values of q and p.

4.8 Examples

In order to illustrate the concepts we will now discuss five examples where we have chosen a very simple SISO model structure. The first two examples, Examples 4.1 en 4.2, illustrate in particular the role of the scaling/weighting functions in the identifiability analysis. The model structure will be approximated using the previously discussed identifiability analysis, where we assume that $\mathbf{P}_v = \mathbf{I}$.

In Examples 4.3, 4.4 and 4.5 we illustrate the relationship between structural identifiability and controllability and observability. Example 4.3 describes a model that is controllable and observable, but poorly structurally identifiable. Example 4.4 describes a model that is poorly controllable and observable as well as poorly structurally identifiable. In the last example the effect of a pole-zero cancelation on the structural identifiability is illustrated.

Example 4.1 *Consider the data-generating system*

$$y(t) = \alpha_0 u(t-1) + \beta_0 u(t-2)$$

with $\alpha_0 = 10^6$ *and* $\beta_0 = 10^{-6}$, *and* $\boldsymbol{\theta}_0 := [\alpha_0 \ \beta_0]^T$. *Consider the input/output model structure*

$$y(t, \boldsymbol{\theta}) = \alpha u(t-1) + \beta u(t-2), \quad \boldsymbol{\theta} := [\alpha \ \beta]^T.$$

The system in controllable canonical form is given by

$$(\mathbf{A}, \mathbf{B}, \mathbf{C}) = \left(\begin{bmatrix} 0 & 0 \\ 1 & 0 \end{bmatrix}, \begin{bmatrix} 1 \\ 0 \end{bmatrix}, \begin{bmatrix} \alpha & \beta \end{bmatrix} \right), \tag{4.61}$$

and the Markov parameters are (α, β). *The controllability and observability matrices are*

$$\begin{bmatrix} 1 & 0 \\ 0 & 1 \end{bmatrix}, \quad \begin{bmatrix} \alpha & \beta \\ \beta & 0 \end{bmatrix} = \begin{bmatrix} 10^9 & 10^{-9} \\ 10^{-9} & 0 \end{bmatrix}, \tag{4.62}$$

respectively.
The scaled Fisher information matrix $\tilde{\mathbf{J}}$ *of (4.18) for a local analysis around* $\boldsymbol{\theta}_0$ *is*

$$\begin{bmatrix} \alpha_0 & 0 \\ 0 & \beta_0 \end{bmatrix} \begin{bmatrix} R_u(0) & R_u(1) \\ R_u(1) & R_u(0) \end{bmatrix} \begin{bmatrix} \alpha_0 & 0 \\ 0 & \beta_0 \end{bmatrix},$$

where $R_u(\tau) = \bar{\mathbb{E}}\left[u(t)u(t-\tau)\right]$. *The relative parameter variance is indicated by* $\tilde{\mathbf{J}}^{-1}$. *In the case of a unit variance white noise input, it follows that*

$$\tilde{\mathbf{J}} = \begin{bmatrix} 10^{12} & 0 \\ 0 & 10^{-12} \end{bmatrix},$$

while the unscaled Fisher information matrix satisfies $\mathbf{J} = \mathbf{I}$. *Analysis of* $\tilde{\mathbf{J}}$ *shows that the second parameter can very well be neglected, leading to an approximate model structure* $y(t) = \alpha u(t-1)$, *while analysis of* $\mathbf{J}$ *does suggest a reduction.*

Structural identifiability analysis without scaling shows that both parameters are structurally identifiable, since $\frac{\partial \mathbf{S}_N^T}{\partial \boldsymbol{\theta}} = \mathbf{I}$. *However, including both scaling matrices* $\boldsymbol{\Gamma}_{\hat{\theta}}$ *and* $\boldsymbol{\Gamma}_S$ *as in (4.44), we obtain*

$$\boldsymbol{\Gamma}_{\hat{\theta}} \frac{\partial \mathbf{S}_N^T}{\partial \boldsymbol{\theta}} \boldsymbol{\Gamma}_S = \begin{bmatrix} 10^{12} & 0 \\ 0 & 10^{-12} \end{bmatrix},$$

also showing that the second parameter can be very well neglected. In light of Section 4.7 we remark that in $\boldsymbol{\theta} = \boldsymbol{\theta}_0$ *this model is poorly observable/controllable and as a result it is also poorly identifiable.*

Example 4.2 *In this example the same data-generating system as in the previous example is considered. Consider the input/output model structure*

$$y(t, \boldsymbol{\theta}) = \alpha u(t-1) + 10^{-6} \gamma u(t-2), \quad \boldsymbol{\theta} := [\alpha \ \gamma]^T.$$

where $\gamma_0 = 1$. *The scaled Fisher information matrix* $\tilde{\mathbf{J}}$ *of (4.18) is*

$$\begin{bmatrix} \alpha_0 & 0 \\ 0 & \gamma_0 \end{bmatrix} \begin{bmatrix} R_u(0) & 10^{-6} R_u(1) \\ 10^{-6} R_u(1) & 10^{-12} R_u(0) \end{bmatrix} \begin{bmatrix} \alpha_0 & 0 \\ 0 & \gamma_0 \end{bmatrix}.$$

Under the same input conditions it follows that

$$\tilde{\mathbf{J}} = \begin{bmatrix} 10^{12} & 0 \\ 0 & 10^{-12} \end{bmatrix},$$

while the unscaled Fisher information matrix is

$$\mathbf{J} = \begin{bmatrix} 1 & 0 \\ 0 & 10^{-12} \end{bmatrix}.$$

Whereas the unscaled matrix is essentially different from the previous example, the scaled analysis shows again that the second parameter can be very well neglected and that the model structure can be approximated with $y(t) = \alpha u(t-1)$.

Structural identifiability analysis without scaling shows that α *is structurally best identifiable, since*

$$\frac{\partial \mathbf{S}_N^T}{\partial \boldsymbol{\theta}} = \begin{bmatrix} 1 & 0 \\ 0 & 10^{-6} \end{bmatrix}.$$

Including both scaling matrices $\boldsymbol{\Gamma}_\theta$ *and* $\boldsymbol{\Gamma}_S$, *we obtain in quadratic form*

$$\boldsymbol{\Gamma}_\theta \frac{\partial \mathbf{S}_N^T}{\partial \boldsymbol{\theta}} \boldsymbol{\Gamma}_S = \begin{bmatrix} 10^{12} & 0 \\ 0 & 10^{-12} \end{bmatrix},$$

being exactly the same as matrix as in the previous example, meaning that the structural identifiability analysis is now scaling-invariant.

Example 4.3 (Controllable/observable, but not structurally identifiable) *Consider the data-generating system*

$$y(t, \theta) = \theta_1 u(t-1) + \theta_2 \theta_3 3 u(t-2), \quad \boldsymbol{\theta} := [\theta_1 \ \theta_2 \ \theta_3]^T.$$

a In $\boldsymbol{\theta} = \boldsymbol{\theta}_0 = [1\,1\,1]^T$ this model will be observable/controllable, but not structurally identifiable.

$$\boldsymbol{\Gamma}_\theta \frac{\partial \mathbf{S}_N^T}{\partial \boldsymbol{\theta}} \boldsymbol{\Gamma}_S = \begin{bmatrix} 1 & 0 \\ 0 & \theta_3 \\ 0 & \theta_2 \end{bmatrix} = \begin{bmatrix} 1 & 0 \\ 0 & 1 \\ 0 & 1 \end{bmatrix}.$$

The singular value decomposition (SVD) hereof is

$$\mathbf{U}\boldsymbol{\Sigma}\mathbf{V}^T = \begin{bmatrix} 0 & -1 & 0 \\ -\frac{1}{2}\sqrt{2} & 0 & -\frac{1}{2}\sqrt{2} \\ -\frac{1}{2}\sqrt{2} & 0 & \frac{1}{2}\sqrt{2} \end{bmatrix} \begin{bmatrix} \sqrt{2} & 0 \\ 0 & 1 \\ 0 & 0 \end{bmatrix} \begin{bmatrix} 0 & -1 \\ -1 & 0 \end{bmatrix}^T.$$

According to the singular values the first two directions in parameter space, given by the first two column vectors of $\mathbf{U}$, are structurally identifiable. The first direction involves θ_2 and θ_3, and shows that we cannot structurally identify θ_2 and θ_3 separately. Only the combination $\theta_2\theta_3$ is structurally identifiable. The second direction shows that θ_1 is structurally identifiable.

b Same example as the previous one, but $\boldsymbol{\theta}_0 = [1\,100\,1]^T$. For these parameter values we obtain

$$\boldsymbol{\Gamma}_\theta \frac{\partial \mathbf{S}_N^T}{\partial \boldsymbol{\theta}} \boldsymbol{\Gamma}_S = \begin{bmatrix} 1 & 0 & 0 \\ 0 & 100 & 0 \\ 0 & 0 & 1 \end{bmatrix} \begin{bmatrix} 1 & 0 \\ 0 & \theta_3 \\ 0 & \theta_2 \end{bmatrix} \begin{bmatrix} 1 & 0 \\ 0 & 100 \end{bmatrix} = \begin{bmatrix} 1 & 0 \\ 0 & 10^4 \\ 0 & 10^4 \end{bmatrix}.$$

The singular value decomposition (SVD) hereof is

$$\mathbf{U}\boldsymbol{\Sigma}\mathbf{V}^T = \begin{bmatrix} 0 & -1 & 0 \\ -\frac{1}{2}\sqrt{2} & 0 & -\frac{1}{2}\sqrt{2} \\ -\frac{1}{2}\sqrt{2} & 0 & \frac{1}{2}\sqrt{2} \end{bmatrix} \begin{bmatrix} \sqrt{2}\times 10^4 & 0 \\ 0 & 1 \\ 0 & 0 \end{bmatrix} \begin{bmatrix} 0 & -1 \\ -1 & 0 \end{bmatrix}^T,$$

which is equal to the previous case, with the exception that the first singular value is a factor 10^4 higher. The parameter combination $\theta_2\theta_3$ is apparently easier to identify. One could argue that a further increase of the value of θ_2 will lead to an approximated model structure in which θ_1 is excluded.

Example 4.4 (Poorly observable/controllable and also poorly structurally identifiable) *Consider the input-output model structure:*

$$y(t,\theta) = \theta_1 u(t-1) + \theta_1\theta_2 u(t-2), \quad \boldsymbol{\theta} := [\theta_1\ \theta_2\ ]^T$$

with $\theta_1 = 10^9$ and $\theta_2 = 10^{-9}$, and $\boldsymbol{\theta}_0 := [\theta_1\ \theta_2]^T$.
In $\boldsymbol{\theta} = \boldsymbol{\theta}_0$ this model will be poorly observable/controllable, and also poorly structurally identifiable.

$$\boldsymbol{\Gamma}_\theta \frac{\partial \mathbf{S}_N^T}{\partial \boldsymbol{\theta}} \boldsymbol{\Gamma}_S = \begin{bmatrix} 10^9 & 0 \\ 0 & 10^{-9} \end{bmatrix} \begin{bmatrix} 1 & \theta_2 \\ 0 & \theta_1 \end{bmatrix} \begin{bmatrix} 10^9 & 0 \\ 0 & 10^{-9} \end{bmatrix} = \begin{bmatrix} 10^{18} & 1 \\ 0 & 1 \end{bmatrix}.$$

The SVD hereof is

$$\boldsymbol{\Gamma}_\theta \frac{\partial \mathbf{S}_N^T}{\partial \boldsymbol{\theta}} \boldsymbol{\Gamma}_S = \mathbf{U}\boldsymbol{\Sigma}\mathbf{V}^T = \begin{bmatrix} 1 & -10^{-36} \\ 10^{-36} & 1 \end{bmatrix} \begin{bmatrix} 10^{18} & 0 \\ 0 & 1 \end{bmatrix} \begin{bmatrix} 1 & -10^{-18} \\ 10^{-18} & 1 \end{bmatrix}^T.$$

According to the SVD only θ_1 is identifiable.

Note that without scaling we obtain

$$\frac{\partial \mathbf{S}_N^T}{\partial \boldsymbol{\theta}} = \mathbf{U}\boldsymbol{\Sigma}\mathbf{V}^T = \begin{bmatrix} 10^{-18} & -1 \\ 1 & 10^{-18} \end{bmatrix} \begin{bmatrix} 10^{9} & 0 \\ 0 & 1 \end{bmatrix} \begin{bmatrix} 10^{-27} & -1 \\ 1 & 10^{-27} \end{bmatrix}^T,$$

indicating that θ_2 is best structurally identifiable. This indicates that scaling can change the results dramatically.

Example 4.5 (Pole-zero cancelation) *Finally, consider the data-generating system*

$$y(t,\theta) = \frac{b_0 + b_1 q^{-1}}{1 + a_1 q^{-1}} u(t), \quad \boldsymbol{\theta} := [\, a_1 \; b_0 \; b_1 \,]^T.$$

The first three Markov parameters are given by

$$\begin{bmatrix} b_0 & (b_1 - b_0 a_1) & -(b_1 - b_0 a_1) a_1 \end{bmatrix}.$$

If $b_1 \neq a_1 b_0$, e.g. $\boldsymbol{\theta}_0 = [1\ 2\ 1\ ]$, then the model in state-space representation is observable/controllable and all three directions in parameters space are structurally identifiable. However, if $b_1 = a_1 b_0$, then there is a pole-zero cancelation and the model is poorly observable/controllable. The SVD of $\boldsymbol{\Gamma}_\theta \frac{\partial \mathbf{S}_N^T(\theta)}{\partial \boldsymbol{\theta}} \boldsymbol{\Gamma}_S$ for $\boldsymbol{\theta}_0 = [1\ 1\ 1\ ]$ is given by

$$\boldsymbol{\Gamma}_\theta \frac{\partial \mathbf{S}_N^T}{\partial \boldsymbol{\theta}} \boldsymbol{\Gamma}_S = \mathbf{U}\boldsymbol{\Sigma}\mathbf{V}^T = \begin{bmatrix} 1 & 0 & 0 \\ 0 & 1 & 0 \\ 0 & 0 & 1 \end{bmatrix} \begin{bmatrix} 1 & 0 & 0 & 0 & 0 \\ 0 & 0 & 0 & 0 & 0 \\ 0 & 0 & 0 & 0 & 0 \end{bmatrix} \begin{bmatrix} 1 & 0 & 0 & 0 & 0 \\ 0 & 1 & 0 & 0 & 0 \\ 0 & 0 & 1 & 0 & 0 \\ 0 & 0 & 0 & 1 & 0 \\ 0 & 0 & 0 & 0 & 1 \end{bmatrix}^T, \tag{4.63}$$

showing that only one direction can be identified. This illustrates that in the case of a pole-zero cancelation ($b_1 = a_1 b_0$) the model is not observable/controllable, and only one direction in parameter space will be structurally identifiable.

In Section 4.7.2 it was shown that under certain assumptions the expression to test structural identifiability can be decomposed into a part related to controllability, a part related to observability and a part related to the sensitivity of a parameter on the system matrix. The last three examples of this section support this demonstrating that lack of structural identifiability can be caused by lack of observability/controllability and by a small sensitivity of a parameter.

4.9 Summary

To increase the predictive capacity of a reservoir model its parameters are estimated from measurements. The question whether a large scale (nonlinear) physical model structure such as a reservoir model is identifiable, is usually considered in a qualitative way (yes or no). It is well known that reservoir models are not identifiable. In this chapter the notions of (local) identifiability and structural

identifiability are quantified and it is shown how the model structure can be approximated so as to achieve identifiability, while retaining the interpretation of the physical parameters.

The identifiability question has been addressed in a prediction error setting, and the analysis has been related to iterative optimization algorithms (like Gauss-Newton and Steepest-Descent) as well as to recursive (sequential) parameter estimation methods. In a Bayesian setting, in which a priori knowledge is included in the cost function, there seems to be no issue regarding identifiability. But in this setting the parameters that cannot be estimated from measurements are determined by the a priori knowledge (i.e. parameter estimate). This could give a false sense of model reliability.

In addition, it is shown how the construction of best identifiable model structure approximations relates to the notions of controllability and observability as discussed in the previous chapter. Furthermore, an analytical expression is developed to test structural identifiability, which is also related to controllability and observability.

In the next chapter these notions will be applied to reservoir models, in which identifiable parameterizations are determined with a significantly reduced number of parameters, and next the parameter values are estimated in an iterative estimation procedure.

4A Diagonal system matrices

In Section 4.7 it was posed that for system matrices with the parameters on the diagonal where $\boldsymbol{\theta} : \theta_i \neq \theta_j$ and where the input and output matrices do not degenerate the observability and controllability matrix it holds that

$$\operatorname{rank}\left(\frac{\partial \overrightarrow{\mathbf{S}}_r^T}{\partial \boldsymbol{\theta}}\left(\frac{\partial \overrightarrow{\mathbf{S}}_r^T}{\partial \boldsymbol{\theta}}\right)^T\right) = q = n, \tag{4A-1}$$

where n is the McMillan degree. It this appendix this will be shown for different values of q and p.

Case 1: siso and $n = 1$

For $p = m = 1$ and $n = q = 1$, then $\mathbf{A} = \theta$, $\mathbf{B} = b$, and $\mathbf{C} = c$. The term

$$\frac{\partial \overrightarrow{\mathbf{S}}_r^T}{\partial \boldsymbol{\theta}}\left(\frac{\partial \overrightarrow{\mathbf{S}}_r^T}{\partial \boldsymbol{\theta}}\right)^T, \tag{4A-2}$$

is for this case given by

$$\mathbf{X} = \begin{bmatrix} \mathbf{C} & \mathbf{CA} & \mathbf{CA}^2 & \dots \end{bmatrix} \begin{bmatrix} \mathbf{B} & \mathbf{AB} & \dots & \\ & \mathbf{B} & \mathbf{AB} & \\ & & \ddots & \ddots \end{bmatrix} = \begin{bmatrix} cb & 2c\theta b & 3c\theta^2 b & \dots \end{bmatrix}.$$

For this case (4A-1) holds, because

$$\operatorname{rank}\left(\frac{\partial \overrightarrow{\mathbf{S}}_r^T}{\partial \boldsymbol{\theta}}\left(\frac{\partial \overrightarrow{\mathbf{S}}_r^T}{\partial \boldsymbol{\theta}}\right)^T\right) = n = q = 1.$$

Case 2: siso and $n > 1$

For $p = m = 1$ and $n = q = 2$, then

$$\mathbf{A} = \begin{bmatrix} \theta_1 & \\ & \theta_2 \end{bmatrix}, \quad \frac{\partial \mathbf{A}}{\partial \boldsymbol{\theta}} = \begin{bmatrix} 1 & 0 \\ 0 & 0 \\ 0 & 0 \\ 0 & 1 \end{bmatrix}, \tag{4A-3}$$

where $\theta_1 \neq \theta_2$. We define $\mathbf{B} = \begin{bmatrix} b_1 \\ b_2 \end{bmatrix}$, $\mathbf{C} = \begin{bmatrix} c_1 & c_2 \end{bmatrix}$. Then $\mathbf{X}$ is given by

$$\mathbf{X} = \begin{bmatrix} \mathbf{C} & 0 & \mathbf{CA} & 0 & \dots \\ 0 & \mathbf{C} & 0 & \mathbf{CA} & \dots \end{bmatrix} \begin{bmatrix} 1 & 0 & & \\ 0 & 0 & & \\ 0 & 0 & & \\ 0 & 1 & & \\ & & 1 & 0 \\ & & 0 & 0 \\ & & 0 & 0 \\ & & 0 & 1 \end{bmatrix} \begin{bmatrix} \mathbf{B} & \mathbf{AB} & \dots & \\ & \mathbf{B} & \mathbf{AB} & \\ & & \ddots & \ddots \end{bmatrix} = \begin{bmatrix} c_1 b_1 & 2c_1\theta_1 b_1 & 3c_1\theta_1^2 b_1 & \dots \\ c_2 b_2 & 2c_2\theta_2 b_2 & 3c_2\theta_2^2 b_2 & \dots \end{bmatrix}. \quad \text{(4A-4)}$$

Due to the structure of system matrix $\mathbf{A}$, all inputs and outputs are decoupled. The Markov parameters of this system are

$$\begin{bmatrix} c_1 b_1 + c_2 b_2 & c_1\theta_1 b_1 + c_2\theta_2 b_2 & c_1\theta_1^2 b_1 + c_2\theta_2^2 b_2 & \dots \end{bmatrix}. \quad \text{(4A-5)}$$

This is equal to the row sum of $\mathbf{X}$, up to an weighing matrix.
Also for this case, considering the structure as mentioned earlier, the rank of (4A-2) is equal to n, and (4A-1) holds.

Case 3: $p > 1$ **and** $n > 1$

We now consider the system with $m = 1$ and $p = n = q = 2$. Matrices $\mathbf{A}$, $\frac{\partial \mathbf{A}}{\partial \theta}$ and $\mathbf{B}$ are equal to the ones in the previous case. We define $\mathbf{C} = \begin{bmatrix} c_{11} & c_{12} \\ c_{21} & c_{22} \end{bmatrix}$. Then $\mathbf{X}$ is given by

$$\mathbf{X} = \begin{bmatrix} \mathbf{C} & 0 & \mathbf{CA} & 0 & \dots \\ 0 & \mathbf{C} & 0 & \mathbf{CA} & \dots \end{bmatrix} \begin{bmatrix} 1 & 0 & & \\ 0 & 0 & & \\ 0 & 0 & & \\ 0 & 1 & & \\ & & 1 & 0 \\ & & 0 & 0 \\ & & 0 & 0 \\ & & 0 & 1 \end{bmatrix} \begin{bmatrix} \mathbf{B} & \mathbf{AB} & \dots & \\ & \mathbf{B} & \mathbf{AB} & \\ & & \ddots & \ddots \end{bmatrix} =$$

$$\begin{bmatrix} c_{11} b_1 & c_{21} b_1 & 2c_{11}\theta_1 b_1 & 2c_{21}\theta_1 b_1 & 3c_{11}\theta_1^2 b_1 & 3c_{21}\theta_1^2 b_1 & \dots \\ c_{12} b_2 & c_{22} b_2 & 2c_{12}\theta_2 b_2 & 2c_{22}\theta_2 b_2 & 3c_{12}\theta_2^2 b_2 & 3c_{22}\theta_2^2 b_2 & \dots \end{bmatrix}. \quad \text{(4A-6)}$$

Also for this case, considering the structure as mentioned earlier, the rank of (4A-2) is equal to n, and (4A-1) holds. For completeness we give the Markov parameters of this system

$$\begin{bmatrix} c_{11} b_1 + c_{12} b_2 & c_{11}\theta_1 b_1 + c_{12}\theta_2 b_2 & c_{11}\theta_1^2 b_1 + c_{12}\theta_2^2 b_2 & \dots \\ c_{21} b_1 + c_{22} b_2 & c_{21}\theta_1 b_1 + c_{22}\theta_2 b_2 & c_{21}\theta_1^2 b_1 + c_{22}\theta_2^2 b_2 & \dots \end{bmatrix}. \quad \text{(4A-7)}$$

In our approach we organize the Markov parameters as one row vector

$$\begin{bmatrix} c_{11}b_1 + c_{12}b_2 & c_{21}b_1 + c_{22}b_2 & c_{11}\theta_1 b_1 + c_{12}\theta_2 b_2 & c_{21}\theta_1 b_1 + c_{22}\theta_2 b_2 & \dots \end{bmatrix}. \tag{4A-8}$$

When we consider the row sum of $\mathbf{X}$ in (4A-6) we obtain (4A-8) up to a weighing matrix.

5 CHAPTER

Model Structure Approximation and Identification of Reservoir Models

Typically, the physical parameters in reservoir models cannot be uniquely estimated from measurements, meaning that the model parameterization is not identifiable. This is problematic, because an incorrect parameter estimate can lead to incorrect long-term predictions and model-based control strategies. This problem is analyzed using the notions of identifiability and structural identifiability as presented in the previous chapter. Structural identifiability is used to determine which parameters can be reliably estimated with perfect inputs, and identifiability is used to determine which parameters can be reliably estimated with given inputs. These notions allow to approximate the model structure and determine an identifiable parameterization with a significantly reduced number of parameters, both for single-phase and two-phase reservoir models. The identifiable parameterizations with reduced numbers of parameters are employed in an iterative procedure to minimize a cost function that is defined as the mismatch between production measurements and model outputs. The analysis is also applied to an object-based parameterization describing channels and barriers in the reservoir.

5.1 Introduction

Typically, the physical parameters in reservoir models cannot be uniquely estimated from measurements, meaning that the model parameterization is not identifiable. In other words, the problem of estimating the parameters in reservoir simulation models using measured production data (i.e. history matching) is generally an ill-posed problem, see e.g. Gavalas et al. (1976) and Oliver et al. (2008). This is particularly true if it is attempted to estimate individual grid block parameters such as permeability or porosity values, which may lead to a very large number (10^5 to 10^6) of unknown parameters that can only be estimated with a

large variance. Another challenging aspect in history matching is the need to retain geological realism while updating the parameter values.

One way to deal with the lack of identifiability in parameter estimation problems is to constrain the solution space for the model parameters through the addition of regularization terms to the cost function - see Section 4.4 and also Gavalas et al. (1976) for an early reference to Bayesian estimation of reservoir parameters. Another way to deal with the lack of identifiability in parameter estimation problems is to reparameterize the parameter space, in which case the number of parameters is strongly reduced, while at the same time it may be possible to better maintain geological realism.

An advantage of reparameterization is that the approach can be used to include prior knowledge. An example hereof is a channel parameterization that is applicable in the situation that channels are present in the reservoir. In case the parameters are estimated from measurements it will result in a realization that is geologically sound. Moreover, the number of parameters to be estimated is usually smaller and therefore the (co)variance of the estimated parameters is smaller, and the parameter identification problem is computationally less demanding to solve. A disadvantage of reparameterization is that a parameterization with less parameters is also less flexible and possibly has an increased bias. If the physical properties cannot be well represented by the new parameterization, then it is difficult to get a feasible solution of the parameter estimation problem. For example, in Gavalas et al. (1976), McLaughlin and Townley (1996) and Evensen (2007) can be found that wrongly assuming that some parameters (or states) are known by e.g. not estimating them, may lead to unrealistic estimates. These estimates usually become unrealistic because they compensate for neglected errors in the model.

Reparameterization techniques previously applied in reservoir engineering include zonation (Jacquard and Jain 1965; Jahns 1966), where each zone is assumed to have constant properties. Adaptive multiscale methods (Grimstad et al. 2003; Berre et al. 2007) are more advanced methods that divide the reservoir model into zones. The number of parameters that need to be estimated is reduced, but these methods possibly lead to discontinuities between the zones that are considered as non-geological. In Reynolds et al. (1996) and Abacioglu et al. (2001) the subspace algorithm as introduced by Oldenburg and Li (1994) is used to solve the identification problem in a computationally efficient way. Other parameterizations that have been used in reservoir engineering are wavelets (Sahni and Horne 2005), principle component analysis of the permeability vector (Sarma et al. 2007), and discrete cosine transform (Jafarpour and McLaughlin 2007). Furthermore, the pilot-point method (RamaRao et al. 1995) and gradual deformation (Hu 2000) are reparameterization techniques used in reservoir engineering which are both based on spatial variograms. According to Oliver et al. (2008) the pilot point method possibly introduces non-physical artifacts in the permeability and porosity fields, and the gradual deformation method might experience difficulties converging to a model that is able to match the measurements.

In Shah et al. (1978) the eigenvectors of the sensitivity matrix (i.e. derivative of

model outputs with respect to parameters) corresponding to the largest eigenvalues are used to reparameterize the parameter space. Both in Oliver (1996) and Reynolds et al. (1996) this approach is applied to determine permeability and/or porosity parameters. Another reparameterization that is based on the sensitivity matrix is the gradzone reparameterization introduced by Bissell et al. (1994). In this approach first an SVD is applied to the sensitivity matrix, and next to the values in each singular vector associated with a large singular value a cutoff is applied to make a division between grid block parameters that are relevant and not relevant for the input-output behavior. As a result, each singular vector results in two basis functions (i.e. zones): one that is associated with grid block parameters corresponding to positive entries above a certain threshold value in the singular vector, and one that is associated with grid block parameters corresponding to negative entries below the threshold value in the same singular vector. In Brun et al. (2004) the gradzone approach is extended from a cost function without prior information to a cost function in which prior information is included, showing the large influence of the prior information. In Rodrigues (2006) the parameter space is reparameterized based on the singular vectors of the dimensionless sensitivity matrix as introduced in Zhang et al. (2002) of water and oil flow rate measurements with respect to permeability parameters in each grid block. Based on the sensitivity matrix, calculated with an adjoint model, the model is reparameterized using the gradzone approach (Bissell et al. 1994). In Vasco et al. (1997) the sensitivity of pressure measurements with respect to grid block permeability is computed with finite differences. Pressure measurements appear to be most sensitive to grid block permeability changes in the vicinity of the wells. In addition, the sensitivity of tracer concentration measurements with respect to grid block permeability is computed with finite differences, all after tracer breakthrough time. The tracer concentration is modeled using a streamline approach (Datta-Gupta and King 1995). Tracer concentration measurements appear to be most sensitive to grid block permeability changes in areas where tracer flow occurs between injector-producer pairs.

In this chapter the reservoir models are also reparameterized, where we use the model structure approximation framework of Chapter 4 to determine identifiable parameterizations using the notions of structural identifiability and identifiability. In the new model structure the parameters to be identified are well identifiable and the physical interpretation of the parameters remains untouched. The reparameterizations that are based on the sensitivity matrix (e.g. by Shah et al. 1978; Bissell et al. 1994; Vasco et al. 1997; Brun et al. 2004; Rodrigues 2006; Tavakoli and Reynolds 2009) all fit in the model structure approximation framework. More precisely, the reparameterization proposed by Shah et al. (1978) is identical to model structure approximation using the notion of identifiability in case a cost function without prior information is used. The other reparameterizations differ by the choice of the cost function (with or without prior information), or post-processing of the gradient information (directly using the gradients as basis functions or using a gradzone approach). As argued in Section 4.4 in this thesis a cost function without prior information is chosen, and also it is chosen to use the basis functions directly and not to use grad zones.

In Section 5.2 model structures will be approximated to determine identifiable parameterizations for grid block parameters. In addition, attention is given to the effect of parameter values on the parameterization. Next, in Section 5.3 a channel parameterization is introduced, where the number of parameters is strongly reduced and geological realism is preserved after updating. Based on two examples the structural identifiability and identifiability of this parameterization is analyzed. In Section 5.4 an iterative algorithm is presented that is subsequently used to estimate the grid block permeability in a single-phase and a two-phase reservoir model. In Section 5.5 the channel parameters are estimated from measurements in a single-phase and a two-phase reservoir model.

5.2 Analysis of reservoir model structures

5.2.1 Structural identifiability

In Section 4.6 it is described how the notion of *structural* identifiability can be used to analyze model structures. The appropriate selection of the identifiable parameter space is obtained from (4.44), leading to

$$\mathbf{\Gamma}_{\theta_m}\frac{\partial \overrightarrow{\mathbf{S}}_r(\boldsymbol{\theta})^T}{\partial \boldsymbol{\theta}}\mathbf{\Gamma}_S^2\left(\frac{\partial \overrightarrow{\mathbf{S}}_r(\boldsymbol{\theta})^T}{\partial \boldsymbol{\theta}}\right)^T\mathbf{\Gamma}_{\theta_m} = \begin{bmatrix} \mathbf{U}_1 & \mathbf{U}_2 \end{bmatrix}\begin{bmatrix} \mathbf{\Sigma}_1 & \mathbf{0} \\ \mathbf{0} & \mathbf{\Sigma}_2 \end{bmatrix}\begin{bmatrix} \mathbf{V}_1^T \\ \mathbf{V}_2^T \end{bmatrix} \tag{5.1}$$

where again the separation between $\mathbf{\Sigma}_1 \in \mathbb{R}^{l\times l}$ and $\mathbf{\Sigma}_2$ is chosen in such a way that the singular values in $\mathbf{\Sigma}_2$ are considerably smaller than those in $\mathbf{\Sigma}_1$. In the examples presented later in this section the value of l, the number of singular values in $\mathbf{\Sigma}_1$, is chosen based on the normalized singular values according to

$$\frac{\sigma_{l+1}}{\sigma_1} < 1\times 10^{-5}. \tag{5.2}$$

The value l is also referred to as the (numerical) rank of $\mathbf{\Gamma}_{\theta_m}\frac{\partial \overrightarrow{\mathbf{S}}_r(\boldsymbol{\theta})^T}{\partial \boldsymbol{\theta}}\mathbf{\Gamma}_S$. Furthermore, we define

$$\mathbf{U} := \begin{bmatrix} \mathbf{U}_1 & \mathbf{U}_2 \end{bmatrix} \tag{5.3}$$

as the singular vectors of the scaled structural identifiability matrix (5.1). Note that (5.1) is a symmetric matrix and therefore the left and right singular values should be equal, i.e. $\mathbf{U} = \mathbf{V}$.

The columns of $\mathbf{U}_1$ act as basis functions in the parameter space, expressing the sensitivity of the Markov parameters with respect to the parameter vector. In case we choose the parameters to be estimated as the permeability in each grid block, each left singular vector has length q and each entry in a left singular vector corresponds to a specific grid block. Consequently, each column of $\mathbf{U}_1$ can be interpreted as a spatial pattern.

Alternatively, for small-scale nonlinear dynamical models $\mathbf{h}(\boldsymbol{\theta})$ (2.70) the (global) structural identifiability can be analyzed by determining the rank of the symbolic

matrix $\frac{\partial \mathbf{h}(\boldsymbol{\theta})^T}{\partial \boldsymbol{\theta}}$. If the symbolic matrix has full-rank the parameters $\boldsymbol{\theta}$ can be identified. However, since symbolic matrices are used it is not possible to investigate which parameter (combinations) are more identifiable than others and the analysis is limited to small-scale models. For an analytical, 1D two-phase reservoir model this analysis has been performed by Watson et al. (1984). See Section 3.4.3 for a description of the model. It is found that the permeability distribution is structurally identifiable from pressure measurements. In case it is assumed that the permeability distribution is known it is found that only the average porosity can be identified from the pressure and flow rate measurements. In case it is assumed that the porosity and permeability distribution are uniform and known it is found that the Corey exponents are structurally identifiable. For the latter case also the covariance is investigated, leading to the observation that the Corey exponents can be most reliably estimated from the combination of pressure drop and flow rate measurements.

In the remainder of this subsection the structural identifiability analysis following a Markov parameter approach is applied to two 2D, single-phase reservoir models to find which permeability parameters can be reliably estimated from pressure measurements, and what factors influence the structural identifiability. The first example is a SISO model with 49 grid blocks where the identifiability of grid block permeability from pressure measurements is analyzed. It mainly serves to show the influence of the permeability values on the determined identifiable parameterization. The second example is a MIMO model with 441 parameters and five inputs and five outputs where also the identifiability of grid block permeability from pressure measurements is analyzed. It demonstrates the influence of the permeability values and also the position of the wells. The examples will show that the grid block permeability cannot be reliably estimated from pressure measurements since

$$\text{rank}\left(\boldsymbol{\Gamma}_{\theta_m}\frac{\partial \overrightarrow{\mathbf{S}}_r(\boldsymbol{\theta})^T}{\partial \boldsymbol{\theta}}\boldsymbol{\Gamma}_S\right) < q, \tag{5.4}$$

where the numerical rank is evaluated. More importantly, based on the structural identifiability analysis the model structure can be approximated, an identifiable parameterization can be determined and the resulting basis functions can be depicted.

Single input, single output example - single-phase

In the first example the identifiability analysis is performed on a single-phase reservoir model with 49 states and an equal number of parameters (i.e. grid block permeabilities). The compressibility is $c = 1 \times 10^{-10}\text{Pa}^{-1}$, the viscosity is $\mu = 1 \times 10^{-3}\text{Pa} \cdot \text{s}$, the porosity is $\phi = 0.2$ in each grid block, and each grid block has dimensions $10\text{m} \times 10\text{m} \times 10\text{m}$. The permeability is 10^{-13}m^2 and equal in each grid block. Figure 5.1 (left picture) depicts the permeability on a log scale as a top view of a 2D representation. The input variables $\mathbf{u}$ denotes total liquid rate in the middle of the reservoir, and the output variable $\mathbf{y}$ denotes measured pressure in the middle of the reservoir.

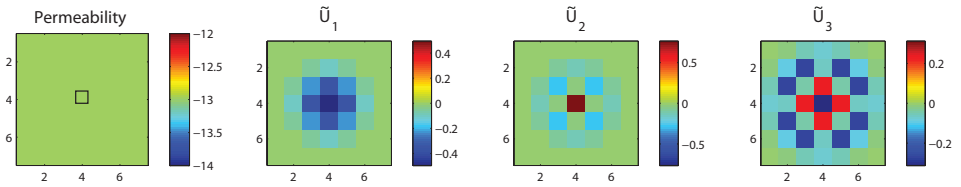

Figure 5.1: Top view of a homogeneous permeability distribution with well location indicated by a rectangle (left) and corresponding dominant spatial patterns in parameter space (middle and right).

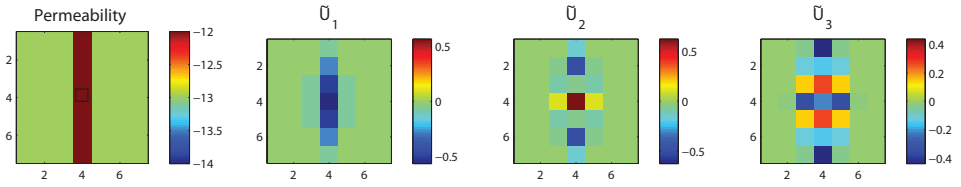

Figure 5.2: Permeability distribution containing a streak with higher permeability values (left) and corresponding dominant spatial patterns in parameter space (middle and right).

We first determine r based on a rank evaluation of the two block Hankel matrices (see Section 4.6.3). Expression (5.1) is calculated with $r = 13$, and next (5.1) is evaluated. The singular values decrease rapidly and $\frac{\sigma_4}{\sigma_1} < 1 \times 10^{-5}$. Therefore, according to (5.2) $l = 3$ and this means that in this case 3 parameters can be identified using pressure measurements. $\mathbf{U}_1$ has consequently dimensions of $q \times 3$ and since each parameter is connected to a grid block each column of $\mathbf{U}_1$ can be depicted as a spatial pattern (see Figure 5.1, three most right pictures, where the i-th singular vector is indicated by $\tilde{\mathbf{U}}_i$). These spatial patterns can be interpreted as the dominant directions in the parameter space to which the Markov parameters are sensitive to changes in $\boldsymbol{\theta}$.

As can be seen in Figure 5.1 the model parameters are mainly structurally identifiable around the well, because the values corresponding to these grid blocks are not equal or close to 0. Also, it is clear that a five-point spatial discretization scheme is used, because the values in the four neighboring grid blocks of the grid block containing the well are equal. Finally, due to the symmetry in the model properties, the dominant directions in the parameter space also display symmetric patterns.

To show the influence of $\boldsymbol{\theta}_0$, we added a high-permeable streak to the uniform permeability distribution (Figure 5.2, left picture). The value of the permeability in the streak is ten times higher. We calculated (5.1) with $r = 11$ and its rank is $l = 3$. Although the value of l is equal to the value of l in the previous example, the dominant directions in the parameter space that are sensitive to changes

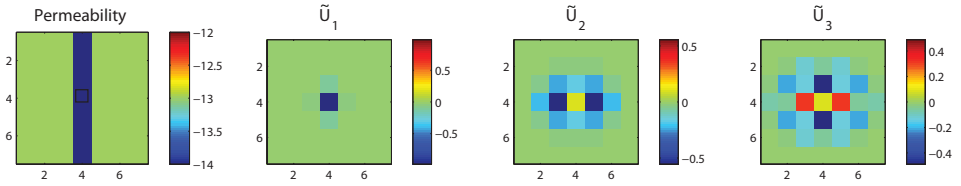

Figure 5.3: Permeability distribution containing a streak with lower permeability values (left) and corresponding dominant spatial patterns in parameter space (right).

in the input-output behavior are different (Figure 5.2, three most right pictures). Apparently, the input-output behavior is more sensitive to permeabilities with high values, since the values in the high-permeable streak have the highest values.

If the permeability in the streak is ten times lower (Figure 5.3, left picture), then according to (5.2) the rank of the information matrix is only $l = 2$. The corresponding dominant directions in parameter space are plotted in the middle two pictures of Figure 5.3, where the direction in the most right picture cannot be reliably identified anymore. These plots show that the input-output behavior is less sensitive to permeabilities with low values.

Multiple input, multiple output example - single-phase

In the second example the structural identifiability analysis is performed on a single-phase reservoir model with 441 states and an equal number of parameters. The permeability distribution consists of three zones: the upper left corner has a high permeability, the lower right corner a low permeability, and the intermediate zone an intermediate permeability (Figure 5.4). The other physical coefficients are chosen the same as in the first example. The model contains five wells, distributed in a characteristic five-spot pattern, indicated in Figure 5.4 by grey squares. For the wells in the four corners of the reservoir the bottom hole pressures are prescribed, and for the well in the middle of the reservoir the total liquid rate is prescribed. All wells have pressure measurement capabilities. This means that the model has five inputs and five outputs.

It was found that in this single-phase case 19 Markov parameters should be taken into account in order to arrive at correct expressions for the local structural identifiability analysis, i.e. $\text{rank}(\mathbf{H}_{r-1}) = \text{rank}(\mathbf{H}_r)$ (see Section 4.6.3). Expression (5.1) is therefore calculated with $r = 19$. The corresponding singular values are plotted in the left part of Figure 5.5. The 30 largest singular values are plotted again in the right part of Figure 5.5. For this example the rank is more difficult to determine, because the difference between two subsequent singular values is less distinct than for the SISO example. However, we do see that at least σ_{18} to σ_{441} are close to machine precision. This means that the maximum number of parameters

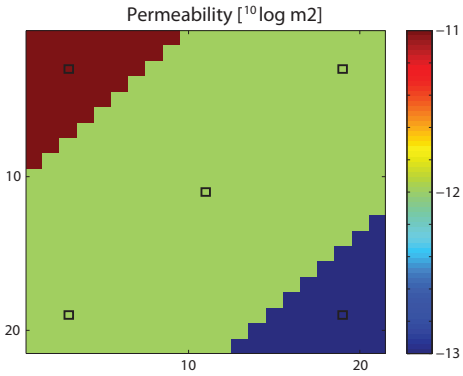

Figure 5.4: Permeability distribution (top view) for MIMO example. Rectangles indicate well positions.

that can be structurally identified with perfect pressure measurements and finite machine precision is only 17 out of a total of 441.

The singular vectors corresponding to the 12 largest singular values are depicted in Figure 5.6. Singular vectors $\tilde{\mathbf{U}}_1$, $\tilde{\mathbf{U}}_2$, $\tilde{\mathbf{U}}_5$, $\tilde{\mathbf{U}}_7$, $\tilde{\mathbf{U}}_8$ and $\tilde{\mathbf{U}}_{12}$ show spatial patterns located around the well in the zone with high permeability. The spatial patterns increase in size with decreasing singular value, indicating that the grid block permeabilities in the area further away from the well are more difficult to identify. The ninth singular vector $\tilde{\mathbf{U}}_9$ is the only vector in this figure that shows a spatial pattern around the well in the zone with low permeability. The remaining singular vectors show spatial patterns located around the wells in the zone with intermediate permeability. These spatial patterns also increase in size with decreasing singular value.

From this example we conclude that grid block permeabilities in an area near a well are most structurally identifiable from pressure measurements. Also we conclude that the value of the grid block permeability affects the extent to which it is structurally identifiable: grid block permeabilities near a well with a lower permeability value are less structurally identifiable than grid block permeabilities near a well with a higher permeability value.

5.2.2 Identifiability

In Section 4.2 it is described how the notion of identifiability can be used to analyze model structures. The appropriate selection of the identifiable parameter space is obtained from (4.17), leading to

$$\mathbf{\Gamma}_{\hat{\theta}} \frac{\partial \mathbf{h}(\boldsymbol{\theta})}{\partial \boldsymbol{\theta}}^T \mathbf{P}_v^{-\frac{1}{2}} = \begin{bmatrix} \mathbf{U}_1 & \mathbf{U}_2 \end{bmatrix} \begin{bmatrix} \mathbf{\Sigma}_1 & \mathbf{0} \\ \mathbf{0} & \mathbf{\Sigma_2} \end{bmatrix} \begin{bmatrix} \mathbf{V}_1^T \\ \mathbf{V}_2^T \end{bmatrix} \tag{5.5}$$

where the separation between $\mathbf{\Sigma}_1$ and $\mathbf{\Sigma}_2$ is chosen in such a way that the singular values in $\mathbf{\Sigma}_2$ are considerably smaller than those in $\mathbf{\Sigma}_1$. In the Bayesian frame-

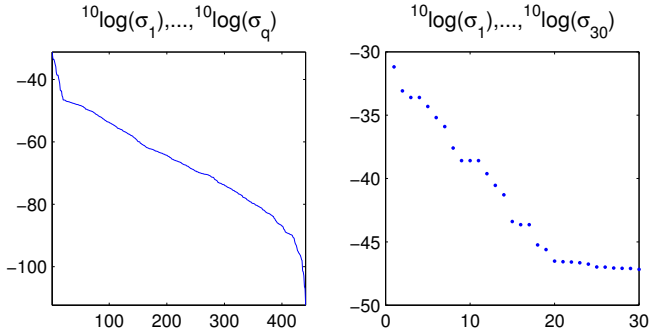

Figure 5.5: All singular values (left) and 30 largest singular values of (5.1) using the permeability distribution depicted in Figure 5.4.

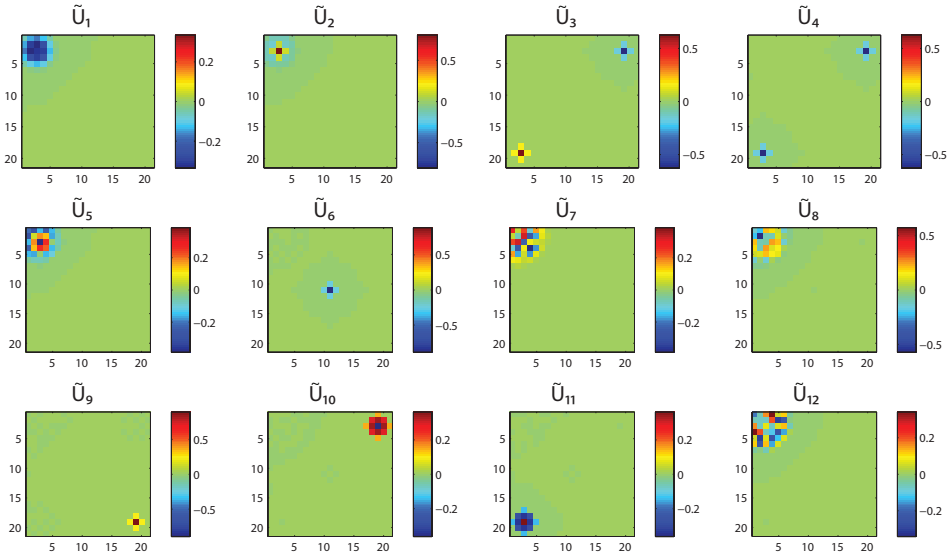

Figure 5.6: Singular vectors corresponding to the first 12 singular values of (5.1) using the permeability distribution depicted in Figure 5.4.

work the appropriate selection of the identifiable parameter space is obtained from (4.27), leading to

$$\mathbf{P}_{\hat{\boldsymbol{\theta}}}^{\frac{T}{2}} \frac{\partial \mathbf{h}(\boldsymbol{\theta})^T}{\partial \boldsymbol{\theta}} \mathbf{P}_v^{-\frac{1}{2}} = \begin{bmatrix} \mathbf{U}_1 & \mathbf{U}_2 \end{bmatrix} \begin{bmatrix} \boldsymbol{\Sigma}_1 & \mathbf{0} \\ \mathbf{0} & \boldsymbol{\Sigma}_2 \end{bmatrix} \begin{bmatrix} \mathbf{V}_1^T \\ \mathbf{V}_2^T \end{bmatrix}, \tag{5.6}$$

which is similar to the dimensionless sensitivity matrix defined by Zhang et al. (2002).

Multiple input, multiple output example - two-phase

Here a small-scale example is presented where the combinations of grid block permeability are shown that are most relevant for the input-output behavior of a two-phase reservoir model. Similar results can be found in e.g. Vasco et al. (1997) and Rodrigues (2006). The reservoir model is identical to the previously described MIMO reservoir model, with the exception that there are both oil and water phase present. Both fluids have density $\rho = 1000\text{kg/m}^3$, compressibility $c = 1 \times 10^{-10}\text{Pa}^{-1}$ and viscosity $\mu = 1 \times 10^{-3}\text{Pa} \cdot \text{s}$. The relative permeability of water and oil as function of water saturation is plotted in Figure 2.4.

Perfect measurements $\mathbf{y}$ are generated by simulating the two-phase reservoir model with the real permeability distribution in an in-house reservoir simulator, using an initial state of $\mathbf{p}_0 = 100 \times 10^5\text{Pa}$, and a manipulated input $\mathbf{u}$ as depicted in Figure 5.7. As input we have used the pressures in the production wells, located in the four corners of the reservoir, and the injection flow rate in the injection well, located in the center of the reservoir. The input signals $\mathbf{u}$ are depicted in Figure 5.7. As measurements we have used the oil and water flow rates in the four production wells, where we note that water breakthrough has occurred in all production wells. In other words, the production wells produce at a certain time both oil and water.

The adjoint model implemented in the reservoir simulator is used to calculate $\frac{\partial \mathbf{h}(\boldsymbol{\theta})^T}{\partial \boldsymbol{\theta}}$ in (5.5) where we have chosen for a non-Bayesian cost function (4.2)[1]. Furthermore, we have chosen $\boldsymbol{\Gamma}_{\hat{\theta}} = \text{diag}(^{10}\log \boldsymbol{\theta})$ and $\mathbf{P}_v^{-\frac{1}{2}} = \mathbf{I}$. As can be clearly seen the singular values of (5.5) in Figure 5.8 drop steeply, however, less steep than the singular values in Figure 5.5 corresponding to the pressure measurements resulting from the structural identifiability analysis (note the difference in vertical scale).

The singular vectors corresponding to the 12 largest singular values are depicted in Figure 5.9. Singular vectors $\tilde{\mathbf{U}}_1$ to $\tilde{\mathbf{U}}_4$ mainly show spatial patterns located around the production wells, although there are also patterns visible between the

[1] In the particular implementation of the adjoint model only the time-averaged value of $\frac{\partial \mathbf{h}(\boldsymbol{\theta})^T}{\partial \boldsymbol{\theta}}$ is given, i.e. a vector with the length of the number of parameters q. In this work matrix $\frac{\partial \mathbf{h}(\boldsymbol{\theta})^T}{\partial \boldsymbol{\theta}} \in \mathbb{R}^{q \times N}$ is obtained column by column, where column i, $i = 1, \ldots, N$, is calculated by the adjoint model by assigning a unit weight to $\mathbf{h}(\boldsymbol{\theta})$ at time step i, and assigning zero weights to $\mathbf{h}(\boldsymbol{\theta})$ at the other time steps.

injection well and production wells. The fifth singular vector $\tilde{\mathbf{U}}_5$ clearly shows a pattern between the injection and production well in the bottom left corner, where the grid blocks in the middle of this area have the highest absolute value (indicated by blue). This means that in case the permeability value in these grid blocks is changed this will have a large effect on the oil and water rates. Together with the plot of the singular values in Figure 5.8, this points into the direction that flow rate measurements contain more information on the permeability distribution than pressure measurements, because also grid block permeabilities located further away from the wells significantly influence the flow rate measurements.

Note that the shape of the patterns in Figure 5.9 is not necessarily related to the presence of geological features such as channels. Also the yellow parts depicted in singular vector $\tilde{\mathbf{U}}_5$, at the edges of the pattern between injection and production well, should not be confused by the presence of geological features in the permeability distribution, since these result from a similar effect as noted by Vasco et al. (1997), i.e. that at a later moment in time the flow rates are also influenced by grid block permeability parameters located in these areas. The remaining singular vectors $\tilde{\mathbf{U}}_6$ to $\tilde{\mathbf{U}}_{12}$ show spatial patterns connecting an injection and production well similar as in $\tilde{\mathbf{U}}_5$.

Also note that the symmetry that is present in the permeability field is not present anymore in the patterns (i.e. patterns related to the bottom left well are not identical to patterns related to the top right well). This is caused by the different input signals that are used for each well, and since identifiability (as opposed to structural identifiability) is used the input signal does influence the identifiable directions.

5.3 Geological parameterizations

5.3.1 Introducing a channel parameterization

As described in Section 5.1, desired features of parameterizations in reservoir engineering applications are that the parameters are identifiable and that after estimation geological realism is preserved. A possible solution to realize these features is to choose a parameterization in terms of a limited number of geological objects (e.g. channels) such that an update in the parameters results in a geologically realistic permeability field. Here, a channel parameterization is presented and subsequently an example is given in which the channel parameters are estimated from measurements.

Estimating channel parameters with production measurements has been considered by e.g. Rahon et al. (1998), Bi et al. (1999) and Phan and Horne (2002). In Phan and Horne (2002) a deterministic method has been used, where the mapping between the 14 channel parameters and the three-dimensional permeability field is unique. In this section we introduce a simple two-dimensional object-based modeling method to create facies and permeability distributions, where the mapping

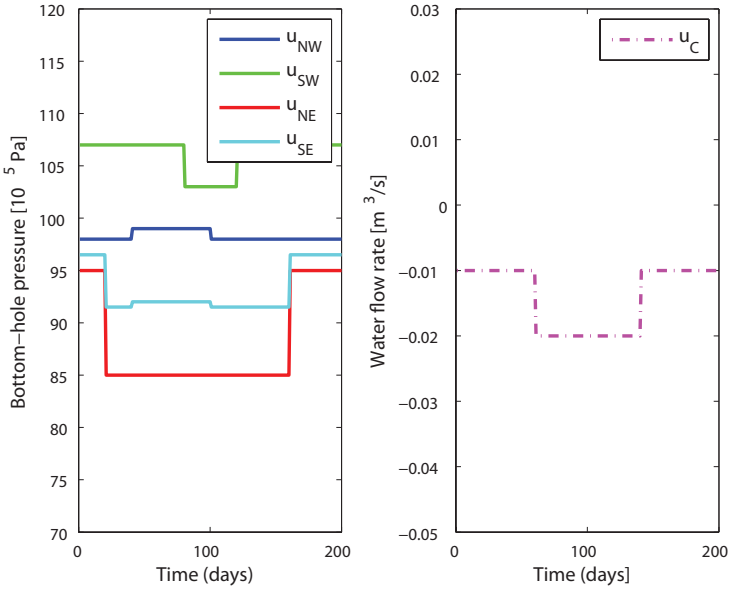

Figure 5.7: Input signals as function of time that are used to excite the two-phase reservoir model. Bottom-hole pressures (left) and liquid flow rates (right).

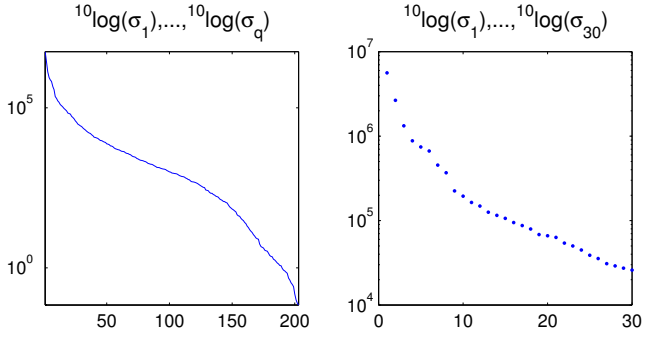

Figure 5.8: All singular values (left) and 30 largest singular values (right) of (5.5) using the permeability distribution depicted in Figure 5.4.

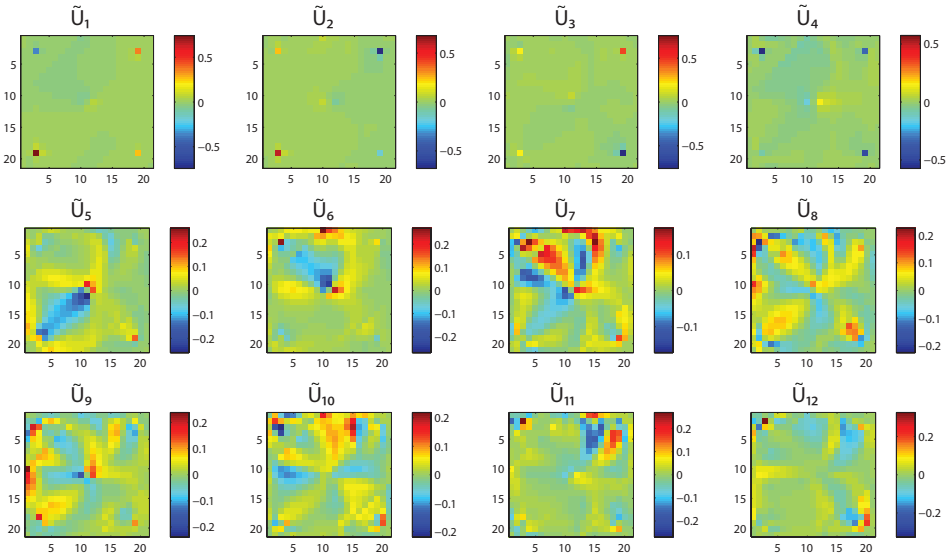

Figure 5.9: Singular vectors corresponding to the first 12 singular values of (5.5) using the permeability distribution depicted in Figure 5.4.

between the parameters and resulting facies or permeability distribution is also unique. It is assumed that the channels are straight and have a uniform permeability distribution. Also the permeability of the background has a uniform distribution. These assumptions are motivated by the fact that we wanted to reduce the number of parameters and only wanted to model those features of the reservoir that are relevant for prediction and control. Additionally, we reasoned that the flow behavior in a channel with a slight curvature would be approximately equal to the flow behavior in a straight channel with a slightly lower permeability.

The advantages of the channel parameterization are that it results in a geologically more realistic permeability distribution after estimation of the parameters, and that the number of parameters that needs to be estimated is relatively small. A difficulty with the channel parameterization is that it is less flexible than the grid block parameterization: if for example the permeability distribution does not contain channels, the procedure of estimating channel parameters will not converge or converge to a different estimate. Examples of more flexible parameterizations are e.g. the discrete cosine transform parameterization, that originates from the image compression community and has been applied in Jafarpour and McLaughlin (2007, 2009) in a parameter estimation procedure for reservoir models.

The channels in our modeling method are modeled with the morphological structuring element *strel* as available in the Image Processing Toolbox of MATLAB. Each channel is described by six parameters: orientation, position in x direction, position in y direction, length, width and channel permeability. An additional parameter describes the permeability of the background permeability of the reservoir

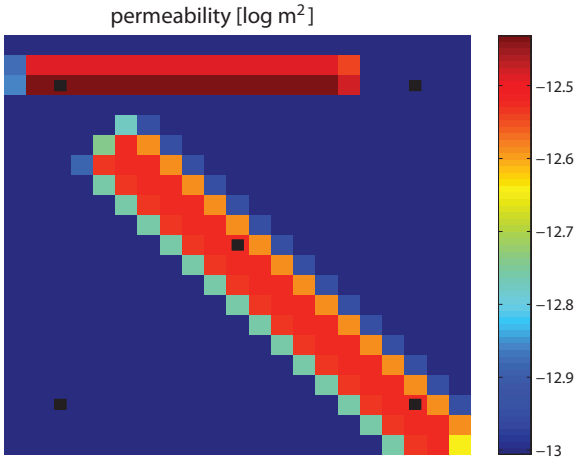

Figure 5.10: Example of permeability distribution generated with the channel and barrier modeling method. The parameter values are given in Table 5.1.

Symbol	Meaning	Value	Unit	$\mathbf{U}_{1:13}$ (1p)	$\mathbf{U}_{1:13}$ (2p)
θ_{ch1}	orientation channel 1	45	[°]	5.6×10^{-5}	2.2×10^{4}
θ_{ch2}	orientation channel 2	90	[°]	4.7×10^{-5}	2.9×10^{4}
θ_{ch3}	position x channel 1	200	[m]	0.2×10^{-5}	0.5×10^{4}
θ_{ch4}	position x channel 2	300	[m]	0.7×10^{-5}	1.5×10^{4}
θ_{ch5}	position y channel 1	1000	[m]	0.5×10^{-5}	0.6×10^{4}
θ_{ch6}	position y channel 2	150	[m]	0.5×10^{-5}	0.1×10^{4}
θ_{ch7}	width channel 1	600	[m]	2.2×10^{-5}	0.6×10^{4}
θ_{ch8}	width channel 2	200	[m]	2.7×10^{-5}	1.1×10^{4}
θ_{ch9}	length channel 1	4400	[m]	5.2×10^{-5}	0.4×10^{4}
θ_{ch10}	length channel 2	3000	[m]	0.9×10^{-5}	0.9×10^{4}
θ_{ch11}	permeability channel 1	300	[mD]	3.9×10^{-5}	1.5×10^{4}
θ_{ch12}	permeability channel 2	600	[mD]	2.8×10^{-5}	0.9×10^{4}
θ_{ch13}	permeability background	100	[mD]	0.2×10^{-5}	0.8×10^{4}

Table 5.1: Channel parameters of the permeability distribution in Figure 5.10. The fifth column gives the value of the measure $\mathbf{U}_{1:13}$ for the single-phase (1p) example, and the last column gives the value of the measure $\mathbf{U}_{1:13}$ for the two-phase (2p) example.

model. This means that the permeability field with two channels in Figure 5.10 is described by $\boldsymbol{\theta}_{gb} = 13$ channel parameters. The values of the channel parameters for the example in Figure 5.10 are given in Table 5.1, where the longest channel is defined as channel 1. If channels intersect with each other, then the younger channel replaces the older channel, where the channel number is representative for the age. In other words, in case channels intersect the grid block permeability is solely determined by the youngest channel only. The channels are generated on a fine-scale grid, and then upscaled to the simulation grid size using the arithmetic mean. For the example depicted in Figure 5.10 we have chosen 420×420 grid blocks which are subsequently upscaled to 21×21 grid blocks of $10 \times 10\text{m}^2$. The parameterization of this example will be analyzed with structural identifiability (Subsection 5.3.2) and with identifiability (Subsection 5.3.3).

5.3.2 Analysis of a channel parameterization - single-phase

For the single-phase example we will use structural identifiability analysis, since the analysis is independent of the chosen input signals and it can be easily applied to linear models. With structural identifiability analysis it is possible to calculate

$$\left.\frac{\partial \overrightarrow{\mathbf{S}}_r(\boldsymbol{\theta}_{gb})^T}{\partial \boldsymbol{\theta}_{ch}}\right|_{\boldsymbol{\theta}_{ch}}, \tag{5.7}$$

where $\boldsymbol{\theta}_{gb}$ denotes grid block permeability and $\boldsymbol{\theta}_{ch}$ denotes the channel parameters. To calculate this expression we simply apply the chain rule

$$\frac{\partial \overrightarrow{\mathbf{S}}_r(\boldsymbol{\theta}_{gb})^T}{\partial \boldsymbol{\theta}_{ch}} = \frac{\partial \boldsymbol{\theta}_{gb}^T}{\partial \boldsymbol{\theta}_{ch}} \frac{\partial \overrightarrow{\mathbf{S}}_r(\boldsymbol{\theta}_{gb})^T}{\partial \boldsymbol{\theta}_{gb}}, \tag{5.8}$$

evaluated at $\boldsymbol{\theta}_{ch}$. The term $\frac{\partial \boldsymbol{\theta}_{gb}^T}{\partial \boldsymbol{\theta}_{ch}}$ is calculated using finite differences adopting a central difference scheme where each geological parameter $\boldsymbol{\theta}_{ch}$ is perturbed in positive and negative direction on the fine-scale grid.

Subsequently, the scaled structural identifiability matrix is analyzed with an SVD according to

$$\boldsymbol{\Gamma}_{\theta_{ch}} \frac{\partial \overrightarrow{\mathbf{S}}_r(\boldsymbol{\theta}_{gb})^T}{\partial \boldsymbol{\theta}_{ch}} \boldsymbol{\Gamma}_S^2 \left(\frac{\partial \overrightarrow{\mathbf{S}}_r(\boldsymbol{\theta}_{gb})^T}{\partial \boldsymbol{\theta}_{ch}} \right)^T \boldsymbol{\Gamma}_{\theta_{ch}} = \mathbf{U}\boldsymbol{\Sigma}\mathbf{V}^T, \tag{5.9}$$

evaluated at $\boldsymbol{\theta}_{ch}$. Since (5.9) is a symmetric matrix the left and right singular vectors should be equal, i.e. $\mathbf{U} = \mathbf{V}$. However, due to round-off errors the matrices can have different values for vectors corresponding to small singular values. In the remainder we have made the choice that the columns of $\mathbf{U}$ are the singular vectors of the scaled structural identifiability matrix. The singular vectors and singular values of (5.9) also offer a means to find which combinations of parameters affect the predicted measurements. The latter greatly adds to the insight in the

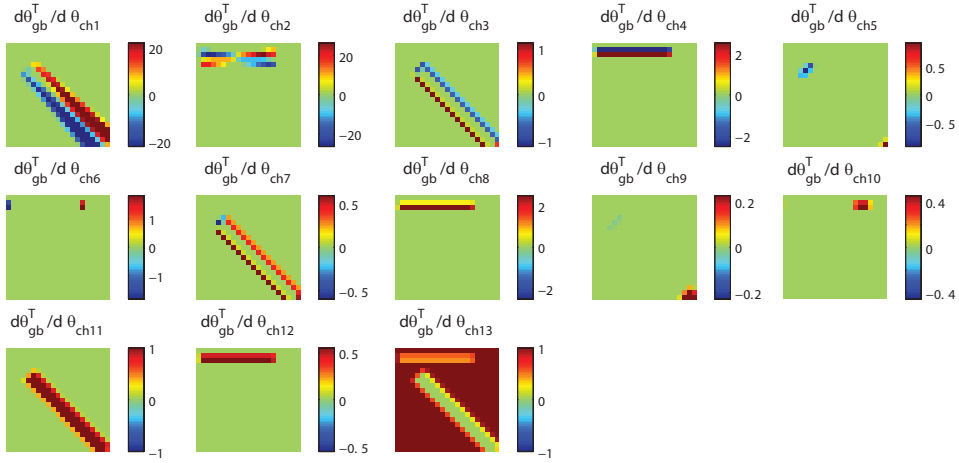

Figure 5.11: Each column of $\frac{\partial \boldsymbol{\theta}_{gb}^T}{\partial \boldsymbol{\theta}_{ch}}$ is visualized onto the reservoir grid. See Table 5.1 for the meaning and value of parameters $\theta_{ch1}, \ldots, \theta_{ch13}$.

reservoir behavior and the parameter estimation process, as will be demonstrated in the next example.

We now present an example in which the parameters of the channel parameterization are to be estimated from pressure measurements. We choose a real permeability field as depicted in Figure 5.10, which is parameterized by 13 parameters. The well configuration and remaining reservoir coefficients are identical to those in the previous example in Section 5.2. The model structure is analyzed with structural identifiability. The term $\frac{\partial \boldsymbol{\theta}_{gb}^T}{\partial \boldsymbol{\theta}_{ch}}$ is computed using finite differences where each geological parameter $\theta_{chi}, i = 1, \ldots, 13$ is perturbed with a perturbation step size of 10^{-5} times the absolute value of the channel parameter to obtain the grid block permeability field $\boldsymbol{\theta}_{gb}$. We obtain, after upscaling, the plots in Figure 5.11, in which each column of $\frac{\partial \boldsymbol{\theta}_{gb}^T}{\partial \boldsymbol{\theta}_{ch}}$ is interpreted as a spatial pattern. For example, in the first plot of this figure the difference in permeability distribution is given as a result of a perturbation of θ_{ch1}, the orientation of channel 1.

The singular vectors contained in $\mathbf{U}$ and singular values $\boldsymbol{\Sigma}$ of (5.9) are computed for this specific example. The logarithm of the singular values, ${}^{10}\log \sigma_i, \quad i = 1, \ldots, 13$, are plotted in Figure 5.12 (left). Specifically, the last singular value has a low value, which indicates that for this example the model structure can be approximated with a reduced number of parameters, being linear combinations of the channel parameters. Equally as in the example dealing with grid block permeability, the singular vectors can be interpreted as combinations of parameters. Matrix $\mathbf{U}$ consisting of the 13 singular vectors as columns is depicted in Figure 5.12 (right), where green colors indicate that the value of the singular vector is zero or close to zero. The first column denotes the first singular vector of (5.9) and is associated with a large singular value. Each subsequent singular vector is

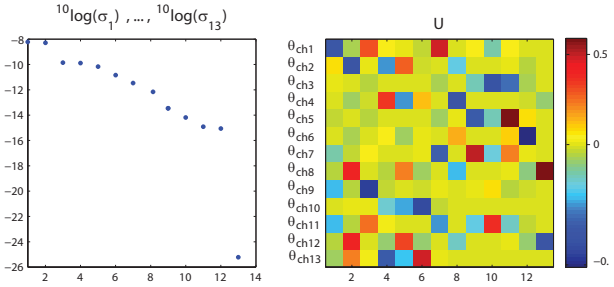

Figure 5.12: Singular values (left) and singular vectors (right) of (5.9) for the channel parameterization in a single-phase reservoir model.

associated with a smaller singular value.

For matrix (5.9) the weighted singular vector $\mathbf{U}_{1:z}$ in (3.7) is calculated for $z = 13$. For each channel parameter the value is denoted in Table 5.1. Based on these values we conclude for this permeability distribution that the orientation of channel 1, θ_{ch1}, and length of channel 1, θ_{ch9}, are best identifiable, since these have the highest values of $\mathbf{U}_{1:z}$. The position in x direction of channel 1, θ_{ch3}, and the background permeability θ_{ch13}, are least identifiable, since these have the lowest values of $\mathbf{U}_{1:z}$. Note that these results are computed before the channel parameters are estimated, which will be done in Section 5.5.1.

5.3.3 Analysis of a channel parameterization - two-phase

The model structure of the two-phase model with channel parameterization will be analyzed using the notion of identifiability. This time we calculate

$$\left.\frac{\partial \mathbf{h}(\boldsymbol{\theta}_{gb})^T}{\partial \boldsymbol{\theta}_{ch}}\right|_{\boldsymbol{\theta}_{ch}} = \frac{\partial \boldsymbol{\theta}_{gb}^T}{\partial \boldsymbol{\theta}_{ch}} \frac{\partial \mathbf{h}(\boldsymbol{\theta}_{gb})^T}{\partial \boldsymbol{\theta}_{gb}}, \tag{5.10}$$

where $\boldsymbol{\theta}_{gb}$ denotes the grid block permeability. Subsequently, the scaled identifiability matrix is analyzed by applying an SVD on

$$\boldsymbol{\Gamma}_{\theta_{ch}} \frac{\partial \mathbf{h}(\boldsymbol{\theta}_{gb})^T}{\partial \boldsymbol{\theta}_{ch}} \boldsymbol{P}_v = \mathbf{U}\boldsymbol{\Sigma}\mathbf{V}^T, \tag{5.11}$$

evaluated at $\boldsymbol{\theta}_{ch}$. In the next example the parameters of the channel parameterization are to be estimated from oil and water flow rate measurements. The permeability, well configuration and remaining reservoir coefficients are identical as in the previous example. Using the adjoint model in the reservoir simulator the term $\frac{\partial \mathbf{h}(\boldsymbol{\theta})^T}{\partial \boldsymbol{\theta}_{ch}}$ is calculated and the term $\frac{\partial \boldsymbol{\theta}_{gb}^T}{\partial \boldsymbol{\theta}_{ch}}$ is computed using perturbations and is plotted in Figure 5.11.

The singular vectors contained in $\mathbf{U}$ and singular values $\boldsymbol{\Sigma}$ of (5.11) are computed for the specific example. The logarithm of the singular values are plotted in Figure 5.13 (left). Again, the last singular value has a low value, which indicates that

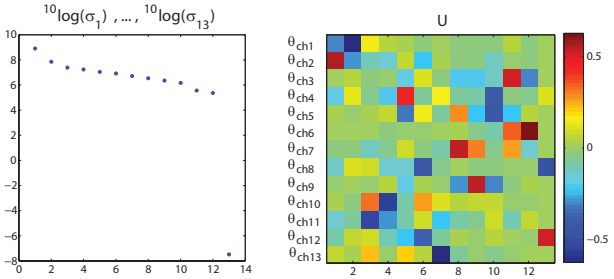

Figure 5.13: Singular values (left) and singular vectors (right) of (5.9) for the channel parameterization in a two-phase reservoir model.

the model structure can be approximated with a reduced number of parameters. Matrix $\mathbf{U}$ is visualized in Figure 5.13 (right). Also for this example $\mathbf{U}_{1:13}$ is computed and denoted in Table 5.1 (last column). We conclude for this example that the orientations of both channels, θ_{ch1} and θ_{ch2}, are best identifiable from water and oil flow rate measurements, since for these parameters the value of $\mathbf{U}_{1:13}$ is the highest. The position in y direction of channel 2, θ_{ch6}, is least identifiable from water and oil flow rate measurements, since for this parameter the value of $\mathbf{U}_{1:13}$ is the lowest.

5.4 Identification of grid block parameters

5.4.1 Identification procedure

In this section the values of grid block parameters of single-phase and two-phase reservoir models are estimated from pressure and flow rate measurements, where we propose to approximate the reservoir model structure using the notions of structural identifiability and identifiability. In (4.45) the relation is given between identifiability and structural identifiability, leading to the observation that in case the input signal is persistently exciting the notions of structural identifiability and identifiability lead to similar results. Therefore, for single-phase reservoir models as presented in this section the reservoir model structure is solely approximated using the notion of structural identifiability.

Subsequently, the reduced-dimensional, identifiable parameters in the approximated model structure are estimated in an iterative identification procedure. The advantage of this formulation is that only those (linear combinations of) parameters are updated that are relevant for the input-output behavior. Parameters with a large effect on flow behavior are the permeabilities in each grid block, and these are also the parameters that will be estimated. However, the same procedure can easily be used to estimate other parameters in the reservoir model.

Since the identifiable parameterization partly depends on the parameter value we use an iterative procedure as depicted in Figure 5.14, similar as in Zandvliet et al.

(2008). Starting from an initial guess $\boldsymbol{\theta}_{\text{init}}$ the model structure is approximated and $\mathbf{U}_1$ is calculated according to (5.1). An extra column containing ones in every entry is added to $\mathbf{U}_1$ to account for an overall increase or decrease in the parameters. Subsequently, $\boldsymbol{\theta}$ is reparameterized as

$$\boldsymbol{\theta} = \bar{\mathbf{U}}_1(\boldsymbol{\theta})\boldsymbol{\rho}, \tag{5.12}$$

where $\boldsymbol{\rho} \in \mathbb{R}^{1+l}$ denotes the reduced-dimensional parameter vector that needs to be estimated and where

$$\bar{\mathbf{U}}_1(\boldsymbol{\theta}) := \begin{bmatrix} I_{q\times 1} & \mathbf{U}_1 \end{bmatrix} \in \mathbb{R}^{q\times(1+l)}. \tag{5.13}$$

An iterative, gradient-based optimization problem is solved to estimate the reduced-dimensional parameter vector, in which $\hat{\boldsymbol{\rho}}_1 = \bar{\mathbf{U}}_1^T(\boldsymbol{\theta}_{\text{init}})\boldsymbol{\theta}_{\text{init}}$. The quadratic cost function without prior information is defined as

$$V\left(\bar{\mathbf{U}}_1\left(\boldsymbol{\theta}\right)\boldsymbol{\rho}\right) := \left(\mathbf{y} - \hat{\mathbf{y}}\left(\bar{\mathbf{U}}_1\left(\boldsymbol{\theta}\right)\boldsymbol{\rho}\right)\right)^T\left(\mathbf{y} - \hat{\mathbf{y}}\left(\bar{\mathbf{U}}_1\left(\boldsymbol{\theta}\right)\boldsymbol{\rho}\right)\right), \tag{5.14}$$

where $\mathbf{y}$ denotes the measured output and $\hat{\mathbf{y}}$, which is a function of $\bar{\mathbf{U}}_1\left(\boldsymbol{\theta}\right)\boldsymbol{\rho}$, denotes the predicted output. The estimated parameter vector is given by

$$\hat{\boldsymbol{\rho}} = \arg\min_{\boldsymbol{\rho}} V\left(\bar{\mathbf{U}}_1\left(\boldsymbol{\theta}\right)\boldsymbol{\rho}\right). \tag{5.15}$$

In the examples presented in this section the Gauss-Newton algorithm as implemented in the MATLAB function `lsqnonlin` is used to minimize the quadratic cost function (5.14).

If the value of the cost function given in (5.14) is not decreasing anymore (i.e. a local minimum is found) we determine a new identifiable parameterization. With the new set of basis functions we might possibly succeed in decreasing (5.14) further. If this is not the case then the parameter estimation problem is said to have converged. It is possible to increase the number of reduced-order parameters in the new parameterization to give additional degrees of freedom in the identification procedure. However, in this work the number of reduced-order parameters is kept fixed.

There is always a risk that the numerical minimization gets stuck in a local minimum since the model is nonlinear in the parameters. Therefore it is advisable to try several different initial parameter values. The resulting estimate could be different when another set of initial parameter values were chosen, especially in the case not all parameters are identifiable.

During the algorithm the SVD of matrices with large dimensions is calculated every iteration. Since we are mainly interested in the singular vectors associated with large singular values it is computationally attractive to use the Lanczos algorithm to calculate only a limited number of singular vectors (e.g. Golub and Van Loan (1996)). The Lanczos algorithm is also used in Rodrigues (2006) and Tavakoli and Reynolds (2009) in a parameter estimation procedure.

Figure 5.14: Iterative procedure for identifying reservoir parameters.

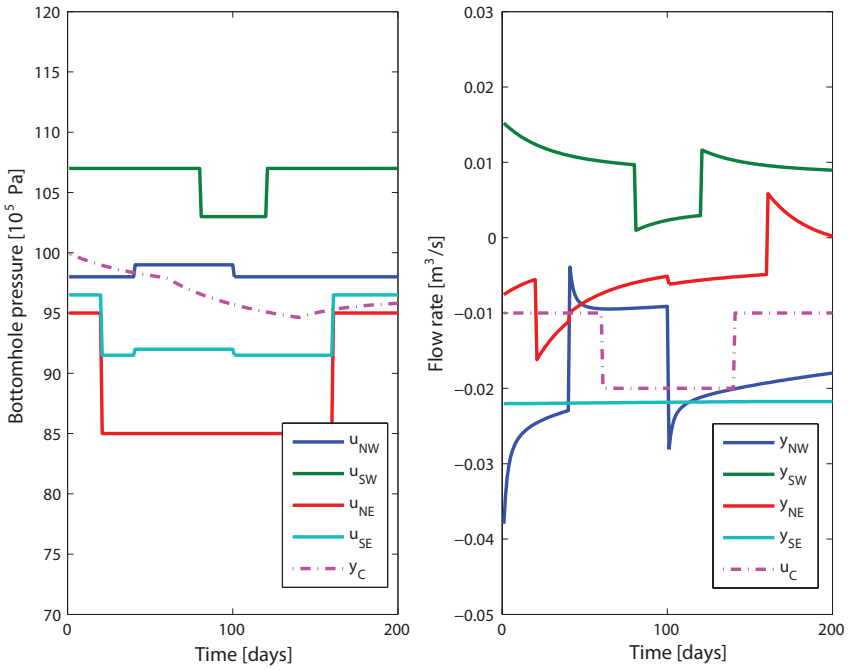

Figure 5.15: Bottom-hole pressures (left) and flow rates (right).

5.4.2 Identification of grid block permeability - single-phase

In this example we use a single-phase, two-dimensional model. The state-space formulation of this model is given in (2.10, 2.11) and further described in Section 2.2.1. The parameter to be estimated is the logarithm of the permeability in each grid block. The permeability field depicted in Figure 5.4 is defined as the real permeability distribution. The 21×21 reservoir grid is penetrated by five wells, which positions are indicated by rectangles. The remaining reservoir coefficients are considered known and are given in Section 5.2.1.

Perfect measurements $\mathbf{y}$ are generated by simulating the single-phase reservoir model (2.10, 2.11) with the real permeability distribution and an initial state of $\mathbf{p}_0 = 100 \times 10^5$Pa. As input $\mathbf{u}$ we have used the pressures in the production wells, located in the four corners of the reservoir, and the injection flow rate in the injection well, located in the center of the reservoir. The measurements $\mathbf{y}$ and input signals $\mathbf{u}$ are depicted in Figure 5.15, where the subscript NW indicates the well in the upper left corner (North West) of Figure 5.4, SW the well in the lower left corner (South West), NE the well in the upper right corner (North East), SE the well in the lower right corner (South East), and C the well in the center. The input consists of step input signals, since these are commonly applied to reservoirs, and

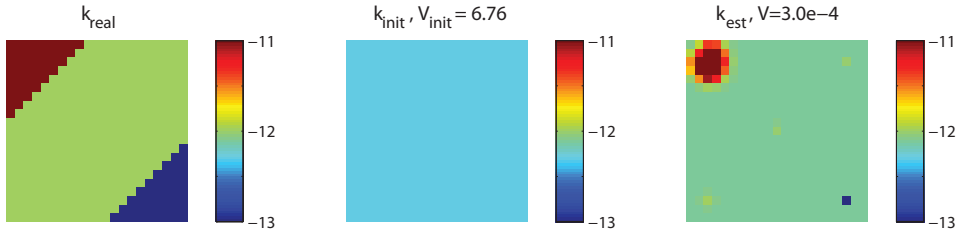

Figure 5.16: Real permeability distribution (left), initial permeability distribution (middle) and estimated permeability distribution (right) obtained with the structurally identifiable parameterization in a single-phase reservoir model.

is persistently exciting[2].

The previously described identification procedure is used to estimate the grid block permeability distribution. As initial guess a homogeneous permeability distribution is chosen with the value $\boldsymbol{\theta}_{\text{init}} = -13.3$ which is equivalent to a permeability value of $5 \times 10^{-13}\text{m}^2$. This permeability distribution is depicted in the middle of Figure 5.16. The corresponding value of the cost function is $V(\boldsymbol{\theta}_{\text{init}}) = 6.76$. Based on $\boldsymbol{\theta}_{\text{init}}$ an identifiable parameterization $\bar{\mathbf{U}}_1$ is determined keeping only the first 12 columns of $\mathbf{U}_1$.

In this example the estimate has converged after three iterations to the permeability distribution depicted in the right of Figure 5.16. The value of the cost function has decreased to $V = 3.0 \times 10^{-4}$. In the situation that pressure measurements are used to estimate the permeability distribution the input-output behavior of the estimated permeability field is according to the low value of the cost function similar to the behavior of the real permeability distribution. Apparently, grid block parameters, which are located in medium and low permeable grid blocks that are penetrated by wells, are structurally most identifiable, together with grid block parameters in a slightly larger area around the well located in the high permeable area. The permeability in the other grid blocks are in the structurally least identifiable directions and these parameters only have a negligible influence on the input-output behavior. The parameter values in this area are solely determined by the initial permeability distribution.

Although the cost function has a small value and one could say that the reservoir model is history matched, this does not mean that the model can be reliably used for prediction and decision making. With the estimated permeability distribution the decision of e.g. finding the optimal position where a new well should be drilled can not be adequately made. Apparently, the information content in the pressure measurements is not sufficient for this purpose.

[2]Formally, according to the definition of persistence of excitation step input signals are not persistently exciting, but step responses completely characterize linear system dynamics (modulo initial conditions). Note that the results obtained using a pseudo-random binary signal (prbs) are similar as the results presented in this chapter.

5.4.3 Identification of grid block permeability - two-phase

Next the grid block permeability of a two-phase reservoir model will be identified. Since the reservoir model contains water and oil, and as a result it is nonlinear, the model structure is analyzed with the notion of identifiability (see Section 5.2.2). The adjoint model as implemented in an in-house reservoir simulator is used to calculate $\frac{\partial \mathbf{h}(\boldsymbol{\theta})^T}{\partial \boldsymbol{\theta}}$ in (5.5). We have chosen for a non-Bayesian cost function (4.2), since we are most interested in the information on the model parameters provided by the measurements. The value of the covariance matrix $\mathbf{P}_v^{-\frac{1}{2}}$ is chosen to be the identity matrix.

In the following example both fluids have density $\rho = 1000\text{kg/m}^3$, compressibility $c = 1 \times 10^{-10}\text{Pa}^{-1}$ and viscosity $\mu = 1 \times 10^{-3}\text{Pa} \cdot \text{s}$. The relative permeability of water and oil as function of water saturation are plotted in Figure 2.4. Perfect measurements $\mathbf{y}$ are generated by simulating the two-phase reservoir model for 200 days in the in-house reservoir simulator with the real permeability distribution (see left plot in Figure 5.18), initial pressure $\mathbf{p}_0 = 100 \times 10^5\text{Pa}$ and initial oil saturation $\mathbf{s}_0 = 0.2$ in every grid block. As input we have used the pressures in the production wells and the injection flow rate in the injection well (see Figure 5.7 for the signals). As measurements we have used the oil and water flow rates in the four production wells (see Figure 5.17 for the signals). As can be seen water breakthrough has occurred in all production wells. Also note that the production well in the SW area is shut in for the first 60 days since the reservoir pressure is lower than the prescribed bottom-hole pressure.

As initial guess a homogeneous permeability distribution is chosen with the value $\boldsymbol{\theta}_{\text{init}} = -13.3$ which is equivalent to a permeability value of $5 \times 10^{-13}\text{m}^2$, identical to the initial guess of the example in Subsection 5.4.2. This permeability distribution is depicted in the middle of Figure 5.18. The corresponding value of the cost function is $V(\boldsymbol{\theta}_{\text{init}}) = 135$. Based on $\boldsymbol{\theta}_{\text{init}}$ the model structure is approximated using (5.5), keeping only the first 15 singular values. To estimate the grid block permeability we have used the Gauss-Newton update rule (4.5.1). In this example the best result is obtained in case the model structure is approximated after each update. The estimate has converged after 30 iterations to the permeability distribution depicted in the right of Figure 5.18. Note that the scale of this plot is different from the two other plots to better see the estimated permeability values in between the injection and production wells. The value of the cost function has decreased to $V = 5.93$. From the estimated permeability distribution we see that the largest changes have occurred in the grid blocks which are penetrated by production wells. Other changes have occurred in grid blocks between injection and production wells, which was to be expected from inspecting the basis functions depicted in Figure 5.9. There is a low permeable zone between the injection well and the production well in the low permeable area, and there is a zone with a slightly higher permeable area in between the injection well and the production well in the high permeable area. Although the real permeability distribution is not recognizable anymore, the flow relevant features are apparently estimated since the cost function has decreased significantly. Next, the geologist and reservoir

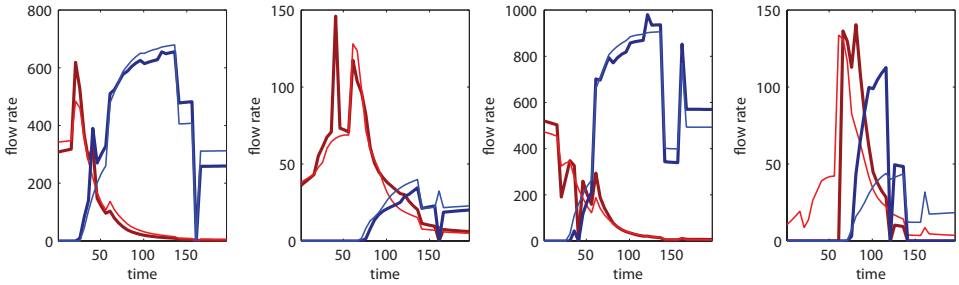

Figure 5.17: Water (blue) and oil (red) flow rates in the four production wells in respectively the NE, SE, NW and SW corner of the reservoir. The thick lines represent the measured flow rates and the thin lines the predicted flow rates of the estimated permeability distribution in a two-phase reservoir model.

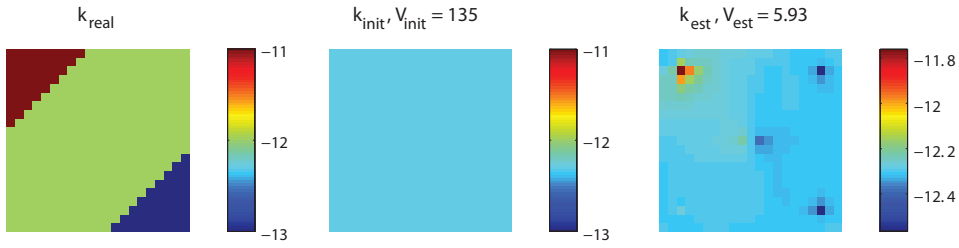

Figure 5.18: Real permeability distribution (left), initial permeability distribution (middle) and estimated permeability distribution (right) obtained with the identifiable grid block parameterization in a two-phase reservoir model.

engineer need to explain what permeability distribution could exhibit the same flow relevant features but has a geologically more realistic appearance. The latter is important because then also the geological model is changed based on measurements, leading to improved geological models. Note that they may add any spatial pattern present in the singular vectors of $\mathbf{U}_2$ without changing the value of the cost function.

Note that in Chapter 4 it has been shown that identifiability is related to controllability and observability. In Chapter 3 it has been demonstrated that the saturation states are most controllable around the oil-water front. Therefore, only after water breakthrough has occurred, i.e. the oil-water front has reached the production wells, the observed measurements of oil-water rates (or tracer concentration) contain significant information on the grid block permeability. This has also been illustrated by Vasco et al. (1997).

5.5 Identification of channel parameters

5.5.1 Identification of channel parameters - single-phase

To estimate the channel parameters and resulting permeability distribution in a single-phase reservoir model we start with initial parameter values resulting in an upscaled permeability field as depicted in the middle of Figure 5.19. The corresponding value of the cost function is $V = 0.06$. With the same persistently exciting inputs as in the previous example, shown in Figure 5.15, the 13 channel parameters are estimated. We have used the Gauss-Newton algorithm as implemented in the MATLAB function `lsqnonlin` to minimize the quadratic cost function (5.14). This results after convergence in the permeability distribution depicted in the right of Figure 5.19. The value of the cost function has decreased to $V = 5.3 \times 10^{-4}$. For this situation the input-output behavior of this permeability distribution is similar to the behavior of the real permeability distribution. However, the estimated permeability distribution is different from the real permeability distribution. Note that the channels are in this example not correctly positioned at the well locations. For example, the channel in the northern part of the reservoir is in the real permeability distribution penetrated by the well in the NW corner. But this is not the case in the estimated permeability distribution. From this example it is concluded that there is insufficient information in the measurements to reliably estimate the channel parameters and resulting permeability distribution.

5.5.2 Identification of channel parameters - two-phase

Next, the channel parameters are estimated in a two-phase reservoir model. The channel parameters are estimated from the water and oil flow rate measurements in the producers depicted in Figure 5.20 with the thick lines. The initial permeability distribution resulting from the initial channel parameters is depicted in the middle of Figure 5.21. The channels are located in a similar configuration as in

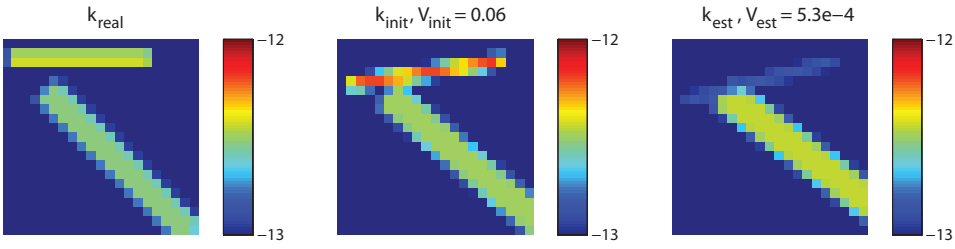

Figure 5.19: Real permeability distribution (left), initial permeability distribution (middle) and estimated permeability distribution (right) obtained with the channel parameterization for the single-phase example.

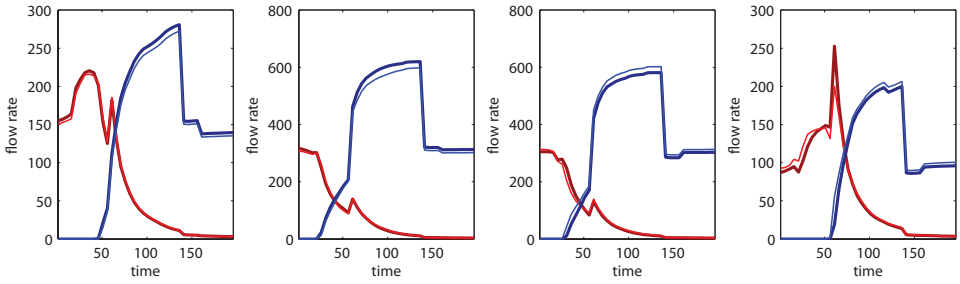

Figure 5.20: Water (blue) and oil (red) flow rates in the four production wells in respectively the NE, SE, NW and SW corner of the reservoir. The thick lines represent the measured flow rates and the thin lines the predicted flow rates of the estimated permeability distribution obtained with the channel parameterization.

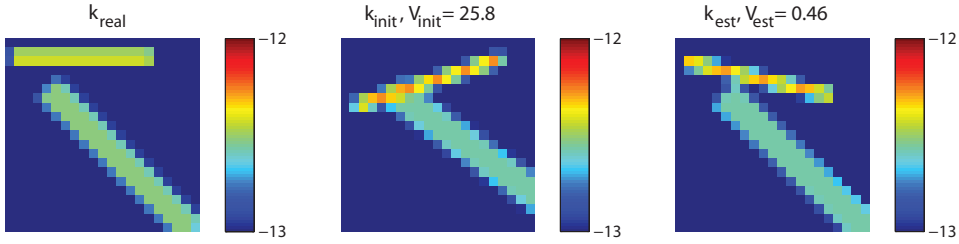

Figure 5.21: Real permeability distribution (left), initial permeability distribution (middle) and estimated permeability distribution (right) obtained with the channel parameterization for the two-phase example.

the previous example, and are not penetrated by the wells. The corresponding value of the cost function is $V = 25.8$. With the same inputs as in the previous two-phase example in Section 5.4.3 we estimate the 13 channel parameters. This results after convergence in the permeability distribution depicted in the right of Figure 5.21. The value of the cost function has decreased to $V = 0.46$. For this situation the input-output behavior of this permeability distribution is similar to the behavior of the real permeability distribution. Also the estimated permeability distribution is similar to the real permeability distribution, and the channels are in this example correctly positioned at the well locations. The latter was not the case in the previous example in which only pressure measurements were used to estimate the channel parameters. Apparently, to estimate permeability the information content in rate measurements is larger than the information content in pressure measurements: in case rate measurements are used the channel parameter values can be estimated in such a way that they are similar to the values of the channel parameters corresponding to the real permeability distribution. This can also be concluded from the singular values in Figure 5.8 which decrease slower than in the case pressure measurements are used, and the singular vectors in Figure 5.9 which clearly show patterns between the injection and production wells, and not only around the wells.

5.6 Conclusions

In this chapter the model structure of reservoir models has been analyzed with the notions of identifiability and structural identifiability. As a result a best identifiable, reduced-dimensional parameterization has been constructed, which is applicable to large-scale, non-linearly parameterized and multi-input, multi-output state-space models.

The approach has been applied to single-phase and two-phase examples in petroleum reservoir engineering, where both pressure measurements and flow rate measurements have been used. In case grid block parameters are analyzed this leads to basis functions or spatial patterns in the original parameter space. These give insight into the information content of the measurements. It appeared that the information content in the pressure and rate measurements on grid block permeability is limited. The pressure measurements only give information on the grid block permeability close to the wells, where the size of the area is proportional to the value of the grid block permeability. The rate measurements also give information on the permeability in the area between the injection and production wells. The basis functions resulting from the identifiability analysis have been used in an iterative procedure to estimate the grid block permeability from production measurements, leading to permeability distributions that are different from the real permeability distribution, but with a low value of the cost function.

In addition, a geological, object-based channel parameterization has been introduced and the identifiability analysis of this parameterization has been applied to single-phase and two-phase examples. Again pressure and rate measurements have been used to estimate the parameters, where the parameters converged to geological realistically looking permeability distributions. Also for these examples the information content in the production measurements was insufficient to estimate the real permeability distribution, but a low value of the cost function has been achieved.

Overall, we can conclude that the information content of the production measurements is insufficient to reliably estimate the permeability distribution, irrespective of the chosen parameterization. Of course a geological parameterization could be used to estimate geologically looking permeability distributions with a low cost function, but still the estimated permeability distribution is only reliable in the area around the wells and in between the injection and production wells. In other areas the permeability distribution has not been reliably estimated, and depends to a large extent on the initial choice of the parameter values.

6 CHAPTER

Conclusions and recommendations

The research objective of this thesis is to investigate the possibilities to obtain petroleum reservoir models that are suitable for model-based operation, and that can be validated from production data. This chapter presents the conclusions of this thesis and gives recommendations for future research.

6.1 Conclusions

- The currently used petroleum reservoir models are nonlinear models that contain a large number of states and physical parameters (typically $10^5 - 10^6$), resulting from the spatial and temporal discretization of the relevant partial differential equations. The states are the grid block pressures and grid block saturations. Physical parameters that play a large role in the long-term flow behavior are the grid block permeabilities.
- Controllability and observability properties of the model determine to a large extent the most relevant dynamics. Based on the analyzed reservoir models with homogeneous and heterogeneous reservoir properties the Hankel singular values of reservoir models decrease rapidly, indicating that they behave as models of much lower order than the state-space models that result after spatial and temporal discretization.
- Pressure states are most controllable and observable around the wells that can control and observe the pressure states. Saturation states are most controllable around the fluid front and most observable around the wells. After balancing, the most relevant pressure states are located around the wells, and the most relevant saturation states are located around the fluid front. This offers an explanation why the control action that is observed in flooding optimization studies of optimal production settings is often at the injection wells at early times, and at the production wells at later times.

- Based on the examples we conclude that the position of the wells and the dynamics of the oil-water front determine the controllability and observability properties of the reservoir. Therefore, for fixed well positions, reduced-order models of flow in porous media should focus on correctly modeling the fluid front(s).
- Identifiability and structural identifiability play a central role in parameter estimation. The notions of (local) identifiability and structural identifiability can be quantified, and can be used to determine which model parameters can be reliably estimated from measurement data. This allows to approximate the model structure so as to achieve identifiability, while retaining the interpretation of the physical parameters.
- Identifiability plays a role both in iterative optimization algorithms (like Gauss-Newton and Steepest-Descent) as well as in recursive (sequential) parameter estimation methods.
- In a Bayesian setting, in which a priori knowledge is included in the cost function, there seems to be no issue regarding identifiability. But in this setting the parameters that cannot be estimated from measurements are determined by the a priori knowledge (i.e. parameter estimate). This could give a false sense of model reliability.
- Both identifiability and structural identifiability are closely related to controllability and observability.
- Reservoir models are not identifiable from production measurements: the parameter values in these models are to a large extent based on qualitative geological information, and to a smaller extent based on information from production measurements.
- The information content of production measurements on grid block permeability in single-phase and two-phase reservoir models is limited. The pressure measurements only contain information on grid block permeabilities in an area close to the wells in which is measured, where the extent of the area is proportional to the value of the grid block permeability. The rate measurements also contain information on grid block permeabilities in the area between the injection and production wells.
- Overall, we conclude that the information content of the production measurements is insufficient to reliably estimate the permeability distribution. This also holds for the introduced geological, object-based channel parameterization. Of course a geological parameterization could be used to estimate geologically looking permeability distributions with a low value of the cost function, but still the estimated permeability distribution is only reliable in the area around the wells and in between the injection and production wells. In other areas the permeability distribution has not been reliably estimated, and depends to a large extent on the initial choice of the parameter values.
- The values of parameter combinations that cannot be estimated from measurements, i.e. directions in parameter space that are not identifiable, can

be freely altered without changing the value of the cost function. This can be considered as additional degrees of freedom in the parameter estimation problem that can be used to include geological information after the parameters have been estimated from measurements.

The overall conclusions of this thesis promote a complexity reduction of hydrocarbon reservoir models for model-based operation: if a part of the reservoir model does not influence the relevant dynamics of the model, or it cannot be validated with measurements, then this should not be modeled.

6.2 Recommendations

Answering one question leads to another, and also research on model-based operations of hydrocarbon reservoirs is far from complete. Suggestions for future research are given below:

- Controllability analysis of two-phase reservoir models has shown that the saturation states are most controllable around the fluid front. Therefore, it is important that models are able to accurately capture the front between the phases in the reservoir model. Gridding and upscaling methods should take advantage of this, and possibly use an adaptive gridding method that uses a fine level of detail around the wells and the fluid fronts, and a coarser level of detail in the rest of the reservoir. The result could be that the total simulation time is decreased and that the accuracy of the solution is increased.
- In this thesis the main focus was on estimating permeability, while certainly for two-phase flow also other parameters are uncertain (e.g. parameters of the relative permeability model or parameters in the geological model). The same analysis could be also be carried out for these parameters.
- Model structure analysis could be used to define a new sensor location that maximizes identifiability and/or observability of the reservoir model. In addition, by solving an hierarchical optimization problem as described in Van Essen et al. (2009), a location can be chosen that also optimizes reservoir performance (e.g. ultimate recovery).
- Identifiability analysis can be used to determine on which part of the reservoir information is gathered. It would be beneficial to determine for each measurement type on what part of the reservoir information is gathered. Based on this it can be decided which measurement types are redundant (i.e. give information on the same part of the reservoir, presumably the near well bore area), and which measurement types give information further away from the wells.

Bibliography

Abacioglu, Y., D. Oliver and A. Reynolds (2001). Efficient reservoir history matching using subspace vectors. *Computational Geosciences* **5**, 151–172.

Antoulas, A. C. (2005). *Approximation of Large-Scale Dynamical Systems*. SIAM.

Asheim, H. (1987). Optimal control of water drive. *SPE Journal (SPE 15978)*.

Astrom, K. J. and B. Wittenmark (1990). *Computer Controlled Systems (2nd Edition)*. Prentice Hall.

Aziz, K. and A. Settari (1986). *Petroleum Reservoir Simulation*. Elsevier Applied Science.

Bai, E. W. (1998). An optimal two-stage identification algorithm for Hammerstein-Wiener nonlinear systems. *Automatica* **34**(3), 333–338.

Bell, A., B. Cheshire, K. Gowans, F. Jahn and C. Wilson (1989). *Petroleum geology for production staff*. The Open University and Shell Internationale Petroleum Maatschappij BV.

Bellman, R. and K. J. Åström (1970). On structural identifiability. *Mathematical Biosciences* **7**, 329–339.

Bennett, A.F. (2002). *Inverse modeling in the ocean and atmosphere*. Cambridge, UK: Cambridge University Press.

Berntsen, H. E. and J. G. Balchen (1973). Identifiability of linear dynamical systems. In P. Eykhoff (Ed.), *3rd IFAC Symposium on Identification and System Parameter Estimation*, The Hague, pp. 871–874.

Berre, I., M. Lien and T. Mannseth (2007). A level-set corrector to an adaptive multiscale permeability prediction. *Computational Geosciences* (11), 27–42.

Bi, Z., D.S. Oliver and A.C. Reynolds (1999). Conditioning 3d stocastic channels to pressure data. In *SPE Annual Technical Conference and Exhibition*, Houston, Texas, USA. SPE.

Bissell, R. C., Y. Sharma and J. E. Killough (1994). History matching using the method of gradients: Two case studies. In *SPE Annual Conference and Exhibition (SPE 28590-MS)*, New Orleans.

BP Statistical Review of World Energy, (2008). BP statistical review of world energy. Technical report, BP.

Brewer, J., Z. Huang, A. K. Singh, M. Misra and J. Hahn (2007). Sensor network design via observability analysis and principal component analysis. In *AiCh*, San Francisco, CA, USA.

Brouwer, D. R. (2004). *Dynamic Water Flood Optimization With Smart Wells Using Optimal Control Theory*. Ph. D. thesis, Delft University of Technology.

Brouwer, D. R. and J. D. Jansen (2004). Dynamic optimization of waterflooding with smart wells using optimal control theory. *SPE Journal (SPE 78278)* **9**(4), 391–402.

Brun, B., O. Gosselin and J. W. Barker (2004). Use of prior information in gradient-based history matching. *SPE Journal (SPE 87680-PA)* **9**(1), 67–78.

Buckley, S.E. and M.C. Leverett (1942). Mechanism of fluid displacement in sands. *Petroleum Transactions AIME* **146**, 107–116.

Cardoso, M. A., L. J. Durlofsky and P. Sarma (2008). Development and application of reduced-order modeling procedures for subsurface flow simulation. *Int. J. Numer. Meth. Eng., to appear*.

Chavent, G. (1975). History matching by use of optimal theory. *SPE Journal* **15**(1), 74–86.

Damen, A. A. H., R. P. Guidorzi, A. K. Hajdasinski and P. M. J. Van den Hof (1985). On multivariable partial realization. *International Journal of Control* **41**(3), 589–613.

Datta-Gupta, A. and M.J. King (1995). A semianalytic approach to tracer flow modeling in heterogeneous permeable media. *Advances in Water Resources* **18**(1), 9.

Dennis Jr., J. E. and R. B. Schnabel (1996). *Numerical Methods for Unconstrained Optimization and Nonlinear Equations*. Classics in Applied Mathematics. Philadelphia: Society of Industrial and Applied Mathematics.

Deutsch, C.V. (2001). *Geostatistical reservoir modelling*. Applied geostatistics. Oxford: Oxford University Press.

Dötsch, H. G. M. and P. M. J. Van den Hof (1996). Test for local structural identifiability of high-order non-linearly parameterized state space models. *Automatica* **32**(6), 875–883.

Douma, S. G. (2008). Personal communication.

Evensen, G. (1994). Sequential data assimilation with a nonlinear quasi-geostrophic model using Monte Carlo methods to forecast error statistics. *J. Geophys. Res.* **99**(C5), 10143–1062.

Evensen, G. (2007). *Data Assimilation*. Springer.

Farmer, C.L. (2002). Upscaling: a review. *Int. J. Numer. Meth. Fluids* **40**, 63–78.

Fyrozjaee, M. H. and Y. C. Yortsos (2006). Control of a displacement front in potential flow using flow rate partition. In *SPE Intelligent Energy Conference and Exhibition (SPE 99524)*, Amsterdam.

Gavalas, G. R., P. C. Shah and J. H. Seinfeld (1976). Reservoir history matching by bayesian estimation. *SPE Journal (SPE 5740-PA)* **16**(6), 337–350.

Gildin, E., H. Klie, A. Rodriguez and M. F. Wheeler (2006). Development of low-order controllers for high-order reservoir models and smart wells. In *SPE Annual Techical Conference and Exhibition (SPE 102214-MS)*, San Antonio.

Glover, K. (1984). All optimal hankel-norm approximations of linear multivariable systems and their $\mathcal{L}^\infty$-error bounds. *International Journal of Control* **39**(6), 1115–1193.

Glover, K. and J. C. Willems (1974). Parameterizations of linear dynamical systems: Canonical forms and identifiability. *IEEE Transactions on Automatic Control* **19**(6), 640–646.

Godfrey, K. R. (1983). *Compartmental Models and their Application*. London: Academic Press.

Golub, G. H. and C. F. Van Loan (1996). *Matrix Computations* (Third ed.). Baltimore, Maryland: The John Hopkins University Press.

Grewal, M. S. and K. Glover (1976). Identifiability of linear and nonlinear dynamical systems. *IEEE Transactions on Automatic Control* **21**(6), 833–837.

Grimstad, A., T. Mannseth and G. Naevdal (2003). Adaptive multiscale permeability estimation. *Computational Geosciences* **7**(1), 1–25.

Gu, Y. and D. S. Oliver (2007). An iterative ensemble Kalman filter for multiphase fluid flow data assimilation. *SPE Journal* **12**(4), 468–446.

Hahn, J., T. F. Edgar and W. Marquardt (2003). Controllability and observability covariance matrices for the analysis and order reduction of stable nonlinear systems. *Journal of Process Control* **13**(2), 115–127.

Heijn, T., R. Markovinović and J. D. Jansen (2004). Generation of low-order reservoir models using system-theoretical concepts. *SPE Journal* **9**(June), 202–218.

Hermann, R. and A. J. Krener (1977). Nonlinear controllability and observability. *IEEE Trans. Automat. Control* **22**(5), 728.

Hjalmarsson, H. (2005). From experiment design to closed-loop control. *Automatica* **41**(3), 393–438.

Ho, Y. C. (1962). On the stochastic approximation method and optimal filtering theory. *J. Math. Analysis and Application* **6**, 152–154.

Hu, L.Y. (2000). Gradual deformation and iterative calibration of gaussian-related stochastic models. *32* **1**, 87–108.

International Energy Outlook, (2009). International energy outlook 2009. Technical report, Energy Information Administration.

Isidori, A. (1995). *Nonlinear Control Systems*. New York: Springer Verlag.

Jacquard, P. and C. Jain (1965). Permeability distribution from field pressure data. *SPE Journal (SPE 1307)* (December), 281–294.

Jafarpour, B. and D. McLaughlin (2009). Reservoir characterization with the discrete cosine transform. *SPE Journal* **14**(1), 182–201.

Jafarpour, B. and D. B. McLaughlin (2007). Efficient permeability parameterization with the discrete cosine transform. In *SPE Reservoir Simulation Symposium (SPE 106453)*, Houston.

Jahns, H. O. (1966). A rapid method for obtaining a two-dimensional reservoir description from well pressure response data. *SPE Journal (SPE 1473-PA)* **6**(4), 315–327.

Jansen, J. D. (2007). Systems theory for reservoir management.

Jansen, J. D., O. H. Bosgra and P. M. J. Van den Hof (2008). Model-based control of multiphase flow in subsurface oil reservoirs. *Journal of Process Control* **18**(9), 846–855.

Jansen, J. D., D. R. Brouwer, G. Naevdal and C. P. J. W. van Kruijsdijk (2005). Closed-loop reservoir management. *First Break* **23**, 43–48.

Jansen, J. D., S. G. Douma, D. R. Brouwer, P. M. J. Van den Hof, O. H. Bosgra and A. W. Heemink (2009). Closed-loop reservoir management. In *Reservoir Simulation Symposium*, The Woodlands, Texas, USA. SPE.

Jansen, J. D., J. F. M. Van Doren, M. H. Fyrozjaee and Y. C. Yortsos (2009). Front controllability in two-phase porous media flow. In P. M. J. Van den Hof, C. Scherer, and P. S. C. Heuberger (Eds.), *Model-Based Control: Bridging Rigorous Theory and Advanced Technology*, pp. 203–219. New York: Springer.

Kailath, T. (1980). *Linear Systems*. Englewood Cliffs: Prentice-Hall.

Kaleta, M. P., R. G. Hanea, J. D. Jansen and A. W. Heemink (2009). Model-reduced variational data assimilation for reservoir model updating. In *ECMOR XI, 11th European Conference on the Mathematics of Oil Recovery*, Bergen , Norway, pp. 1–10.

Kokotovic, P. V., H. K. Khalil and J. O'Reilly (1986). *Singular Perturbation Methods in Control: Analysis and Design*. London: Academic Press.

Lall, S., J. E. Marsden and S. A. Glavaski (2002). A subspace approach to balanced truncation for model reduction of nonlinear control systems. *International Journal of Robust Nonlinear Control* **12**(6), 519.

Li, R., A. C. Reynolds and D. S. Oliver (2003). History matching of three-phase flow production data. *SPE Journal* **8**(4), 328–340.

Ljung, L. (1979). Asymptotic behavior of the Extended Kalman Filter as a parameter estimator for linear systems. *IEEE Trans. Automat. Control* **24**(1), 36–50.

Ljung, L. (1999). *System Identification - Theory for the User* (2nd ed.). Information and System Sciences. Upper Saddle River, NJ: Prentice-Hall.

Ljung, L. and T. Glad (1994). On global identifiability for arbitrary model parameterizations. *Automatica* **30**(2), 265–276.

Ljung, L. and T. Söderström (1983). *Theory and Practice of Recursive Identification*, Volume 4 of *The MIT Press Series in Signal Processing, Optimization, and Control*. Cambridge: The MIT Press.

Lund, B. F. and B. A. Foss (2008). Parameter ranking by orthogonalization - applied to nonlinear mechanistic models. *Automatica* **44**, 278–281.

Markovinović, R., E. L. Geurtsen, T. Heijn and J. D. Jansen (2002). Generation of low-order reservoir models using POD, empirical Gramians and subspace identification. In *8th European Conference on the Mathematics of Oil Recovery*, Freiberg.

Markovinović, R. and J. D. Jansen (2006). Accelerating iterative solution methods using reduced-order models as solution predictors. *Int. J. Numer. Meth. Engng* **68**, 525–541.

McKelvey, T. and A. Helmersson (1997). System parameterization of an overparameterized model class: Improving the optimization algorithm. In *36th IEEE Conference on Decision and Control*, San Diago, CA, USA, pp. 2984–2989.

McKelvey, T., A. Helmersson and T. Ribarits (2004). Data driven local coordinates for multivariable linear systems and their application to system identification. *Automatica* **40**, 1629–1635.

McLaughlin, D. and L.R. Townley (1996). A reassesment of the groundwater inverse problem. *Water Resources Research* **32**(5), 1131–1161.

Moore, B. C. (1981). Principal component analysis in linear systems: Controllability, observability, and model reduction. *IEEE Trans. Automat. Control* **26**, 17–32.

Naevdal, G., D. R. Brouwer and J. D. Jansen (2006). Waterflooding using closed-loop control. *Computational Geosciences* **10**(1), 37–60.

Naevdal, G., L. M. Johnsen, S. I. Aanonsen and E. H. Vefring (2005). Reservoir monitoring and continuous model updating using ensemble kalman filter. *SPE Journal (SPE 84372)* **10**(1), 66–74.

Nijmeijer, H. and A. van der Schaft (1996). *Nonlinear Dynamical Control Systems*. New York: Springer.

Norton, J. P. (1980). Normal-mode identifiability analysis of linear compartmental systems in linear stages. *Mathematical Biosciences* **50**, 95–115.

Oldenburg, D. W. and Y. Li (1994). Subspace linear inverse method. *Inverse Problems* **10**, 915–935.

Oliver, D., A. C. Reynolds and N. Liu (2008). *Inverse Theory for Petroleum Reservoir Characterization and History Matching*. Cambridge University Press.

Oliver, D. S. (1996). Multiple realizations of the permeability field from well-test data. *SPE Journal* **2**, 145–154.

Parry, P., V. Davidson, A. Clark and Z. Guilford (2006). Labour and skills crisis could stall oil and gas boom. Technical report, BoozAllenHamilton.

Peaceman, D. W. (1978). Interpretation of well-block pressures in numerical reservoir simulation. *SPE Journal (SPE 6893-PA)* (June), 183–194.

Phan, V. and R. N. Horne (2002). Fluvial channel parameter estimation constrained to static, production, and 4d seismic data. In *SPE Annual Technical Conference and Exhibition*, San Antonio, Texas, USA.

Pohjanpalo, H. (1978). System identifiability based on the power series expansion of the solution. *Math. Biosc.* **41**, 21–33.

Press, F. and R. Siever (1994). *Understanding Earth*. New York: W.H.Freeman.

Przybysz-Jarnut, J. K., R. G. Hanea, J. D. Jansen and A. W. Heemink (2007). Application of the representer method for parameter estimation in numerical reservoir models. *Computational Geosciences* **11**(1), 73–85.

Rahon, D., P.F. Edoa and M. Masmoudi (1998). Identification of geological shapes in reservoir engineering by history matching production data. In *SPE Annual Technical Conference and Exhibition*, New Orleans, Louisiana, USA. SPE.

RamaRao, B.S., A.M. LaVenue, G. Marsily and M.G. Marietta (1995). Pilot point methodology for automated calibration of an ensemble of conditionally simulated transmissivity fields: 1. theory and computational experiments. *Water resource engineering* **31**(3), 475–493.

Ramirez, W. F. (1987). *Applications of Optimal Control Theory to Enhanced Oil Recovery*. Elsevier Science Publishers.

Reynolds, A., M. Zafari and G. Li (2006). Iterative forms of the Ensemble Kalman Filter. In *10th European Conference on the Mathematics of Oil Recovery*, Amsterdam.

Reynolds, A. C., N. He, L. Chu and D. S. Oliver (1996). Reparameterization techniques for generating reservoir descriptions conditioned to variograms and well-test pressure data. *SPE Journal* **1**(4), 413–426.

Rodrigues, J.R.P. (2006). Calculating derivatives for automatic history matching. *Computational Geosciences* **10**(1), 119–136.

Rommelse, J. R., O. Kleptova, J. D. Jansen and A. W. Heemink (2006). Data assimilation in reservoir management using the representer method and the ensemble kalman filter. In *10th European Conference on the Mathematics of Oil Recovery*, Amsterdam.

Rowley, C. W. (2005). Model reduction for fluids, using balanced proper orthogonal decomposition. *Int. J. on Bifurcation and Chaos* **15**(3), 997–1013.

Russell, T. F. and M. F. Wheeler (1983). Finite element and finite difference methods for continuous flows in porous media. In R. E. Ewing (Ed.), *The Mathematics of Reservoir Simulation*. SIAM.

Sahni, I. and R. N. Horne (2005). Multiresolution wavelet analysis for improved reservoir description. *SPEREE* **8**(1), 53–69.

Sarma, P., L. J. Durlofsky, K. Aziz and W. H. Chen (2006). Efficient real-time reservoir management using adjoint-based optimal control and model updating. *Computational Geosciences* **10**(1), 3–36.

Sarma, P., L. J. Durlofsky, K. Aziz and W. H. Chen (2007). A new approach to automatic history matching using Kernel PCA. In *SPE Reservoir Simulation Symposium (SPE 106176)*, Houston.

Scherpen, J. M. A. (1993). Balancing of nonlinear systems. *Syst. Control Lett.* **21**, 143–153.

Shah, P. C., G. R. Gavalas and J. H. Seinfeld (1978). Error analysis in history matching: The optimum level of parameterization. *SPE Journal (SPE 6508-PA)* (June), 219–228.

Singh, A. K. and J. Hahn (2007). Effect of finite-dimensional approximation on observability analysis of distributed parameter models. In *IFAC Symposium of Dynamics and Control of Process Systems*, Cancun, Mexico, pp. 199–204.

Stigter, J. D. and R. L. M. Peeters (2007). On a geometric approach to the structural identifiability problem and its application in a water quality case study. In *European Control Conference*, Koss.

Sudaryanto, B. and Y. C. Yortsos (2000). Optimization of fluid front dynamics in porous media using rate control 1. equal mobility fluids. *Physics of Fluids* **12**(7), 1656–1670.

Tarantola, A. (2005). *Inverse Problem Theory and Methods for Model Parameter Estimation*. SIAM.

Tavakoli, R. and A. C. Reynolds (2009). History matching with parameterization based on the SVD of a dimensionless sensitivity matrix. In *SPE RSS*, Texas, USA.

Tavassoli, Z., J. N. Carter and P. R. King (2004). Errors in history matching. *SPE Journal (SPE 86883-PA)* **9**(3), 352–361.

Toth, R., P. S. C. Heuberger and P. M. J. Van den Hof (2007). LPV system identification with globally fixed orthonormal basis functions. In *46th IEEE Conf. Decision and Control*, New Orleans, LA, pp. 3646–3653.

USGS World Petroleum Assessment, (2000). USGS world petroleum assessment 2000. Technical report, US Geological Survey.

Vajda, S., H. Rabitz, E. Walter and Y. Lecourtier (1989). Qualitative and quantitative identifiability analysis of nonlinear chemical kinetic models. *Chem. Eng. Comm.* **83**, 191–219.

Vakili, A., J. D. Jansen, T. E. H. Esmaiel and C. P. J. W. van Kruijsdijk (2005). On the adjoint of a nonlinear diffusion-convection equation to describe flow in porous media. In *14th SPE Middle East Oil and Gas Show and Exhibition*, Barhain.

Van den Hof, P. M. J., J. D. Jansen, G. M. van Essen and O. H. Bosgra (2009). Model-based control and optimization of large scale physical systems - challenges in reservoir engineering. In *21st Chinese Control & Decision Conference*, Guilin, China.

Van den Hof, P. M. J., J. F. M. Van Doren and S. G. Douma (2009). Identification of parameters in large scale physical model structures, for the purpose of model-based operations. In P. M. J. Van den Hof, C. Scherer, and P. S. C. Heuberger (Eds.), *Model-Based Control: Bridging Rigorous Theory and Advanced Technology*, pp. 125–146. New York: Springer.

Van Doren, J.F.M., R. Markovinović and J.D. Jansen (2004). Reduced-order optimal control of water flooding using pod. In *ECMOR IX, conference proceedings*, Cannes, France, pp. 1–8. EAGE.

Van Doren, J. F. M., S. G. Douma, P. M. J. Van den Hof, J. D. Jansen and O. H. Bosgra (2009). Identifiability: from qualitative analysis to model structure approximation. In *15th IFAC Symposium on System Identification*, St. Malo, France.

Van Doren, J. F. M., P. M. J. Van den Hof, J. D. Jansen and O.H. Bosgra (2008a). Determining identifiable parametrizations for large-scale physical models in reservoir engineering. In P. Misra M.J. Chung and H. Shim (Eds.), *7th IFAC World Congress*, Seoul, Korea, pp. 11421–11426.

Van Doren, J. F. M., J. D. Jansen, P. M. J. Van den Hof and O. H. Bosgra (2008b). Structural identifiability of grid block and geological parameters in reservoir simulation models. In *European Conference Mathematical Oil Recovery (ECMOR) XI*, Bergen, Norway, pp. 1–10.

van Essen, G. M., P. M. J. Van den Hof and J. D. Jansen (2009). Hierarchical economic optimization of oil production from petroleum reservoirs. In *Submitted to International Symposium on Advanced Control of Chemical Processes ADCHEM*, Istanbul, Turkey.

van Essen, G. M., M. J. Zandvliet, P. M. J. Van den Hof, O. H. Bosgra and J. D. Jansen (2009). Robust waterflooding optimization of multiple geological scenarios. *SPE Journal* **14**(1), 202–210. DOI: 10.2118/102913-PA.

Van Wingerden, J. W. and M. Verhaegen (2009). Subspace identification of bilinear and LPV systems for open- and closed-loop data. *Automatica* **45**(2), 372–381.

Vasco, D. W., A. Datta-Gupta and J. C. S. Long (1997). Resolution and uncertainty in hydrologic characterization. *Water Resource Engineering* **33**(3), 379–397.

Vasco, D. W., S. Soon and A. Datta-Gupta (1999). Integrating dynamic data into high-resolution reservoir models using streamline-based analytical sensitivity coefficients. *SPE Journal* **4**(4), 389–399.

Verdult, V. (2002). *Nonlinear System Identification: A State-Space Approach*. Ph. D. thesis, University of Twente, The Netherlands.

Verdult, V. and M. Verhaegen (2002). Subspace identification of multivariable linear parameter-varying systems. *Automatica* **38**(5), 805–814.

Verriest, E. I. and T. Kailath (1983). On generalized balanced realizations. *IEEE Trans. Automat. Control* **28**(8), 833.

Virnovsky, G. A. (1991). Water flooding strategy design using optimal control theory. In *European IOR Symposium*, Stavanger.

Voss, S. and T. Patel (2007). *Total, Shell Chief Executives Say "Easy Oil" Is Gone*. www.bloomberg.com.

Walter, E. (Ed.) (1987). *Identifiability of Parametric Models*. Oxford: Pergamon Press.

Watson, A. T., G. R. Gavalas and J. H. Seinfeld (1984). Identifiability of estimates of two-phase reservoir properties in history matching. *SPE Journal*.

Willcox, K. and J. Peraire (2002). Balanced model reduction via the Proper Orthogonal Decomposition. *Journal of American Institute of Aeronautics and Astronautics* **40**(11), 2323–2330.

Wills, A. and B. Ninness (2008). On gradient-based search for multivariable system estimates. *IEEE Trans. Automat. Control* **53**(1), 298–306.

Zandvliet, M. J. (2008). *Model-based Lifecycle Optimization of Well Locations and Production Settings in Petroleum Reservoirs*. Ph. D. thesis, Delft University of Technology.

Zandvliet, M. J., O. H. Bosgra, J. D. Jansen, P. M. J. Van den Hof and J. F. B. M. Kraaijevanger (2007). Bang-bang control and singular arcs in reservoir flooding. *Journal of Petroleum Science and Engineering* **58**(1&2), 186–200.

Zandvliet, M. J., M. Handels, G. M. van Essen, D. R. Brouwer and J. D. Jansen (2008). Adjoint based well placement optimization under production constraints. *SPE Journal* **13**(4), 392–399.

Zandvliet, M. J., J. F. M. Van Doren, O. H. Bosgra, J. D. Jansen and P. M. J. Van den Hof (2008). Controllability, observability and identifiability in single-phase porous media flow. *Computational Geosciences* **12**(4), 605–622.

Zhang, F., A. C. Reynolds and D.S. Oliver (2002). Evaluation of the reduction in uncertainty obtained by conditioning a 3d stochastic channel to multiwell pressure data. *Mathematical Geology* **34**(6), 715–742.

Zhu, Y. C. (2002). Estimation of an N-L-N Hammerstein-Wiener model. *Automatica* **38**(9), 1607–1614.

List of Symbols and Notation

Notation
Unless stated otherwise, scalars are denoted in this thesis with small letters in italic font, vectors are denoted in small letters in bold font, and matrices are denoted with capital letters in bold font.

Partial derivatives of a column vector $\mathbf{a} \in \mathbb{R}^n$ with respect to a column vector $\mathbf{b} \in \mathbb{R}^m$ are denoted with

$$\frac{\partial \mathbf{a}^T}{\partial \mathbf{b}} = \begin{bmatrix} \frac{\partial \mathbf{a}_1}{\partial \mathbf{b}_1} & \cdots & \frac{\partial \mathbf{a}_n}{\partial \mathbf{b}_1} \\ \vdots & & \vdots \\ \frac{\partial \mathbf{a}_1}{\partial \mathbf{b}_m} & \cdots & \frac{\partial \mathbf{a}_n}{\partial \mathbf{b}_m} \end{bmatrix} \in \mathbb{R}^{m \times n},$$

where the subscripts denote the element of the vector.

Latin symbols

$\mathbf{A}_c$, $\mathbf{B}_c$	continuous-time state-space matrices for single-phase flow
$\mathbf{A}_c^*$, $\mathbf{B}_c^*$, $\mathbf{C}_c^*$, $\mathbf{D}_c^*$	continuous-time state-space matrices for two-phase flow
$\mathbf{A}$, $\mathbf{B}$, $\mathbf{C}$, $\mathbf{D}$	discrete-time state-space matrices
$\bar{\mathbf{A}}$, $\bar{\mathbf{B}}$, $\bar{\mathbf{C}}$	weighted discrete-time state-space matrices
$\mathcal{C}_n$	controllability matrix
$\mathcal{C}_{k_i:k_f}$	LTV controllability matrix where k_i initial time step and k_f final time step
c_t	total compressibility
c_r, c_o, c_w	compressibility of rock, oil, water
D	diffusion coefficient
$\mathbb{E}$	expectation
$\bar{\mathbb{E}}$	generalized expectation of a quasi-stationary process
f_w	fractional flow function in CDE
$\mathbf{f}$, $\mathbf{g}$, $\mathbf{h}$	smooth vector fields on $\mathcal{M}$
$G(q, \boldsymbol{\theta})$	transfer function
$\mathbf{F}_o$, $\mathbf{F}_w$	fractional flow matrix of oil, water
$\mathbf{H}$	block Hankel matrix
$\mathbf{h}(\boldsymbol{\theta}, \mathbf{u}; \mathbf{x}_0)$	discrete time, nonlinear dynamical model parameterized in $\boldsymbol{\theta}$
h_w	nonlinear function of water saturation in CDE

$\mathbf{I}$	identity matrix
$\mathbf{J}_p$, $\mathbf{J}_q$	matrix of well indices
J	Fisher Information Matrix
J_{con}	minimal required input energy
J_{obs}	maximal produced output energy
k_{ro}, k_{rw}	relative permeability of oil, water
$k_{r0,o}$, $k_{r0,w}$	end-point relative permeability of oil, water
k	absolute permeability
L	length of 1D reservoir model
$\mathbf{M}(k, \boldsymbol{\theta})$	Markov parameters
$\overrightarrow{\mathbf{M}}(k, \boldsymbol{\theta})$	vector of decomposed Markov parameters (MISO)
$\mathcal{M}$	state-space manifold
m	number of inputs
N_{gb}	number of grid blocks
n	number of states
n_o, n_w	Corey exponents of oil and water
$\mathcal{O}_n$	observability matrix
$\mathcal{O}_{k_i:k_f}$	LTV observability matrix where k_i initial time step and k_f final time step
$\mathbf{P}_v$	covariance matrix of noise $\mathbf{v}$
$\mathbf{P}_{\boldsymbol{\theta}}$	covariance matrix of $\boldsymbol{\theta}$
$\mathcal{P}$	controllability Gramian for infinite time
$\mathcal{P}_n$	controllability Gramian for finite time
$\mathcal{P}_e$	empirical controllability Gramian
P_c	capillary pressure
$\mathbf{p}_1$	vector of pressures in grid blocks without wells
$\mathbf{p}_2$	vector of pressures in grid blocks with flow-rate controlled wells
$\mathbf{p}_3$	vector of pressures in grid blocks with pressure controlled wells
$\breve{\mathbf{p}}_{well}$	vector of prescribed pressures
$\bar{\mathbf{p}}_{well}$	vector of measured pressures
$\mathbf{p}$	vector of grid block pressures
$\mathbf{p}_k$	vector of grid block pressures at time-step k
P	Peclet number
p	number of outputs
p_t	fluid pressure
$\mathcal{Q}$	observability Gramian for infinite time
$\mathcal{Q}_n$	observability Gramian for finite time
$\mathcal{Q}_e$	empirical observability Gramian
$\breve{\mathbf{q}}_{well}$	vector of prescribed flow rates
$\bar{\mathbf{q}}_{well}$	vector of measured flow rates
$\mathbf{q}$	well flow rates
q	forward shift operator
q	number of parameters
q_t	flow rate per unit volume
q_o, q_w	flow rate per unit volume of oil and water
$\mathbf{R}_u(i)$	autocovariance function of the input
$\mathbb{R}$	set of real numbers
r_w	wellbore radius

$\overrightarrow{\mathbf{S}}(\boldsymbol{\theta})$	map containing decomposed Markov parameters
S	skin factor
$\bar{S}$	variable in Corey model
s	water saturation
s_{or}	residual oil saturation
s_{wc}	connate water saturation
$\mathbf{T}$	transformation matrix
$\mathbf{T}_{ij}$	transmissibility matrix, $i = 1, 2, 3$, $j = 1, 2, 3$
$\mathbf{T}_o$, $\mathbf{T}_w$	transmissibility matrix of oil, water
t	time
$\mathbf{U}$	matrix with left singular vectors
$\mathbf{U}_{1:z}$	weighted vector with first z left singular vectors of $\mathbf{U}$
$\tilde{\mathbf{U}}_i$	i-th column of $\mathbf{U}$
$\mathbf{u}$	vector of inputs
$\mathbf{u}_k$	vector of inputs at time step k
$\mathbf{V}$	matrix with right singular vectors
$\mathbf{V}_{ii}$	accumulation matrix, $i = 1, 2, 3$
$\mathbf{V}_{wp}$,$\mathbf{V}_{ws}$,$\mathbf{V}_{op}$,$\mathbf{V}_{os}$	accumulation matrices
V	cost function
V_p	cost function which includes prior parameter vector
$\mathbf{v}$	output noise
v	total liquid velocity
$\mathbb{X}^{\text{con}}$	controllable subspace
$\mathbb{X}^{\text{unobs}}$	unobservable subspace
$\mathbf{x}$	vector of states
$\mathbf{x}_k$	vector of states at time step k
$\mathbf{x}'_k$	vector of dual states at time step k
$\check{\mathbf{x}}_k$	vector of transformed states at time step k
$\mathbf{y}$	vector of outputs (measured output)
$\mathbf{y}_k$	vector of outputs at time step k
$\hat{\mathbf{y}}$	vector of predicted outputs

Greek symbols

γ	scalar damping factor
Δt	discretization time-step
$\boldsymbol{\epsilon}(\boldsymbol{\theta})$	vector of prediction errors
ϵ	constant
$\boldsymbol{\theta}$	vector of parameters
$\boldsymbol{\theta}_{ch}$	vector of channel parameters
$\boldsymbol{\theta}_{gb}$	vector of grid block parameters
$\hat{\boldsymbol{\theta}}$	vector of estimated parameters
θ_i	i-th parameter
$\boldsymbol{\Lambda}$	matrix with eigenvalues on diagonal
$\boldsymbol{\Lambda}_\theta$	weighting matrix
λ_i	i-th eigenvalue
λ_{min}	most negative eigenvalue

λ_o, λ_w	mobility of oil, water
μ	viscosity
μ_o, μ_w	viscosity of oil, water
$\boldsymbol{\rho}$	reduced-order parameter vector
$\boldsymbol{\Sigma}$	matrix with singular values on diagonal
σ_i	i-th singular value
σ_e^2	variance of white noise input
ϕ	porosity

Abbreviations

CFL	Courant-Friedrich-Lewy
CDE	Convection Diffusion Equation
EnKF	Ensemble Kalman Filter
EVD	Eigenvalue Decomposition
LTI	Linear Time Invariant
LTV	Linear Time Varying
MIMO	Multiple Inputs, Multiple Outputs
MISO	Multiple Inputs, Single Output
ode	ordinary differential equation
pde	partial differential equation
PEM	Prediction Error Methods
POD	Proper Orthogonal Decomposition
SISO	Single Input, Single Output
SVD	Singular Value Decomposition

List of Publications

Journal papers

Van Doren, J. F. M., Zandvliet, M. J., Jansen, J. D., Van den Hof, P. M. J., Bosgra, O. H. (2010). Controllability and observability in two-phase porous media flow. *In preparation.*

De Jager, G., J. F. M. Van Doren, J. D. Jansen, and S. M. Luthi (2008). An evaluation of relevant geological parameters for predicting the flow behavior of channelized reservoirs. *Petroleum Geosciences* **15** (4):345-354.

Zandvliet, M. J., J. F. M. Van Doren, O. H. Bosgra, J. D. Jansen, and P. M. J. Van den Hof (2008). Controllability, observability and identifiability in single-phase porous media flow. *Computational Geosciences* **12**:605-622.

Van Doren, J. F. M., R. Markovinović, J. D. Jansen (2006). Reduced-order optimal control of water flooding using proper orthogonal decomposition. *Computational Geosciences* **10**:139-158 .

Book chapters

Van den Hof, P. M. J., J. F. M. Van Doren, S. G. Douma (2009). Identification of parameters in large scale physical model structures, for the purpose of model-based operations. In: P.M.J. Van den Hof et al. (Eds.), Model-Based Control: Bridging Rigorous Theory and Advanced Technology, Springer-Verlag, New York, USA, ISBN 978-1-4419-0894-0, pp. 125-146.

Jansen, J. D., J. F. M. Van Doren, M. Heidary-Fyrozjaee, Y. C. Yortsos (2009). Front controllability in two-phase porous media flow. In: P.M.J. Van den Hof et al. (Eds.), Model-Based Control: Bridging Rigorous Theory and Advanced Technology, Springer-Verlag, New York, USA, ISBN 978-1-4419-0894-0, pp. 203-219.

Conference proceedings

Van Doren, J. F. M., P. M. J. Van den Hof, J. D. Jansen, and O. H. Bosgra (2008). Identifiability: from qualitative analysis to model structure approximation. In Proc. *System Identification 2009 (SysID)*, St. Malo, France.

Van Doren, J. F. M., J. D. Jansen, P. M. J. Van den Hof, and O. H. Bosgra (2008). Structural identifiability of grid block and geological parameters in reservoir simulation models. In Proc. *11th European Conference on Mathematics in Oil Recovery (ECMOR IX)*, Bergen, Norway.

De Jager, G., J. F. M. Van Doren, and S. M. Luthi(2008). Efficient model selection based on connectivity for geologically complex reservoirs. In Proc. *70th EAGE Conference & Exhibition incorporating SPE EUROPEC*, Rome, Italy.

Van Doren, J. F. M., P. M. J. Van den Hof, J. D. Jansen, and O. H. Bosgra (2008). Determining identifiable parameterizations for large-scale physical models in reservoir engineering. In Proc. *IFAC World Congress*, Seoul, Korea.

Van Doren, J. F. M., G. De Jager, J. D. Jansen, S. M. Luthi, and S. G. Douma (2007). Sensitivity of geostatistical modeling parameters on reservoir flow behavior. In Proc. *EAGE Petroleum Geostatistics*, Cascais, Portugal.

Van Doren, J.F.M., R. Markovinović, and J. D. Jansen (2006). Use of POD in control of flow through porous media. In Proc. *European Conference on Computational Fluid Dynamics - ECCOMAS CFD*, Egmond aan Zee, The Netherlands.

Van Doren, J.F.M., R. Markovinović, and J.D. Jansen (2004). Reduced-order optimal control of waterflooding using POD. In Proc. *9th European Conference on Mathematics in Oil Recovery (ECMOR IX)*, Cannes, France.

Seminar

J.F.M. Van Doren, J.D. Jansen, M. Zandvliet, P.M.J. Van den Hof, O.H. Bosgra (2009). Identifiability, controllability and observability in hydrocarbon reservoir models. Mini-symposium contribution presented at the 2009 SIAM Conference on Mathematical and Computational Issues in the Geosciences, Leipzig, Germany, 14-18 June 2009.

Summary

The demand for petroleum is expected to increase in the coming decades, while the production of petroleum from subsurface reservoirs is becoming increasingly complex. To meet the demand petroleum reservoirs should be operated more efficiently. Recent technological developments, such as subsurface valves and measurement devices, provide possibilities to accomplish this, but it is not yet clear how these can be optimally used. Physics-based petroleum reservoir models that describe the flow in subsurface porous media can play an important role here. In this thesis possibilities are investigated to determine on one hand models with a complexity that is suitable for model-based operation, i.e. the relevant dynamic processes can be adequately described, and on the other hand models that only contain parameters that can be validated by production measurements.

The first part of the research objective is about the most relevant dynamics of the model. These are to a large extent determined by the controllability and observability properties of the model. The Hankel singular values, which are related to controllability and observability, decrease rapidly for one-phase and two-phase reservoir models. This indicates that reservoir models behave as models of much lower order than the currently used models that result after spatial and temporal discretization. This explains why models of lower order are found to be suitable for model-based operation. Based on the analyzed homogenous and heterogeneous examples we conclude that the dynamics of the oil-water front and the position of the wells determine the controllability and observability properties of the reservoir. Therefore, for fixed well positions, reduced-order models of flow in porous media should focus on correctly modeling the fluid front(s). The analysis of controllability and observability can aid in finding optimal positions for a well to increase production, or finding optimal positions of measurement devices.

Then we turn to the second part of the research objective. From a model-based operations point of view (monitoring, control, optimization) it makes sense to limit the complexity of an identified model to a level where the model can be reliably validated from measurement data. If not, the parameter estimates might be highly determined by the (random) experiment that is done, leading to unreliable model predictions. In identification this problem is addressed by the notion of identifiability of a model structure, and is directly coupled to the variance of estimated pa-

rameters. Identifiability and structural identifiability have been quantified in this thesis, and used to determine which model parameters can be reliably estimated from measurement data. This allows to approximate the model structure so as to achieve identifiability, while retaining the interpretation of the physical parameters. Identifiability is also related to iterative optimization algorithms (e.g. Gauss-Newton and Steepest-Descent) and recursive (sequential) parameter estimation methods that minimize a cost function consisting of the mismatch between the measurements and the simulated measurements. In a Bayesian setting, in which a priori knowledge is included in the cost function, there seems to be no issue regarding identifiability. But in this setting the (combinations of) parameters, which cannot be estimated from measurements, are determined by the a priori knowledge.

From the analysis of one-phase and two-phase reservoir models it can be concluded that these are not identifiable from production measurements (i.e. pressure and phase-rate measurements in the wells). The parameter values in these models are to a large extent based on qualitative geological information, and only to a smaller extent based on information from production measurements. This underpins the need to use information from other measurement types. Pressure measurements only contain information about grid block permeabilities in an area close to the wells in which measurements are taken, and phase-rate measurements (after water breakthrough) contain information about grid block permeabilities in the area between the injection and production wells. Overall, we conclude that the information content of the production measurements is insufficient to reliably estimate the permeability distribution and depends to a large extent on the initial choice of the parameter values. This also holds for geological, object-based channel parameterizations. The values of parameter combinations that cannot be estimated from measurements, i.e. directions in parameter space that are not identifiable, can be freely altered without changing the value of the cost function. These can be considered as additional degrees of freedom in the parameter estimation problem that can be used to include geological information.

Samenvatting

De vraag naar olie en gas neemt de komende decennia naar verwachting toe, terwijl de productie van olie en gas steeds complexer wordt. Om te kunnen voldoen aan de vraag moet de winning van petroleum uit ondergrondse reservoirs efficiënter worden. Recente technologische ontwikkelingen, zoals ondergrondse kleppen en sensoren, bieden hiertoe mogelijkheden, maar het is nog onduidelijk hoe deze optimaal benut kunnen worden. Op fysica gebaseerde modellen, die de stroming in ondergrondse, poreuze gesteentes beschrijven, kunnen hierin een belangrijke rol spelen. In dit proefschrift worden mogelijkheden onderzocht om aan de ene kant modellen te bepalen met een complexiteit die voldoende is om te worden gebruikt voor model-gebaseerde operatie van petroleumreservoirs, dat wil zeggen de relevante dynamische processen worden adequaat beschreven, en aan de andere kant modellen met parameters die kunnen worden gevalideerd door meetgegevens, in dit geval productiemetingen.

Het eerste deel van het onderzoeksdoel gaat over de meest relevante dynamica van de modellen. Deze wordt voornamelijk bepaald door de regelbaarheid- en waarneembaarheideigenschappen van het model. De Hankel singuliere waarden, die gerelateerd zijn aan regelbaarheid en waarneembaarheid, dalen snel voor eenfase en twee-fase reservoirmodellen. Dit geeft aan dat de modellen zich gedragen als modellen van veel lagere orde dan de huidig gebruikte modellen die ontstaan na ruimtelijke en temporele discretisatie. Dit verklaart waarom lage-orde modellen nog steeds geschikt blijken zijn voor model-gebaseerde operatie. Op basis van de geanalyseerde voorbeelden met homogene en heterogene permeabiliteit concluderen we dat de regelbaarheid en waarneembaarheid grotendeels worden bepaald door de dynamiek van het olie-water front en de positie van de putten. Daarom moeten lage-orde reservoirmodellen met vaste putposities zich concentreren op het juist modelleren van het vloeistoffront. De analyse van regelbaarheid en waarneembaarheid kan ook helpen bij het vinden van een optimale positie van een put om de productie te verhogen, of het vinden van een optimale positie om sensoren te plaatsen.

Het tweede deel van het onderzoeksdoel beschrijft dat het model uit een oogpunt van model-gebaseerde operaties (waarnemen, regelen, optimalisatie) uitsluitend parameters moet bevatten die kunnen worden gevalideerd door meetgegevens. Als dit niet het geval is, dan kunnen de parameterschattingen sterk worden bepaald door het willekeurige experiment dat wordt uitgevoerd. Dit kan leiden tot onbetrouwbare modelvoorspellingen. In identificatie wordt dit

probleem geadresseerd door de notie van identificeerbaarheid van een modelstructuur, wat direct gekoppeld is aan de variantie van de geschatte parameters. In dit proefschrift worden identificeerbaarheid en structurele identificeerbaarheid gekwantificeerd en gebruikt om te bepalen welke modelparameters betrouwbaar kunnen worden geschat op basis van meetgegevens. Dit laat toe dat de modelstructuur benaderd kan worden, teneinde te komen tot een identificeerbare modelstructuur met fysieke parameters. Ook wordt aangetoond dat identificeerbaarheid een rol speelt in iteratieve (bv. Gauss-Newton en Steepest-Descent) en recursieve / sequentiële parameterschattingmethoden, die de kostenfunctie minimaliseren bestaande uit het verschil tussen de metingen en de gesimuleerde metingen. In een Bayesiaanse omgeving, waarbij a priori kennis is opgenomen in de kostenfunctie, lijkt er geen probleem met betrekking tot identificeerbaarheid te zijn. Maar in dit geval worden de (combinaties van) parameters, die niet kunnen worden geschat met behulp van meetgegevens, bepaald door a priori kennis.

Uit de analyse van een-fase en twee-fase reservoirmodellen blijkt dat ze niet identificeerbaar zijn met behulp van productiemetingen (i.e. druk- en debietmetingen in de putten). De parameterwaarden in deze modellen zijn in grote mate gebaseerd op kwalitatieve geologische informatie, en slechts in mindere mate gebaseerd op informatie van de productiemetingen. Dit onderbouwt de noodzaak om informatie van andersoortige metingen te gebruiken. Drukmetingen bevatten alleen informatie over de permeabiliteit dicht bij de putten waarin wordt gemeten, en debietmetingen bevatten (na waterdoorbraak) alleen informatie over de permeabiliteit in het gebied tussen de injectie- en productieputten. Algemeen concluderen we dat de informatie van productiemetingen onvoldoende is om een betrouwbare schatting van de permeabiliteit te geven, en deze hangt voor een groot deel af van de initiële keuze van de parameterwaarden. Dit geldt ook voor geologische, object-gebaseerde kanaal parametrisaties. De waarden van de parametercombinaties die niet kunnen worden geschat op basis van meetgegevens, d.w.z. richtingen in de parameterruimte die niet identificeerbaar zijn, kunnen worden veranderd zonder dat de waarde van de kostenfunctie verandert. Deze kunnen worden beschouwd als extra vrijheidsgraden in het parameterschattingsprobleem en worden gebruikt om bijvoorbeeld geologische informatie toe te voegen.

About The Author

Jorn Van Doren was born on December 21, 1978 in Sittard, the Netherlands. He received his secondary education between 1991 and 1997 at the "Jeanne d'Arc College" (gymnasium) in Maastricht. From 1997 to 2004 he studied Applied Earth Sciences at Delft University of Technology. The title of his MSc thesis was "Reduced-order optimal control of water flooding using Proper Orthogonal Decomposition". Hereafter he joined the Delft Center for Systems and Control and Department of Petroleum Engineering as a PhD student in the VALUE and ISAPP programmes. During his PhD project he took graduate courses at the Dutch Institute for Systems and Control (DISC) and received the DISC certificate. In 2009 he has joined Shell International Exploration and Production as a reservoir engineer in quantitative reservoir management.